SIMULATION OF HYDRODYNAMIC FRAGMENTATION FROM A FUNDAMENTAL AND AN ENGINEERING PERSPECTIVE

A Thesis
Presented to
The Academic Faculty

by

Nayan Patel

In Partial Fulfillment
of the Requirements for the Degree
Doctor of Philosophy in the
School of Aerospace Engineering

Georgia Institute of Technology
August 2007

SIMULATION OF HYDRODYNAMIC FRAGMENTATION FROM A FUNDAMENTAL AND AN ENGINEERING PERSPECTIVE

Approved by:

Prof. Suresh Menon, Committee Chair
School of Aerospace Engineering
Georgia Institute of Technology

Prof. Lakshmi Sankar
School of Aerospace Engineering
Georgia Institute of Technology

Assoc. Prof. Jerry Seitzman
School of Aerospace Engineering
Georgia Institute of Technology

Prof. Paul Neitzel
School of Mechanical Engineering
Georgia Institute of Technology

Prof. Jechiel Jagoda
School of Aerospace Engineering
Georgia Institute of Technology

Date Approved: 14 June 2007

To my Parents, Bena-masi, & Daku-masi

ACKNOWLEDGEMENTS

I would like to express my deep and sincere gratitude to my research advisor, Professor Menon, for his understanding nature, encouragement, guidance, and infinite patience during the course of my graduate studies. Special thanks to my thesis Committee members: Professor Jagoda, Professor Seitzman, Professor Sankar, and Professor Neitzel for evaluating this work and giving excellent suggestions.

I would also like to thank my sponsors General Electric (GE), National Aeronautics and Space Administration (NASA), and Army Research Office (ARO). Without their financial support and computational resources, this research would not have been possible. In addition, I want to thank Department of Defense (DoD) Major Shared Resources Centers (MSRC) at the Naval Oceanographic Office (NAVOCEANO) for providing the High Performance Computing (HPC) resources.

This work is a collaborative effort of everyone, past and present, at the Computational Combustion Laboratory (CCL). Special thanks (in no particular order) to Mr. Franklin Genin, Dr. Mehmet Kirtas, Dr. Vaidyanathan Sankaran, Dr. Ion Porumbel, Mr. Matthieu Masquelet, Ms. Nathalie Tramecourt, Ms. Ayse Gungor, Mr. Radu Cazan, Dr. Chris Stone, Mr. Jean-Pierre (JP) de la Croix, Mr. Sumit Soni, Dr. Srikant Srinivasan, and Dr. Gilles Eggenspieler. Special thanks are also reserved for Dr. Homayoon Feiz for unflinching willingness to help in matters of academia and others alike.

I cannot end without thanking my family, on whose constant encouragement and love I have relied throughout my graduate and undergraduate studies. I indebted to my parents for creating an environment conducive for learning and pursuing my dreams. I owe my loving thanks to my wife, Ishita, whose constant encouragement and understanding made this effort manageable.

TABLE OF CONTENTS

LIST OF TABLES

LIST OF FIGURES

NOMENCLATURE

Roman Symbols

$\mathbf{A}$	Jacobian matrix
A	Arrhenius pre-exponential constant
B_o	Bond number
Ca	Capillary number
C_ϵ	model coefficient for subgrid dissipation
C_ν	model coefficient for turbulent viscosity
c	speed of sound
c_p	specific heat at constant pressure per unit mass
c_v	specific heat at constant volume per unit mass
C_D	Drag coefficient
D_k	$k-$th species diffusion constant
D^{sgs}	dissipation of turbulent kinetic energy
$d\mathbf{A}_i$	$i-$th cell face area vector
E	total energy per unit mass
E_a	activation energy
E_o	E*ö*tv*ö*s number
e	internal energy per unit mass
$\mathbf{F}$	flux vector in $x-$direction
f	flux component on a cell face
$\mathbf{G}$	flux vector in $y-$direction
H	total enthalpy per unit mass
$\mathbf{H}$	flux vector in $z-$direction

H_i	enthalpy flux
h	specific enthalpy per unit mass
k	turbulent kinetic energy
l_i	left eigenvector
L	characteristic length scale
L_2	Error norm
La	Laplace number
ℓ	integral length scale
Le	Lewis number
$\overrightarrow{\mathbf{m}}$	volume fraction gradient vector
M, M^{-1}	Grid transformation matrix
MW	molecular weight
$\overrightarrow{\mathbf{n}}$	normalized vector
N_s	total number of species
P^{sgs}	production of turbulent kinetic energy
p, P	pressure
Pr	Prandtl number
$\mathbf{Q}$	state vector
q_i	heat flux
Re	Reynolds number
R	mixture gas constant
$\mathbf{R}$	Roe dissipative flux vector
r	spatial position
r_i	right eigenvector
S_{ij}	rate of strain tensor
s	spatial coordinate along the LEM line
T	temperature

t	time
U	characteristic velocity
u, v, w, u_i	Cartesian velocity vector components
u'	rms velocity
v'	turbulent intensity
u'_{sgs}	subgrid scale turbulence intensity
V	volume
$\mathbf{V}$	primitive state vector
$V_{i,m}$	diffusion velocity of species m
$\mathbf{W}$	conservative state vector
We	Weber number
x, y, z	Cartesian coordinate directions
y_i	$i-$th species/phase mass fraction
$Y_{i,m}$	flux of species m
Z, Oh	Ohnesorge number

Greek Symbols

α	thermal diffusivity
α_k	phase volume fraction
γ	entropy exponent
$\overline{\Delta}$	grid size
δ_{ij}	Kronecker delta
$\Delta h'_f$	specific heat
Δh_f	enthalpy of formation per unit mass
ε	specific internal energy
ϕ	arbitrary function, equivalence ratio

$\Phi_{i,m}$	convective mass flux of species m
η	Kolmogorov length scale
$\theta_{i,m}$	diffusive flux of species m
κ	thermal conductivity, local interface curvature
λ, λ_i	stirring frequency, $i-$th eigenvalue
μ	dynamic viscosity
ν	kinematic viscosity
ρ	density
τ	time scale
τ_{ij}	viscous stress tensor
σ	surface tension coefficient
σ_{ij}	viscous work tensor
ς_i	wave strengths
ξ, η, ζ	spatial directions in computational space
ψ_{ij}	capillary stress tensor
ω	turbulent frequency
ω_n	interface oscillation frequency of n^{th} mode
$\dot{\omega}$	reaction rate per unit volume

Subscripts

b	breakup quantity
c	center-of-mass quantity
g	gas-phase quantity
i, j, k	Cartesian tensor indices, species or phase indices
I	material interface quantity
inj	injection quantity

l	liquid-phase quantity
LES	quantity at the LES level
m	chemical index
n	time step index
R, L	right and left states
t, T	turbulent quantity
∞	quantity at infinity downstream (or far-field)

Superscripts

0	reference quantity
LEM	quantity at the LEM level
sgs	subgrid scale
$stir$	stirring
$test$	test filter scale

Other Symbols

∂	partial derivative operator
∇	gradient operator
$\nabla\cdot$	divergence operator
$\sum$	summation operator
Π	product operator
Δ	difference operator
$\pounds$	characteristic wave amplitude
$\mathscr{M}$	Mach number
$\tilde{}$	Favre spatial filter

$\widehat{}$	test filter
$\bar{}$	space average
$'$, $''$	fluctuating quantity

Abbreviations

CFD	Computational Fluid Dynamics
CFL	Courant-Friedrichs-Lewy number
CPU	Central Processing Unit
CRZ	Central Recirculation Zone
CSF	Continuum Surface Force
DDB	Droplet Deformation and Breakup
DDM	Discrete Droplet Model
DIM	Diffuse Interface Methods
DNS	Direct Numerical Simulation
FI	Takeno Flame Index
EBU	Eddy Break-Up (combustion) model
EOS	Equation of State
KH	Kelvin-Helmholtz aerodynamic breakup model
LDI	Lean-Direct Injection technique
LDKM	Localized Dynamic k-equation Model
LEM	Linear-Eddy Mixing model
LES	Large-Eddy Simulation
LS	Level-Set method
LODI	Local One-Dimensional Inviscid
MPI	Message Passing Interface
MUSCL	Monotone Upstream Centered Schemes for Conservation Laws

PDE	Partial Differential Equation
PDF	Probability Density Function
PPM	Piecewise Parabolic Method
PVC	Precessing Vortex Core
RANS	Reynolds Averaged Navier - Stokes
RT	Rayleigh-Taylor Instability
SMD	Sauter-Mean Diameter
SMR	Sauter-Mean Radius
SSF	Stochastic Separated Flow
TAB	Taylor Analogy Breakup model
TKE	Turbulent Kinetic Energy
TPS	Time-per-Step
TV	Total Variation
rms	Root Mean Square, variance
VBB	Vortex Breakdown Bubble
VOF	Volume of Fluid method

SUMMARY

Liquid fragmentation phenomenon is explored from both a fundamental (fully resolved) and an engineering (modeled) perspective. The dual objectives compliment each other by providing an avenue to gain further understanding into fundamental processes of atomization as well as to use the newly acquired knowledge to address practical concerns.

A compressible five-equation interface model based on a Roe-type scheme for the simulation of material boundaries between immiscible fluids with arbitrary equation of state is developed and validated. The detailed simulation model accounts for surface-tension, viscous, and body-force effects, in addition to acoustic and convective transport. The material interfaces are considered as diffused zones and a mixture model is given for this transition region. The simulation methodology combines a high-resolution discontinuity capturing method with a low-dissipation central scheme resulting in a hybrid approach for the solution of time- and space-accurate interface problems. Such an approach is designed to retain advantages of each scheme in different parts of the flow field and enabling the combined scheme to resolve diverse effects. The main advantage of the model is its simplicity of algorithm both as a single solver for different phases as well as demonstrated multi-dimensional capability. The approach also provides a comprehensive consideration in a cost-effective manner of several processes inherent to interface dynamics.

Several multi-dimensional test cases are considered over a wide range of physical situations involving capillary, viscosity, and gravity effects with simultaneous presence of large viscosity and density ratios. Laplace-Young pressure jump across material interface is quantified and compared with analytical estimates. Dynamics of interface

movement of initially deformed elliptical droplet is also considered. Four stages of energy interchange modes are visualized and its frequency is compared with theoretical estimates. Bubble rise in liquid bulk is found to recover different shape regimes following Clift *et al.* Gravitation induced drop breakup undergoes large deformation of material interface and eventually fragments into multiple droplets. Drag over both a cylinder and a sphere are studied for a range of Reynolds and Weber numbers. Transient drag is observed to be larger than steady state drag based on rigid sphere at the same Reynolds number. Presence of "Hill Vortex" is also confirmed in the case of a non-deforming drop. Head-on binary collision case indicated the impact of initial momentum on the collision outcome. Coalescence is noted when variation in capillary-induced surface energy does not exceed the initial surface energy. Based on multiple test cases, the model is shown to accurately capture interface dynamics as well as to deal with dynamic appearance and disappearance of material boundaries.

Simulation of atomization processes and its interaction with the flow field in practical devices is the secondary objective of this study. Three modeling requirements are identified to perform Large-Eddy Simulation (LES) of spray combustion in engineering devices. These requirements involved (i) parameter-free simulation approach, (ii) realistic inflow boundary information, and (iii) inclusion of atomization processes. Accordingly, LES of an experimental liquid-fueled Lean Direct Injection (LDI) combustor is performed using a subgrid mixing and combustion model. This approach has no adjustable parameters and the entire flow-path through the inlet swirl vanes is resolved. The inclusion of the atomization aspects within LES eliminates the need to specify dispersed-phase size-velocity correlations at the inflow boundary.

Kelvin-Helmholtz (or aerodynamic) breakup model by Reitz is adopted for the combustor simulation. Two simulations (with and without breakup) are performed and compared with measurements of Cai *et al.* Time-averaged velocity prediction

comparison for both gas- and liquid-phase with available data show reasonable agreement. The major impact of breakup is on the fuel evaporation in the vicinity of the injector. Further downstream, a wide range of drop sizes are recovered by the breakup simulation and produces similar spray quality as in the no-breakup case.

CHAPTER I

INTRODUCTION AND REVIEW

1.1 Introduction

Multiphase flows with distinct interfaces between fluids of different physical or thermodynamic properties occur in many natural and industrial processes. Fluid jets in automotive engines, industrial combustors, spray deposition, and casting applications are few application areas involving flows with interfaces. Of particular interest to the combustion community, is the understanding, prediction and control of atomization processes in internal combustion engines and gas-turbine combustors. Atomization and the spray-distribution pattern control the evaporation, mixing and combustion, and hence are key to a fuel-efficient, non-polluting combustor design. Moreover, the interface between the fluids is the region where complex physics, such as heat and mass transfer, surface-tension effects, etc., may occur.

The fundamental mechanisms of atomization have been under extensive theoretical and experimental study for more than a century. Reviews of liquid atomization mechanisms were provided by Reitz and Bracco [168], Pilch *et al.* [151], Hsiang and Faeth [77], Chigier [32], Chigier and Reitz [33], and Eggers [44]. In spite of the importance and wide range of application areas of atomization, the mechanisms of breakup are still not well understood even though extensive studies on multiple fronts (measurement, analytical, computational) have been documented. Based on experimental observations, researchers have tried to divide the atomization phenomena into different regimes, where each regime is dominated by specific breakup mechanism. For example, Reitz and Bracco [168] addressed four major regimes of for liquid jets, viz:

the Rayleigh, the First Wind, the Second Wind, and the Atomization regime. Detailed description of these regimes have been documented elsewhere [32].

Analytical methods, including linear and non-linear theories, have also been used to study the instability and disintegration aspects. One of the first mathematical descriptions of the jet instability process was introduced by Lord Rayleigh in 1878. He used a linear theory to study low-speed capillary jets in absence of viscous effects and found that there is an optimal wavelength for perturbations grow the fastest, and sets the typical size of drops. A general linear theory for jet instability was summarized by Reitz and Bracco [168]. Non-linear theories were investigated by Chaudary and Redekopp [27, 28]. Development of non-linear theories were inspired by the fact that the linear theory failed to predict the occurrence of the satellite (distinct entity formed after breakup and disassociated from the parent or main body) drops seen in the Rayleigh regime [168]. However, both linear and non-linear theories have difficulty accounting for effects of finite initial disturbances, turbulence, and other effects that may have significant impact on the breakup processes. Therefore, computational methods have become indispensible in predictions of instability and disintegration processes.

Two major approaches have been used extensively in computational spray simulations: Lagrangian and Eulerian methods. In the Lagrangian [42, 47] method, the liquid jet/drop is represented in form of a discrete particle and its motion is governed by Newtonian mechanics. This amounts to a statistical (Monte-Carlo) formulation. However, interactions between carrier fluid (gas) and discrete particle (liquid drop) are based on empirical relations as the flow field in and around the particle typically is not resolved. This amounts to a so-called point-volume approach [114]. The Eulerian [84, 40] method, on the other hand, resolves the detailed structures within and around the liquid jet/drop. Transport equations are used to track the mean properties of the two phases and the liquid phase is represented by some indicator function. Examples

of Eulerian methods (described later) include Volume of Fluid (VOF) method [76], the level-set (LS) method [141], and the vortex method [109, 30]. A common disadvantage of these methods is that they need a very fine mesh to resolve the liquid-gas interface.

Several engineering models, based on the Lagrangian [42, 47] approach, such as the Taylor Analogy Breakup (TAB) [138], wave-breakup [169] model and other theories [8, 144] have successfully calculated macroscopic post-breakup features such as spray penetration and spray angle. But they do not reproduce detailed features of atomization, such as droplet sizes and velocities. Moreover, the primary breakup mechanisms related to turbulence within the injector nozzle, cavitation and Kelvin-Helmholtz instability in the sheared liquid-gas interface cannot be captured by the aforementioned engineering breakup models. It is also not clear what triggers the onset of these mechanisms and its relationship to the injector design, and the properties (density, viscosity ratios, surface-tension, etc.) of the fluids.

Experimental investigation of these interfacial processes are hindered by the presence of highly transient small-scale (10^{-8} m) processes [148, 44]. Moreover, the onset of atomization rapidly shrouds the liquid jet with small droplets, preventing optical access to the internal region where the atomization is occurring. These difficulties are particularly severe when the injection velocities are higher and the spray cone angles are narrower.

Numerical simulations are, in principle, ideally suited to study these complex interfacial flows. However, because of the limitations of the numerical approaches, in dealing with the local lack of smoothness of the material properties across the interfaces, it still remains a challenge to develop an affordable, yet complete methodology for simulating such flows. The complexity of physics involved at interfaces precludes any simple but comprehensive mathematical model, and thus proper simulation of

the atomization phenomena and spray formation in full-scale devices is still a daunting task. Nonetheless, there have been several studies [67, 76, 218] to model and simulate multi-fluid flows with interfaces.

Various approaches [187] on modeling fluid flows with free surface/interfaces can be classified primarily as Lagrangian- or Eulerian-based. In general, Lagrangian-based [59, 216] methods track the interface (discretized with markers which are moved at local velocity) and offer its precise location. However, they are not suited for flows that involve merging and separation of the interface. An excellent review of these methods is given in Benson [14]. In contrast, the Eulerian-based [76, 141, 4] methods capture, in lieu of tracking, the interface on a fixed computational grid. These are better suited for flows with complex topological changes and interface deformations. Also, no additional algorithmic details are required to account for interface deformations and their extension to three spatial dimensions is straight-forward. The Volume-of-Fluid method [76] and the level set method [141] are examples of Eulerian-based methods that have been widely used within an incompressible framework [63, 223]. Both methods employ a phase function, volume fraction in the case of VOF and a distance function for the LS method, to track the interface based on a transport equation.

The Level-Set approach was originally introduced by Osher and Sethian [141] and has since been applied to a wide variety of problems. In the LS method, the interface is represented as the level-set of some function ϕ, which represents the signed distance from the interface at every instant. A conservation equation for ϕ is used to track the interface. Level-set methods have the the advantage of not requiring any special procedures to model topological changes of the interface. However, the volume/mass of the fluids are not automatically conserved and loss of mass has been reported in some of the studies using this approach [200]. Moreover, expensive reinitialization procedures of the level-set function ϕ is required [152].

In the VOF approach, an indicator function such as the volume occupied by each of the fluids in a cell is tracked explicitly. As a result, the volume fraction can be used to approximate the location of the interface at each instant. VOF methods also share the advantage of not requiring any special procedures to model topological changes of the interface such as the droplet break-up and coalescence processes. In addition, they conserve volumes (and thereby, mass, although strictly valid only for incompressible flows) more accurately than the other approaches. VOF methods have been in use for several decades. One of the early algorithms using VOF was reported by Noh and Woodward [136]. Another variation of this approach was used by Hirt and Nichols [76]. The fundamental difficulties that still remain with the use of VOF and LS methods is that, it is very difficult to simulate flows that are simultaneously at (1) large Reynolds number, (2) large Weber number, (3) large values of density ratio, and (4) large values of viscosity ratio. Moreover, sophisticated procedures are required for interface reconstruction process leading to some level of complexity in three dimensions. Both the Reynolds and the Weber number are defined later.

Even though there have been many studies on interfacial flows, most of them treat both fluids/phases as incompressible [159, 187, 188, 63, 218]. While this approach is successful in simulating some of the observed breakup features such as ligament formation and stripping, it still cannot capture the effects of cavitation induced breakup [12] and the acoustic-vortex interaction [12] at the interface that triggers the Kelvin-Helmholtz instability. Other applications [65, 184] where compressibility is of prime concern involve shock-wave gas-bubble interaction, shock-induced mixing of liquids, combustion of fuel droplets, etc. To address these difficulties, Caiden *et al.* [21] proposed an approach where the liquid is modeled as an incompressible fluid and the gas is modeled as a compressible fluid. This involved coupling a compressible solver with an incompressible solver with an appropriate jump conditions at the interface. The liquid-gas interface was modeled using a level-set approach. As the

algorithm requires two different numerical solvers, an appropriate coupling between them can become unmanageable for complex geometries. Besides, due to the incompressible formulation of the other (here, liquid) phase, its applicability is limited. Similar other techniques have also been reported [18, 50].

An alternate approach is to retain the compressible nature of the phases and model both the liquid and the gas phase as compressible fluids [183, 184]. In such an approach, the fully compressible Navier-Stokes equations are employed with a different equation of state (EOS) for each phase. The main advantage of the compressible approach is that all physically relevant processes and their drivers such as acoustic, viscous, capillary (related to surface-tension), and convection are included in a single formulation.

A change in the equation of state across the material interface poses its own challenges [184] in form of oscillations in numerical solutions. More specifically, the difficulty arises in the discontinuous variation of equation of state coefficients [184] leading to incorrect pressure evaluation. To alleviate this difficulty, Saurel and Abgrall [184] proposed a method where some numerical diffusion is tolerated leading to a mixture zone and the same algorithm is used at each mesh point–liquid, solid, or gas–and at all interfaces.

This approach, called Diffuse Interface Methods (DIM) [1, 4, 148], amounts to a smooth transition of thermodynamic properties from one medium to the other creating an artificial mixture zone in the vicinity of the interface. Such a transition region is analogous to that observed for the VOF approach where, because of numerical diffusion, the volume fraction can take intermediate values between 0 and 1. The main advantage of the DIM approach is its comprehensive consideration of mass, momentum, and energy within the compressible formulation leading to a sound physical modeling of the mixture and individual phases. Also, it uses a single numerical method to solve the same equations everywhere, simplifying the implementation and

the algorithm complexity. Separate mass conservation equations are employed for each phase allowing for potential phase-change phenomenon. Numerical diffusion is at the heart of this method, however there are sharpening techniques [102] available to limit this effect.

The DIM method was first employed to compute multi-component gas flows [106, 1], and then extended to immiscible materials [92, 184, 183, 194]. Within the context of immiscible multifluids, two different approaches have been followed. In the relatively detailed approach, called two-phase flow mixture method [40, 11, 184], each fluid has its own velocity and pressure leading to phase-specific momentum and energy equations. These equations are supplemented by one (or several, depending on number of phases) topological/indicator equations. Thus, in one dimension and for non-isentropic flows, a two-phase model of this type leads to seven (two mass, two momentum, two energy, one indicator) equations. There are several advantages [131, 184] of this method: (1) the model is hyperbolic, (2) it is able to treat multiphase mixtures as well as interface problems between pure fluids, and (3) it allows the treatment of fluids characterized by different thermodynamics due to phase-specific equation of state. However, this method is numerically complex to solve due to large number of waves in the system. Also, the system of equations contains unclosed interfacial pressure and velocity terms, both of which need to be modeled. Modeling of the unclosed terms is quite delicate and the results exhibits sensitivity to the relaxation procedure among the phases.

The second approach relies on reducing the aforementioned seven equations to a five equation system based either on a-priori closures [4, 118] or using an asymptotic analysis [131, 90, 148] in the limit of zero relaxation times. Such simplification specializes the model to interface problems involving artificial mixture zones. The method entails five (two mass, one momentum, one energy, and one indicator) equations in an one-dimensional framework. This model is usually referred to as the

homogeneous mixture method [4, 131, 118] and is the level of modeling considered in this study. The physical interpretation of resulting single/mixture momentum and energy equation for two fluids is that both phases are in mechanical equilibrium [148]. The major advantage of this method is that it is relatively computationally efficient to solve. Also, this method retains most of the physical information relevant to interface problems from the seven equation method, thereby making it physics-based. Comprehensive consideration of processes relevant for atomization applications within a single formulation make this approach attractive. The method is also simple to implement and is easily extendible to an arbitrary number of materials. For example, in three dimensions, for a number m of different materials, the homogeneous model needs only $2m$+3 equations whereas the two velocity, two pressure model uses $6m$-1 equations.

In this study, we are interested in compressible flows with interfaces separating immiscible fluids such as air/water whose density ratio may be large. Three key modeling issues arise for such flows: (1) capillary/surface-tension effects, (2) viscous effects, and (3) numerical algorithm to solve this model. We proceed with the aforementioned five-equation method of Allaire *et al.* [4], and extend it to include capillary effects within a Roe-type scheme. In addition, effects of viscosity as well as body-force are considered. Also, it is our goal to introduce a model demonstrating three-dimensional (3D) capability for solving interface problems. Additionally, due to the presence of large gradients (in density, momentum, and energy) on a fixed grid, a computational method must be able to capture strong discontinuities without numerical dispersion. However, the classical high-resolution (upwind) schemes are not suited [213, 52, 58] for resolving unsteady shear flows, e.g., recirculation region behind a moving liquid drop. So, in this study, a hybrid approach following Génin and Menon [58, 57] is employed. In this approach, the algorithm automatically switches between a high resolution upwind method and a second-order low-dissipation scheme

based on a smoothness parameter. Such an approach is designed to retain advantages of each scheme in different parts of the flow field and enabling the combined scheme to resolve diverse effects. This hybrid approach was first demonstrated by Frxyell and Menon [52] and Génin *et al.* [58] for Richtmyer-Meskov Instability and shock-turbulence interactions in the context of gas mixtures. In this study, we modify the smoothness parameter to take into account the presence of the interface.

The primary limitation of the detailed modeling approach is the resolution requirement. In order to capture the flow motion within and around a liquid drop of 100 μm, a typical grid resolution in the order of $3 - 10$ μm is required. This order of resolution is capable of capturing interface dynamics leading to simulation of fundamental processes like deformation and interface breakup. However, from an engineering design point of view, the flow resolution within and around the vicinity of the drop is prohibitive. This is due to a wide range of scales (fuel drop of $O(10^{-6}\text{m})$ and combustor width $O(10^{-1})$m) present in the flow.

Instead, the aforementioned point-volume [114, 47] engineering breakup models can be employed within the context of a Large-Eddy Simulation (LES) [127, 146] framework to study flow processes within a practical device. A LES framework allows for accurate description of turbulence phenomenon at a reasonable computational domain. Unlike a Direct Numerical Simulation (DNS), not all scales of motion are resolved; rather scales smaller than the grid size are filtered and the effects of these scales are accounted for in the form of subgrid effects.

The compressible two-phase approach developed here compliments the engineering models used for LES applications by providing basic closures from first principles like drag effects, time-dependent deformation and atomization, evaporation rates, etc., which are currently empirically based. Also, the detailed two-phase approach provides avenues to develop curve-fits for a wide range of conditions, typically not available via measurements, which can be used within a LES simulation. It is also feasible to link

the compressible two-phase approach to LES combustor simulation where the detailed approach resolves the primary/secondary breakup regimes (defined later) close to the injector and further downstream dilute regime (defined later) is evolved using the point-volume [114, 47] method.

In this study, we are also interested in an application of liquid atomization within the context of gas turbine combustors. Accordingly, we also report on the LES of spray combustion in an axial-swirler type combustor [20] with a particular emphasis on the impact of the break-up model on the predictions. The present focus is not on developing a new break-up model, but rather, on evaluation of an existing breakup model in a LES of a complex combustor flow field.

For liquid fueled systems, several approaches have been proposed to achieve high efficiency and low emissions. One particular concept, called Lean-Direct Injection (LDI), has been of active interest due to its potential for low emissions at operational (high temperature, high pressure) conditions [204, 210, 192]. In the LDI concept, the liquid fuel is injected from a venturi directly into the incoming swirling airstream, and the swirling airflow is used both for atomizing the injected liquid and for fuel-air mixing. Auto-ignition and/or flashback are minimized since the fuel is neither premixed nor pre-vaporized [205]. Low CO and NO_x emissions with no combustion instability have been reported in experimental studies [204, 192].

These experimental observations have not fully explained the dynamics of the mixing and combustion processes that resulted in the measured low emission and stable performance. Measurements are rather crude and (in the past) have been limited to observation of the exhaust emissions. Focussed experimental and numerical studies are currently underway, and the results reported here are part of an effort to explain some of the underlying unsteady physics of the LDI combustor.

In order to achieve a physical insight into the mixing and the combustion processes the simulation approach needs to resolve not only the fluid dynamic processes created

by the swirl vanes but also capture the combustion process occurring in the small scales in the combustor. Fluid dynamic mixing can be (perhaps) addressed with reasonable accuracy by resolving the entire inlet swirl assembly (as done here) and the swirling shear layer mixing regions in the combustor. However, scalar mixing and combustion offer new challenges since these processes occur at the small scales that are not typically resolved in a conventional LES and ad hoc modeling of these processes at the resolved scale cannot adjust accurately to the subtle changes at the small-scales.

An earlier study [146] that used a dilute spray model is revisited here using a break-up model. Also, new data on the droplet size and velocity field have been used to evaluate the sensitivity of predictions on the liquid phase model employed for the simulation. For all these studies the full LDI combustor (including the swirl vanes) is simulated and this approach eliminates a major ambiguity regarding the inflow conditions.

In summary, this research provides both detailed as well as engineering solutions to study atomization processes and the aspect of linking the two solutions is left for future studies.

1.2 Literature Review

In this section, we will review past attempts for compressible two-phase approach, engineering breakup models, and simulation of LDI combustor.

1.2.1 Compressible Two-phase Approach

The DIM approach has been exclusively used for compressible two-phase formulations. As was pointed out in the introduction, essentially either seven-equation or five-equation models are employed to study compressible multifluid flows. A survey of approaches for computing compressible multifluid flows is reported by Abgrall and Karni [2].

1.2.1.1 Seven Equation model

In general, two-phase models are usually derived using a averaging (kinetic based) procedure. In this procedure, referred to as ensemble averaging, one phase is considered to be consisting of an ensemble of particles embedded in a carrier fluid medium. The particles are allowed to interact (undergo collisions, coalescence, etc.) with each other and their number density in coordinate-velocity space obeys a Boltzmann-type equation. This distribution function is then integrated over the phase-space to yield the balance equations for the medium. This was done by Drew [40] for incompressible two-phase flows.

In the context of compressible fluids, Saurel and Abgrall [184] applied the averaging procedure of Drew to obtain a seven equation model consisting of phase-specific mass, momentum, and energy conservation equations. A transport equation for volume fraction (of one of the phases) complete the system of equations. Similar other efforts are reported by Butler *et al.* [17], Powers *et al.* [160], Baer and Nunziato [11], and Schwendeman *et al.* [191]. However, these studies were for detonation waves in granular materials and were not [186] suitable for solution of interface problems. The main difference between Baer and Nunziato's work and that of Saurel and Abgrall is related to the use of relaxation terms (discussed next). Saurel and Abgrall introduced the notion of relaxtion parameters enabling wider application of the seven equation model. The approach by Saurel and Abgrall [184] has been shown to apply to both interface as well as homogenous two-phase flows.

The balance laws for each phase are similar to those for an isolated gas, i.e., the Euler equations, except for two important differences. First, source terms appear in the transport equations of each phase representing the exchange of mass, momentum, and energy. Second, the governing equations, although hyperbolic (as each phase is considered to be compressible), cannot be cast in a conservative form. Such non-conservative terms, often referred to as *nozzling terms* by analogy to similar terms

appear in the equations of 1D flow in variable-area duct, are not closed (interfacial pressure and velocity) and must be modeled [191]. Because of several difficulties [39] relating to non-conservation property of the balance equations, the derivation of efficient algorithms for solving the equations has been a very challenging task. Also, since the nozzling terms do not represent fluxes, they have to integrated as source terms. This has led to documented [7] numerical instabilities and spurious oscillations. In certain studies, these nozzling terms have been ignored either by choice, Gonthier and Powers [61], or by convenience, Papalexandris [142]. However, to guarantee the entropy inquality is satisfied [191] these terms are required. Saurel and Abgrall [184] introduced discrete approximations for the nozzling terms based on a condition by Abgrall [1]. This condition states that a two-phase flow with initially uniform velocity and pressure should remain as such for all times.

In their approach [184], Saurel and Abgrall omitted mass and energy transfer terms to arrive at a hyperbolic system of equations supplemented by pressure and velocity relaxation terms. These terms account for microscopic motion behind the pressure waves and for drag forces in the two-phase mixture, respectively. The solution strategy is based on a two-step process: (1) integration of system of equations with a hyperbolic solver, and (2) integration for relaxation terms. The numerical method is based on high resolution modified Godunov-HLL scheme with a flux function following Rusanov [175]. The discretization scheme for the non-conservation terms as well as volume fraction transport equation is based on the aformentioned condition of Abgrall [1]. Several 1D test problems were presented demonstrating the capability of the method to deal with strong shock waves as well as complex equation of state. The major contribution of this method is its capability to dynamically account for interfaces. Further extensions to include mass and energy transfer terms, and to an arbitrary number of fluids were proposed by Saurel and LeMetayer [186].

Abgrall and Saurel [3] proposed a class of schemes in the context of compressible

multiphase mixtures that were able to converge to the correct solution for situations when shock waves interact with volume fraction discontinuities. They provided more accurate estimate of nozzling terms in addition to an accurate resolution method for the conservative fluxes as well as non-conservative terms. The governing equations were derived by considering pure phase Euler equations at the micro-scale and providing numerical approximations of these equations via the Godunov scheme. These approximations were then averaged over the set of all realizations to provide corresponding scheme for the averaged multiphase flow equations. This is in contrast to the usual multiphase flow equations where they are first ensembled averaged and then approximated (at macro-scale) by the numerical method. They reported on several 1D test cases involving shock tubes, sedimentation problems, and fluidized bed (of dense and small solid particles).

A common theme among all the above studies is the lack of capillary and viscous effects in the model formulation. Additionally, the appearance of non-conservative products in the governing equations and their closure leads to several complications in the design of algorithms. Added complexity in both governing equations as well as numerical methods to solve them has hindered efforts for their application in multi-dimensional flow fields. Several recent studies [191, 39] have proposed new and sophisticated numerical procedures for solving the seven equation model, however issues regarding multi-dimensional extension, capillarity, etc., were not addressed.

1.2.1.2 Five Equation model

The origins of the five equation model lies in studies of multi-component non-reacting gas flows. Primary concern [1] there was related to differences between the equation of state parameters for each gas across the fluid interface. This led to non-positive solution for mass fraction and non-physical pressure oscillation across the interface. The negative mass fraction concern was addressed by Larrouturou [106] by proposing

a modification of the numerical flux to guarantee the positivity of mass fraction solution. However, this modification did not address pressure oscillations [26]. Karni [91, 92] proposed a non-conservative scheme to properly simulate the fluid interface (or contact discontinuity) limiting pressure oscillations. This scheme also addressed the positivity of the mass fraction. Further extension was proposed by Abgrall [1] to handle strong discontinuities. A common condition emerged from studies of Karni and Abgrall requiring the formulation to enable any physical contact discontinuity to remain a contact discontinuity. In practical terms, this condition implies that a flow with initially uniform pressure and velocity should remain uniform at all times [1, 92].

To fulfill this condition, an extra [1] non-conservative transport equation for the quantity $1/(\gamma - 1)$, where γ is the adiabatic exponent of the perfect gas (a coefficient of equation of state) was introduced and tracked in addition to the usual conservation equations. The resulting quasi-conservative approach suppressed the spurious pressure oscillations for several 1D test cases [1]. Saurel and Abgrall [184] and Shyue [194] further extended this approach to compressible multi-material (solid, liquid, gas) flows in hydrodynamic regime. Within this regime [184], the hydrodynamic part of the stress tensor becomes predominant relative to its deviatoric part, and the Euler equations become a valid model for such flows. Also, under high pressures, these materials can be reasonably described by using the Stiffened gas equation of state [66]. Its algebraic form is similar to the ideal gas EOS. Two constant material-specific parameters are necessary to describe the Stiffened EOS. For example, an ideal gas can be described with one parameter being the ratio of specific heats and the other as zero.

Across a material interface, the coefficients of the Stiffened EOS will vary discontinuously from one medium to another leading to aforementioned difficulty in pressure evaluation at the interface. Saurel and Abgrall [184] followed the diffused approach to allow for a smooth variation of EOS parameters across the interface. This also

enabled to employ same algorithm for all mesh points – pure phase and interface locations. Several test cases in multi-dimensions were reported showing the ability of the method to capture interface dynamics and allowing for high density ratios across the interface. However, the main limitation of this approach is that it requires to add as many transport equations as there are parameters defining the EOS. Therefore, the complexity increases with the number of parameters required to define the EOS.

Allaire *et al.* [4] extended this approach to a wide range of equations of state. The key idea employed was to replace the closure relations (or individual EOS parameters) by a single supplementary transport equation. So, each EOS parameter can be ascertained based on fluid-specific constants and the supplementary advection equation. As a result, making the number of equations in the model independent of parameters needed for EOS. The supplementary transport equation tracks the volume fraction of one of the fluids. The approach also considers mass conservation of individual fluids in addition to conservation for the total momentum and energy of the mixture resulting in the five equation model (in 1D). The model can be extended to treat more than two fluids by adding a mass conservation equation and a volume fraction advection equation for each new fluid.

As stated, the five equation model is not closed [4] as it is not possible to compute pressure with the sole knowledge of the conserved quantities. So, Allaire *et al.* [4] suggested two different closure laws based on physical assumptions: the isobaric closure and the isothermal closure. For these closures, the system of equations is supplemented with an algebraic relation of either equal phase pressures for the isobaric case or equal phase temperatures for the isothermal closure. Various mathematical properties of the resulting models were studied showing consistency, hyperbolicity, and existence of a mathematical entropy. However, testing for Abgrall's condition showed that the isothermal closure does not retain the uniform pressure and velocity requirement. Therefore, the isobaric closure was used for the model and a scheme

based Roe's approximate solver [172] was developed. The mathematical structure of the model was shown to be very close to the structure of the Euler equations. Several 1D and 2D test cases were presented showing the accuracy of the method.

Murrone and Guillard [131] derived a similar five equation model from a more general seven equation model of Baer-Nunziato [11] type using an asymptotic analysis in the limit of zero relaxation time. The procedure is similar to the one proposed for detonation studies by Kapila *et al.* [90]. The limit system is determined based on imposition of instantaneous pressure and velocity equilibrium and an asymptotic reduction close to the mechanical equilibrium state. The resulting model is very similar to that of Allaire [4] except that the volume fraction equation involves a velocity divergence term. This extra term indicates volume fraction variation across acoustic waves. Major drawback [148] of this term in the context of flows involving interfaces separating pure fluids is that the model does not ensure the positivity of the volume fraction. Also, derivation of jump conditions is an issue [90].

A quasi-conservative formulation was proposed by Perigaud and Saurel [148] extending the five equation model to include capillary and viscous effects. The basic system of equations was derived following asymptotic analysis of Murrone and Guillard applied to the seven equation model, however further simplification of neglecting the volume fraction variation across acoustic waves was made. The same simplification was also done by Allaire [4]. This specialized the resulting five equation model for interface problems. In order to deal [1] with artificial mixture zones, Allaire's isobaric closure was chosen and shown to be fully consistent with assumptions of pressure equilibrium (made during the asymptotic analysis). A Godunov-type scheme based on an exact Riemann solver is implemented to solve the model.

Two primary concerns arise when capillarity (surface-tension effect) is considered within a compressible framework. First, most of the physical problems involving surface-tension have been considered in an incompressible framework. However,

within a compressible formulation, energy equation is part of system of equations and surface-tension contribution on energy balance needs to be included. Second, special consideration is required for geometric variables of the model (interface curvature) in relation to the flow variables during the solution step. Perigaud and Saurel [148] extended the Continuum Surface Flows (CSF) method following Brackbill *et al.* [16] to compressible fluids. Also, the local interface curvature was considered *frozen* rendering Rankine-Hugoniot relations and Riemann invariants unaffected by the presence of capillarity.

In this study, we follow similar steps in extending Allaire's five equation model [4] to include capillary effects within a Roe-type scheme. In addition, effects of viscous as well as body-force are considered. Consistent with our overall goal of developing a model demonstrating 3D capability for solving interface problems, an approximate Riemann solver is retained. The main advantage of our approach is that we consider an approximate Riemann solver which does not need iterative Riemann solution of flow variables at a cell boundary. A linearized Jacobian matrix and resulting set of eigenvectors admit face fluxes directly. A recent study by Toro and Chou [212] has shown computing savings by a factor of about four relative to the use of exact Riemann solvers. Also, Roe solver is exact on isolated contact discontinuities. Further, a hybrid approach is applied that combines a high resolution upwind method (appropriate for capturing large gradients) and a low dissipation central scheme (appropriate for smooth field). Such an approach is designed to retain advantages of each scheme in different parts of the flow field and enabling the combined scheme to resolve diverse effects. Previous studies [52, 58, 57] on shock-turbulence interactions have demonstrated the accuracy of the hybrid approach.

1.2.2 Engineering Breakup Models

The classical picture of atomization involve primary breakup of liquid core into ligaments or large drops followed by secondary breakup into smaller drops with negligible effects of collisions [48]. In the dense regime [46], effect of discrete inter-drop spacing on transport rates, drop-drop collisions, turbulence modulation due to volume occupied by liquid phase, etc., become significant. The dilute regime involves no particle-particle interactions and the effect of liquid phase volume on transport becomes negligible [47, 48]. Therefore, the single-drop transport rates can be employed directly. In general, in the near-field of the injector both regimes can co-exist but further downstream the dense regime is very rare.

Numerous researchers have studied and proposed computational models to account for droplet breakup as a subgrid process and in this section we will present a comprehensive review of these efforts. The first published drop breakup model was proposed by Reitz and Diwakar [168] for secondary breakup. The focus of their study was to assess the implications of initial drop size on the spray structure and to establish the importance of secondary atomization due to breakup. The simulations were performed using KIVA [5] solver employing Reynolds Averaged-Navier Stokes (RANS) methodology. They studied both hollow-cone and solid-cone sprays and compared the spray tip penetration rate with experiments of Shearer and Groff [193] and Hiroyasu and Kadota [74], respectively. The droplet parcels (based on stochastic approach following Dukowicz [42]) were given initial size distribution (based on experiments or nozzle rating) and were tracked as discrete parcels. For each drop parcel, stability criteria [168] were checked at each iteration (or time-step). If the criteria continued to be met for a time equal to the lifetimes [168] of unstable droplets, then a new drop size for the parcel was specified. The liquid mass at breakup was conserved by adjusting the number of (physical) drops in the parcel (computational drops). The authors concluded that drop breakup has a dominant effect on spray drop size

in hollow-cone sprays as coalescence is minimized due to expanding/diverging spray structure. Also, the drop size in solid-cone sprays is influenced by both coalescence and breakup.

Obvious limitations of the above model [168] were the need to specify drop/parcel initial conditions, which were based on correlations, and thereby, details of spray structure (like intact core, primary breakup, etc.) were not considered. Also, in the previous model [168], the parcels were broken up abruptly to the stable drop size at the instant when the drop lifetime was reached. Reitz and Diwakar [169] addresses these two issues in their next breakup model which is based on the hypothesis that atomization of injected liquid and the subsequent drop breakup are indistinguishable processes within a dense spray near the nozzle exit. The atomization is prescribed by injecting parcels (or *blobs*) having characteristic size of spray nozzle diameter which due to their interaction with carrier fluid (gas in which they penetrate) breakup (their radius decreases continuously with time) and the stable drop size specified using experimental breakup correlations [168].

In this model, a rate equation (which enables continuous variation of drop size) for drop radius is specified based on mass loss measurements [164] from a (parent) drop in a high relative velocity flow. No quantification of size of stripped drops were made or given in their experiments [164] and accordingly, the parent and stripped were not distinguished rather the mass conservation was acheived by adjusting the number of (physical) drops per parcel. The reduction in radius continues as long as the stability criteria [168] are exceeded. Major achievement of this approach is its ability to predict a core (intact) region (consisting of large drops near the nozzle exit travelling at nozzle discharge velocity until they breakup) as seen in conductivity measurements [9, 29] and spray photographs of Reitz and Bracco [166]. Their near-field structure study for solid-cone spray showed rapid decrease in drop size close to nozzle exit (decrease from 140μm to 52μm SMR in 10 mm) and largest drops on the

spray axis with smaller drops found near the periphery of the spray.

The liquid volume fraction (fraction of volume occupied by liquid mass) contours showed that it falls to less than 4% within 5 mm of nozzle exit due to divergence of spray. Conservation equations (gas and liquid) which assume thin-sprays (negligible liquid volume fraction) are strictly not valid very close to the nozzle (which showed 11% liquid fraction). The authors then incorporated the dense-spray corrections [139] for finite liquid volume fraction and re-analyzed the spray structure finding that the results were essentially unchanged. Reasoning for this insensitivity was explained by noting the counteracting tendencies of increasing droplet drag for dense spray and small drop deceleration for large drops found in finite liquid volume fraction regions.

Continuing with the hypothesis of indistinguishable processes of atomization and subsequent drop breakup, Reitz [165] proposed several improvements over the Reitz and Diwakar model [169]. Among them, new parcels containing product drops (as a result of continuous decrease of radius owing to the rate equation) are added to the computations which themselves potentially can undergo breakup. The size of product drop was based on wavelength of unstable waves on the surface of *blobs* rather than experimental correlations. The impetus for creating new parcels based on mass stripping was the observation that the previous model [169] predicted negligible fuel vapor in the core region (near-field) which was not consistent with vapor measurements. This model is entirely based on stability analysis (of Kelvin-Helmholtz (KH) waves) done by Reitz and Bracco [167] which examined the stability of a cylindrical liquid surface to perturbations using a first order linear theory. The Kelvin-Helmholtz (KH) or aerodynamic instability is due to either a velocity shear present within a continuous fluid or velocity difference across the interface between two fluids. In contrast, the Rayleigh-Taylor (RT) instability is due to a dense or heavy fluid is being accelerated into a light fluid. The dense/light fluid interface is RT stable when the acceleration is directed into the heavier fluid.

The analysis leads to a dispersion equation which relates the growth rate (ω) of an initial perturbation to its wavelength (λ or wavenumber $k = 2\pi/\lambda$). Numerical solutions for the dispersion relation indicate a single maximum [33] in the wave growth rate curve ($\omega(k)$) and their curve-fits for the said maximum growth rate $max(\omega = \Omega)$ and the corresponding wavelength $max(\lambda = \Lambda)$ gives their (Ω, Λ) variation in terms of Ohnesorge parameter ($Z = \sqrt{We_l}/Re_l$, accounts for influence of liquid viscosity on breakup) and carrier Weber number(We_g, ratio of aerodynamic to surface-tension force).

The author also derived the breakup time (τ) for two extremes of carrier Weber number as: $\tau = 1.72B_1\sqrt{\frac{\rho_l r^3}{2\sigma}}$ for $We_g \to 0$; and $\tau = B_1\frac{r}{U_{rel}}\sqrt{\rho_l/\rho_g}$ for $We_g \to \infty$. Various values (=20 [169]; =8 [134]; =$\sqrt{3}$ [138]) of breakup time constant (B_1) has been used by different researchers, indicating some uncertainty. In addition, the spray cone angle (Θ) was also based on the maximum growth rate and its wavelength as $tan(\Theta/2) = A_1\Lambda\Omega/U_o$, where A_1 depends on nozzle design and U_o is the injection velocity (based on pressure differential and liquid density). This is one of the two breakup models that is implemented and validated against experiments [74] in the current study.

In a different approach, O'Rourke and Amsden [138] proposed a method for drop aerodynamic breakup based on an analogy, suggested by Taylor, between an oscillating & distorting droplet and a spring-mass system (forced, damped harmonic oscillator). The authors related the spring force (restoring) to the surface-tension forces; external force (driver) to carrier (gas) aerodynamic force; and damping forces to the liquid viscosity – calling this model *TAB* (Taylor Analogy Breakup) model. The main contribution of the model is its ability to predict the state of oscillation and distortion (shape) which may affect the exchange rate between the gas and the droplets.

The TAB model keeps track of one oscillation mode (fundamental mode) which

is the longest-lived, but the authors concede that for large Weber numbers other modes are possible and contribute to the breakup. The drop breakup is based on distortion amplitude equalling half drop radius and it is instantaneously broken up once maximum distortion limit is reached. The Taylor analogy equations do not give drop size information and so the product drop sizes are estimated based on energy conservation argument. The authors show that, for large Weber numbers, the product drop sizes are determined by a Weber number criterion. A major hindrance with this model is that the product drop sizes are under-predicted and the change-over from parent to product drop is also quick (in the form of a step function rather than continuous variation seen in previous models) giving no estimate of intact length. The authors concur with findings of Reitz [169] that drop breakup is an important phenomenon in high-pressure spray. This is the second model for breakup that is implemented, and validated using measurements [74] in the current study.

Liu *et al.* [111] conducted an evaluation of two drop breakup models (TAB [138] and KH [165]) using measured [112] trajectories and sizes of single drops injected in transverse gas flow. They reported the sensitivity of drop drag coefficient (C_D) and breakup time constant (B_1, determines rate of mass loss of parent drop undergoing breakup) on both trajectory and drop size comparsions leading them to propose a new submodel for droplet drag which accounts for effects of drop distortion (shape). The authors modeled the variation of the drag coefficient between the limits of a rigid sphere (no distortion) and a disk (maximum distortion) leading to a simple linear relation to distortion as: $C_D = C_{D,sphere}(1 + 2.632y)$, where y is non-dimensional distortion obtained using the TAB [138] model. Comparisons of two models with experimental data showed that both models were able to predict the trajectory of drops across the width of the (gas) jet, however the TAB model significantly under-estimated the measured drop sizes (for cases in which the stripped parent droplet made it across the gas jet). This indicated an over-estimation of breakup events

(leading to much smaller droplets with lower inertia that quickly reach equilibrium with gas momentum) and the drop drag effect was also under-estimated (due to lower relative velocity). The authors noted that the combination of these two effects would either give good trajectory comparisons or good final droplet sizes but not both simulateneously.

Among many model evaluation study, Kim *et al.* [99] studied two existing drop breakup models: TAB [138] and KH [169] model for both non-evaporating and evaporating (non-reacting) configurations. They used RANS methodology for the study with stochastic [42] particle method. For non-evaporating case, the authors reported fair agreement with each other and experiments for spray tip penetration, however the TAB model displayed generic rapid breakup near the nozzle exit causing significant underpredicts the intact core length. Similarly, for the evaporating solid-cone case, there is overall agreement for both models in penetration depth, however the TAB model again underpredicts the depth initially. In summary, the authors conclude that Reitz's KH model [169] is better suitable for predicting dense spray dynamics.

In an effort to further validate and improve the hybrid (KH-RT) model, Beale and Reitz [13] utilized the concept [73] of liquid breakup length which says that breakup occurs at a different rate within and beyond the length of liquid core. This concept was used in the past by Ricart *et al.* [171] and Xin *et al.* [229]. In their approach, the accelerative (Rayleigh-Taylor or RT) instabilities did not compete with aerodynamic (Kelvin-Helmholtz or KH) instabilities until after the drops had passed beyond the intact core in view of the idea that secondary breakup occured only downstream of the intact liquid core. Beale and Reitz [13] noted that liquid within the intact core is unlikely to be influenced by the RT instability, however drops outside the liquid core would be affected as they are decelerated by drag of carrier fluid. So, in their model, the drops not only beyond the breakup length but also those adjacent to the liquid core and within the breakup length, were considered for RT breakup. Thus,

a new drop created due to KH breakup of a blob in the core region, RT waves were allowed to grow as long as RT instability conditions (wavelength smaller than drop diameter) were satisfied. To take into account the liquid breakup length concept, they used different RT breakup time-constant for drops within and outside the core region. They also used Rosin-Rammler distribution (parameter q=3.5) for newly created drops with mean radius given by RT wavelength.

Beale and Reitz [13] also modeled hollow-cone spray by assuming conical liquid sheet near the nozzle following Han *et al.* [64] in form of discrete blobs with initial diameters equal to sheet thickness. The initial blobs are not subject to the effects of drag or turbulent dispersion as they represent an intact liquid sheet. After travelling a distance greater than the breakup length, they are treated as normal drops. In the case of Han *et al.* [64], the sheet breakup was handled with the TAB model whereas, in this case, Beale used aerodynamic instability theory. The secondary breakup of drops were determined by competing mechanisms of the RT and KH instabilities. Their study showed that effect of grid sensitivity on spray predictions could be minimized by gradually introducing spray particles into to the computational domain. Use of blob injection technique in conjunction of breakup length concept presents such an option. Their study also showed comparisons with measurements for liquid and vapor penetration lengths for both solid- and hollow-cone sprays. No detailed drop size spatial distribution were presented.

Huh *et al.* [80] have proposed atomization model for plain-orifice sprays which considers both turbulent fluctuations within the liquid jet and wave growth by gas inertia due to relative velocity (between gas and liquid phase). Novelty of this approach is that it couples the nozzle effects (flow inside the nozzle) to the exterior atomization process. In previous studies, this was represented by an arbitrary nozzle-dependent constant. Based on order-of-magnitude comparison of relevant forces (such

as surface-tension (σ/D), gas inertia ($\rho_g U_{inj}^2$), turbulent stress in liquid jet ($\rho_l u_l^2$), turbulent stress in gas ($\rho_g u_g^2$), viscous stress in liquid jet ($\mu_l U_{inj}/L$), viscous stress in gas ($\mu_g U_{inj}/L$), and gravity ($\rho_f g D$)) for atomization revealed that gas inertia and jet internal turbulent stress emerge as dominant forces of comparable magnitude. Similar to other models discussed above, either primary or secondary parcel breakup is activated by Weber number criterion of $We_g > 6$ (where, $We_g = \frac{\rho_g U_{rel}^2 r}{\sigma}$). The breakup dynamics including drop-size and velocity specification is based on scale relationships for atomization, turbulence, and surface wave perturbations. More details of scale relations and their implementations are reported elsewhere [80].

It suffices to mention that they have used two hypotheses proposed by Huh and Gosman [79] calling for turbulence length-scale (L_t) as dominant atomization length-scale (L_A) such that $L_A = C_1 L_t = C_2 L_w$ and atomization time-scale (τ_A) represented as linear sum of turbulence (τ_t) and wave (τ_w) growth time-scales as: $\tau_A = C_3\tau_t + C_4\tau_w$; where $C_i, i = 1, .., 4$ are various proportionality constants determined via tuning against experimental data. The breakup rate for droplet is set proportional to the ratio of length- and time-scale such that: $\frac{dD_p}{dt} = k_1 \frac{L_A}{\tau_A}$ for primary parcel under atomization mode and $\frac{dD_{p,s}}{dt} = k_2 \frac{L_w}{\tau_w}$ under wave-growth mode for either primary or secondary parcel. The constants again need to be tuned to measured data. The authors have tested their model against measured data for plain-orifice injectors, however it is not clear its impact for other configurations especially those injectors that impart swirl to the liquid jet.

Apte *et al.* [8] have used stochastic approach of Gorokhovski [62] based on relaxation of particle radius distribution function from initial Dirac-delta to long-time log-normal distribution. As in the original model [62], the atomization of liquid blobs is considered in the framework of uncorrelated breakup events, independent of initial droplet size. The approach does not consider or identify any (dominant) mechanism driving the atomization rather, the size and number-density of product droplets is

dictated by the evolution of the radius distribution function from Dirac-delta (initial condition) to log-normal (long-time, steady state) distribution. Certain studies [64, 108] have indicated that Rosin-Rammler distribution better represents the droplet size distribution. Apte *et al.* [8] have also noted that assumption of a particular distribution function giving best representation for all cases is not advisable. This approach necessarily requires apriori knowledge of distribution function (PDF) for the droplet sizes. Also, the assignment of drop sizes between the two extremes of initial and long-time condition is based on the gradual relaxation of PDF from delta function to log-normal. The approach lacks the ability to fundamentally assign drop sizes and velocity after breakup based on physics as it rather relies on stochastic character. The breakup time is also not available from the approach rather, is obtained using correlations ($\approx \sqrt{\rho_l/\rho_g}(r_{parent}/u_{rel})$ for large Weber numbers). And the critical (or maximum stable) radius for breakup is based on a balance between hydrodynamic and capillary forces and estimating the rms of relative velocity from mean viscous dissipation and a Stokes time-scale. The authors point out the superiority of LES approach in providing accurate, local estimates of the gas-phase turbulent properties due to accurate predictions of mixing and momentum transport.

In another hybrid approach, Park and Lee *et al.* [144], proposed a Kelvin-Helmholz instability/droplet deformation & breakup [83] (KH-DDB) competition model. It was proposed to overcome the well-known under-estimation of product droplet sizes for the TAB [138] and spray penetration when applied to a high-pressure injector (like gasoline-direct injection or common-rail injection system). This model is based on competition between drop deformation and wave (aerodynamic) instability. They have applied the model to atomization process happening in the catastrophic regime [151] due to high injection pressure. Reasoning for using such a competition model is based on observations of flattening of droplets at high (150-200 m/s) relative velocities and belief that in catastrophic regime [151], droplet breakup is due

to wave instabilities on the liquid surface. Based on these observations, atomization within the core/breakup length was determined by both the wave and deformation models whereas, past the breakup length, deformation dynamics governs breakup. The breakup/core length was based on Levich theory [13] ($L_b \approx d_{nozzle}\sqrt{\rho_l/\rho_g}$).

The breakup time of DDB model was determined by the breakup criterion of semi-major axis exceeding a certain distance (linearly based on parent radius and gas Weber number We_g), whereas, the wave breakup was assumed to occur at every calculation cycle if DDB breakup does not occur. No justification was given as to why the original KH breakup time was not employed. Also, the breakup criterion for DDB model presents difficulties [143] at large We_g as it is linearly proportional to it. For small We_g ($< 6\pi$), DDB breakup criterion yields breakup at any time without unrealistic deformation [143]. No effect of drop deformation on aerodynamic force was considered. Axial sauter-mean diameter (SMD) comparisons with measurements and KH-RT [147], showed better predictions with KH-RT model. Also, the transient spray-tip penetration comparisons showed KH-DDB model under-estimates at the early stages of injection whereas KH-RT was better able to represent the measurement trends. Their results of temporal and spatial characteristics of breakups for the KH-DDB model indicated that both KH and DDB breakup happen most actively around 0.4-0.8 ms after injection and spatially 10 mm downstream from the injector. It was also indicated that the atomization process is almost over at about 25 mm downstream of the injector.

Based on initial effort by Huh *et al.* [80] to employ nozzle turbulence effects on the atomization process, Trinh *et al.* [214] combined those effects with KH model [165] for primary breakup and that with TAB model [138] for secondary breakup. This provides framework for coupling the flow inside the nozzle to the external atomization process. The authors have quoted few recent experimental studies [227, 228, 176, 177] of large-size liquid jets indicating that the turbulence developed inside the jet column,

starting at the nozzle exit, remained dominant and contributed to spray development. In this approach, terms accounting for the nozzle turbulence effects within the liquid are incorporated into the existing (KH and TAB) models.

The above review of previous efforts for the engineering breakup models indicates that they are essentially empirical/semi-empirical in nature. Each of the above models includes associated coefficients whose determination is necessarily referenced to some form of measurement data. Ideally, detailed simulation of flow dynamics in both liquid and gas is desired to better understand and elucidate the process of atomization. However, these engineering models do provide an opportunity to study atomization in practical devices as these models are based on a point-volume approach [114], which relaxes the grid resolution requirements by averaging relevant processes within a computational cell.

1.2.3 LDI Combustor

In this study, we are also interested in an application of liquid atomization within the context of gas turbine combustors. Accordingly, we also report on the LES of spray combustion in an axial-swirler type LDI combustor [20] with a particular emphasis on the impact of the break-up model on the predictions. The present focus is not on developing a new break-up model, but rather, on evaluation of an existing breakup model in a LES of a complex combustor flow field.

In the past, numerical efforts to simulate the flow field in an axial-swirler type LDI have been limited to mostly non-reacting flows [231, 232]. Even the non-reacting studies used a different configuration such as (1) 5 blades per swirler [231] as opposed to 6 blades per swirler in the present study, (2) 9 swirl cup combustors as opposed to a single cup used here, or (3) the discrete jet swirlers instead of the swirl cup assembly [82, 81, 209]. Therefore, a direct comparison between the earlier non-reacting studies and the present LES is not possible.

Recently, Kirtas *et al.* [101] reported the first LES for this setup. The entire test facility, including the wind tunnel walls and the flow through the swirl vanes are resolved in the study. This was done to remove the ambiguity of specifying gas-phase inflow velocity profiles. An Eulerian-Lagrangian two-phase formulation was employed and subgrid momentum closure was achieved by a localized dynamic model [97, 145]. An Eulerian-Lagrangian formulation allowed for liquid fuel particles to be tracked in a Lagrangian [47] manner whereas the gaseous species were transported on an Eulerian cells with liquid/gas interphase exchange terms [137] to account for evaporation, drag, and energy transfer. Both non-reacting and reacting simulations were conducted. A subgrid eddy breakup [54] (EBU) model for reacting closure was employed. In this model, the filtered reaction rate is computed as the minimum of the kinetic reaction rate and the mixing rate based on turbulence. A primary limitation of the EBU approach is that it has no inherent mechanisms to account for either molecular mixing processes or strain rate effects leading to need for $ad-hoc$ conditions for flame dynamics. Non-reacting velocity comparisons (mean and fluctuations) indicated a reasonable agreement, whereas the reacting case showed some under-prediction for turbulence properties.

Further, Patel *et al.* [146] employed the Linear-Eddy Mixing (LEM) model [94, 127] for the reacting closure within the context of LES to improve beyond the subgrid EBU approach. The unique aspect of the study was that the species equations are not "LES" filtered nor are they solved along with the gas phase LES equations. Rather, a subgrid Eulerian reaction-diffusion model is combined with a 3D LES-resolved Lagrangian advection of the subgrid scalar fields to simulate the conservation of species. In this two-scale approach, called LEM modeling for LES (LEMLES, hereafter) [127, 23, 182], all physical subgrid processes such as molecular diffusion, chemical reactions, subgrid mixing by eddies smaller than the grid resolution, and

volumetric expansion due to heat release are all simulated separately but concurrently at their respective time scales inside each LES cell. The LEM approach allows inclusion of molecular diffusion and kinetics within the subgrid without requiring any closure.

The LEMLES approach has been successfully applied with no model changes to a wide variety of flows, including scalar mixing [24, 181], and premixed [179, 182, 43], non-premixed [122, 120] and spray [127, 126, 180] combustion. The combination of the localized dynamic model for k_{sgs} with LEMLES results in a simulation approach that has no model parameters to adjust regardless of the physical problem to be simulated. This is considered an unique aspect of the current approach.

The study [146] reported on unsteady flow features dictating spray dispersion, fuel-air mixing, and flame stabilization. The swirling shear layer plays a major role in spray dispersion and the recirculation region provides an efficient flameholding mechanism to stabilize the flame. Presence of a precessing vortex core (PVC) was observed for both non-reacting and reacting simulations. It was noted to be a helical (or spiral) filament with anti-clockwise winding in space and clockwise rotation in time. They reported 2.3 kHz as the rotational frequency of the PVC. Both non-reacting and reacting steady-state velocity prediction comparison with measurement [20] data showed good agreement at nearly all locations.

Both the previous LES studies [101, 146] employed a dilute [47, 127, 146] spray model that does not account for liquid atomization processes. The inflow condition for such a model necessitates specification of droplet size-velocity correlations at the inflow boundary. So, incorporating a engineering liquid breakup model removes the ambiquity of specifying such correlations, which are not known $a - priori$. In summary, for the current study, we are primarily interested in evaluating existing engineering breakup models in a LES of a complex combustor flow field.

1.3 Thesis Outline

The thesis is organized as follows: research objectives are detailed in Chapter 2. This is followed by formulation of the governing equations of the two-phase flow model including the point-volume liquid phase advection in Chapter 3. Details of the numerical method employed for solving the governing equations along with application of initial and outflow boundary conditions are presented in Chapter 4. Validation test cases for the compressible two-phase flow model are reported in Chapter 5. This is followed by validation of two engineering breakup models and results of LES simulation of a LDI combustor in Chapter 6. Conclusions of this research study are presented in Chapter 7 followed by recommendations for future work in Chapter 8.

CHAPTER II

RESEARCH OBJECTIVES

The primary objective of this study is to develop a first-principles simulation approach to study flows involving liquid/gas interfaces over a wide range of operating conditions. With such a simulation capability, several fundamental processes such as, interface instability and deformation, liquid filament formation and ensuing breakup, evaporation, etc. can be simulated to gain further knowledge about their behavior and their underlying mechanisms. This detailed simulation approach can also help in providing correlations for processes like drag effects, collision laws, evaporation rates, etc., for use in simulations of engineering devices.

In this study, a comprehensive and fully compressible formulation for all phases is considered allowing for acoustic, capillary, viscous, and body-force effects. The compressible aspect of the formulation addresses application areas in high pressure, super-critical environments in addition to general material interface processes like deformation and atomization. In addition, this study also addresses the need for a three-dimensional (3D) simulation capability for interface problems by extending the Roe-type scheme of Allaire [4]. This is considered an unique aspect of the study.

A secondary objective of this study is to identify the modeling requirements to perform Large-Eddy Simulation (LES) of spray combustion in engineering devices. These requirements fall into three categories: (a) simulation methodology free of model parameters, (b) realistic inflow boundary information, and (c) inclusion of atomization processes. The emphasis here is to develop physics-based simulation approach accounting for all processes characteristic to engineering devices. In addition, time-to-solution is also a relevant parameter especially in cases of LES being used

as a design tool. Development of such a methodology under these constraints and its application to engineering devices to study relevant processes forms the second contribution of this research.

The following goals are defined to meet the above objectives:

(1) **To formulate capillary effects within a five-equation interface model for Roe-scheme**

This study extends the five-equation model of Allaire *et al.* [4] to include the effects of surface-tension within the Roe-scheme formulation. Additional effects of viscosity as well as body-forces are also considered in the model formulation. Mathematical analysis is carried out to determine the relevant Jacobian matrices, eigenvalues, eigenvectors, and associated approximate jump conditions. Further, a Roe matrix is defined incorporating capillarity which leads to a quasi-conservative Roe scheme. A non-conservative transport equation of volume fraction is discretized based on the condition of Abgrall [1]. A higher-order extension of the discretization is achieved by using the MUSCL method. A hybrid solver is then constructed by means of a dynamic switch/condition which applies upwind scheme in the vicinity of the interface.

(2) **To implement and validate the compressible two-phase model for interface flow problems**

The resulting two-phase formulation is implemented on a multi-processing environment with a particular view towards multi-dimensional applications. Several validation studies are performed with increasing complexity: (a) 2D and 3D Laplace case, (b) 2D and 3D oscillating drop case, (c) 2D bubble rise, (d) 2D pendant drop case, (e) 2D and 3D drag over a liquid drop, and (f) head-on binary drop collision. Parallel processing efficiency of the algorithm is also documented.

(3) **To implement and validate existing engineering breakup models for LES application**

For the secondary objective of applying atomization to LES of a gas turbine combustor, two well-known engineering breakup models–Taylor Analogy Breakup (TAB) and Kelvin-Helmholtz (KH) aerodynamic breakup–are implemented within a LES framework. A standard test case of non-evaporating, solid-cone, high-speed liquid atomization in a cylindrical chamber by Hiroyasu and Kadota [74] is used to validate the implementation of the breakup models. Several characteristics like transient tip penetration, spray-cone angle, and drop sizes are compared with measurement data for three back pressure conditions.

(4) **To study effects of engineering breakup model in LES of a LDI combustor**

LES with Localized Dynamic $k-$equation Model (LDKM, for momentum closure), Linear-Eddy Mixing (LEM, for scalar transport), and an engineering atomization model is employed for a liquid-fueled LDI combustor. Simulation is carried out by resolving the entire inlet flow path through the swirl vanes and the combustor. Two simulations (with- and without-breakup) are performed to study the effects of breakup on the combustor flow field. Both gas- and liquid-phase characteristics are compared with available data. Various unsteady features like Precessing Vortex Core (PVC), spray-flame-PVC interactions, and thermo-chemical correlations are presented and discussed.

CHAPTER III

MATHEMATICAL FORMULATION

In the context of Diffuse Interface Methods (DIM), two approaches are available for the solution of two-phase flow problems: five-equation [4, 131, 118] and seven-equation models [40, 11, 184]. Detailed reduction of the seven-equation model to the five-equation model is first presented. The reduction is done on the basis of asymptotic analysis of the general seven-equation model and follows that of Perigaud and Saurel [148]. This is followed by mathematical properties of the reduced two-phase flow model and a study of the Riemann wave structure.

The secondary objective of two-phase flow application to practical configurations leads to the need for the Large-Eddy Simulation (LES) approach. Fully compressible LES governing equations for reactive flow environment are presented along with two-way coupling with the particle (spray) field. Lagrangian equations of motion for the particle (spray) phase along with the LES closure relations are also documented in this chapter.

3.1 The Seven-equation Model

The two-phase flow model is obtained by employing the averaging procedure of Drew and Passman [40, 41] to the compressible Navier-Stokes equations for each constituent phase. This leads to equations similar to the Navier-Stokes relations except for some additional terms related to inter-fluid interactions. Such a model was developed by Saurel and Abgrall [184] for compressible two-phase flow systems. It followed the work of Baer and Nunziato [11], which was in the context of granular materials. The model [184, 186] is composed of a set of five (in 1D, seven in 3D) partial differential equations for each phase k:

$$\frac{\partial \alpha_k}{\partial t} + u_{I,j}\frac{\partial \alpha_k}{\partial x_j} = \Pi_k + \dot{m}_k/\rho_X \quad (1)$$

$$\frac{\partial \rho_k \alpha_k}{\partial t} + \frac{\partial \rho_k \alpha_k u_{k,j}}{\partial x_j} = \dot{m}_k \quad (2)$$

$$\frac{\partial \rho_k \alpha_k u_{k,i}}{\partial t} + \frac{\partial}{\partial x_j}[\rho_k \alpha_k u_{k,i} u_{k,j} + \alpha_k P_k \delta_{ij} - \alpha_k \tau_{k,ij}] = P_I \frac{\partial \alpha_k}{\partial x_j}\delta_{ij} + \dot{m}_k u_{I,i} - \tau_{I,ij}\frac{\partial \alpha_k}{\partial x_j} + F_{k,i} \quad (3)$$

$$\frac{\partial \rho_k \alpha_k E_k}{\partial t} + \frac{\partial}{\partial x_j}[\alpha_k(\rho_k E_k + P_k)u_{k,j} - \alpha_k u_{k,i}\tau_{k,ji}] = P_I u_{I,j}\frac{\partial \alpha_k}{\partial x_j} + \dot{m}_k E_{k,I} - u_{I,i}(\tau_{I,ij}\frac{\partial \alpha_k}{\partial x_j}) + F_{k,j}u_{I,j} - \Pi_k \phi_I + Q_{k,I} \quad (4)$$

$$\frac{\partial N_k}{\partial t} + \frac{\partial N_k u_{k,j}}{\partial x_j} = \dot{N}_k \quad (5)$$

with following average interface conditions:

$$\sum_k \dot{m}_k = 0$$

$$\sum_k P_I \frac{\partial \alpha_k}{\partial x_j}\delta_{ij} + \dot{m}_k u_{I,i} - \tau_{I,ij}\frac{\partial \alpha_k}{\partial x_j} + F_{k,i} = 0$$

$$\sum_k P_I u_{I,j}\frac{\partial \alpha_k}{\partial x_j} + \dot{m}_k E_{k,I} - u_{I,i}(\tau_{I,ij}\frac{\partial \alpha_k}{\partial x_j}) + F_{k,j}u_{I,j} - \Pi_k \phi_I + Q_{k,I} = 0$$

where, α_k is the volume fraction defined as the ratio of the volume occupied by phase k over the total cell volume. The saturation constraint imposes the condition: $\sum_k \alpha_k = 1$. The density, velocity, pressure, and total specific energy are represented by ρ, u, P, and $E = e + \frac{1}{2}u_j u_j$, respectively. Here, ε is the specific internal energy and the stress tensor is: $\tau_{ij} = \mu[\frac{\partial u_i}{\partial x_j} + \frac{\partial u_j}{\partial x_i}] + \lambda \frac{\partial u_l}{\partial x_l}\delta_{ij}$ where, μ is the molecular viscosity and $\lambda = -2/3\mu$ is the bulk viscosity based on the Stokes hypothesis. Equations of state are required for each constituent and these are generally of the form: $P_k = P_k(\rho_k, \varepsilon_k)$. The subscripts k and I are related to phase k and the interface averaged variables, respectively.

The first equation expresses the advection of the phase volume fraction. In a system with two phases, transport equation for only one of the phases is needed due to the forementioned saturation constraint. Equations 2, 3, and 4 represent,

respectively, the conservation of mass, momemtum, and energy. Several terms appear on the right-hand side related to inter-fluid interactions: $\dot{m}_k$ is the mass-transfer term; $F_{k,i}$ is the $i-$th component drag force; Π_k is the pressure relaxation term; and $Q_{k,I}$ is the heat transfer term. Non-conservative terms also appear: $P_I \nabla \alpha_k$ and $P_I u_I \nabla \alpha_k$. These terms [186] are also called "nozzling terms" by analogy to similar terms appearing in the equations of 1D flow in variable-area ducts.

Equation 5 expresses the transport of the number density of an individual entity composing phase k. For example, if phase k represents solid particles, then N_k is the number of density of particles per cell volume. The term $\dot{N}_k$ models breakup or coalescence of individual particles and usually given by empirical relations [184]. The transport of the number density function enables empirically-based inter-fluid transfer properties like mass, momentum, and energy. It is also interesting to note that the number density transport relations are uncoupled [184] from the system (Eqns. 1- 4), and therefore, has no effect on its mathematical properties.

The pressure P_I and the velocity u_I represent averaged values of the interfacial pressure and velocity over the two-phase control volume. These terms are unclosed and must be modeled. Several expressions have been proposed: Baer and Nunziato [11] considered P_I equal to the gas pressure while u_I was related to the condensed phase velocity; Saurel and Abgrall [184] employed the mixture pressure as: $P_I = \sum_k \alpha_k P_k$; and used the velocity of the center of mass as the estimate for the u_I as: $\sum_k \alpha_k \rho_k u_k / \sum_k \alpha_k \rho_k$. Following Perigaud and Saurel [148], the simplest analytical guess of $P_I = P_{k'}$ and $u_I = u_k$ is retained for the asymptotic analysis. Here, the subscript k' denote fluid properties of the other phase k'. The choice of P_I and u_I has no consequence on the analysis as expansions are considered close to an equilibrium state where there is an equality [148] all pressures and velocities.

The model also contains unclosed inter-fluid interaction terms [184, 186] in relation to the pressure relaxation process, Π_k, and to the velocity equilibrium or the

drag force, $F_{k,i}$. The pressure relaxation term is modeled as: $\Pi_k = \chi[(P_k - P_{k'}) + (P_{\mu_k} - P_{\mu_{k'}})]$ where, the variable χ controls the rate at which the pressure equilibrium is reached. This term represents the rate of expansion of the volume fraction so that the pressure equalizes. Physically [186], it means that the volume of each phase must adjust so that the pressure among phases present reaches equilibrium. Similar term, $\Pi_k \phi_I$, in the energy equation represents the pressure work during the pressure relaxation process. Here, $\phi_I = P_I + P_{\mu_I}$ is the average interface pressure including the viscous effects. The rate factor χ depends on the compressibility of each fluid as well as on the mixture topology rendering it difficult [11] to estimate. For most applications, it is considered as infinite.

The term P_{μ_k} represents [148] the integration of viscous stresses over the interfaces present in the control volume. Following Saurel *et al.* [185] and Perigaud and Saurel [148], the viscous pressure is taken as: $P_{\mu_k} = \frac{4}{3}\mu_k \frac{\dot{\alpha_k}\alpha_{k'}}{\alpha_k}$ where, μ_k is the viscosity of phase k and $\dot{\alpha_k} = \chi\Delta(P + P_\mu)$ is the volume fraction variation. The velocity relaxation term is represented [148, 185] by the drag force which can be written as: $F_{k,i} = \psi(u_{k',i} - u_{k,i})$ where, ψ is a positive number controlling the rate at which the phase velocities tend towards equilibrium. For interface problems separating two pure fluids, a velocity equality at the interface is imposed [184] leading to an infinite velocity relaxation rate coefficient (amounting to the zero relaxation time).

The mass-transfer term, $\dot{m_k}$, is usually given [185] by empirical relations depending on the process under study. For example, evaporation of liquid drops can be described by the D^2-law [217] as: $\dot{m_d} = K\frac{\rho_d S_d}{8R_d}$ where, the subscript d denotes liquid drop, $S_d = 4\pi R_d^2$ is the drop surface area, ρ_d is the drop density, and K is an empirical constant. Similarly, the heat transfer term, $Q_{k,I}$, is usually provided by empirical correlations based on the Nusselt number [185]. An extra source term, $\dot{m_k}/\rho_X$, appears in the volume fraction transport equation when mass-transfer occurs. It involves a density, ρ_X, which is proposed to be chosen equal to that of the less

compressible material [185].

Thus, the system of equations (Eqns. 1- 5) is able to model non-equilibrium, two-phase flows in the presence of wide variety of effects ranging from mass, momentum, and energy transfer among fluids to viscous and fragmentation processes. The general model is hyperbolic and applies both to multifluid and to multiphase flows. The distinction [184] between multifluid and multiphase flows is related to the number of interfaces present within a control volume. In multiphase flows, a control volume contains a large number of individual entities (particles, bubbles, etc.) with many interfaces whereas, in multifluid flows, nearly all control volumes contain pure phases except for the cells in the vicinity around the interface. For computational purposes, homogenized equations where all physical processes occuring within a control volume have been averaged are used in multiphase applications.

Our focus in this study relates to two-phase multifluid flows with interfaces separating immiscible fluids such as liquid/gas. Therefore, terms relating to mass transfer and to cell-averaged multiphase processes can be omitted leading to the following system of equations [148]:

$$
\begin{aligned}
&\frac{\partial \alpha_k}{\partial t} + u_{I,j}\frac{\partial \alpha_k}{\partial x_j} = \chi[(P_k - P_{k'}) + (P_{\mu_k} - P_{\mu_{k'}})] \\
&\frac{\partial \rho_k \alpha_k}{\partial t} + \frac{\partial \rho_k \alpha_k u_{k,j}}{\partial x_j} = 0 \\
&\frac{\partial \rho_k \alpha_k u_{k,i}}{\partial t} + \frac{\partial}{\partial x_j}[\rho_k \alpha_k u_{k,i} u_{k,j} + \alpha_k P_k \delta_{ij} - \alpha_k \tau_{k,ij}] = P_I \frac{\partial \alpha_k}{\partial x_j}\delta_{ij} - \tau_{I,ij}\frac{\partial \alpha_k}{\partial x_j} + \psi(u_{k',i} - u_{k,i}) \\
&\frac{\partial \rho_k \alpha_k E_k}{\partial t} + \frac{\partial}{\partial x_j}[\alpha_k(\rho_k E_k + P_k)u_{k,j} - \alpha_k u_{k,i}\tau_{k,ji}] = P_I u_{I,j}\frac{\partial \alpha_k}{\partial x_j} - u_{I,i}(\tau_{I,ij}\frac{\partial \alpha_k}{\partial x_j}) \\
&\qquad\qquad + \psi(u_{k',j} - u_{k,j})u_{I,j} - \chi\phi_I[(P_k - P_{k'}) + (P_{\mu_k} - P_{\mu_{k'}})]
\end{aligned}
\tag{6}
$$

The simplified system (Eqn. 6) of equations indicates presence of pressure and velocity relaxation terms which drive the system to mechanical equilibrium. Our interest here is in situations where the relaxation times are small compared to other characteristic time scales of the flow. Thus, we present an asymptotic analysis in close proximity to an equilibrium point and obtain a reduced two-phase flow model for interface

problems.

3.2 Asymptotic Analysis

An asymptotic reduction of the system in Eqn. 6 has been performed by Murrone and Guillard [131] in the absence of viscous effects and by Perigaud and Saurel [148] in the context of interface problems including viscosity. Here, we outline major steps in the reduction process and interested readers are referred back to the original works for additional details. Typically, it is convenient to work with primitive variable formulation and use the quasi-linear form of the equations.

Consider a hyperbolic system with stiff source term:

$$\frac{\partial U}{\partial t} + A(U)\frac{\partial U}{\partial x} = \frac{R(U)}{\epsilon} \tag{7}$$

where, $U = U(x,t)$ is a primitive state vector, $A(U) = \frac{\partial F(U)}{\partial U}$ is its Jacobian matrix, $F(U)$ is the flux vector, and $R(U)$ is the source vector. We are interested in the behavior of solutions of the above system in the limit $\epsilon \to 0$. Therefore, we expect these solutions to be close to some equilibrium state (U_o) such that $R(U_o) = 0$. Murrone and Guillard [131] demonstrated solutions of the form: $U = U_o + \epsilon U_1$ where, U_1 is an adjacent state in the neighborhood of the equilibrium state, U_o. Substitution of this solution form in the above system and taking the limits leads to the following expressions [148]: (a) At $O(\epsilon^{-1})$, a necessary condition is obtained for the system to be consistent: $R(U_o) = 0$; (b) At $O(\epsilon^0)$, the first form of the reduced model is obtained:

$$\frac{\partial U_o}{\partial t} + A(U_o)\frac{\partial U_o}{\partial x} = \frac{\partial R}{\partial U}(U_o)U_1$$

where, the right-hand side term is of order ϵ and is neglected in the reduced model.

The above analysis can be applied to the system in Eqn. 6 by considering the two phases denoted by subscripts 1 and 2. Also, we recall that: $P_I = P_2$, $\phi_I = \phi_2$, and $\overrightarrow{u_I} = \overrightarrow{u_1}$ for the interface variables [148]. The pressure and velocity relaxation

terms are cast in the following form: $\chi = 1/\epsilon$ and $\psi = 1/\epsilon$, respectively. The quasi-conservative form in the Eqn. 6 can be re-written in the general form of Eqn. 7 under primitive variable U such that:

$$U = \begin{pmatrix} \alpha_1 \\ \alpha_1\rho_1 \\ \overrightarrow{u_1} \\ P_1 \\ \alpha_2\rho_2 \\ \overrightarrow{u_2} \\ P_2 \end{pmatrix} \quad and \;\; R(U) = \begin{pmatrix} P_1 + P_{\mu_1} - P_2 - P_{\mu_2} \\ 0 \\ (\overrightarrow{u_2} - \overrightarrow{u_1}) \\ -(\phi_2 - \rho_1^2 K_1)(P_1 - P_2 + P_{\mu_1} - P_{\mu_2}) \\ 0 \\ -(\overrightarrow{u_2} - \overrightarrow{u_1}) \\ (\phi_2 - \rho_2^2 K_2)(P_1 - P_2 + P_{\mu_1} - P_{\mu_2}) - \|\overrightarrow{u_2} - \overrightarrow{u_1}\|^2 \end{pmatrix}$$

where, constant $K_j = c_{j,I}^2 \kappa_j;\; j = 1, 2$ is based on the sound speed $(c_{j,I})$ of phase j at the interface and the coefficient κ_j is the differential of specific internal energy with respect to pressure at constant density for phase j.

The condition $R(U_o) = 0$ when applied to the general flow model in Eqn. 6 indicates that the velocity and presures of each phase are equal at $O(\epsilon^0)$. The viscous pressure contribution, P_{μ_k}, vanish at $O(\epsilon^0)$ as the time derivative of the volume fraction, $\dot{\alpha_k}$, is zero when equilibrium is reached. The mechanical equilibrium is thus reached in the limit when the relaxation coefficients tend to infinity. By equating $P_1 = P_2 = P$ and $\overrightarrow{u_1} = \overrightarrow{u_2} = \overrightarrow{u}$, which now represent the mixture pressure and velocity, respectively, the reduced flow model is obtained [131, 148]:

$$\begin{aligned} &\frac{\partial \alpha_1}{\partial t} + u_j \frac{\partial \alpha_1}{\partial x_j} = \Psi[\frac{\partial u_l}{\partial x_l}] \\ &\frac{\partial \rho_1\alpha_1}{\partial t} + \frac{\partial}{\partial x_j}[\rho_1\alpha_1 u_j] = 0 \\ &\frac{\partial \rho_2\alpha_2}{\partial t} + \frac{\partial}{\partial x_j}[\rho_2\alpha_2 u_j] = 0 \\ &\frac{\partial \rho u_i}{\partial t} + \frac{\partial}{\partial x_j}[\rho u_i u_j + P\delta_{ij} - \tau_{ij}] = 0 \\ &\frac{\partial \rho E}{\partial t} + \frac{\partial}{\partial x_j}[(\rho E + P)u_j - u_i\tau_{ji}] = 0 \end{aligned} \tag{8}$$

where, subscripts "1" and "2" represent gas and liquid phases, respectively. The saturation constraint gives: $\alpha_2 = 1 - \alpha_1$. Also, variables u_i, P, E now represent phase mixture velocity, pressure, and total specific energy, respectively. Individual phase densities are denoted by ρ_1 and ρ_2 for phases 1 and 2, respectively. The mixture density is defined as: $\rho = \sum_k \alpha_k \rho_k$ and is a conserved variable. The stress tensor is $\tau_{ij} = 2\mu[S_{ij} - \frac{1}{3}S_{kk}\delta_{ij}]$, where $S_{ij} = \frac{1}{2}(\frac{\partial u_i}{\partial x_j} + \frac{\partial u_j}{\partial x_i})$ is the rate of strain tensor and $\mu = \sum_k \alpha_k \mu_k$ is the mixture viscosity. The source term in the volume fraction transport involves: $\Psi[\frac{\partial u_l}{\partial x_l}]$ where, $\Psi = (\rho_2 c_2^2 - \rho_1 c_1^2)(\rho_1 c_1^2/\alpha_1 + \rho_2 c_2^2/\alpha_2)$.

The specific total mixture energy is defined by $E = \varepsilon + \frac{1}{2}u_j u_j$ with the specific internal energy of the mixture is given by the relation: $\rho\varepsilon = \sum_k \alpha_k \rho_k \varepsilon_k(P, \rho_k)$. Equations of state for each constituent link the pressure and phase-specific internal energy based on the phase-specific density. The speed of sound in phase k is given by: $c_k^2 = (\partial P_k/\partial \rho_k)_{s_k}$ where, s_k is the phase entropy. Murrone and Guillard [131] employed a harmonic average of $\rho_k c_k^2$, also known as Woods' relation [90], for the mixture speed of sound, c. This relation has been validated by measurements in liquid/gas mixtures. However, in cases of artificial mixtures, the use of this relation may [148] yield computational failure due to unphysical appearance of sonic points within the numerical diffusion zone.

The reduced model in Eqn. 8 represents conservation of mass of individual phases in addition to volume fraction transport for one of the phases. Conservation of momentum and energy are accomplished in the mixture mode. The model retains the hyperbolic characteristic of the seven-equation model for convex ($c_k^2 = -(\frac{\partial \varepsilon_k}{\partial s_k})_{\rho_k}$ is positive) equation of state for each phase [131]. Also, it possesses phase-specific entropies and they remain constant along the streamlines [148]. This model had initially been derived, in absence of viscous effects, by Kapila *et al.* [90] in the context granular materials. Allaire [4] and Massoni *et al.* [118], in the absence of viscous effects, independently recovered similar form of the reduced model except for an extra

source term on the right-hand side of the volume fraction transport. This velocity divergence term, $\Psi[\frac{\partial u_l}{\partial x_l}]$, indicates volume fraction variation across acoustic waves. A major drawback [148] of this term in the context of flows involving interfaces separating pure fluids is that the model does not ensure the positivity of the volume fraction. Also, derivation of jump conditions is an issue [90].

Following Perigaud and Saurel [148], simplification of the reduced model in Eqn. 8 is done by neglecting the $\Psi[\frac{\partial u_l}{\partial x_l}]$ term in the volume fraction transport. Implication of this assumption results in the model reverting to the Navier-Stokes equations in each pure phase and constancy of volume fraction across acoustic waves. Also, the assumption makes the model strictly valid only for interface problems [148] and no longer applicable for fluid mixtures. The simplified hydrodynamic five-equation model for interfaces is then given by [148, 4, 118]:

$$\begin{aligned}
&\frac{\partial \alpha_1}{\partial t} + u_j \frac{\partial \alpha_1}{\partial x_j} = 0 \\
&\frac{\partial \rho_1 \alpha_1}{\partial t} + \frac{\partial}{\partial x_j}[\rho_1 \alpha_1 u_j] = 0 \\
&\frac{\partial \rho_2 \alpha_2}{\partial t} + \frac{\partial}{\partial x_j}[\rho_2 \alpha_2 u_j] = 0 \\
&\frac{\partial \rho u_i}{\partial t} + \frac{\partial}{\partial x_j}[\rho u_i u_j + P\delta_{ij} - \tau_{ij}] = 0 \\
&\frac{\partial \rho E}{\partial t} + \frac{\partial}{\partial x_j}[(\rho E + P)u_j - u_i \tau_{ji}] = 0
\end{aligned} \tag{9}$$

where, the hyperbolicity and viscous effects are retained. The same simplification was made by Allaire [4] and Massoni *et al.* [118] in their models, however viscous effects were not considered. Addition of a capillary term and body-force to the above system of equations will complete the model. This is detailed next.

3.3 The Five-equation Model with Capillary and Viscous Effects

Conventional modeling for physical problems involving surface-tension effects have relied on an incompressible formulation of system of equations. In this framework,

the fluid interface is considered as a discontinuity and is tracked either by Eulerian- or Lagrangian-based methods [187]. For the latter approach, the capillarity is enforced as a boundary condition for the pressure. In the fixed-grid or Eulerian approach, surface-tension effects are directly incorporated into the system of equations via capillary tensor terms in the momentum equation. This was based on the pioneering work of Brackbill *et al.* [16]. They proposed a Continuum Surface Force (CSF) [16] method for modeling capillarity in form of a surface force, which is proportional to the normalized curvature of the interface. It is non-zero in the transition region of finite thickness representing a diffused interface.

The main contribution of the CSF method was the reformulation of a discontinuous interface effect in a continuum framework. This has led to simplification of the calculation of the surface-tension effects without imposing any modeling restrictions on the number, complexity, or dynamic evolution of fluid interfaces [187]. Also, no special treatment is needed for flows in three-dimensions. The method has been widely employed in the area of incompressible flows [187, 63, 218, 200].

Very few attempts at incorporating the capillarity within the compressible framework have been reported. Jamet *et al.* [87, 88] proposed thermodynamic method based on the Cahn-Hilliard model [19] to account for the capillary effects. These are the so-called phase-field or second-gradient methods [88]. In this method, the energy of the system depends on the order parameter (density or mass concentration of one of the phases) and its gradient. This allows for the interface to have a finite thickness and surface-tension (interpreted as an energy). This result in equations that are thermodynamically consistent but require the interfacial region to be resolved by the computation mesh. In contrast, surface-tension effects in the CSF method are characterized in form of an equivalent volume force, which acts on scale lengths comparable to the grid spacing rather than the thickness of the interface. Thus, the need for excessive computational resolution for the interface coupled with its specialization to

binary fluid mixtures (water/steam) limits its extension to interface flows separating immiscible fluids.

Perigaud and Saurel [148] proposed an extension to the CSF method in the context of a compressible framework. The resulting model structure is very similar to the second gradient theory models of Jamet *et al.* [87, 88], however interface resolution requirement is absent. In their extension to compressible flows, the surface-tension contribution to the energy balance was specified. The capillarity appears in form a source term in the momentum balance and is considered as a continuum volume force similar to that proposed in the CSF method.

Following Perigaud and Saurel [148], the five-equation model for compressible flows with interfaces including capillary, viscous, and gravity effects is given by:

$$\begin{aligned}
\frac{\partial \alpha_1}{\partial t} &= -u_j \frac{\partial \alpha_1}{\partial x_j} \\
\frac{\partial \rho_1 \alpha_1}{\partial t} &= -\frac{\partial}{\partial x_j}[\rho_1 \alpha_1 u_j] \\
\frac{\partial \rho_2 \alpha_2}{\partial t} &= -\frac{\partial}{\partial x_j}[\rho_2 \alpha_2 u_j] \\
\frac{\partial \rho u_i}{\partial t} &= -\frac{\partial}{\partial x_j}[\rho u_i u_j + P\delta_{ij} - \tau_{ij}] - \sigma\kappa\frac{\partial \alpha_1}{\partial x_i} + \rho g_i \\
\frac{\partial \rho E}{\partial t} &= -\frac{\partial}{\partial x_j}[(\rho E + P)u_j - u_i\tau_{ji}] - \sigma\kappa u_j\frac{\partial \alpha_1}{\partial x_j} + \rho u_i g_i
\end{aligned} \tag{10}$$

where, α_1 is the gas volume fraction, $\alpha_2 = 1 - \alpha_1$ is the liquid volume fraction, ρ_k and $\rho = \sum_k \alpha_k \rho_k$, respectively, are the density of phase k and the mixture density, u_i, P, and $E = \varepsilon + \frac{1}{2}u_i u_i$ are the mixture velocity, pressure, and total specific energy, respectively. Here, $\rho\varepsilon = \sum_k \alpha_k \rho_k \varepsilon_k$ is the mixture internal energy with ε_k as the phase-specific internal energy. Also, g_i is the gravitational acceleration, τ_{ij} is the viscous stress tensor, σ is the surface-tension coefficient, and the local curvature is defined as: $\kappa = \nabla \cdot [\frac{\nabla \alpha_1}{|\nabla \alpha_1|}]$.

The current five-equation model is not closed. There are five equations (in 1D) and six variables (in 1D), which are α_1, ρ_1, ρ_2, u, ε_1, ε_2. This can be seen by recognizing

Material	ρ (kg/m^3)	γ	P_∞ (Pa)	c (m/s)
Air	1.2	1.4	0	374
Ethanol	788	2.1	4.3×10^8	1083
Water	1000	4.1	4.4×10^8	1650
Granite	2627	2.6	142×10^8	3749
Copper	8924	4.0	341×10^8	3911

Table 1: Stiffened gas EOS parameters [184] for several materials.

that the conserved quantities do yield the values of α_1, ρ_1, ρ_2, u but not those of ε_1 and ε_2. Merely a linear combination of them is known. Therefore, an extra relation is needed to close the system. This missing relation in conjunction with the conserved quantities will enable to compute the mixture pressure, P.

3.4 Thermodynamic Closure

In the DIM approach, the interface spans a narrow region with a finite thickness. For flow problems involving pure fluids on either sides of the interface, the numerical diffusion creates an artificial mixture of fluids. Knowledge of fluid-specific equation of state (EOS) enables to compute thermodynamic properties within the cells containing pure fluids, however these properties are not known in the mixture zone due to lack on apriori knowledge of the EOS for the artificial mixture. To alleviate this difficulty, a mixture equation of state is constructed, which is applicable in all regions, i.e., both in pure fluids and mixture zones, of the domain.

For applications involving liquid and gas, the Stiffened gas EOS [66] is typically employed to describe the thermodynamics of pure fluids:

$$P_k = (\gamma_k - 1)\rho_k\varepsilon_k - \gamma_k P_{\infty_k} \tag{11}$$

where, P_k, ρ_k, and ε_k are the pressure, density, and specific internal energy of phase k, respectively. The constants γ_k and P_{∞_k} are the characteristic parameters of the material. This expression is identical to the ideal gas EOS when $\gamma_k = 1.4$ representing the ratio of specific heats and $P_{\infty_k} = 0$. The parameters γ_k and P_{∞_k} are

determined by adjusting the experimental and the theoretical Hugonoit curves. Details of this procedure are reported elsewhere [184]. Table 1 shows corresponding EOS parameters [184] for several materials at standard state. The Stiffened EOS has been reported [184, 148] to be convex so that $c_k^2 = -(\frac{\partial \varepsilon_k}{\partial s_k})_{\rho_k} > 0$. The speed of sound is then expressed as: $c_k = \sqrt{\gamma_k \frac{P_k + P_{\infty_k}}{\rho_k}}$.

The mixture fluid EOS will also be a Stiffened gas as a result of the EOS for pure fluids. Following Allaire [4] and Perigaud and Saurel [148], an isobaric closure for the mixture state is implemented to derive the mixture state EOS. This closure is fully consistent with the assumptions of pressure equilibrium made during the asymptotic analysis. Using the forementioned definition of the mixture internal energy: $\rho\varepsilon = \sum_k \alpha_k \rho_k \varepsilon_k$ and replacing each product term $\rho_k \varepsilon_k$ by a function of pressure from Eqn. 11, we get:

$$\rho\varepsilon = \sum_k \frac{\alpha_k P_k}{\gamma_k - 1} - \sum_k \frac{\alpha_k \gamma_k P_{\infty_k}}{\gamma_k - 1}$$

where, P_k, ρ_k, and ε_k are the pressure, density, and specific internal energy of phase k, respectively. Implementing the isobaric closure leads to $P_1 = P_2 = P$ and the resulting mixture fluid EOS is given as:

$$P = (\gamma - 1)\rho\varepsilon - \gamma P_\infty \tag{12}$$

where, the mixture fluid EOS parameters are given by:

$$\frac{1}{\gamma - 1} = \sum_k \frac{\alpha_k}{\gamma_k - 1} \qquad \gamma P_\infty = \frac{\sum_k \frac{\alpha_k \gamma_k P_{\infty_k}}{\gamma_k - 1}}{\sum_k \frac{\alpha_k}{\gamma_k - 1}}$$

The resulting mixture EOS provides a link to compute the mixture pressure from the conserved variables and the volume fraction. This constituitive relation in Eqn. 12 closes the system of equations (in Eqn. 10) and the two-phase five-equation model with capillary and viscous effects is now complete.

Allaire [4] has demonstrated that the two-phase model can be extended to a wide range of EOS by replacing algebraic thermodynamic closure relations for the mixture

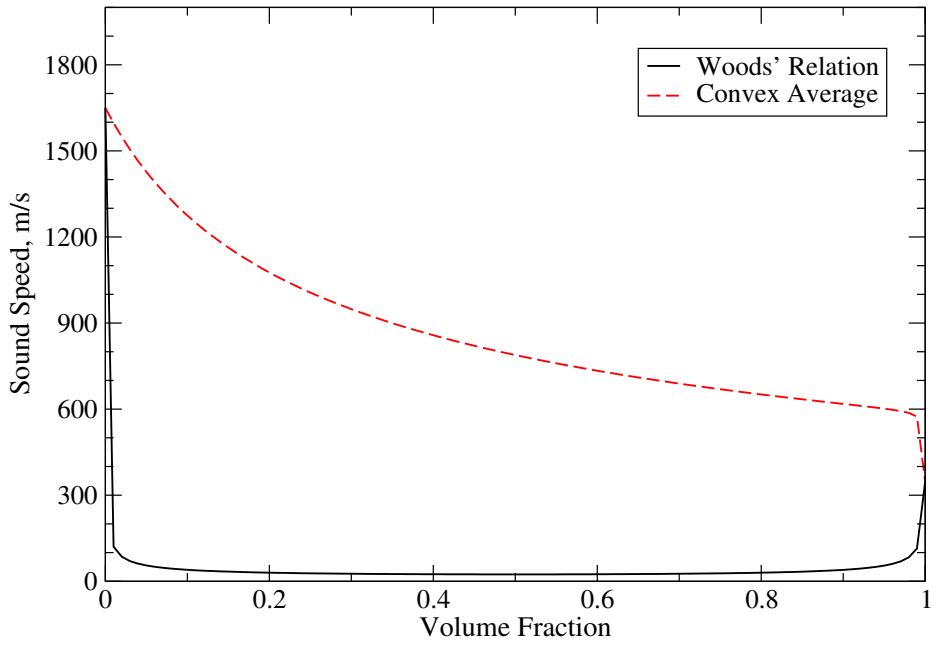

Figure 1: Variation of sound speed of an air-water mixture as a function of gas volume fraction in the interface region.

by a single supplementary transport equation (like the volume fraction advection relation). This property is retained in our formulation, and therefore, the current model is not restricted to the above formulated Stiffened EOS. Other EOS can be employed with the only change need will be in the computation of the EOS parameters [4].

The mixture speed of sound has been reported to be deduced in several forms. For example, Murrone and Guillard [131] employed a harmonic average of phase sonic speeds in the form of: $\frac{1}{\rho c^2} = \sum_k \frac{\alpha_k}{\rho_k c_k^2}$, also known as the Woods' relation [90]. On the other hand, Allaire [4], and Perigaud and Saurel [148] have expressed the mixture sonic speed as:

$$\rho c^2 = \frac{1}{\gamma - 1} \sum_k \frac{\alpha_k \rho_k c_k^2}{\gamma_k - 1} \tag{13}$$

with ρ and $\frac{1}{\gamma-1}$ as the mixture properties. It is noted to be a convex average of phase-specific properties and can be written as a function of mixture pressure as: $\rho c^2 = \gamma(P + P_\infty)$. The behavior of Woods' relation is in agreement with experimental observations in the context of physical fluid mixtures [148]. However, in cases of flows

with artificial mixture zones, the Woods' relation predicts low speed of sound within the interface region, as shown in Fig. 1. This creates difficulty in solution convergence [148] by artificial appearance of sonic points within the interface region without any physical flow acceleration. The sound speed expression in Eqn. 13 results in a smooth variation between the sonic speeds of pure fluids and is observed to be larger than the sound speed given by the Woods' relation in the interface zone. Thus, Eqn. 13 does not exhibit such drawbacks and is retained in this study.

3.5 Mathematical Analysis of the model

The systems of equations (Eqn. 10) developed to solve the two-phase interface flows exhibits non-conservative character. Particularly, this is related to the volume fraction transport equation. Abgrall [1] and Karni [92] have shown that to obtain good stability properties at the material interface it is necessary to forego strict conservative character of the computational method. The numerical method adopted in this study to solve Eqn. 10 relies on a Roe-type scheme following Allaire [1]. The main advantage of this approximate Riemann approach lies in the simplicity of the numerical implementation as well as iteration-free Riemann solution. This study extends the work of Allaire [4] by including capillary effects within a Roe-type scheme. In addition, effects of viscosity as well as body-force are considered in the model. Also, the model formulation and implementation is done in a three-dimensional framework.

The primary aim of this section is to describe the mathematical model used in a Roe-type approximate Riemann solver. Capillary effects are built-in into the mathematical analysis, however both the viscous and body-force terms are neglected. This is a generic procedure to perform analysis on the convective portion of the system of equations and postpone the consideration of the dissipative and external effects till the system is solved. Conventional hyperbolic systems analysis [184] cannot be performed on the current quasi-conservative system. Difficulty arises due to the forementioned volume fraction transport equation and the presence of the local curvature

$\kappa = \nabla \cdot [\frac{\nabla \alpha_1}{|\nabla \alpha_1|}]$ term in the momentum and the energy conservation. Following Perigaud and Saurel [148], the gradient vector $(\frac{\nabla \alpha_1}{|\nabla \alpha_1|})$ is considered as an independent variable. Thus, it is assumed that the local curvature is frozen at a given location and time. This simplifies the term $\sigma\kappa\nabla\alpha_1$ as a first order derivative in volume fraction for the analysis.

The analysis is performed on a system written in the set of variables $\mathbf{W} = [\alpha_1\rho_1, \alpha_2\rho_2, \rho u, \rho v, \rho w, \rho E, \alpha_1]^T$. The system is then written in the following quasi-linear form:

$$\frac{\partial \mathbf{W}}{\partial t} + A(\mathbf{W})\frac{\partial \mathbf{W}}{\partial x} + B(\mathbf{W})\frac{\partial \mathbf{W}}{\partial y} + C(\mathbf{W})\frac{\partial \mathbf{W}}{\partial z} = 0 \tag{14}$$

where, A, B, C are the Jacobian matrices of the system and are given by:

$$A(\mathbf{W}) = \begin{pmatrix} uy_2 & -uy_1 & y_1 & 0 & 0 & 0 & 0 \\ -uy_2 & uy_1 & y_2 & 0 & 0 & 0 & 0 \\ (\beta_1 - u^2) & (\beta_2 - u^2) & (2 - \frac{1}{\xi})u & -\frac{v}{\xi} & -\frac{w}{\xi} & \frac{1}{\xi} & \Omega + \sigma\kappa \\ -uv & -uv & v & u & 0 & 0 & 0 \\ -uw & -uw & w & 0 & u & 0 & 0 \\ u(\beta_1 - H) & u(\beta_2 - H) & (H - \frac{u^2}{\xi}) & -\frac{uv}{\xi} & -\frac{uw}{\xi} & u(\frac{1}{\xi} + 1) & \Omega u + \sigma\kappa u \\ 0 & 0 & 0 & 0 & 0 & 0 & u \end{pmatrix}$$

$$B(\mathbf{W}) = \begin{pmatrix} vy_2 & -vy_1 & 0 & y_1 & 0 & 0 & 0 \\ -vy_2 & vy_1 & 0 & y_2 & 0 & 0 & 0 \\ -uv & -uv & v & u & 0 & 0 & 0 \\ (\beta_1 - v^2) & (\beta_2 - v^2) & -\frac{u}{\xi} & (2 - \frac{1}{\xi})v & -\frac{w}{\xi} & \frac{1}{\xi} & \Omega + \sigma\kappa \\ -vw & -vw & 0 & w & v & 0 & 0 \\ v(\beta_1 - H) & v(\beta_2 - H) & -\frac{uv}{\xi} & (H - \frac{v^2}{\xi}) & -\frac{vw}{\xi} & v(\frac{1}{\xi} + 1) & \Omega v + \sigma\kappa v \\ 0 & 0 & 0 & 0 & 0 & 0 & v \end{pmatrix}$$

$$C(\mathbf{W}) = \begin{pmatrix} wy_2 & -wy_1 & 0 & 0 & y_1 & 0 & 0 \\ -wy_2 & wy_1 & 0 & 0 & y_2 & 0 & 0 \\ -uw & -uw & w & 0 & u & 0 & 0 \\ -vw & -vw & 0 & w & v & 0 & 0 \\ (\beta_1 - w^2) & (\beta_2 - w^2) & -\frac{u}{\xi} & -\frac{v}{\xi} & (2-\frac{1}{\xi})w & \frac{1}{\xi} & \Omega + \sigma\kappa \\ w(\beta_1 - H) & w(\beta_2 - H) & -\frac{uw}{\xi} & -\frac{vw}{\xi} & (H - \frac{w^2}{\xi}) & w(\frac{1}{\xi}+1) & \Omega w + \sigma\kappa w \\ 0 & 0 & 0 & 0 & 0 & 0 & w \end{pmatrix}$$

where, $y_i = \alpha_i\rho_i/\rho$ is the mass fraction, $H = E + P/\rho$ is the specific total enthalpy, the coefficient $\beta_i = (\frac{u^2+v^2+w^2}{2} - \delta_i)/\xi$, and $\Omega = \frac{1}{\xi}[(\rho_1\delta_1 - \rho_1\varepsilon_1) - (\rho_2\delta_2 - \rho_2\varepsilon_2)]$ arises due to the differential of mixture pressure with respect to α_1. Here, $\xi = 1/(\gamma - 1)$ and $\delta_i = (\frac{\partial\rho_i\varepsilon_i}{\partial\rho_i})_{P_i} = 0$ for the Stiffened EOS [4]. The total differential of the pressure in terms of the variable $\mathbf{W}$ is given by [4]: $dP = \frac{1}{\xi}d(\rho E) - \frac{u}{\xi}d(\rho u) - \frac{v}{\xi}d(\rho v) - \frac{w}{\xi}d(\rho w) + \beta_i d(\rho_i\alpha_i) + \Omega d\alpha_1$

An alternative choice of variables, and formulations, is the vector of primitive or physical variables: $\mathbf{V} = [\rho_1, \rho_2, u, v, w, P, \alpha_1]^T$. The governing equations take a similar form: $\partial_t\mathbf{V} = A(\mathbf{V})\partial_x\mathbf{V} + B(\mathbf{V})\partial_y\mathbf{V} + C(\mathbf{V})\partial_z\mathbf{V}$, where the coefficient matrices in x-, y-, and z-directions are, respectively, given by:

$$\underbrace{\begin{pmatrix} u & 0 & \rho_1 & 0 & 0 & 0 & 0 \\ 0 & u & \rho_2 & 0 & 0 & 0 & 0 \\ 0 & 0 & u & 0 & 0 & \frac{1}{\rho} & \frac{\sigma\kappa}{\rho} \\ 0 & 0 & 0 & u & 0 & 0 & 0 \\ 0 & 0 & 0 & 0 & u & 0 & 0 \\ 0 & 0 & \rho c^2 & 0 & 0 & u & 0 \\ 0 & 0 & 0 & 0 & 0 & 0 & u \end{pmatrix}}_{A(\mathbf{V})}, \underbrace{\begin{pmatrix} v & 0 & 0 & \rho_1 & 0 & 0 & 0 \\ 0 & v & 0 & \rho_2 & 0 & 0 & 0 \\ 0 & 0 & v & 0 & 0 & 0 & 0 \\ 0 & 0 & 0 & v & 0 & \frac{1}{\rho} & \frac{\sigma\kappa}{\rho} \\ 0 & 0 & 0 & 0 & v & 0 & 0 \\ 0 & 0 & 0 & \rho c^2 & 0 & v & 0 \\ 0 & 0 & 0 & 0 & 0 & 0 & v \end{pmatrix}}_{B(\mathbf{V})}, \underbrace{\begin{pmatrix} w & 0 & 0 & 0 & \rho_1 & 0 & 0 \\ 0 & w & 0 & 0 & \rho_2 & 0 & 0 \\ 0 & 0 & w & 0 & 0 & 0 & 0 \\ 0 & 0 & 0 & w & 0 & 0 & 0 \\ 0 & 0 & 0 & 0 & w & \frac{1}{\rho} & \frac{\sigma\kappa}{\rho} \\ 0 & 0 & 0 & 0 & \rho c^2 & w & 0 \\ 0 & 0 & 0 & 0 & 0 & 0 & w \end{pmatrix}}_{C(\mathbf{V})}$$

Eigenvalues and eigenvectors of the corresponding Jacobian matrices are evaluated next. For both formulations, the system has the following seven eigenvalues:

$$\lambda_1 = u_n - c, \quad \lambda_2 = \ldots = \lambda_6 = u_n, \quad \lambda_7 = u_n + c \tag{15}$$

where, u_n is the velocity component such that: $u_n = \overrightarrow{u} \cdot \overrightarrow{n}$ with $\overrightarrow{n} = (n_x, n_y, n_z)$ as the unit vector in direction x, y, z. It is interesting to note that the eigenvalues of the system with capillarity are the same as for the Euler system. Also, with $c^2 > 0$ due to the Stiffened EOS, the eigenvalues are real.

The corresponding right and left eigenvectors differ for each formulation. The right eigenvectors $r_i(\mathbf{W})$ (for $i \in 1, \ldots, 7$) which verify the relation $A(\mathbf{W})r_i(\mathbf{W}) = \lambda_i(\mathbf{W})r_i(\mathbf{W})$ are given as:

$$r_1(\mathbf{W}) = \begin{pmatrix} y_1 \\ y_2 \\ (u-c) \\ v \\ w \\ (H-uc) \\ 0 \end{pmatrix}, \; r_2(\mathbf{W}) = \begin{pmatrix} 1 \\ 0 \\ u \\ v \\ w \\ \Lambda + \delta_1 \\ 0 \end{pmatrix}, \; r_3(\mathbf{W}) = \begin{pmatrix} 0 \\ 1 \\ u \\ v \\ w \\ \Lambda + \delta_2 \\ 0 \end{pmatrix}, \; r_4(\mathbf{W}) = \begin{pmatrix} 0 \\ 0 \\ 0 \\ 0 \\ 0 \\ -(\Omega + \sigma\kappa)\xi \\ 1 \end{pmatrix}$$

$$r_5(\mathbf{W}) = \begin{pmatrix} 0 \\ 0 \\ 0 \\ 1 \\ 0 \\ v \\ 0 \end{pmatrix}, \; r_6(\mathbf{W}) = \begin{pmatrix} 0 \\ 0 \\ 0 \\ 0 \\ 1 \\ w \\ 0 \end{pmatrix}, \; r_7(\mathbf{W}) = \begin{pmatrix} y_1 \\ y_2 \\ (u+c) \\ v \\ w \\ (H+uc) \\ 0 \end{pmatrix}$$

where, $\Lambda = \frac{u^2+v^2+w^2}{2}$ is the kinetic energy. Similarly, the right eigenvectors for the primitive-variable formulation are given by:

$$r_1(\mathbf{V}) = \frac{1}{2c} \begin{bmatrix} \rho_1, & \rho_2, & -c, & 0, & 0, & \rho c^2, & 0 \end{bmatrix}^T$$

$$r_2(\mathbf{V}) = \begin{bmatrix} 1, & 0, & 0, & 0, & 0, & 0, & 0 \end{bmatrix}^T$$

$$r_3(\mathbf{V}) = \begin{bmatrix} 0, & 1, & 0, & 0, & 0, & 0, & 0 \end{bmatrix}^T$$

$$r_4(\mathbf{V}) = \begin{bmatrix} 0, & 0, & 0, & 1, & 0, & 0, & 0 \end{bmatrix}^T$$

$$r_5(\mathbf{V}) = \begin{bmatrix} 0, & 0, & 0, & 0, & 1, & 0, & 0 \end{bmatrix}^T$$

$$r_6(\mathbf{V}) = \begin{bmatrix} 0, & 0, & 0, & 0, & 0, & -\sigma\kappa, & 1 \end{bmatrix}^T$$

$$r_7(\mathbf{V}) = \frac{1}{2c} \begin{bmatrix} \rho_1, & \rho_2, & c, & 0, & 0, & \rho c^2, & 0 \end{bmatrix}^T$$

Corresponding left eigenvectors which obey the relation $l_i(\mathbf{W})A(\mathbf{W}) = \lambda_i(\mathbf{W})l_i(\mathbf{W})$ are given as:

$$l_1(\mathbf{W}) = \frac{1}{2c^2} \begin{pmatrix} \beta_1 + uc, & \beta_2 + uc, & -c - \frac{u}{\xi}, & -\frac{v}{\xi}, & -\frac{w}{\xi}, & \frac{1}{\xi}, & \Omega + \sigma\kappa \end{pmatrix}$$

$$l_2(\mathbf{W}) = \frac{1}{\xi c^2} \begin{pmatrix} \xi c^2 + y_1\delta_1 - y_1\Lambda, & y_1\delta_2 - y_1\Lambda, & uy_1, & vy_1, & wy_1, & -y_1, & -y_1\xi(\Omega + \sigma\kappa) \end{pmatrix}$$

$$l_3(\mathbf{W}) = \frac{1}{\xi c^2} \begin{pmatrix} y_2\delta_1 - y_2\Lambda, & \xi c^2 + y_2\delta_2 - y_2\Lambda, & uy_2, & vy_2, & wy_2, & -y_2, & -y_2\xi(\Omega + \sigma\kappa) \end{pmatrix}$$

$$l_4(\mathbf{W}) = \begin{pmatrix} 0, & 0, & 0, & 0, & 0, & 0, & 1 \end{pmatrix}$$

$$l_5(\mathbf{W}) = \begin{pmatrix} -v, & -v, & 0, & 1, & 0, & 0, & 0 \end{pmatrix}$$

$$l_6(\mathbf{W}) = \begin{pmatrix} -w, & -w, & 0, & 0, & 1, & 0, & 0 \end{pmatrix}$$

$$l_7(\mathbf{W}) = \frac{1}{2c^2} \begin{pmatrix} \beta_1 - uc, & \beta_2 - uc, & c - \frac{u}{\xi}, & -\frac{v}{\xi}, & -\frac{w}{\xi}, & \frac{1}{\xi}, & \Omega + \sigma\kappa \end{pmatrix}$$

It can be easily verified that the product of the left and the right eigenvectors reduce to: $l_i^T(\mathbf{W}) \cdot r_j(\mathbf{W}) = \delta_{ij}$. The system is thus confirmed to be hyperbolic since the Jacobian matrices are diagonizable and their eigenvectors span the whole space. It is also noted that the inclusion of capillarity does not influence the system's hyperbolic characteristic.

Similarly, the left eigenvectors for the primitive system of equations are given by:

$$l_1(\mathbf{V}) = \left(\begin{array}{ccccccc} 0, & 0, & -1, & 0, & 0, & \frac{1}{\rho c}, & \frac{\sigma\kappa}{\rho c} \end{array} \right)$$

$$l_2(\mathbf{V}) = \left(\begin{array}{ccccccc} 1, & 0, & 0, & 0, & 0, & 0, & -\frac{y_1}{c^2} \end{array} \right)$$

$$l_3(\mathbf{V}) = \left(\begin{array}{ccccccc} 0, & 1, & 0, & 0, & 0, & 0, & -\frac{y_2}{c^2} \end{array} \right)$$

$$l_4(\mathbf{V}) = \left(\begin{array}{ccccccc} 0, & 0, & 0, & 1, & 0, & 0, & 0 \end{array} \right)$$

$$l_5(\mathbf{V}) = \left(\begin{array}{ccccccc} 0, & 0, & 0, & 0, & 1, & 0, & 0 \end{array} \right)$$

$$l_6(\mathbf{V}) = \left(\begin{array}{ccccccc} 0, & 0, & 0, & 0, & 0, & 1, & \sigma\kappa \end{array} \right)$$

$$l_7(\mathbf{V}) = \left(\begin{array}{ccccccc} 0, & 0, & 1, & 0, & 0, & \frac{1}{\rho c}, & \frac{\sigma\kappa}{\rho c} \end{array} \right)$$

With the eigenvalues and eigenvectors available we can ascertain the nature of the characteristic fields associated with each pair $(\lambda_i, r_i(\mathbf{W}))$. For example, the characteristic field associated with $\lambda_2 = \ldots = \lambda_6 = u$ is seen to be linearly degenerate as: $\nabla_{\mathbf{W}}\lambda_i \cdot r_i(\mathbf{W})$=0, where $i \in 2, \ldots, 6$. As for the eigenvalues $\lambda_1 = u - c$ and $\lambda_7 = u + c$, the characteristic fields are all genuinely non-linear, i.e. $\nabla_{\mathbf{W}}\lambda_i \cdot r_i(\mathbf{W}) \neq 0$, where $i = 1$ & 7.

The corresponding wave strengths [213] can also be determined. They are obtained by projecting the jump $\Delta\mathbf{W}$ onto the left eigenvectors as:

$$\varsigma_i(\mathbf{W}) = l_i(\mathbf{W}) \cdot \Delta\mathbf{W}$$

where, the jump $\Delta\mathbf{W} = \mathbf{W}_R - \mathbf{W}_L$. Here, $\mathbf{W}_R$ and $\mathbf{W}_L$ are the right and left states across the wave structure, respectively. The wave strengths corresponding to the $A(\mathbf{W})$ matrix are then obtained as:

$$\varsigma_1(\mathbf{W}) = \frac{1}{2c^2}\left[-\rho c\Delta u + \Delta P + \sigma\kappa\Delta\alpha_1\right]$$

$$\varsigma_2(\mathbf{W}) = \left[\Delta(\rho_1\alpha_1) - \frac{y_1}{c^2}\Delta P - \frac{y_1}{c^2}\sigma\kappa\Delta\alpha_1\right]$$

$$\varsigma_3(\mathbf{W}) = \left[\Delta(\rho_2\alpha_2) - \frac{y_2}{c^2}\Delta P - \frac{y_2}{c^2}\sigma\kappa\Delta\alpha_1\right]$$

$$\varsigma_4(\mathbf{W}) = \Delta\alpha_1$$

$$\varsigma_5(\mathbf{W}) = \rho\Delta v$$

$$\varsigma_6(\mathbf{W}) = \rho\Delta w$$

$$\varsigma_7(\mathbf{W}) = \frac{1}{2c^2}\left[\rho c\Delta u + \Delta P + \sigma\kappa\Delta\alpha_1\right]$$

Similar wave strengths can be deduced by the above procedure for the primitive-variable formulation and are given as:

$$\varsigma_1(\mathbf{V}) = \frac{1}{2\rho c^2}\left[-\rho c\Delta u + \Delta P + \sigma\kappa\Delta\alpha_1\right]$$

$$\varsigma_2(\mathbf{V}) = \left[\Delta\rho_1 - \frac{\rho_1}{\rho c^2}\Delta P - \frac{\rho_1}{\rho c^2}\sigma\kappa\Delta\alpha_1\right]$$

$$\varsigma_3(\mathbf{V}) = \left[\Delta\rho_2 - \frac{\rho_2}{\rho c^2}\Delta P - \frac{\rho_2}{\rho c^2}\sigma\kappa\Delta\alpha_1\right]$$

$$\varsigma_4(\mathbf{V}) = \Delta v$$

$$\varsigma_5(\mathbf{V}) = \Delta w$$

$$\varsigma_6(\mathbf{V}) = \Delta\alpha_1$$

$$\varsigma_7(\mathbf{V}) = \frac{1}{2\rho c^2}\left[\rho c\Delta u + \Delta P + \sigma\kappa\Delta\alpha_1\right]$$

Based on the Jacobian matrices and their corresponding eigenvalues, eigenvectors, and wave strengths, a Roe matrix [4] and associated flux leading to a Roe-type scheme can be developed. Also, the mathematical analysis of the model provides information on the effect of the capillarity on the Riemann wave structure and this is discussed next.

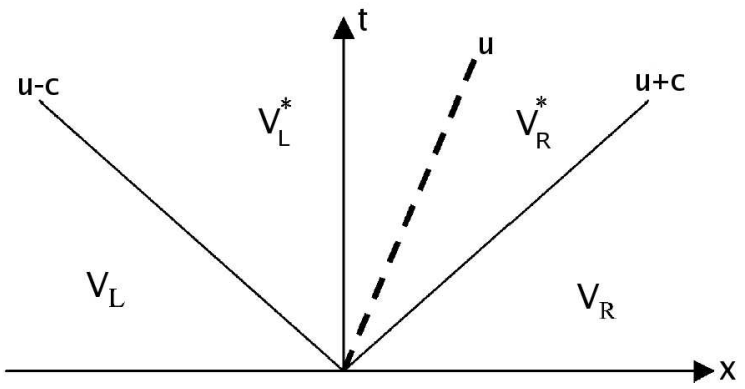

Figure 2: Wave structure of an idealized Riemann problem.

3.6 Riemann Problem Structure

An idealized Riemann problem with the following initial data and a prescribed curvature for the interface is considered. Two constant states are assumed: $\mathbf{V}_L = [\rho_1, \rho_2, u, v, w, P, \alpha_1]_L^T$ and $\mathbf{V}_R = [\rho_1, \rho_2, u, v, w, P, \alpha_1]_R^T$. Figure 2 shows the wave structure along with the initial states. The interface is shown in form of a dashed line corresponding to a linearly degenerate wave ($\lambda = u$).

The wave strengths in conjunction with the right eigenvectors provide the star-states across each wave. These are given as follows:

$$V_R^* = V_R - \varsigma_7(\mathbf{V}) r_7(\mathbf{V})$$

$$V_L^* = V_L + \varsigma_1(\mathbf{V}) r_1(\mathbf{V})$$

where, $V_R^* - V_R$ and $V_L^* - V_L$ are approximate jumps across the $\lambda_7 = u + c$ and $\lambda_1 = u - c$ waves, respectively. We are interested in the pressure jump across the wave $\lambda = u$ and this is given by:

$$P_R^* - P_L^* = (P_R - P_L) - \rho c^2(\varsigma_7 + \varsigma_1)$$

which with further simplification gives the following pressure jump:

$$\Delta P^* = -\sigma\kappa\Delta\alpha_1 \quad \Rightarrow \quad \Delta P^* + \sigma\kappa\Delta\alpha_1 = 0$$

Similarly, for the normal velocity component (u) and the volume fraction (α_1) jump are given as:

$$\Delta u^* = 0; \qquad \Delta\alpha_1^* = \Delta\alpha_1 = \alpha_R - \alpha_L$$

This is in agreement with the Riemann invariants [148] across a curved contact discontinuity. The effect of the capillarity appears in form of a pressure jump which is proportional to the surface-tension coefficient and the interface curvature. The associated pressure increase/decrease is consistent with the Laplace-Young law [105, 56]. Perigaud and Saurel [148] have demonstrated the consistency of the pressure jump and fulfillment of the Laplace-Young law for various situations involving curved interface separating two pure fluids.

This completes the formulation and analysis for the five-equation interface model. Both the convective part as well as the capillarity term were included in the analysis. Dissipative and external effects on the system of equations will be considered in the solution of the five-equation model discussed in the next chapter.

As was pointed out in the introduction, the primary limitation of the detailed modeling of interface problems is the grid resolution requirement especially in cases involving practical configurations. Point-volume approaches [114] can be employed to study atomization processes and its effects on the flow field of practical devices albeit at an expense of invoking empirical relations. Explicit computation of large, energy-containing scales is a necessary requirement [157] for accurate resolution of unsteady motions such as vortex shedding and flame associated interactions. LES provides such a capability to resolve geometry-dependent scales and model scales smaller than the grid size. In the following sections, we will present LES gas phase equations with primary emphasis on the species closure and two-way coupling with the discrete particle (or spray) evolution.

3.7 LES Equations

Large-Eddy Simulation (LES) fully resolves the large-scale dynamics and employs models (called subgrid-scale SGS models) at the unresolved scales. Therefore, an operation is required which can separate or $filter$ the governing Navier-Stokes equations into (resolved) large-scale and (unresolved) SGS components. This is achieved, following Erlebacher *et al.* [45], by applying a spatial filtering operation to the governing equations such that $f = \widetilde{f} + f''$, where: $\sim$ and $''$ denote the resolved super-grid and unresolved sub-grid quantities, respectively. The resolved super-grid quantities are determined by Favre filtering [153, 157]:

$$\widetilde{f} = \frac{\overline{\rho f}}{\overline{\rho}} \tag{16}$$

where, the over-bar represents spatial filtering defined [153, 157] as:

$$\overline{\rho f(x_i, t)} = \int \rho f(z_i, t) G(x_i - z_i, \overline{\Delta}) dz_i. \tag{17}$$

where, G is the filter kernel, x_i corresponds to the point of interest, z_i is the dummy variable, the integral is over the entire computational domain, and $\overline{\Delta}$ is filter size, defined as $\overline{\Delta} = (\Delta x \Delta y \Delta z)^{1/3}$, where $(\Delta x, \Delta y, \Delta z)$ are the local grid size in streamwise, transverse, and spanwise directions respectively. The filter function, G, must satisfy the normalization condition [157]:

$$\oint_{total\ \ volume} G(\overrightarrow{x} - \overrightarrow{z}, \overline{\Delta}) d\overrightarrow{z} = 1 \tag{18}$$

The filter so applied is spatial in character rather than temporal as in the case of Reynolds Averaged Navier-Stokes (RANS) formulation. Contrary to RANS averaging, the filtered value of a LES perturbation is not zero: i.e., $\widetilde{f''} \neq 0$. Also, the filtered and double filtered values are not equal (except when cut-off filter in spectral space is used for filtering): i.e., $\widetilde{\widetilde{f}} \neq \widetilde{f}$. The derivation of LES governing equations in terms of filtered quantities ($\widetilde{f}$) requires commutability of filter and derivative operations. The filtering approach can be viewed [157, 137] as applying a linear operator that is

commutative with both the space and time derivatives. In this study, a box filter is employed, which is appropriate for finite-volume schemes [189]. For a given direction ($i = 1, 2, 3$), this filter function G is of the form:

$$G = \begin{cases} 1/\overline{\Delta} & -\frac{\overline{\Delta}}{2} \leq (x_i - z_i) \leq \frac{\overline{\Delta}}{2} \\ 0 & \text{otherwise} \end{cases} \tag{19}$$

Applying the filtering operation, using a low-pass box filter, to the instantaneous Navier-Stokes equations (Eqn. 2, 3, 4 with $\alpha_k = 1$), following filtered LES equations are obtained:

$$\begin{aligned} \frac{\partial \bar{\rho}}{\partial t} &= \widetilde{\dot{\rho}_s} - \frac{\partial \bar{\rho}\tilde{u}_j}{\partial x_j} \\ \frac{\partial \bar{\rho}\tilde{u}_i}{\partial t} &= \widetilde{\dot{F}_{s,i}} - \frac{\partial}{\partial x_j}[\bar{\rho}\tilde{u}_i\tilde{u}_j + \bar{p}\delta_{ij} - \bar{\tau}_{ij} + \tau_{ij}^{sgs}] \\ \frac{\partial \bar{\rho}\tilde{E}}{\partial t} &= \widetilde{\dot{Q}_s} - \frac{\partial}{\partial x_i}[(\bar{\rho}\tilde{E} + \bar{p})\tilde{u}_i + \bar{q}_i - \tilde{u}_j\bar{\tau}_{ji} + H_i^{sgs} + \sigma_i^{sgs}] \end{aligned} \tag{20}$$

where, $\overline{\rho}$ is filtered mass density, $\widetilde{u}_i$ is the resolved velocity vector, $\overline{p}$ is the filtered pressure determined from filtered equation of state for ideal gas, $\widetilde{E}$ is resolved total energy per unit mass, $\overline{\tau}_{ij}$ is filtered viscous stress, and $\overline{q}_i$ is the heat flux vector. The sub-grid terms resulting from the filtering operation, denoted with super-script ^{sgs}, represent the small-scale effects upon the resolved-scales in the form of additional stresses and fluxes. Subscript s denote source terms from dispersed phase. Filtered equations for k-species mass fraction $\tilde{Y_k}$ are not shown here since they are solved using a sub-grid approach, as described later.

The viscous stress tensor ($\overline{\tau}_{ij}$) and heat flux vector ($\overline{q}_i$) are given as:

$$\begin{aligned} \overline{\tau}_{ij} &= \bar{\mu}\left(\frac{\partial \widetilde{u_i}}{\partial x_j} + \frac{\partial \widetilde{u_j}}{\partial x_i}\right) - \frac{2}{3}\bar{\mu}\left(\frac{\partial \widetilde{u_k}}{\partial x_k}\right)\delta_{ij} \\ \overline{q}_i &= \underbrace{-\overline{\kappa}\frac{\partial \widetilde{T}}{\partial x_i}}_{\textbf{Conduction}} + \underbrace{\bar{\rho}\sum_{k=1}^{N_s}\tilde{h}_k\tilde{Y}_k\widetilde{V_{i,k}}}_{\textbf{Mass Diffusion}} + \sum_{k=1}^{N_s} q_{i,k}^{sgs} \end{aligned}$$

where, the diffusion velocities are approximated using Fickian diffusion as $\widetilde{V_{i,k}} = (-\bar{D}_k/\tilde{Y}_k)(\partial\tilde{Y}_k/\partial x_i)$, molecular viscosity ($\bar{\mu}$) is approximated by Sutherland's Law

based on resolved temperature ($\widetilde{T}$), and the thermal conductivity ($\bar{\kappa}$) is approximated as $\bar{\kappa} = \bar{\mu}\bar{C}_p/Pr$, where $\bar{C}_p$ is the specific heat at constant pressure for gaseous mixture and Pr is the Prandtl number. Also, $\bar{D}_k$ is $k-th$ species diffusion coefficient and the index k for species varies from 1 to N_s, where N_s is the total number of species present in the system.

The pressure is determined from the filtered equation of state,

$$\bar{p} = \bar{\rho} R_u \sum_{k=1}^{N_s} [\frac{\tilde{Y}_k \tilde{T}}{MW_k} + \frac{T_k^{sgs}}{MW_k}]$$

where, R_u and MW_k are the universal gas constant and $k-th$ species molecular weight, respectively. The subgrid temperature-species correlation term is defined as, $T_k^{sgs} = [\widetilde{Y_k T} - \tilde{Y}_k \tilde{T}]$.

The filtered total energy per unit volume is given by: $\bar{\rho}\tilde{E} = \bar{\rho}\tilde{e} + \frac{1}{2}\bar{\rho}\tilde{u}_i\tilde{u}_i + \bar{\rho}k^{sgs}$ where, the sub-grid kinetic energy (discussed later) is defined as, $k^{sgs} = (1/2)[\widetilde{u_k u_k} - \tilde{u}_k\tilde{u}_k]$. The filtered specific internal energy is given by:

$$\tilde{e} = \sum_{k=1}^{N_s} [\tilde{Y}_k \tilde{h}_k + (\widetilde{Y_k h_k} - \tilde{Y}_k \tilde{h_k})] - \bar{p}/\bar{\rho}$$

where, $\widetilde{h_k} = \Delta h_{f,k}^o + \int_{T^o}^{\widetilde{T}} C_{p,k}(T')dT'$ is the specific enthalpy at filtered temperature ($\widetilde{T}$). Also, assuming calorically perfect gas, the filtered specific internal energy equation simplifies to:

$$\tilde{e} = \sum_{k=1}^{N_s} [c_{v,k}\tilde{Y}_k\tilde{T} + \tilde{Y}_k \Delta h_{f,k}^{'}]$$

where, $\Delta h_{f,k}^{'} = \Delta h_{f,k}^0 - c_{p,k}T^0$ and $\Delta h_{f,k}^0$ is the standard heat of formation at a reference temperature T^0.

The SGS terms that require closure are: the sub-grid stress tensor, the sub-grid enthalpy flux, the sub-grid viscous work, the sub-grid heat flux, and the subgrid temperature-species correlation, respectively:

$$
\begin{aligned}
\tau_{ij}^{sgs} &= \overline{\rho}\,(\widetilde{u_i u_j} - \widetilde{u}_i\widetilde{u}_j) \\
H_i^{sgs} &= \overline{\rho}\,(\widetilde{E u_i} - \widetilde{E}\widetilde{u}_i) + (\overline{p u_i} - \overline{p}\widetilde{u}_i) \\
\sigma_i^{sgs} &= \widetilde{u_j \tau_{ij}} - \widetilde{u}_j \overline{\tau}_{ij} \\
q_{i,k}^{sgs} &= [\overline{h_k D_k \partial Y_k/\partial x_i} - \tilde{h}_k \tilde{D}_k \partial \tilde{Y}_k/\partial x_i] \\
T_k^{sgs} &= \widetilde{Y_k T} - \tilde{Y}_k \tilde{T}
\end{aligned}
\tag{21}
$$

The source terms for the dispersed phase, seen as first terms on the right-hand-side of equation (20), are obtained by volume averaging the contributions from individual parcels (statistical droplets) currently residing in the Eulerian cell volume of interest. The closure of these terms and the SGS terms resulting from the filtering operation are described below.

3.7.1 Momentum Transport Closure

The sub-grid stress tensor τ_{ij}^{sgs} is modeled using an eddy viscosity concept as:

$$
\tau_{ij}^{sgs} = -2\overline{\rho}\,\nu_t(\widetilde{S}_{ij} - \frac{1}{3}\widetilde{S}_{kk}\delta_{ij}) + \frac{2}{3}\overline{\rho} k^{sgs}\delta_{ij} \tag{22}
$$

where, the resolved strain-rate is given as $\widetilde{S_{ij}} = (1/2)[\frac{\partial \widetilde{u_i}}{\partial x_j} + \frac{\partial \widetilde{u_j}}{\partial x_i}]$. The sub-grid eddy viscosity is modeled as: $\nu_t = C_\nu(\sqrt{k^{sgs}})\overline{\Delta}$ where, $\overline{\Delta}$ is the local filter width. Here, the velocity scaling is provided by dynamically varying sub-grid kinetic energy, k^{sgs}.

A transport model for the sub-grid kinetic energy (k^{sgs}) is also solved [128, 98, 123]:

$$
\frac{\partial \overline{\rho}\, k^{sgs}}{\partial t} + \frac{\partial}{\partial x_i}\left(\overline{\rho}\,\widetilde{u}_i k^{sgs}\right) = P^{sgs} - D^{sgs} + \frac{\partial}{\partial x_i}\left(\overline{\rho}\,\frac{\nu_t}{\sigma_k}\frac{\partial k^{sgs}}{\partial x_i}\right) + \dot{F}_d \tag{23}
$$

where, σ_k is a model constant typically equal to unity. Here, $P^{sgs} = -\tau_{ij}^{sgs}(\partial \widetilde{u}_i/\partial x_j)$ and $D^{sgs} = C_\varepsilon \overline{\rho}(k^{sgs})^{3/2}/\overline{\Delta}$ are, respectively, the production and the dissipation of k^{sgs}. In the above equation, $\dot{F}_d = \widetilde{u_i \dot{F}_{s,i}} - \widetilde{u}_i\widetilde{\dot{F}_{s,i}}$ is the source term due to the particle phase (this term can be closed exactly, as shown earlier [125, 47]).

The two coefficients in this model, C_ν and C_ε, are obtained locally and dynamically as part of the solution using the Localized Dynamic $k-$Equation (LDKM) procedure

[123, 96]. This procedure employs a scale similarity approach that was observed in experimental studies in high Reynolds number (Re) turbulent jet [113]. It suggested that the sub-grid stress τ_{ij}^{sgs} at the grid filter level $\overline{\Delta}$ and the Leonard's stress $L_{ij}(= [\langle \overline{\rho}\widetilde{u_i}\widetilde{u_j}\rangle - \langle \overline{\rho}\widetilde{u_i}\rangle\langle \overline{\rho}\widetilde{u_j}\rangle]/\widehat{\overline{\rho}})$ at the test filter level $\widehat{\Delta}(= 2\overline{\Delta})$ are self-similar. Here (and, henceforth), $< f >$ and $\widehat{f}$ both indicate test filtering. Since L_{ij} can be explicitly computed at the test filter level, a simple scale-similar sub-grid model of the form $\tau_{ij}^{sgs} = C_L L_{ij}$, where C_L is an adjustable constant, was proposed earlier [113] but was found to lack proper dissipation.

In the LDKM model, the above observation is extended and it is assumed that L_{ij} and the sub-grid stress $\widehat{\tau}_{ij}^{sgs}$ at the test filter level are also similar (i.e., $\widehat{\tau}_{ij}^{sgs} = \widehat{C_L} L_{ij}$). Then, $\widehat{\tau}_{ij}^{sgs}$ is modeled using the same form as for τ_{ij}^{sgs} (Eq. 22) with all variables defined at the test filter level. We define the sub-grid kinetic energy at the test filter level as $k_{test} = \frac{1}{2}[\frac{\widehat{\overline{\rho}\widetilde{u_k}^2}}{\widehat{\overline{\rho}}} - \frac{\widehat{\overline{\rho}\widetilde{u_k}}^2}{\widehat{\overline{\rho}}^2}]$ and obtain a model expression for C_ν as [123, 96, 97]:

$$C_\nu = -\frac{(\widehat{C_L} L_{ij} - \frac{2}{3}\widehat{\overline{\rho}}\ k_{test}\delta_{ij})}{2\widehat{\overline{\rho}}\sqrt{k_{test}}\widehat{\Delta}(\langle \tilde{S_{ij}}\rangle - \frac{1}{3}\langle \tilde{S_{kk}}\rangle\delta_{ij})} \tag{24}$$

The value of C_ν is obtained from this over-determined system of equations by applying the least-square method [110]:

$$C_\nu = -\frac{L'_{ij} M_{ij}}{2 M_{ij} M_{ij}} \tag{25}$$

In the above expression, $\widehat{C_L} \approx 1$ is assumed, $L'_{ij} = L_{ij} - \frac{2}{3}\widehat{\overline{\rho}}\ k_{test}\delta_{ij}$, and $M_{ij} = \widehat{\overline{\rho}}\ \sqrt{k_{test}}\widehat{\Delta}(\langle \tilde{S_{ij}}\rangle - \frac{1}{3}\langle \tilde{S_{kk}}\rangle\delta_{ij})$. A similar approach is used to obtain the dissipation coefficient C_ε such that:

$$C_\epsilon = \frac{\widehat{\Delta}(\overline{\mu} + \mu_t)}{\widehat{\overline{\rho}}\ k_{test}^{3/2}}[\langle \widetilde{T_{ij}}\frac{\partial \widetilde{u_j}}{\partial x_i}\rangle - \widehat{\widetilde{T_{ij}}}\frac{\widehat{\partial \widetilde{u_j}}}{\partial x_i}] \tag{26}$$

where $\mu_t = \overline{\rho}\nu_t$, the tensor $\widetilde{T_{ij}}$ is $[\frac{\partial \widetilde{u_i}}{\partial x_j} + \frac{\partial \widetilde{u_j}}{\partial x_i} - \frac{2}{3}\frac{\partial \widetilde{u_k}}{\partial x_k}\delta_{ij}]$, and $\widehat{\widetilde{T_{ij}}}$ is the tensor at the test-filter level.

The LDKM approach satisfies all of the realizability [190] conditions at majority of grid points even in complex reacting flows. Seven realizability conditions need

to satisfied [224] for a sub-grid scale stress tensor to guarantee a realizable solution. Those conditions are: (1-3) $\tau_{ii} \geq 0$, where $i = 1, 2, 3$; (4-6) $|\tau_{ij}| \leq \sqrt{\tau_{ii}\tau_{jj}}$, where $i \neq j$; and (7) $\det(\tau_{ij}) \geq 0$. For the current LES simulations all the seven conditions were satisfied simultaneously at over 96% of the grid points for the non-reacting case and over 90% for the reacting case. Both cases indicated over 95% realizability for normal stress components (condition 1-3). Only the last condition imposed the most stringent requirement for realizability.

Key features of this LDKM have been reported elsewhere [96, 97, 127] and not repeated here, for brevity. It is worth noting, however that the dynamic evaluation using this approach is stable locally (in both space and time) without requiring any averaging or smoothing, and can also be used in the near-wall region [53]. Past studies by other independent researchers [53, 86], and the recent evaluation in several commercial codes (CFD-ACE v2004, Fluent v6.2.16 and CFX v5.7.1) [100] has demonstrated the ability of the LDKM closure.

3.7.2 Energy Transport Closure

The sub-grid total enthalpy flux, H_i^{sgs} is modeled using the eddy viscosity and a gradient assumption as:

$$H_i^{sgs} = -\overline{\rho}\frac{\nu_t}{Pr_t}\frac{\partial \widetilde{H}}{\partial x_i} \tag{27}$$

Here, $\widetilde{H}$ is the filtered total enthalpy and Pr_t is a turbulent Prandtl number that can also be computed using a dynamic procedure but is currently assumed to be unity. The total enthalpy term $\widetilde{H}$ is evaluated as sum of specific enthalpy of mixture, specific kinetic energy, and specific sub-grid scale energy: $\widetilde{H} = \widetilde{h} + \frac{\tilde{u}_i\tilde{u}_i}{2} + k^{sgs}$, where $\widetilde{h} = \sum_{k=1}^{N_s} \widetilde{h}_k\widetilde{Y}_k$.

The sub-grid viscous work term (σ_i^{sgs}) is often neglected [55] as is the case here. The remaining unclosed terms such as $q_{i,k}^{sgs}$ and T_k^{sgs} are also neglected [55] in the current study.

3.7.3 Species Transport Closure

The Linear-Eddy Mixing (LEM) is a stochastic approach that attempts to simulate turbulent mixing, molecular diffusion, and chemical reaction in a one-dimensional domain that is embedded in an Eulerian LES domain. Kerstein [93] originally formulated LEM for non-reacting flows and later extended it to reactive flows [95].

In the LEM approach [94, 124], the gas-phase species transport is not spatially filtered. Rather, molecular diffusion, small- and large-scale turbulent convection, and chemical reaction are all modeled separately, but concurrently at their respective time scales using a two-scale approach. This combined technique is called LEMLES, hereafter.

To describe this model mathematically, we split the velocity field as: $u_i = \tilde{u_i} + (u_i')^R + (u_i')^S$. Here, $\tilde{u_i}$ is the LES-resolved velocity field, $(u_i')^R$ is the LES-resolved sub-grid fluctuation (obtained from k^{sgs}) and $(u_i')^S$ is the unresolved sub-grid fluctuation. Then, consider the *exact* species equation (i.e., without any explicit LES filtering) for the k-th scalar Y_k written in a slightly different form as:

$$\rho\frac{\partial Y_k}{\partial t} = -\rho[\tilde{u_i} + (u_i')^R + (u_i')^S]\frac{\partial Y_k}{\partial x_i} - \frac{\partial}{\partial x_i}(\rho Y_k V_{i,k}) + \dot{w}_k + \dot{S}_{s,k} \tag{28}$$

In LEMLES, the above equation is rewritten as:

$$\frac{{Y_k}^* - {Y_k}^n}{\Delta t_{LES}} = -[\tilde{u_i} + (u_i')^R]\frac{\partial {Y_k}^n}{\partial x_i} \tag{29}$$

$${Y_k}^{n+1} - {Y_k}^* = \int_t^{t+\Delta t_{LES}} -\frac{1}{\rho}[\rho(u_i')^S\frac{\partial {Y_k}^n}{\partial x_i} + \frac{\partial}{\partial x_i}(\rho Y_k V_{i,k})^n - \dot{w}_k^n - \dot{S}_{s,k}^n]dt' \tag{30}$$

Here, Δt_{LES} is the LES time-step. Equation (29) describes the large-scale 3D LES-resolved convection of the scalar field, and is implemented by a Lagrangian transfer of mass across the finite-volume cell surfaces [122, 25]. Equation (30) describes the sub-grid LEM model, as viewed at the LES space and time scales. The integrand includes four processes that occur within each LES grid, and represent, respectively, (i) sub-grid stirring, (ii) sub-grid molecular diffusion, (iii) reaction kinetics, and (iv) phase

change of the liquid fuel. These processes are modeled on a 1D domain embedded inside each LES grid where the integrand is rewritten in terms of the sub-grid time- and space-scales.

We first describe the sub-grid processes in Eq. (30) and then the 3D advection process in Eq. (29).

3.7.3.1 Sub-grid reaction-diffusion processes

Within each LES cell, the following 1D reaction-diffusion model is solved:

$$\rho \frac{\partial {Y_k}^m}{\partial t^s} = {F_k}^m - \frac{\partial}{\partial s}(\rho {Y_k}^m {V_{s,k}}^m) + \dot{w}_k + \dot{S}^m_{s,k} \tag{31}$$

$$\rho C^m_{p,mix} \frac{\partial T^m}{\partial t^s} + {F_T}^m = -\sum_{k=1}^{N_s} [\rho C_{p,k} {Y_k}^m {V_{s,k}}^m \frac{\partial T^m}{\partial s}] + \frac{\partial}{\partial s}\left(\overline{\kappa} \frac{\partial T^m}{\partial s}\right) - \sum_{k=1}^{N_s} [h_k \dot{\omega_k}] \tag{32}$$

Here, t^s indicates a local LEM time scale and the superscript m indicates that the sub-grid field within each LES cell is discretized by N_{LEM} number of sub-grid cells along the local coordinate s, such that, the LES-resolved quantity $\widetilde{Y_k}$ is obtained by an Favre average of the sub-grid field. Thus, $\widetilde{Y_k} = \frac{1}{\sum_{m=1}^{N_{LEM}} \rho^m} \sum_{m=1}^{N_{LEM}} (\rho Y_k)^m$. ${F_k}^m$ and ${F_T}^m$ represent turbulent advection of k^{th}-species and temperature, respectively, at sub-grid scales. Mixture specific heat is evaluated as: $C^m_{p,mix} = \sum_{k=1}^{N_s} C_{p,k} Y^m_k$.

The LEM domain is aligned in the direction of the maximum scalar gradient [94], its length is equal to that of the local LES filter width, $\overline{\Delta}$, and the number of LEM cells N_{LEM} is chosen so that all the relevant scales are resolved. Typically, the smallest eddy (e.g., the Kolmogorov scale, η) is resolved using 6 LEM cells, and η is estimated from the relation $\frac{\overline{\Delta}}{\eta} \approx {Re_{\overline{\Delta}}}^{3/4}$. Here, $Re_{\overline{\Delta}} = u' \overline{\Delta}/\nu$ is the local sub-grid Reynolds number and $u' = \sqrt{2k^{sgs}/3}$ is the sub-grid turbulence intensity.

In practical applications, the optimal N_{LEM} varies locally in space since the sub-grid turbulence varies over a range. Computational implementation of this local variation requires significant programming for dynamic load balancing in a parallel simulation model (employed here). Therefore, in the present study, N_{LEM} is chosen

based on the resolution requirement in the primary region of interest (typically, regions of high shear flow where scalar mixing and combustion is occurring). Then, this LEM resolution is used in all LES cells.

Equation (31) is solved using a standard finite-difference scheme along the 1D domain s. The time step for this integration Δt_{LEM} is determined as the minimum of the local diffusion Δt_{diff} or the chemical Δt_{chem} time scales.

Diffusion time scale is associated with the transport of species and temperature from a region of higher to a lower concentration due to random motion of the molecules. This is the slowest physical process among the other sub-grid processes and is computed [178] as: $\Delta t_{diff} = \Omega \frac{\Delta s^2}{max[D_k]}$ where, Δs is the LEM grid size and D_k is the mass diffusivity of the species "k". Ω is set to 0.25 for numerical stability. The chemical time scale is associated with the rate of conversion of reactant species to intermediate and/or product species. Most of the time, this is the fastest time scale in the flow, barring few situations, when turbulent time scales can be competing with the chemical time scales.

Inflow and outflow conditions to Eq. 31 are prescribed by the mass transport in the Lagrangian step, Eq. 29. The inflow is prescribed at one end of the LEM domain and the outflow at the other end. Both these conditions are implemented by the *splicing* process described in the sub-grid scalar transport subsection. Once this transport is completed the finite-difference of Eq. 31 is carried out using zero gradient condition at each end. To maintain strict mass conservation, inflow-outflow by the splicing process occurs at every LES time-step.

Detailed multi-component kinetics can be included within this model using either direct integration or using in-situ adaptive tabulation (ISAT) [158]. Since all the turbulent scales below the grid are resolved in this approach, both molecular diffusion and chemical kinetics are closed in an exact manner. As a result, unclosed terms typically seen in conventional LES approaches, such as $\bar{\rho}[\widetilde{u_i Y_k} - \tilde{u}_i \tilde{Y}_k]$, $\bar{\rho}[\widetilde{V_{i,k} Y_k} - \widetilde{V}_{i,k} \widetilde{Y}_k]$,

and $\bar{\dot{w}}_k$ do not arise, and need no closure.

The phase change of the liquid fuel into its gaseous form results in the source term in Eq. (31). This source term is determined from the Lagrangian solver, as described later.

3.7.3.2 Sub-grid stirring

In the LEM domain, the effect of eddies smaller than the grid scale $\overline{\Delta}$ is physically accounted for as sub-grid stirring. This effect is symbolically represented as ${F_k}^m$ in Eqn. (31), and represents the term $\int (u_i')^S \frac{\partial {Y_k}^n}{\partial x_i} dt'$ in Eqn. (30). Similarly, the term ${F_T}^m$ in Eqn. (32) represents $\int (u_i')^S \frac{\partial T^n}{\partial x_i} dt'$.

In the 1D LEM domain, this 3D term is approximated assuming locally isotropic conditions and is implemented using stochastic re-arrangement events [94] that represent *instantaneous* actions of a 3D (but isotropic) small turbulent eddy on the sub-grid scalar field. The mapping process compresses and increases the scalar gradient so that the local scalar field reflects the aforementioned orientation of the 1D domain in the direction of the scalar gradient.

Since all scalar processes are resolved in a 1D line, it is implicitly assumed that the turbulent scales involved in the stirring of the scalar fields are isotropic. This assumption is quite reasonable since it is consistent with LES approach, which assumes all scales below the grid scale are isotropic.

To implement this subgrid stirring, three parameters have to be prescribed: the local eddy size, the frequency of stirring, and the location of the stirring event within the LEM 1D line. The eddy size l is picked randomly from an eddy size distribution $f(l)$ in the range $\overline{\Delta}$ to η (Kolmogorov scale), and stirring events occur at a specified frequency, λ and the location of this stirring event is chosen from a uniform distribution. Both $f(l)$ and λ are obtained using 3D inertial-range scaling laws (for isotropic scales) derived from Kolmogorov's hypothesis as:

$$\lambda = \frac{54}{5}\frac{\nu Re_{\overline{\Delta}}}{C_\lambda \overline{\Delta}^3}\frac{[(\overline{\Delta}/\eta)^{5/3}-1]}{[1-(\eta/\overline{\Delta})^{4/3}]} \tag{33}$$

C_λ is a constant determined to be 0.067[24]. The eddy size (l) is chosen from the following PDF:

$$f(l) = \frac{(5/3)l^{-8/3}}{\eta^{-5/3} - \overline{\Delta}^{-5/3}} \tag{34}$$

where, $\eta = N_\eta \overline{\Delta} Re_{\overline{\Delta}}^{-3/4}$. The empirical constant N_η reduces the effective range of scale between the integral length scale and η but does not change the turbulent diffusivity. Past studies have investigated the sensitivity of predictions to N_η, and we use $N_\eta = 11$ based on past studies [195]. The time-scale associated with the sub-grid turbulent convection is estimated [178] as: $\Delta t_{stir} = 1/\lambda\overline{\Delta}$. It is a strong function of the sub-grid Reynolds number ($Re_{\overline{\Delta}}$), i.e., higher $Re_{\overline{\Delta}}$ implies a smaller stirring time scale. Additional details are presented elsewhere [178, 127].

3.7.3.3 Sub-grid scalar transport

The transport of the sub-grid scalar field, Equation (29) is carried out across the LES cell faces in a Lagrangian manner reminiscent of the turbulent transport used in the PDF method [156]. However, unlike in PDF methods where the transport is random, in LEMLES this transport is deterministic and is achieved by a procedure that "cuts-and-pastes" the sub-grid scalar fields from adjacent LES cells based on mass conservation. The mass-flux on each of the six control-surface (for hexahedral control volume) is first sorted in an ascending order following sign-convention of positive influx and negative efflux. The number of LEM cells is then determined based on the amount of mass flux that needs to be transported across each LES cell face (at many locations, fractional LEM cells have to be transported to maintain mass conservation). Mass transported out of the LEM domain is taken out from one end of the 1D domain and mass transport in, is added to the other end of the 1D domain in a deterministic manner. Thus, in LEMLES the sub-grid scalar structure is transported and recovered. This capability allows LEMLES to include molecular diffusion effect

explicitly within the small-scales. Further details are given elsewhere [124, 122, 25].

3.7.3.4 Volumetric expansion

Combustion at the sub-grid level increases the temperature and decreases the local density (since pressure is assumed to be constant in the sub-grid between LES time step). This effect results in a volumetric expansion and is included explicitly by expanding the LEM domain by an amount equal to:

$$\Delta V^{*}_{LEM,i} = \frac{\rho^{n}_{i}}{\rho^{*}_{i}}$$

where $\Delta V_{LEM,i}$ is the change in volume of LEM cell i. ρ^{n}_{i} and ρ^{*}_{i} are, respectively, the density of the "$i-th$" cell at the previous, and the current time integration levels in the LEM simulation (not at the fluid-dynamic time-step (Δt_{LES}) at LES level)

Chemical reaction at the LEM level determines heat release and thermal expansion at the LEM level, which at the LES level generates flow motion that, in turns, transports the species field at the LEM level. Full coupling is maintained in the LEMLES to ensure local mass conservation.

This completes the Eulerian formulation of the LES gas-phase system of equations. To study the spray phenomenon, a point-volume approach [114] is employed for the discrete phase. The discrete phase interactions with the Eulerian-gas field is averaged over the cell volume and considered as source terms in the LES gas equations, as shown earlier. In the next section, discrete phase equations are introduced along with couple of engineering breakup models.

3.8 Lagrangian Spray Equations

In this study, an approach, typically known as the "discrete droplet model" (DDM), representing a spray as a collection of discrete particles, is employed. The particle motion is tracked using a Lagrangian formulation [47]. This approach eliminates errors

due to numerical diffusion [46] and better represents physical aspects of spray. Additionally, complex processes like drop/drop collisions, drop/wall interaction, and drop breakup can be considered within the DDM. Also, to maintain computational expediency, following Dukowicz [42] characteristic groups of droplets, all having identical size, location, velocity and temperature, are represented as "computational parcels", and are then tracked. However, the number of particles per group depends on the diameter/volume of the particle to avoid unrealistic averaging [8] of drop properties.

Two flow regimes [46, 48] can be classified for sprays: (1) dense, and (2) dilute spray. The dense spray region is characterized [46] by discrete liquid drops/ligaments effects such as inter-drop spacing on transport rates, drop-drop collisions, turbulence modulation due to volume occupied by liquid phase, etc., which become significant within this region. Following Faeth [48], the classical picture of atomization within dense sprays involves primary breakup of the liquid core into ligaments or large drops followed by secondary breakup into smaller drops with negligible effects of collisions.

The dilute spray region involves no particle-particle interactions and effects of liquid phase volume on transport characteristics within the gas phase are negligible [47, 48]. Therefore, the single-drop transport rates can be employed directly. In typical swirl-stabilized spray combustion applications, the effect of swirl increases dispersion (shown later) of droplets, and therefore, there is ever increasing inter-drop spacing as the spray evolves. Generally accepted inter-drop distance of two particle diameters [48] for application of the dilute regime is easily exceeded under swirling configurations.

The filtered values of turbulent velocity and other gas-phase variables are obtained from the LES equations for these variables. Additionally, the effect of small-scale (or sub-grid) turbulence upon drop dispersion is incorporated using k^{sgs}. Thus, the presence of particles on gas-phase is incorporated both via direct source terms in the filtered LES variables (mass, momentum, energy, scalar concentration) and indirectly

by modification of the sub-grid kinetic energy (k^{sgs}). This ensures two-way coupling among the phases. An additional effect is included in the force term in the droplet momentum equations by including an effect of sub-grid turbulence in the gas phase velocity. This approach is an extension of the stochastic separated flow (SSF) approach [47] and is summarized below. More details of these equations and coupling issues are given elsewhere [127].

3.8.1 Engineering Breakup Model

The secondary breakup of liquid drops into even smaller drops is primarily driven by aerodynamic forces due to the surrounding carrier phase [198]. An initially spherical drop undergoes distortion caused by the forces that eventually leads to breakup. The dimensionless drop Weber number [48] (We) provides a characteristic measure of the breakup behavior. Based on We, five different drop breakup regimes [49, 198] are reported. All five regimes typically co-exist in spray combustion configurations, however the catastrophic breakup closer to the injection is dominant and determines the spray evolution.

The blob-injection model [165] is employed to feed liquid fuel into the combustor. In this approach, the liquid jet is approximated in form of large droplet/"blob" with a characteristic size equal to the injector nozzle diameter. The number of blobs injected in unit time is a function of liquid mass flow rate. During the injection, new blobs/particles introduced in the domain are pure drops (one particle per parcel). These drops evolve downstream and undergo breakup producing new particles, which are then tracked as parcels. The blob injection velocity is dependent [165] on the net injection pressure and the nozzle discharge coefficient. Two models: the Taylor Analogy Breakup (TAB) [138] and the Kelvin-Helmholtz (KH) aerodynamic breakup [165] models have been implemented and compared in the current study. The details of these models are in the cited references and therefore, avoided here for brevity. Also,

advantages and disadvantages of both these models were discussed in the literature review.

In the LES implementation, once a parent blob (with radius, a_0 and one particle per group, N_0) is injected into the computational domain, a rate expression is used to reduce its size. While waiting for sufficient product drops to accumulate, the parent number of particles per group (N) is adjusted so that $Na^3 = N_0 a_0^3$. This accounts for the mass conservation. After this, the Lagrangian droplet evolution occurs, but during this evolution if certain criteria [165, 138] are exceeded, a breakup event is executed creating new product parcel (of radius r), which takes both the temperature and physical location of the parent. Product droplets inherit the parent droplet velocity plus a normal velocity in the cross-plane accounting for rim expansion. The parent number of particles per group is then restored to N_0 following the creation of the new product parcel. Then, both the parent and product parcels are tracked by the Lagrangian solver and are equally likely to undergo further breakup depending on local stability criterion.

One significant difference in the numerical implementation of the TAB and KH breakup models is related to the co-existence of parent/product parcels. In the TAB model, the parent parcel is replaced by one parcel of identically sized product droplets after breakup, whereas in the KH model, a bimodal size distribution with small droplets shearing off the parent blob and larger but reduced size parent parcel are allowed.

In this study, the non-evaporating solid-cone spray measurements of Hiroyasu and Kadota [74] are used to validate both these breakup models. These results are presented in a latter section. At present, particle-particle interaction is not included in the current implementation as this study is focused on global characteristics of spray evolution with and without breakup and its effects on combustion phenomena.

3.8.2 Lagrangian Equation-of-motion

The Lagrangian equation of motion governing an instantaneous droplet, under the assumptions that the particle density is much greater than that of the carrier fluid ($\rho_p/\rho_g \approx 10^3$), negligible particle-particle interactions occur, and the Kolmogorov scale is of the same order or larger than the largest droplet, can be expressed as [37, 137, 47]:

$$\begin{aligned} \frac{dx_{i,p}}{dt} &= u_{i,p} \\ \frac{du_{i,p}}{dt} &= \frac{f}{\tau_V}[(\widetilde{u_i} + u_i'') - u_{i,p}] + g_i \end{aligned} \tag{35}$$

where, $u_{i,p}$ is the i-th component of the parcel velocity, u_i is the i-th component of gas-phase velocity, $x_{i,p}$ is the i-th component of parcel position, f is the *drag factor* (ratio of the drag coefficient to Stokes drag), τ_V is the particle velocity response time, and g_i is the i-th gravity component. Subscript p represents liquid phase quantities and unsubscribed quantities correspond to gas-phase (except as noted). Here, the sum $\widetilde{u_i} + u_i''$ represents instantaneous (u_i) gas-phase velocity components, consisting of both the LES resolved velocity $\widetilde{u_i}$ and a stochastic term u_i'' that is obtained using k^{sgs} at intervals coincident with the local characteristic eddy lifetime. Thus, the effect of turbulence on the droplet motion is simulated using the SSF [47]. Interaction of droplet with an eddy is assumed for a time taken as the smaller of either eddy lifetime or the transit time required to traverse the eddy. The drag factor and particle velocity response time are:

$$f = \frac{C_D Re_d}{24} \tag{36}$$

$$\tau_V = \frac{\rho_p d_p^2}{18\mu_g} \tag{37}$$

where, ρ_p is the liquid density, d_p is the parcel diameter ($= 2r_p$, r_p is parcel radius), μ_g is gas-phase dynamic viscosity, ν_g is gas-phase kinematic viscosity (μ_g/ρ_g), C_D is the drag coefficient, and Re_d is the relative particle Reynolds number expressed as $Re_d = (d_p/\nu_g)|u_i - u_{i,p}|$.

The drag coefficient accounts for the dynamic influence of pressure and viscous forces acting on droplet surfaces. Following Crowe *et al.* [37], the drag coefficient (assuming drops retain the spherical shape) is given by:

$$C_D = \begin{cases} \frac{24}{Re_d}(1 + \frac{1}{6}Re_d^{2/3}) & Re_d \leq 1000 \\ 0.4392 & Re_d > 1000 \end{cases} \tag{38}$$

A range of $0.424 - 0.44$ in the drag coefficient for $Re_d > 1000$ is reported in the literature and the current variation is based on Crowe *et al.* [37]. The effect of droplet distortion on the drag coefficient can be accounted by an engineering breakup model [83, 111]. This relies on tracking droplet distortion and its orientation in relation to the carrier-phase. It is important to note that the above correlation is based on rigid spheres in steady flows. However, it is a well known fact [208] that the isolated liquid drop moving in the gas field has different drag characteristics. It is precisely in this context, the comprehensive five-equation interface model can provide the necessary correlations and aid in performing physics-based engineering simulation for practical applications.

The droplet mass-transfer is governed by the droplet continuity equation,

$$\frac{dm_p}{dt} = -\dot{m}_p \tag{39}$$

where, m_p is the mass of particle given by $\frac{4}{3}\rho_p \pi r_p^3$, and $\dot{m}_p (> 0)$ is the net mass transfer rate (or vaporization rate) for a droplet in a convective flow field can be expressed [137] as:

$$\frac{\dot{m}_p}{\dot{m}_{p,Re_{d=0}}} = 1 + \frac{0.278\sqrt{Re_d}Sc^{(1/3)}}{[1 + \frac{1.232}{Re_d Sc^{(4/3)}}]^{(1/2)}} \tag{40}$$

where, $Re_{d=0}$ is the Reynolds number for particle at rest. Under quiescent conditions, the mass-transfer rate reduces to:

$$\dot{m}_{p,Re_{d=0}} = 2\pi\rho_s \mathscr{D}_{sm} d_p ln(1 + B_M) \tag{41}$$

where, ρ_s and $\mathscr{D}_{sm}$ respectively, are the gas mixture density and the mixture diffusion coefficient at the droplet surface. Also, B_M is the Spalding mass-transfer number [46]

given by:

$$B_M \equiv b_\infty - b_s = \frac{(Y_{F,s} - Y_{F,\infty})}{(1 - Y_{F,s})}; \quad where\ b \equiv \frac{Y_F}{Y_{F,s} - 1}$$

In above relations, Sc ($\equiv \nu_{g,s}/\mathscr{D}_{sm}$, ratio of momentum to mass transport) is the Schmidt number. Subscript s represents quantities at droplet surface and ∞ indicates far-field. Also, Y_F is the fuel species (that is evaporating) mass fraction. Surface fuel mass fraction is obtained from Raoult's Law [31], which assumes that the mole fraction at the droplet surface is equal to the ratio of the partial pressure of fuel vapor (p_{vap}) to the total pressure of gas-phase ($\bar{p}$). Various correlations exist [163] to evaluate the partial pressure of fuel vapor that are typically specific for particular fuels and dependent on critical temperature and pressure of fuel vapor. Note that the gas-phase variables (like $\widetilde{T}$ and $\widetilde{Y_F}$) correspond to the far-field conditions [129] for the droplets and must be interpolated from the Eulerian numerical grid to the droplet location during the simulations.

Droplet heat transfer is governed by the droplet energy equation, which consists of external and the internal energy, as well as, the energy associated with surface-tension. The equation governing the internal temperature distribution based on this uniform temperature model [46, 137] is:

$$m_p C_l \frac{dT_p}{dt} = \dot{Q}_{conv} - \dot{m}_p \mathscr{L}_v = h_p \pi d_p^2 (\widetilde{T} - T_p) - \dot{m}_p \mathscr{L}_v \tag{42}$$

where, $\dot{Q_{conv}}$ is the convective thermal energy transfer rate, m_p is particle mass, C_l is liquid heat capacity, h_p is the heat transfer coefficient, and $\mathscr{L}_v$ is the latent heat of vaporization. Additional details of this model, including the heat transfer coefficient and the latent heat of vaporization, are given elsewhere [46, 137, 129].

Equations (35, 39, 42) are integrated using a fourth-order Runge-Kutta scheme [137]. The integration is carried out based on the smallest of the time scales [137, 178] (i.e., the smallest of the particle velocity relaxation time, the droplet life-time, the turbulent eddy interaction time, the droplet surface temperature constraint time, and the LES

gas-phase time) governing the particle evolution. Initial conditions for the Lagrangian system involve the specification of initial parcel positions, velocities, masses, temperatures, and the number of droplets represented by each parcel. This latter quantity is determined at the inlet boundary via drop distribution in conjunction with fuel mass flow rate.

3.9 Eulerian-Lagrangian Coupling

Eulerian-Lagrangian coupling is through the inter-phase exchange terms [137] (not presented here, for brevity). If n_p number of particles are present per parcel/group, then the volume-averaged source terms (seen in Eqn. 20) for all the droplet parcel/group trajectories that cross a computational cell (of volume ΔV) are computed by summing the contribution from every parcel/group as follows:

$$\begin{pmatrix} \widetilde{\dot{\rho}_s} \\ \widetilde{\dot{F}_{s,i}} \\ \widetilde{\dot{Q}_s} \\ \widetilde{\dot{S}_{s,k}} \end{pmatrix} = \frac{1}{\Delta V} \begin{pmatrix} \sum_m n_p[\dot{m}_p] \\ \sum_m n_p[\dot{m}_p u_{i,p} - \frac{4\pi}{3}\rho_p r_p^3 \frac{du_{i,p}}{dt}] \\ \sum_m n_p[\dot{m}_p h_{v,s} - h_p \pi d_p^2 (T - T_p) - u_{i,p} m_p \frac{du_{i,p}}{dt} + \dot{m}_p(\frac{1}{2}u_{i,p}^2)] \\ \sum_m n_p[\dot{m}_p] \end{pmatrix}$$

where, the summation index "m" is over all the droplet parcels/groups crossing a computational cell (of volume ΔV). Also, note that the species source term ($\widetilde{\dot{S}_{s,k}}$) for all species ($k$) is *zero*, except for the species that is present in liquid form and evaporating.

3.10 Combustion Modeling

Although, in the LEMLES approach detailed reaction mechanism with any number of species can be used computational expediency requires some reduction in the kinetics model. In the LES study, we have employed liquid fuel ($C_{12}H_{23}$) to approximate experimental Jet-A fuel. A three-step, seven-species, global reduced mechanism [225,

135] of the form:

$$C_{12}H_{23} + (35/2)O_2 \longrightarrow 12CO + (23/2)H_2O$$

$$2CO + O_2 \longrightarrow 2CO_2 \quad and \quad N_2 + O_2 \longrightarrow 2NO$$

is employed in this study.

For the first step, the rate expression ($Ae^{(-E_a/R_uT)}[C_{12}H_{23}]^m[O_2]^n$) [225] has pre-exponential factor (A) and activation energy ($E_a, kcal/gmol$) of 4.7×10^{11} and 30, respectively. Empirical coefficients (m, n) are chosen to be 0.25 and 1.5, respectively. The CO oxidation step involves both forward ($10^{14.6}e^{(-40/R_uT)}[CO][H_2O]^{0.5}[O_2]^{0.25}$) and reverse ($5 \times 10^8 e^{(-40/R_uT)}[CO_2]$) rates. The NO global mechanism accounts for both thermal and non-thermal pathways [135].

CHAPTER IV

NUMERICAL METHOD

In the preceeding chapter, the mathematical formulation for both the five-equation interface model and the LEMLES engineering model were documented. In this chapter, we proceed with the numerical solution of these models. The conservation laws of fluid motion can be expressed mathematically either in differential or integral form. In case of differential form of equations, the numerical scheme involves discretizing the domain of interest into points upon which the finite-difference equations are solved. On the other hand, when the integral form of conservation laws is employed, the domain of solution is divided into discrete volumes upon which strict conservation of mass, momentum, and energy is enforced. A finite-volume approach has two major advantages when compared with a finite-difference scheme: (i) the finite-volume approach can handle skewed grids and, thereby, geometrical boundaries can be reconstructed, and (ii) the finite-volume approach solves the discretized governing equations in a conservative form ensuring strict mass, momentum, and energy conservation. Thus, a finite-volume approach is retained in this study.

The presence of large gradients in flow variables requires a special treatment in order to minimize dispersion errors. In such cases, classical high-resolution upwind schemes [213] are preferred and retained in this study for the solution of the large gradient regions in the five-equation interface model. A primary drawback of upwind schemes is that they are more dissipative [213] compared with central schemes, thereby making them poorly suitable for resolving unsteady shear flows. So, a hybrid approach following Génin and Menon [58, 57] is employed in the solution for the five-equation interface model which automatically switches to a second- or fourth-order

low dissipation scheme based on a smoothness parameter. We have modified the smoothness parameter to account for the presence of capillary interface region.

Also, a dispersion-free resolution of large gradients by an upwind scheme is often computationally expensive. A primary requirement for engineering-design tools like the LEMLES is a "quick" turn-around time (approximately a week or so) for a few characteristic cycles. Therefore, aforementioned low dissipation scheme is employed for the solution of the LES equations of motion. The presence of large gradients in the vicinity of the flame are resolved along a 1D line within each LES cell by the sub-grid LEM model. Particle phase is considered in the Lagrangian framework thereby eliminating the need for resolution around the fuel droplets. However, a two-way coupling among the gas- and liquid-phase is accounted for in terms of forementioned volume-averaged source terms.

This chapter is organized as follows. A generic finite-volume approach is presented in the first section. This is followed by details about the MacCormack [116] approach which is a low-dissipation central scheme. A high-resolution Roe-type scheme [213, 4] is then presented for the solution of large gradient regions. A hybrid switch is then formulated which dynamically combines the above two schemes.

4.1 Finite-Volume Scheme

The governing equations of motion can be written in a conservative vector form as:

$$\frac{\partial \mathbf{Q}}{\partial t} + \nabla \cdot \mathbf{F} = \mathbf{S} \tag{43}$$

where, $\mathbf{Q}$ is the state vector containing the conserved variables, $\mathbf{F}$ is the flux vector through a cell surface area $\mathbf{A}$, and $\mathbf{S}$ is the source term. This equation can be integrated over a computational cell, as shown in Fig. 3, which encloses a constant volume V and is bounded by control surfaces $\mathbf{A}$:

$$\int_V \frac{\partial \mathbf{Q}}{\partial t}\, dV + \int_V \nabla \cdot \mathbf{F}\, dV = \int_V \mathbf{S}\, dV$$

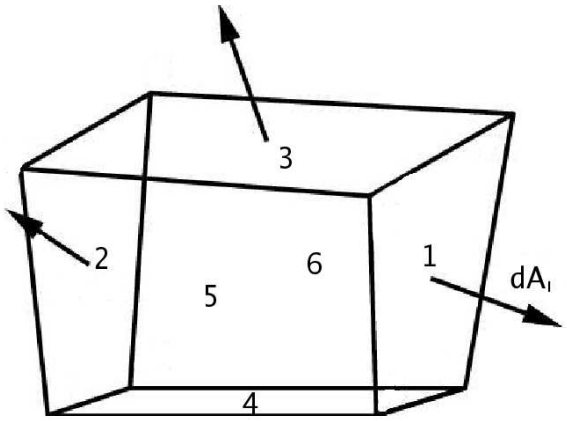

Figure 3: Finite volume computational cell with outwardly oriented surface normals.

Using the Green's theorem: $\int_V \nabla \cdot \mathbf{F}\, dV = \oint\!\!\!\!\!\!\diagup_S \mathbf{F} \cdot d\mathbf{A}$ and permuting the time derivative and the volume integration, the expression results in:

$$\frac{\partial}{\partial t} \int_V \mathbf{Q}\, dV + \oint_A \mathbf{F} \cdot d\mathbf{A} = \int_V \mathbf{S}\, dV, \tag{44}$$

The above expression is exact for any arbitrary cell volume shape. The time-derivative term can be determined by assuming that the quantities of $\mathbf{Q}$ are the mean value for the local control volume (V). A similar argument applies to the source term $\mathbf{S}$. Additionally, the second integral representing the net flux out of the control volume can be replaced by a summation. Thus, the equation for a finite volume scheme is obtained:

$$\frac{\partial \mathbf{Q}}{\partial t} + \frac{1}{V} \sum_i^m \int_{dA_i} \mathbf{F} \cdot d\mathbf{A}_i = \mathbf{S},$$

where, the vector $d\mathbf{A}_i$ is the surface normal vector of the cell face i. In this study, we consider a structured grid employed such that each cell is a hexagon. The fluxes can now be averaged over the cell surface area leading to a discretized finite volume scheme as:

$$\frac{\partial \mathbf{Q}}{\partial t} + \frac{1}{V} \sum_i^m \mathbf{F} \cdot d\mathbf{A}_i = \mathbf{S}, \tag{45}$$

The computational solution is now obtained by evaluating the fluxes at each cell faces and integrating the above finite volume expression in time. Both the five-equation

interface model as well as the LEMLES engineering model employs the same time integration scheme following MacCormack [116]. However, the computations of fluxes for each of the models is different.

4.2 MacCormack Time Integration

Two categories of time integration scheme are available. They are known as explicit or implicit schemes. When a direct computation of the dependent variables at time $t + \Delta t$ can be made in terms of quantities known at time t, the scheme is said to be explicit. Implementation of explicit schemes is straightforward. In contrast, when information at time $t + \Delta t$ is used in the computation of the dependent variables the scheme is said to be implicit in nature. This results in coupled sets of equations, and either a matrix inversion or iterative technique is needed to obtain the solution. The associated computational cost significantly outweighs the stability gains of an implicit scheme. Therefore, we retain the explicit time integration as our solution method.

The MacCormack method [116] integrates Eqn. 45 with respect to time in a two-step process. These two steps are known as the *predictor* and the *corrector* step. The combination of the two steps leads to a scheme with a global second order accuracy in time. These are defined as:

$$\begin{aligned} \mathbf{Q}^{(\star)} &= \mathbf{Q}^{(n)} + d\mathbf{Q}^{(n)} && (Predictor) \\ \mathbf{Q}^{(n+1)} &= \tfrac{1}{2}\left[\mathbf{Q}^{(n)} + \mathbf{Q}^{(\star)} + d\mathbf{Q}^{(\star)}\right] && (Corrector) \end{aligned} \tag{46}$$

where, the cell flux $\mathbf{F}$ and the volumetric source term $\mathbf{S}$ have been combined into the residual $d\mathbf{Q}$, i.e.,

$$\begin{aligned} d\mathbf{Q}^{(n)} &= -\Delta t \left[\tfrac{1}{V}\textstyle\sum_i \left(\mathbf{F}_i^{+^{(n)}} \cdot d\mathbf{A}_i\right) - \mathbf{S}^{(n)}\right] \\ d\mathbf{Q}^{(\star)} &= -\Delta t \left[\tfrac{1}{V}\textstyle\sum_i \left(\mathbf{F}_i^{-^{(\star)}} \cdot d\mathbf{A}_i\right) - \mathbf{S}^{(\star)}\right] \end{aligned} \tag{47}$$

Quantities denoted with a superscript $(\star)$ are evaluated using quantities at the *predictor* or intermediate time-level. Both the *predictor* and the *corrector* steps use Δt as the time integration step and the factor $\frac{1}{2}$ in Eqn. 46 ensures that $\mathbf{Q}^{(n+1)}$ represents the

state of the conserved variables at $t+\Delta t$. The $(+)$ and $(-)$ superscripts indicate that the fluxes are to be evaluated using forward or backward differences, respectively. The combination of the alternating directions results in a central scheme. In order to avoid any bias caused by the forward and backward difference methods, the computation of the fluxes are alternated as a function of the direction (i, j, k) and the time-step (n).

While an explicit scheme is generally much simpler to implement, the maximum allowable Δt is restricted by the numerical stability and accuracy requirements. Also, for time-accurate simulations, Δt larger than the physical time-scale of interest is not desirable. For simple wave equations, stability analysis can be performed to yield restrictive conditions. However, for the Navier-Stokes equations, no analytically derived stability condition is known [116]. The maximum allowable time-step based on physical arguments and numerical experimentation, has been reported in the literature [116]:

$$\Delta t = CFL \times \left(\frac{V/|d\mathbf{A}|}{v_p} \right) \tag{48}$$

where, CFL is the *Courant-Friedrich-Levy* number (generally, on the order of unity), V is the volume of the hexagon, $|d\mathbf{A}|$ is the norm of the cell surface area vector, and v_p is the propagation velocity of *information* (wave velocity). Physically, Eqn. 48 implies that the information cannot propagate farther than some fraction of the local grid size in a single time-step. The grid spacing here is evaluated as $V/|d\mathbf{A}|$. A single time-step must be used for the entire computational domain. If min_D stands for the minimum value over the entire computational domain, the computational time-step is then defined as:

$$\Delta t = CFL \times min_D \left(\frac{V}{|d\mathbf{A}|v_p} \right)$$

For a compressible, conducting fluid, v_p can be divided into the superposition of convective (v_c), acoustic (v_a), diffusive (v_d), and capillary (v_σ) velocities (*i.e.*, $v_p = v_c + v_a + v_d + v_\sigma$). For this finite-volume algorithm, these different velocities are

computed as,

$$\begin{aligned} v_c &= [|\mathbf{u}\, d\mathbf{A}_i| + |\mathbf{u}\, d\mathbf{A}_j| + |\mathbf{u}\, d\mathbf{A}_k|]/|d\mathbf{A}| \\ v_a &= c \\ v_d &= \frac{2\gamma\mu}{\rho Pr}\frac{|d\mathbf{A}|}{V} \\ v_\sigma &= \sqrt{\frac{\sigma\pi}{(\rho_l+\rho_g)(V/|d\mathbf{A}|)}} \end{aligned}$$

where, c is the speed of sound, μ is the coefficient of viscosity, γ is the isentropic exponent, Pr is the Prandtl number, ρ_l and ρ_g are the density of liquid and gas, respectively, in a flows involving capillary interface. At room conditions, the capillary speed is approximately (1/50) the speed of sound in air. Therefore, the sound speed is still dominant of all propagation speeds.

4.3 Lagrangian (dispersed-phase) Time-step

Introduction of a dispersed phase into the Eulerian gas-phase flow field brings to light new time-scales, which are to be considered for time-accurate simulations. For accurate integration of the particle trajectory, its size, and temperature, the Lagrangian time-step used for the integration of equation of motion of the dispersed phase has to be the smallest of the various physical time-scales. At any instant, the smallest of the following time-scales is used for particle evolution [47, 31, 137, 178], viz: (1) LES gas-phase CFL time (Δt_{gas}); (2) droplet velocity relaxation time (τ_{relax}); (3) droplet lifetime (τ_{life}); (4) turbulent eddy droplet interaction time (τ_{eddy}); (5) droplet surface temperature constraint time (τ_{evap}).

Droplet velocity relaxation time: The local linearized droplet equations of motion of a particle in a uniform flow have an exact solution in terms of the droplet Reynolds number, which gives the following expression for the *droplet relaxation time*,

$$\tau_{relax} = [16\rho_d r_d^2 (C_D Re_d)^{-1}]/[3\rho_g \nu]$$

Droplet lifetime: In flows involving vaporizing droplets, to ensure that the droplet size remains positive in a given time step, *droplet lifetime* is estimated based on the

evaporation rate of the droplet as follows:

$$\tau_{life} = \frac{4\pi r_d^3 \rho_d}{3\dot{m}_d}$$

Eddy-droplet interaction time: A particle is assumed to interact with an eddy for a time which is the minimum of eddy lifetime and the transit time for the particle to traverse the eddy. The *eddy lifetime* is determined by assuming that the characteristic size of a randomly sampled eddy is the dissipation length scale, proportional to the LES filter width, Δ and is given by:

$$\tau_{eddy} = \Delta / \sqrt{(2k^{sgs}/3)})$$

and the *transit time* is determined from the following equation:

$$\tau_{transit} = \tau_{relax} \ln(1 - \frac{\Delta}{(\tau_{relax}|u_i - u_{i,d}|}))$$

Therefore, the *eddy-droplet interaction time* is estimated as,

$$\tau_{eddy\ int} = \begin{cases} \tau_{eddy} & , \quad \Delta > \tau_{relax}|u_i - u_{i,d}| \\ min(\tau_{eddy}, \tau_{transit}), & \Delta \leq \tau_{relax}|u_i - u_{i,d}| \end{cases}$$

Droplet surface temperature constraint or heating time: If the boiling temperature of the fuel is very low or close to room temperature, then the droplet surface temperature rise becomes another constraint. If the Lagrangian time-step is large, then the droplet temperature rises abruptly, leading to an increased evaporation and mass loading locally. This might affect the stability of the calculation. For the uniform temperature model, the *droplet heating time* is thus given by [31]:

$$\tau_{evap} = (\rho_d C_v d_d)/(6h_d)$$

The subscripts d in the above expressions pertain to the dispersed phase properties. The Lagrangian equation of motions are integrated in time using a fourth-order Runga-Kutta method [180, 103].

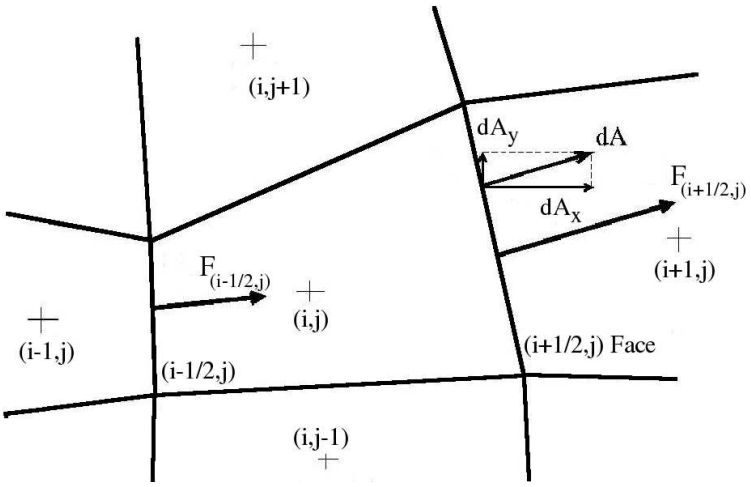

Figure 4: Control volume showing the flux vector ($\mathbf{F}$) and cell-surface area vector ($d\mathbf{A}$) orientation in relation to the cell faces.

4.4 Central Scheme Flux Computation

In a finite volume scheme, all information is known at the center of each control volume. However, cell-faced quantities are needed by the flux vector and therefore, some form of interpolation technique is required to evaluate flow variables at the cell face. The accuracy of the interpolation controls the overall spatial accuracy of the numerical integration scheme.

A schematic of a control volume is shown in Fig. 4. For illustration purposes, a two-dimensional example is considered. Extension to a three-dimensional framework is straightforward. The control volume is identified by a (i, j), where i and j are in the $x-$ and $y-$directions respectively. Along with this central cell volume are its adjoining neighbors in the $i-$ and $j-$directions ($i \pm 1$ and $j \pm 1$) and its cell face quantities are labelled as $(i, j \pm \frac{1}{2})$ in the $j-$direction and $(i \pm \frac{1}{2}, j)$ in the $i-$direction. Structured grid readily provides the identification of neigboring cell volumes as well as the cell surfaces based on the (i, j) indices. Figure 4 also shows the fluxes residing on each cell surface in the $i-$direction.

There are several methods available for computing the flux vectors in Eqn. 47. The

original method proposed by MacCormack [116] considered the cell-centered values of the primitive variables for the cell-face approximation:

$$\begin{aligned} \mathbf{F}^{+}_{i+\frac{1}{2}} &= \mathbf{F}_{i+1} &= \mathbf{F}\big(\mathbf{U}_{i+1}\big) \\ \mathbf{F}^{-}_{i+\frac{1}{2}} &= \mathbf{F}_{i} &= \mathbf{F}\big(\mathbf{U}_{i}\big) \end{aligned} \tag{49}$$

where, $\mathbf{F}_{i+1}$ and $\mathbf{F}_i$ are calculated using the cell-centered values. This interpolation is first order accurate in space. However, since both the backward and the forward differencing are used within one Δt via the *predictor−corrector* process, the resulting algorithm is second order accurate in space [206].

A higher-order spatial interpolation is possible and several attempts have been made to extend the MacCormack approach. Gottlieb and Turkel [117] were the first to propose an extension of the scheme to fourth order spatial accuracy, by defining the fluxes with:

$$\begin{aligned} \mathbf{F}^{+}_{i+\frac{1}{2}} &= \tfrac{1}{6}\left(7\,\mathbf{F}_{i+1} - \mathbf{F}_{i+2}\right) \\ \mathbf{F}^{-}_{i+\frac{1}{2}} &= \tfrac{1}{6}\left(7\,\mathbf{F}_{i} - \mathbf{F}_{i-1}\right) \end{aligned} \tag{50}$$

Nelson [133] conducted a stability analysis of this scheme, and showed that it was strictly third order accurate and leading to a fourth order accuracy as the CFL number tends to zero. Following this, Nelson proposed the computation of the fluxes as:

$$\begin{aligned} \mathbf{F}^{+}_{i+\frac{1}{2}} &= \tfrac{1}{6}\left(2\,\mathbf{F}_{i} + 5\,\mathbf{F}_{i+1} - \mathbf{F}_{i+2}\right) \\ \mathbf{F}^{-}_{i+\frac{1}{2}} &= \tfrac{1}{6}\left(2\,\mathbf{F}_{i+1} + 5\,\mathbf{F}_{i} - \mathbf{F}_{i-1}\right) \end{aligned} \tag{51}$$

As previously seen for the second order scheme, the combination of the two second-order differencing with the MacCormack time integration method presented earlier leads to an overall higher order of accuracy.

It has been practically observed that, rather than having a flux extrapolation, as performed in Eqn. 51, computing fluxes based on extrapolated variables was more stable, for a strictly equivalent order of accuracy:

$$
\begin{aligned}
\mathbf{Q}^{+}_{i+\frac{1}{2}} &= \tfrac{1}{6}\left(2\,\mathbf{Q}_{i} + 5\,\mathbf{Q}_{i+1} - \mathbf{Q}_{i+2}\right) \\
\mathbf{Q}^{-}_{i+\frac{1}{2}} &= \tfrac{1}{6}\left(2\,\mathbf{Q}_{i+1} + 5\,\mathbf{Q}_{i} - \mathbf{Q}_{i-1}\right) \\
\mathbf{F}^{+}_{i+\frac{1}{2}} &= F(\mathbf{Q}^{+}_{i+\frac{1}{2}}) \\
\mathbf{F}^{-}_{i+\frac{1}{2}} &= F(\mathbf{Q}^{-}_{i+\frac{1}{2}})
\end{aligned}
\tag{52}
$$

Such a higher-order interpolation of fluxes is available in the general solver, however in this study we employed the original flux interpolation following MacCormack [116].

The computation of the viscous fluxes requires an evaluation of gradients of primitive variables like velocity, temperature, etc., the cell boundaries. This operation is performed using a finite-difference approach, where the order of accuracy used for the convective terms is conserved. In the MacCormack method, the computation of the fluxes are direction biased, therefore, the computation of the gradients also has to be direction biased. For example, gradients in the $i-$direction are considered. The $i-$direction derivatives are computed using either a backward or a forward formula, depending upon the MacCormack step. The other derivatives in the transverse directions are computed using a central difference scheme with averaged values at the cell faces. The second-order accurate derivatives for some given variable ϕ are expressed through:

$$
\left(\frac{\partial \phi}{\partial \xi}\right)^{+}_{i+1/2,j} = \phi_{i+1,j} - \phi_{i,j} \tag{53}
$$

$$
\left(\frac{\partial \phi}{\partial \xi}\right)^{-}_{i+1/2,j} = \phi_{i,j} - \phi_{i-1,j} \tag{54}
$$

$$
\left(\frac{\partial \phi}{\partial \eta}\right)_{i+1/2,j} = \frac{\phi^{av}_{i+1/2,j+1} - \phi^{av}_{i+1/2,j-1}}{2} \tag{55}
$$

where, the (+) and (-) represent the forward and backward differences for the gradient computations. No directional biasing is applied in the computation of the volumetric source terms. Therefore, the central scheme is applied for all derivatives. This same method is also used to compute spatial derivatives needed in the LDKM method.

The computation of local curvature at the cell center and the cell boundaries is also needed for the five-equation interface model. We employ the gradient strategy

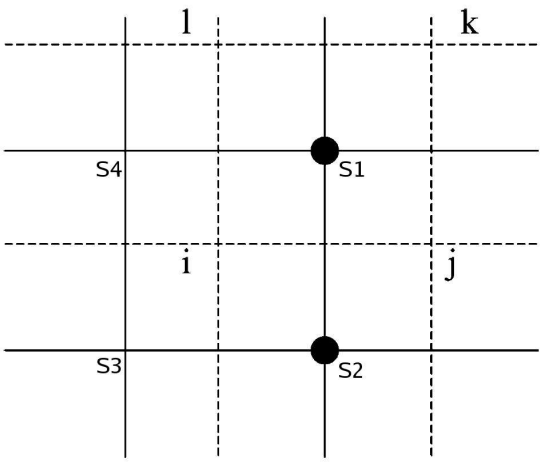

Figure 5: Primary and secondary mesh for computing the local interface curvature.

of Perigaud and Saurel [148] to compute the curvature. Figure 5 shows the finite volume mesh (or primary) in form of solid lines with four cells: i, j, k, l. A secondary grid is constructed based on the primary mesh cell centers and is shown in form of dashed lines with edges as ij, jk, kl, and li. Considering ϕ as a local volume fraction, the value of ϕ on these segments is assumed to be the arithmetic average of the values at the ends (or cell-center values of the finite volume grid). Thus, the approximation yields on the ij segment is given by:

$$\phi_{ij} = \frac{\phi_i + \phi_j}{2}$$

Now to compute the gradient of ϕ at the secondary mesh cell-center $S1$ (which happens to be the primary mesh node), Green's formula is applied:

$$(\overrightarrow{\nabla\phi})_{S1} = \frac{1}{V}\sum_{k=1} \phi_k \overrightarrow{n}_k l_k$$

where, V is the cell area (volume in 3D), l_k is the segment length (area in 3D), and k is the edge number starting from 1 to 4 for ij, jk, kl, and li, respectively. Also, $\overrightarrow{n}_k$ is the outward normal to segment k. Thus, the gradient at the cell boundary of the primary mesh is obtained by taking the arithmetic mean of the node values as:

$$(\overrightarrow{\nabla\phi})_{S1S2} = \frac{1}{2}[(\overrightarrow{\nabla\phi})_{S1} + \overrightarrow{\nabla\phi})_{S2}]$$

The cell-center mean curvature (κ_i) for the cell i then is obtained by a discrete approximation of the divergence theorem:

$$\kappa_i = -\frac{1}{V}\sum_k \mathbf{m}_{ik} \cdot \overrightarrow{n}_{ik} l_{ik}$$

where, $\mathbf{m}_{ik} = \frac{\overrightarrow{\nabla \phi_{ik}}}{|\overrightarrow{\nabla \phi_{ik}}|}$ is the normalized volume fraction gradient such that it is zero for $|\overrightarrow{\nabla \phi_{ik}}| = 0$. Also, the summation k is over the four segments $S1S2$, $S2S3$, $S3S4$, and $S4S1$. Aritmetic average is then applied to obtain the curvature at the cell-boundary between the cell i and j as: $\kappa_{ij} = \frac{\kappa_i + \kappa_j}{2}$.

4.5 Generalized Grid Coordinates

In engineering problems, geometries are rarely simple and, therefore, the grids associated with these geometries are also not trivial. As a result, the mesh can be highly skewed and/or highly stretched and the computational cell is often not orthogonal. To account for these non-uniformities, modifications to the above described algorithm becomes necessary.

The geometrical grid is transformed to a so-called computational grid which is Cartesian and the grid spacing is equal to unity. Let the coordinates of the geometrical grid be (x,y,z) and the coordinates of the computational grid be (ξ,η,ζ). For example, computing the second order derivative of ϕ with regard to x is done using the following formula:

$$\frac{\partial \phi}{\partial x} = \frac{\partial \xi}{\partial x}\frac{\partial \phi}{\partial \xi} + \frac{\partial \eta}{\partial x}\frac{\partial \phi}{\partial \eta} + \frac{\partial \zeta}{\partial x}\frac{\partial \phi}{\partial \zeta}$$

where, the derivatives (second-order accurate) of ϕ with regard to ξ, η, and ζ are easily computed as follows. Here, $\Delta\xi$=$\Delta\eta$=$\Delta\zeta$=1.

$$\begin{aligned}
\frac{\partial \phi}{\partial \xi} &= \phi_{(i+1,j,k)} - \phi_{(i-1,j,k)} \\
\frac{\partial \phi}{\partial \eta} &= \phi_{(i,j+1,k)} - \phi_{(i,j-1,k)} \\
\frac{\partial \phi}{\partial \zeta} &= \phi_{(i,j,k+1)} - \phi_{(i,j,k-1)}
\end{aligned}$$

The following set of formulas describes how the derivatives like $\partial\xi/\,\partial x$ are computed.

$$\begin{aligned}
\frac{\partial x}{\partial \xi} &= \frac{x_{(i+1,j,k)} - x_{(i-1,j,k)}}{2} \\
\frac{\partial x}{\partial \eta} &= \frac{x_{(i,j+1,k)} - x_{(i,j-1,k)}}{2} \\
\frac{\partial x}{\partial \zeta} &= \frac{x_{(i,j,k+1)} - x_{(i,j,k-1)}}{2} \\
\frac{\partial y}{\partial \xi} &= \frac{y_{(i+1,j,k)} - y_{(i-1,j,k)}}{2} \\
\frac{\partial y}{\partial \eta} &= \frac{y_{(i,j+1,k)} - y_{(i,j-1,k)}}{2} \\
\frac{\partial y}{\partial \zeta} &= \frac{y_{(i,j,k+1)} - y_{(i,j,k-1)}}{2} \\
\frac{\partial z}{\partial \xi} &= \frac{z_{(i+1,j,k)} - z_{(i-1,j,k)}}{2} \\
\frac{\partial z}{\partial \eta} &= \frac{z_{(i,j+1,k)} - z_{(i,j-1,k)}}{2} \\
\frac{\partial z}{\partial \zeta} &= \frac{z_{(i,j,k+1)} - z_{(i,j,k-1)}}{2}
\end{aligned}$$

Furthermore, using the chain rule, we have:

$$\underbrace{\begin{bmatrix} \frac{\partial x}{\partial \xi} & \frac{\partial x}{\partial \eta} & \frac{\partial x}{\partial \zeta} \\ \frac{\partial y}{\partial \xi} & \frac{\partial y}{\partial \eta} & \frac{\partial y}{\partial \zeta} \\ \frac{\partial z}{\partial \xi} & \frac{\partial z}{\partial \eta} & \frac{\partial z}{\partial \zeta} \end{bmatrix}}_{M} \begin{bmatrix} \frac{\partial}{\partial x} \\ \frac{\partial}{\partial x} \\ \frac{\partial}{\partial x} \end{bmatrix} = \begin{bmatrix} \frac{\partial}{\partial \xi} \\ \frac{\partial}{\partial \eta} \\ \frac{\partial}{\partial \zeta} \end{bmatrix}$$

$$\underbrace{\begin{bmatrix} \frac{\partial \xi}{\partial x} & \frac{\partial \xi}{\partial y} & \frac{\partial \xi}{\partial z} \\ \frac{\partial \eta}{\partial x} & \frac{\partial \eta}{\partial y} & \frac{\partial \eta}{\partial z} \\ \frac{\partial \zeta}{\partial x} & \frac{\partial \zeta}{\partial y} & \frac{\partial \zeta}{\partial z} \end{bmatrix}}_{M^{-1}} \begin{bmatrix} \frac{\partial}{\partial \xi} \\ \frac{\partial}{\partial \eta} \\ \frac{\partial}{\partial \zeta} \end{bmatrix} = \begin{bmatrix} \frac{\partial}{\partial x} \\ \frac{\partial}{\partial y} \\ \frac{\partial}{\partial z} \end{bmatrix}$$

The forward grid transformation matrix M^{-1}, or as it commonly known, the *grid metrics*, is used to compute spatial derivatives in (x, y, z) from variables mapped onto (ξ, η, ζ). Because derivatives are computed at each surfaces of the control volume, a set of three *grid metrics* (one for each directions) is needed. Also, for volumetric source

terms and filtered rate-of-tensor used by the LDKM method require cell-centered derivatives. In all, a total of four different M^{-1} are needed.

In cases when the geometrical grid is uniform and aligned with the coordinate axis, the metrics degenerate to an identity matrix. Then, both the grids are completely aligned and the gradient computations shown before apply directly.

4.6 Upwind Scheme Flux Computation

In smooth regions of the flow, where the flow variables can be considered as continuous, the forementioned central scheme can be applied with any order of spatial accuracy. This is facilitated by Taylor series expansions based on the knowledge of the function's value and all its derivatives at a local position. Such series expansions allow to reconstruct the function in an increasingly large domain around that location. However, presence of discontinuities destroys this process and in order to resolve the non-linear behavior more physical input is required.

The introduction of the physical properties of the flow into the solution of the discretized equations has led to the family of techniques known as "upwinding" [75]. In general, the term "upwind" applies to schemes which apply discretization that depends on the wave propagation direction. The primary basis for taking into account the physical properties of the equations is to prevent the oscillatory behavior in the vicinity of the discontinuity. Such behavior is common place in all second-order central schemes. The origin of the upwinding technique can be traced back to Courant *et al.* [36] and this technique has developed into a variety of approaches such as flux vector splitting, flux difference splitting, and other flux-controlling methods.

The flux vector splitting approach is based on the eigen-decomposition of the hyperbolic system of equations. Specifically, the information on the sign of the eigenvalues is used to split the flux terms and directionally discretized. This was first introduced by Steger and Warming [197]. Alternatively, properties derived from the

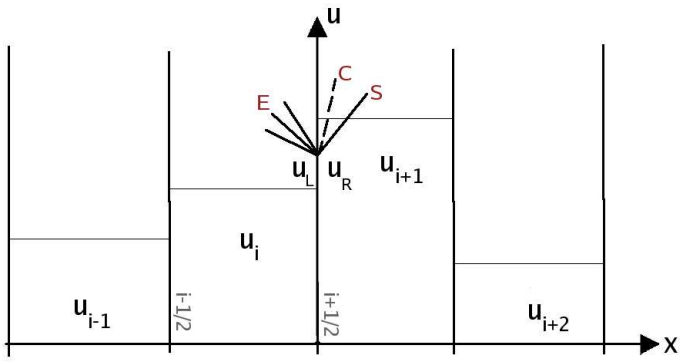

Figure 6: Schematic of the Godunov scheme for a scalar variable u. The exact resolution of the Riemann problem at the cell-interfaces is also shown in form of a shock wave (S), a contact discontinuity (C) and an expansion fan (E).

local solution of the system of equations can be introduced into the discretization scheme. This higher level approach, referred to as the flux difference splitting, of introduction of physical properties into the discretization was originally proposed by Godunov [60].

In the Godunov scheme, the flow field is considered in form of piecewise constant states over the mesh cells at each time-step and the temporal evolution is based on the exact solution of the Riemann problem at the cell boundaries [75]. The cell interface separates two different fluid states U_L on the left side and U_R on the right side as shown in the Fig. 6. The resulting local interaction can be exactly resolved in form of the shock-tube (or Riemann) problem. The Riemann problem has an exact solution generally composed of a shock wave, a contact discontinuity, and an expansion fan. Based on this solution, flux components at the cell boundaries are then constructed. This produces an explicit conservative scheme of first-order spatial accuracy.

The exact solution of the Riemann problem requires the resolution of a non-linear algebraic equation leading to an iteration-type solution approach. This can be quite time-consuming especially in cases where a 3D field is considered. A recent study by Toro and Chou [212] has shown computing savings by a factor of about four relative

to the use of exact Riemann solvers. To alleviate this difficulty, approximate Riemann solutions could be considered. Approximate Riemann solvers have been developed by Roe [172], Osher [140], and Harten *et al.* [70]. Several variants of these approximate solvers have also been reported [213].

The Godunov scheme is composed of basically a three-step process [75] involving piecewise constant approximation of the initial state, solution of the local Riemann problem at the cell boundary, and averaging the state variables after Δt time-step. The first and third steps considered as a "projection" stage [220] are independent of the second or physical step. Therefore, the projection stage can be modified without affecting the physical evolution. This knowledge has led to the definition of second-order space-accurate schemes. However, a straight-forward replacement of the first-order space differences by an appropriate second-order expressions leads to oscillatory behavior around discontinuities.

The higher-order accuracy is achieved by replacing the piecewise constant state approximation with either a piecewise linear or a piecewise parabolic extrapolation of a state at the cell boundary. It has been shown [75] that oscillations seen in higher-order schemes is related to excessively large gradients used in the variable extrapolation. Thus, the extrapolation gradients are controlled within the proper bounds by means of non-linear correction factors, called limiters. They were first introduced by Van Leer [219] and independently by Boris and Book [15].

The role of these limiters is to enforce the variation-bounded properties of the governing equations. These non-oscillatory properties of the Euler equations have been listed [75] to be: the entropy condition, monotonicity, and total variation diminishing (TVD). The entropy condition [107] is not connected to the non-oscillatory behavior but is associated with physically acceptable solution. For example, Roe's scheme admit expansion shock solutions and are associated with a decrease in entropy which is not consistent with the second law of thermodynamics. These unphysical solutions

must therefore be rejected.

A scheme is considered as "monotone" if it does not lead to a solution with an oscillatory behavior. The condition of monotonicity for any linear scheme can be written as: $u_i^{n+1} = \sum_k g_k u_{i+k}^n$ where, all the coefficients g_k need to be non-negative. Also, it is shown by Harten [69] that monotone scheme solutions always correspond to physically acceptable states. However, the the conservative monotone schemes for the non-linear equations are only of first-order accuracy [75]. A weaker condition than monotonicity is provided by the concept of total variation of a solution introduced by Harten [70, 68]. It allows for definition of higher accuracy schemes generating solutions without overshoots at discontinuities. This condition is more general than monotonicity, however it does not ensure the satisfaction the entropy condition. The total variation (TV) in x of a discrete solution to a scalar conservation law is given by $TV(u) = \sum_i |u_{i+1} - u_i|$, and the scheme is said to be TVD if the following is satisfied: $TV(u^{n+1}) \leq TV(u^n)$.

The first extension to higher order reconstruction satisfying the above conditions is due to [221] in the development of the Monotone Upstream Centered Schemes for Conservation Laws (MUSCL) scheme. In this approach, instead of having piecewise constant variables, a reconstruction procedure is used, that gives piecewise linear data towards each interface, thus leading to an improved spatial accuracy. A further higher order of accuracy is gained in the Piecewise Parabolic Method (PPM) approach following Colella and Woodward [35], in which the data are re-constructed using quadratic interpolation of the variables along each cell interface.

In the present study, we retain the approximate Roe-type Riemann solver for computing an approximate Riemann solution and the associated flux at the cell boundary following Allaire [4]. This is primarily done to reduce the computational load for capturing a discontinuity in the flow field, especially in 3D applications. Also, Roe solver

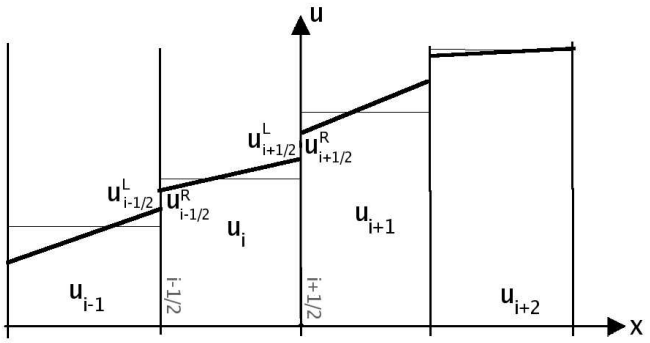

Figure 7: Piecewise linear representation of a scalar variable U within each cells following the MUSCL approach.

is exact on isolated contact discontinuities. In addition, a higher order spatial accuracy is achieved by employing the MUSCL approach with a minmod limiter for the variable extrapolation. This variable extrapolation process is applied to the primitive set of variables $[\alpha_1\rho_1, \alpha_2\rho_2, u, v, w, P, \alpha_1]^T$. The five-equation interface model also contains a transport equation for the gas volume fraction which has to be discretized in accordance to the Abgrall's condition [1] of pressure and velocity uniformity at the liquid/gas interface.

4.6.1 MUSCL Approach

A piecewise constant approximation of state variables on the cell boundary limits the spatial accuracy of the scheme to first order. Hence, a linear approximation of the solution on each cell leads to second order of accuracy. This was first introduced in form of a Monotone Upstream Centered Schemes for Conservation Laws (MUSCL) by Van Leer [221]. The main idea behind this method is construct a linear extrapolation of a variable towards the cell boundaries using both the cell value and the information in the neighboring cells. The MUSCL approach was applied by Génin and Menon [58, 57] in the context of shock-turbulence studies. Here, we apply the same technique to capture discontinuities present at the material interface.

Consider a cell i with cell center (or averaged) value of $U-$variable as U_i. Within

that cell, a linear profile can be constructed to give the variation of U as a function of the distance from the cell center location (x_i) as: $U(x) = \beta(x - x_i) + U_i$. The piecewise linear distribution so obtained have to average out to the cell center values. Here, $x \in [x_{i-\frac{1}{2}}, x_{i+\frac{1}{2}}]$ and a linear combination of the derivatives of the $U-$variable leads to the extrapolated values as:

$$\begin{aligned} U^L_{i+1/2} &= U_i + \tfrac{\epsilon}{4}\left[(1-\kappa)\,\Delta^+_{i-1/2}(U) + (1+\kappa)\,\Delta^-_{i+1/2}(U)\right] \\ U^R_{i+1/2} &= U_{i+1} - \tfrac{\epsilon}{4}\left[(1+\kappa)\,\Delta^+_{i+1/2}(U) + (1-\kappa)\,\Delta^-_{i+3/2}(U)\right] \end{aligned} \tag{56}$$

where, ϵ is a coefficient that can be set to 0 in order to get the piecewise constant field with first-order spatial accuracy. This case leads to the original Godunov extrapolation. For higher order spatial accuracy, $\epsilon = 1$, and the differencing $\Delta^\bullet_{i-1/2}(U)$, where $\bullet = +/-$, is approximated as a centered difference:

$$\Delta^+_{i+1/2}(U) = \Delta^-_{i+1/2}(U) = \Delta_{i+1/2}(U) = U_{i+1} - U_i \tag{57}$$

The interface values can now be constructed based on a combination of the backward nad forward extrapolations depending on the value of κ. For $\kappa = -1$, a linear one-sided extrapolation at the cell boundary is obtained:

$$\begin{aligned} U^L_{i+1/2} &= U_i + \tfrac{\epsilon}{2}\,(U_i - U_{i-1}) \\ U^R_{i+1/2} &= U_{i+1} - \tfrac{\epsilon}{2}\,(U_{i+2} - U_{i+1}) \end{aligned} \tag{58}$$

based on the two upstream and two downstream cells leading to a second-order fully one-sided scheme. Similarly, for $\kappa = 0$, the boundary value is approximated by a linear interpolation between one upstream and one downstream cell. A third-order accurate space discretization can be obtained by $\kappa = 1/3$ which generates a parabolic representation. Finally, with $\kappa = 1$, the cell boundary values are the arithmetic mean of the adjacent cell values and the upwind character is lost. This corresponds to a central scheme.

This representation of the higher-order extrapolation does not necessarily prevent oscillations in the vicinity of a discontinuity. The primary reason for this undesirable

behavior is the excessively large gradients employed in the extrapolation. Non-linear correction factors, also called limiters, are employed to limit the gradients within proper bounds. This also ensures the property of total variation. The difference relations in Eqn. 57 must be limited as:

$$\begin{aligned} \Delta^{+}_{i+1/2}(U) &= lim\_(\Delta_{i+1/2}(U), \Delta_{i+3/2}(U)) \\ \Delta^{-}_{i+1/2}(U) &= lim\_(\Delta_{i+1/2}(U), \Delta_{i-1/2}(U)) \end{aligned} \tag{59}$$

and the limit functions ensure monotonicity of the solution. Another classical notation for the limiters is given by:

$$\begin{aligned} \Delta^{+}_{i+1/2}(U) &= \Delta_{i+1/2}(U)\phi(r^{+}_{i+1/2}) & r^{+}_{i+1/2} &= \tfrac{\Delta_{i+3/2}(U)}{\Delta_{i+1/2}(U)} \\ \Delta^{-}_{i+1/2}(U) &= \Delta_{i+1/2}(U)\phi(r^{-}_{i+1/2}) & r^{-}_{i+1/2} &= \tfrac{\Delta_{i-1/2}(U)}{\Delta_{i+1/2}(U)} \end{aligned} \tag{60}$$

where, ϕ is the so-called limiter. Using these relations in Eqn. 56, the extrapolation then reads:

$$\begin{aligned} U^{L}_{i+1/2} &= U_i + \tfrac{\epsilon}{4}\left[(1-\kappa)\,\phi(r^{+}_{i-1/2})(U_i - U_{i-1}) + (1+\kappa)\,\phi(r^{-}_{i+1/2})(U_{i+1} - U_i)\right] \\ U^{R}_{i+1/2} &= U_{i+1} - \tfrac{\epsilon}{4}\left[(1-\kappa)\,\phi(r^{-}_{i+3/2})(U_{i+2} - U_{i+1}) + (1+\kappa)\,\phi(r^{+}_{i+1/2})(U_{i+1} - U_i)\right] \end{aligned}$$

With the knowledge that $r^{+}_{i-1/2} = 1/r^{-}_{i+1/2}$, and $r^{+}_{i+1/2} = 1/r^{-}_{i+3/2}$, one can rewrite the same set of equations in the following form:

$$\begin{aligned} U^{L}_{i+1/2} &= U_i + \tfrac{\epsilon}{4}\left[(1-\kappa)\,\phi(r^{+}_{i-1/2}) + (1+\kappa)\,\phi(\tfrac{1}{r^{+}_{i-1/2}})r^{+}_{i-1/2}\right](U_i - U_{i-1}) \\ U^{R}_{i+1/2} &= U_{i+1} - \tfrac{\epsilon}{4}\left[(1-\kappa)\,\phi(r^{-}_{i+3/2}) + (1+\kappa)\,\phi(\tfrac{1}{r^{-}_{i+3/2}})r^{-}_{i+3/2}\right](U_{i+2} - U_{i+1}) \end{aligned} \tag{61}$$

The TVD formulation of the variable extrapolation – MUSCL – method is now completely defined after a limiter function is chosen. Several limiters have been proposed in the past and have been applied to a variety of flow configurations. Following is a list of most often used [75]:

Minmod Limiter:

The Minmod function is defined as the function that selects the number with the smallest modulus from a series of numbers when they all have the same sign, and zero otherwise. For two arguments:

$$minmod(x,y) = sgn(x) \cdot max[0,\ min(|x|, sgn(x) \cdot y)] \tag{62}$$

with $x = 1$, a particular case of the minmod function can be obtained as:

$$\phi_{mm}(r) = max\big[0, min(r,1)\big] \tag{63}$$

Chakravarthy and Osher [22] proposed the following extension to the above minmod function as:

$$\phi_{mm}(r) = max\big[0, min(r,\beta)\big] \quad with \quad \beta = \tfrac{3-\kappa}{1-\kappa} \tag{64}$$

Superbee Limiter:

Roe [173] proposed the following limiter known for excellent resolution properties for contact discontuities. It is defined by:

$$\phi_{sb}(r) = max\big[0, min(2r,1), min(r,2)\big] \tag{65}$$

It is interesting to note that the Minmod and Superbee limiters are part of a family of limiters described by Sweby [201]:

$$\phi_{\beta}(r) = max\big[0, min(\beta r,1), min(r,\beta)\big] \qquad 1 \le \beta \le 2 \tag{66}$$

where, the Minmod corresponds to $\beta = 1$ and the Superbee corresponds to $\beta = 2$.

Monotonized Central Limiter:

It is defined as:

$$\phi_{mc}(r) = max\big[0, min(2r, 2, \frac{1+r}{2})\big] \tag{67}$$

All of these limiters, except for the minmod extension by Chakravarthy, share the following symmetry property:

$$\frac{\phi(r)}{r} = \phi\left(\frac{1}{r}\right) \tag{68}$$

indicating that forward and backward gradients are treated in the same way. Also, all these limiter functions satisfy the TVD property ensuring that the numerical scheme is monotonicity preserving. In addition, when using a limiter that satisfies the symmetry condition, Eqn. 61 can be simplified and re-written as:

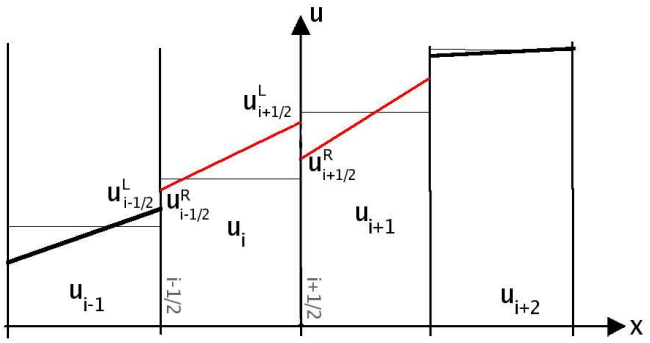

Figure 8: Gradient violation in the reconstruction of a scalar variable U following the MUSCL approach.

$$\begin{aligned} U^L_{i+1/2} &= U_i + \tfrac{\epsilon}{2}\phi(r^+_{i-1/2})(U_i - U_{i-1}) \\ U^R_{i+1/2} &= U_{i+1} - \tfrac{\epsilon}{2}\phi(r^-_{i+3/2})(U_{i+2} - U_{i+1}) \end{aligned} \tag{69}$$

The above expressions are devoid of the coefficient κ originally used in the MUSCL approach. This is due to their cancellation when symmetric limiters are used. Overall, a second-order spatial accuracy is obtained with the above TVD preserving variable extrapolation.

The TVD approach presented above ensures the variable reconstruction at the cell boundary will lead to a monotonic field extrapolated variables. However, there is one more instance that may lead to a non-monotonic field and need to be checked. This instance is related to the sign of the gradient of the reconstructed variable.

Gradient of the reconstructed variable:

The monotonicity of the field, as expressed previously, ensures the following at the cell boundary $(i + \frac{1}{2})$:

$$\begin{aligned} max(U_i, U_{i+1}) \geq U^L_{i+\frac{1}{2}} \geq min(U_i, U_{i+1}) \\ max(U_i, U_{i+1}) \geq U^R_{i+\frac{1}{2}} \geq min(U_i, U_{i+1}) \end{aligned} \tag{70}$$

However, this does not ensure that the gradient of the reconstructed variable also varies monotonically. Figure 8 shows an instance where the extrapolated variable

satisfies the monotonicity condition, however the gradient shows an oscillatory behavior. It is seen that: $(U_{i+1} - U_i)(U^R_{i+\frac{1}{2}} - U^L_{i+\frac{1}{2}}) < 0$ leading to a change in the sign for the gradient at the cell boundary. This condition has to be checked after the extrapolation at the cell boundary is performed. In such cases, the left and the right states are adjusted to:

$$U^{L,new}_{i+\frac{1}{2}} = \frac{1}{2}(U^{L,old}_{i+\frac{1}{2}} + U^{R,old}_{i+\frac{1}{2}}) \qquad\qquad U^{R,new}_{i+\frac{1}{2}} = U^{L,new}_{i+\frac{1}{2}} \tag{71}$$

It can be observed that the adjusted left and right states preserve the monotonicity condition as both the $U^{L,old}_{i+\frac{1}{2}}$ and $U^{R,old}_{i+\frac{1}{2}}$ lie between the cell-center values of the neighboring cells.

4.6.2 Roe-type Approximate Riemann Solver

The approximate Riemann solver developed by Roe [172, 173] is based on a characteristic decomposition of the flux differences while ensuring the conservation properties of the scheme. The approach relies on extending the linear wave decomposition [75] to non-linear equations.

The exact Riemann problem can be characterized as:

$$\mathbf{U}_t + \mathbf{F}(\mathbf{U})_x = 0 \tag{72}$$

with the following initial conditions: $\mathbf{U}(x,0) = \mathbf{U}_L$ if $x < 0$ and $\mathbf{U}(x,0) = \mathbf{U}_R$ if $x > 0$, where x is the cell boundary location and the subscripts L and R are the left and the right states across the cell boundary, respectively. Here, $\mathbf{U}$ is a vector of conserved variables and $\mathbf{F}(\mathbf{U})$ represents the flux vector. The exact Riemann solution wave structure consists of a shock wave, a contact discontinuity, and an expansion fan as was shown previously.

Roe [172, 173] solved the Riemann problem in Eqn. 72 approximately by introducing the Jacobian matrix $\mathbf{A}(\mathbf{U}) = \partial\mathbf{F}/\partial\mathbf{U}$ such that the equations can be written as: $\mathbf{U}_t + \mathbf{A}(\mathbf{U})\mathbf{U}_x = 0$. The approximation arises by replacing the Jacobian matrix by a constant Jacobian matrix such that:

$$\widetilde{\mathbf{A}} = \widetilde{\mathbf{A}}(\mathbf{U}_L, \mathbf{U}_R) \tag{73}$$

as function of the left and right states. The original non-linear partially differential equation in Eqn. 72 is replaced by:

$$\mathbf{U}_t + \widetilde{\mathbf{A}}\mathbf{U}_x = 0 \tag{74}$$

which is a linear system with constant coefficient matrix ($\widetilde{\mathbf{A}}$). The resulting approximate Riemann problem is then solved exactly with the initial data of the exact problem. The Roe Jacobian matrix is sought satisfying the following properties [213, 75]:

- Property (1): Hyperbolicity of the system. This implies that $\widetilde{\mathbf{A}}$ must have real eigenvalues with linearly independent eigenvectors.
- Property (2): Consistency with the exact Jacobian matrix: $\widetilde{\mathbf{A}}(\mathbf{U}, \mathbf{U}) = \mathbf{A}(\mathbf{U})$ for $\mathbf{U}_i = \mathbf{U}_{i+1} = \mathbf{U}$.
- Property (3): Conservation across discontinuities:

$$\mathbf{F}(\mathbf{U}_R) - \mathbf{F}(\mathbf{U}_L) = \widetilde{\mathbf{A}}(\mathbf{U}_R - \mathbf{U}_L)$$

The construction of matrices satisfying the above properties for general hyperbolic systems of equations can be very complicated [213]. However, for the specific case of the Euler equations, Roe [173] proposed an approach of constructing the constant matrix. Roe and Pike [173] suggested a simpler approach whereby the explicit construction of the constant matrix is avoided.

Once the Roe Jacobian is defined and its eigenvalues and eigenvectors are available, the approximate Riemann problem in Eqn. 74 is solved by a application of methods [213] pertaining to linear hyperbolic systems. The approximate Riemann solution at the cell boundary is given by:

$$\mathbf{U}_{i+\frac{1}{2}}(0) = \mathbf{U}_L + \sum_{\lambda_i \leq 0} \varsigma_i \mathbf{r}_i \quad or$$
$$\mathbf{U}_{i+\frac{1}{2}}(0) = \mathbf{U}_R - \sum_{\lambda_i \geq 0} \varsigma_i \mathbf{r}_i$$

where, λ_i, ς_i, and $\mathbf{r}_i$ are the $i-$th eigenvalue, wave strength, and corresponding right eigenvector of the Roe matrix, respectively. The second term on the right-hand side of the above expressions represents [75] the variations of the conservative variables as a sum of simple waves $\mathbf{r}_i$ with amplitudes (or wave strengths) ς_i. The corresponding numerical flux at the cell boundary is given as:

$$\mathbf{F}_{i+\frac{1}{2}} = \frac{1}{2}[\mathbf{F}_L + \mathbf{F}_R] - \frac{1}{2}\sum_{i=1}^{n} |\lambda_i| \varsigma_i \mathbf{r}_i \tag{75}$$

where, n is the total number of eigenvalues of the Roe matrix. The summation on the right-hand side represents the dissipative part of the Roe numerical flux. Here, flux states $\mathbf{F}_L = \mathbf{F}(\mathbf{U}_L)$ and similarly $\mathbf{F}_R = \mathbf{F}(\mathbf{U}_R)$.

Roe [172] observed that the column vectors of the state variables and the corresponding fluxes can be expressed as quadratic function of the variable $\mathbf{Z}$ such that: $\mathbf{U} = \mathbf{U}(\mathbf{Z})$ and $\mathbf{F} = \mathbf{F}(\mathbf{Z})$. Further, the changes in these vectors can also be expressed in terms of the change $\Delta\mathbf{Z} = \mathbf{Z}_R - \mathbf{Z}_L$ such that: $\Delta\mathbf{U} = \widetilde{\mathbf{B}}\Delta\mathbf{Z}$ and $\Delta\mathbf{F} = \widetilde{\mathbf{C}}\Delta\mathbf{Z}$. Finally, the Roe matrix is obtained by consolidating the expressions as: $\Delta\mathbf{F} = (\widetilde{\mathbf{C}}\widetilde{\mathbf{B}}^{-\mathbf{1}})\Delta\mathbf{U}$ and comparison with the third property results in the averaged matrix as: $\widetilde{\mathbf{A}} = \widetilde{\mathbf{C}}\widetilde{\mathbf{B}}^{-\mathbf{1}}$.

It was also observed by Roe [172] that the averaged matrix ($\widetilde{\mathbf{A}}$) was identical to the Jacobian matrix ($\mathbf{A}$) with the variables are replaced by an average weighted by the square root of the densities. This was the engenious choice of the parameter vector ($\mathbf{Z}$) that simplified the construction of the Roe matrix. Roe and Pike [173] have shown that these averages are the unique choice satisfying the forementioned three conditions on the Roe matrix. It was also noted that this result remains unchanged for multi-dimensional field. Thus, the advantages of iteration-free evaluation of the flux at the cell boundary and a simplified algorithm structure for multidimensional flows justifies the selection of this approach.

We now define a Roe-type linearization for the five-equation interface model in Eqn. 10. Allaire [4] has noted the quasi-conservative nature of the model due to

the presence of non-conservative volume fraction transport equation. Abgrall [1] have shown that the strong conservative character of the system of equations must be relaxed in order to retain good stability properties in the vicinity of the material interface. Following Allaire [4], a variant of the Roe's scheme is used which, instead of requiring a linearization of the pressure jump, it relies on the definition of an average sound speed at the cell boundary. This procedure enables the scheme to be applied to any type of fluid with general equations of state. More details in this regard is reported elsewhere [4].

The following notation associated with the Roe matrix definition is noted:

$$\overline{a} = \frac{a_L\sqrt{\rho_L}+a_R\sqrt{\rho_R}}{\sqrt{\rho_L}+\sqrt{\rho_R}}, \qquad \underline{a} = \frac{a_R\sqrt{\rho_L}+a_L\sqrt{\rho_R}}{\sqrt{\rho_L}+\sqrt{\rho_R}} \tag{76}$$

where, a is any vector or scalar quantity weighted-averaged by the square-root of the density in the left and right state. Also, jump in quantity a in form of $\Delta a = a_R - a_L$ is noted. Based on the discussion above, the Roe matrix must have the same structure as the Jacobian matrix of Eqn. 14 for a set of quasi-conservative variables ($\mathbf{W}$). The Roe matrix in $x-$direction is given by $\widetilde{\mathbf{A}}(\mathbf{W})$:

$$\begin{pmatrix}
u^*y_2^* & -u^*y_1^* & y_1^* & 0 & 0 & 0 & 0 \\
-u^*y_2^* & u^*y_1^* & y_2^* & 0 & 0 & 0 & 0 \\
(\beta_1^* - (u^*)^2) & (\beta_2^* - (u^*)^2) & (2-\frac{1}{\xi^*})u^* & -\frac{v^*}{\xi^*} & -\frac{w^*}{\xi^*} & \frac{1}{\xi^*} & \Omega^* + \sigma\kappa^* \\
-u^*v^* & -u^*v^* & v^* & u^* & 0 & 0 & 0 \\
-u^*w^* & -u^*w^* & w^* & 0 & u^* & 0 & 0 \\
u^*(\beta_1^* - H^*) & u^*(\beta_2^* - H^*) & (H^* - \frac{(u^*)^2}{\xi^*}) & -\frac{u^*v^*}{\xi^*} & -\frac{u^*w^*}{\xi^*} & u^*(\frac{1}{\xi^*}+1) & \Omega^*u^* + \sigma\kappa^*u^* \\
0 & 0 & 0 & 0 & 0 & 0 & u^*
\end{pmatrix}$$

where, the coefficient $\beta_i^* = \left(\frac{(u^*)^2+(v^*)^2+(w^*)^2}{2} - \delta_i^*\right)/\xi^*$ ensures that the Roe martix is diagonizable [4] with eigenelements given by Eqn. 15. The subscripts $*$ indicate values represent weighted averages such that: $u^* = \overline{u}$, $v^* = \overline{v}$, $w^* = \overline{w}$, $y_i^* = \overline{y_i}$, and $H^* = \overline{H}$. The coefficient c^* in the eigenelements is defined by:

$(c^*)^2 = \left[\overline{H} - \frac{(\bar{u})^2+(\bar{v})^2+(\bar{w})^2}{2} - \sum_i \overline{y_i}\delta_i^*\right]/\xi^*$.

Similarly, the Roe matrix in the y- and z-directions, respectively, are given as:

$$\begin{pmatrix}
v^*y_2^* & -v^*y_1^* & 0 & y_1^* & 0 & 0 & 0 \\
-v^*y_2^* & v^*y_1^* & 0 & y_2^* & 0 & 0 & 0 \\
-u^*v^* & -u^*v^* & v^* & u^* & 0 & 0 & 0 \\
(\beta_1^* - (v^*)^2) & (\beta_2^* - (v^*)^2) & -\frac{u^*}{\xi^*} & (2-\frac{1}{\xi^*})v^* & -\frac{w^*}{\xi^*} & \frac{1}{\xi^*} & \Omega^* + \sigma\kappa^* \\
-v^*w^* & -v^*w^* & 0 & w^* & v^* & 0 & 0 \\
v^*(\beta_1^* - H^*) & v^*(\beta_2^* - H^*) & -\frac{u^*v^*}{\xi^*} & (H^* - \frac{(v^*)^2}{\xi^*}) & -\frac{v^*w^*}{\xi^*} & v^*(\frac{1}{\xi^*}+1) & \Omega^*v^* + \sigma\kappa^*v^* \\
0 & 0 & 0 & 0 & 0 & 0 & v^*
\end{pmatrix}$$

$$\begin{pmatrix}
w^*y_2^* & -w^*y_1^* & 0 & 0 & y_1^* & 0 & 0 \\
-w^*y_2^* & w^*y_1^* & 0 & 0 & y_2^* & 0 & 0 \\
-u^*w^* & -u^*w^* & w^* & 0 & u^* & 0 & 0 \\
-v^*w^* & -v^*w^* & 0 & w^* & v^* & 0 & 0 \\
(\beta_1^* - (w^*)^2) & (\beta_2^* - (w^*)^2) & -\frac{u^*}{\xi^*} & -\frac{v^*}{\xi^*} & (2-\frac{1}{\xi^*})u^* & \frac{1}{\xi^*} & \Omega^* + \sigma\kappa^* \\
w^*(\beta_1^* - H^*) & w^*(\beta_2^* - H^*) & -\frac{u^*w^*}{\xi^*} & -\frac{v^*w^*}{\xi^*} & (H^* - \frac{(w^*)^2}{\xi^*}) & w^*(\frac{1}{\xi^*}+1) & \Omega^*w^* + \sigma\kappa^*w^* \\
0 & 0 & 0 & 0 & 0 & 0 & w^*
\end{pmatrix}$$

As is noted by Allaire [4] that explicit values of ξ^*, δ_i^*, and Ω^* can be found for perfect gases, however this is not the case for a general equation of state. Hence, the existence of ξ^*, δ_i^*, and Ω^* is assumed. The choice of $\xi^* = \overline{\xi}$ and $\delta_i^* = \overline{\delta_i}$ following Allaire [4] is retained in this study.

If the surface tension coefficient (σ) taken equal to zero, the above Roe matrix reverts back to that of Allaire [4]. This shows that the presence of surface tension does not alter the Euler eigenstructure. We also observe the presence of local interface curvature κ^*. This term was assumed to be frozen at a given point and a given time. Therefore, $\kappa^* = \kappa$ is considered as it derives its value without Roe averaging procedure. Similarly, the surface tension coefficient is assumed to be an independent constant not affected by the averaging.

For the above Roe matrix, the eigenvalues and eigenvectors of the corresponding Jacobian matrix apply. We are now interested in deriving the dissipative flux components corresponding to the Roe numerical flux in Eqn. 75. Various coefficients like ξ^*, δ_i^*, and Ω^* appear in the Roe matrix, however it is possible to write the dissipative flux components such that these coefficients cancel out and only the average sound speed remains. Using the wave strengths ($\varsigma_i(\mathbf{W})$) and the right eigenvectors ($\mathbf{r_i}(\mathbf{W})$) in the summation term:

$$\mathbf{R} = \sum_{j=1}^{7} |\lambda_j| \varsigma_j \mathbf{r}_j \tag{77}$$

The coefficients Ω^* and δ_i^* only appear in the right eigenvectors corresponding to the eigenvalue $\lambda_j = u$ where, $j \in [2, 4]$. Writing out the partial sum as:

$$\sum_{j=2}^{4} |\lambda_j| \varsigma_j \mathbf{r}_j = |u| \left[\varsigma_2, \varsigma_3, \overline{u}(\varsigma_2 + \varsigma_3), \overline{v}(\varsigma_2 + \varsigma_3) + \varsigma_5, \overline{w}(\varsigma_2 + \varsigma_3) + \varsigma_6, B, \varsigma_4\right]^T \tag{78}$$

where,

$$B = \left[(\varsigma_2 + \varsigma_3)[\frac{(\bar{u})^2 + (\bar{v})^2 + (\bar{w})^2}{2}] - (\Omega^* + \sigma\kappa)\xi^*\varsigma_4 + \bar{v}\varsigma_5 + \bar{w}\varsigma_6 + \varsigma_2\delta_1^* + \varsigma_3\delta_2^*\right]$$

Upon simplification [4] this coefficient reduces to:

$$B = \left[[\frac{(\bar{u})^2 + (\bar{v})^2 + (\bar{w})^2}{2}]\Delta\rho + \Delta(\rho\varepsilon) - \frac{\bar{H}}{(c^*)^2}[\Delta P + \sigma\kappa\Delta\alpha_1] + \underline{\rho}\bar{v}\Delta v + \underline{\rho}\bar{w}\Delta w\right] \tag{79}$$

and is observed to depend only on the average sound speed c^*. The resulting dissipative flux for the first six components can be given as:

$$\begin{aligned}
R_1 &= |\bar{u} - c^*|\varsigma_1\bar{y_1} + |\bar{u}|\varsigma_2 + |\bar{u} + c^*|\varsigma_7\bar{y_1} \\
R_2 &= |\bar{u} - c^*|\varsigma_1\bar{y_2} + |\bar{u}|\varsigma_3 + |\bar{u} + c^*|\varsigma_7\bar{y_2} \\
R_3 &= |\bar{u} - c^*|\varsigma_1(\bar{u} - c^*) + |\bar{u}|(\varsigma_2 + \varsigma_3)\bar{u} + |\bar{u} + c^*|\varsigma_7(\bar{u} + c^*) \\
R_4 &= |\bar{u} - c^*|\varsigma_1\bar{v} + |\bar{u}|[(\varsigma_2 + \varsigma_3)\bar{v} + \varsigma_5] + |\bar{u} + c^*|\varsigma_7\bar{v} \\
R_5 &= |\bar{u} - c^*|\varsigma_1\bar{w} + |\bar{u}|[(\varsigma_2 + \varsigma_3)\bar{w} + \varsigma_6] + |\bar{u} + c^*|\varsigma_7\bar{w} \\
R_6 &= |\bar{u} - c^*|\varsigma_1(\bar{H} - \bar{u}c^*) + |\bar{u}|B + |\bar{u} + c^*|\varsigma_7(\bar{H} + \bar{u}c^*)
\end{aligned} \tag{80}$$

where, $\mathbf{R} = [R_1, R_2, R_3, R_4, R_5, R_6, R_7]^T$ is the dissipative flux vector of the Roe numerical flux in the $x-$direction. Similar expressions arise for the other two directions. Also, the wave strengths $\varsigma_i(\mathbf{W})$ and B were defined previously. The seventh component (R_7) is not considered as the gas volume fraction equation is integrated in a non-conservative mode (to be discussed later).

Roe's approximate Riemann solver admit expansion shock solutions and are associated with a decrease in entropy which is not consistent with the second law of thermodynamics. The reason [75] behind this inconsistent situation is that the Roe's scheme does not see the sonic point. For the case of a sonic point within the left and right state interval, the Roe's scheme connects the two states by a direct, discontinuous jump. Hence, to alleviate this difficulty, an additional flux contribution can be introduced when an expansion through a sonic point is detected. This approach was proposed by Roe and Pike [173]. Alternatively, Harten and Hyman [70] advocated a technique to avoid the expansion shock. They suggested introducing a local expansion fan in the approximate Riemann solution when an expansion through a sonic point is detected. This approach is employed in the current study. The modulus of the eigenvalue λ in Eqn. 75 is modified such that:

$$|\lambda|_{MOD} = \begin{cases} |\lambda| & \text{if } |\lambda| \geq \eta; \\ \frac{1}{2}\left(\frac{\lambda^2+\eta^2}{\eta}\right) & \text{if } |\lambda| < \eta. \end{cases}$$

where, the quantity η is derived on the basis of:

$$\eta = max\left[0, (\lambda - \lambda_L), (\lambda_R - \lambda)\right]$$

Here, λ is the eigenvalue evaluated at the cell boundary based on the above weighted averages. The subscripts L and R represent left and right states, respectively. The eigenvalues in the adjacent states are evaluated on the respective properties in that state.

4.6.3 Overall Scheme

The time integration of the overall upwind scheme encompasses an update to the conservative part of the quasi-conservative scheme in Eqn. 10 as well as non-conservative transport of the gas volume fraction.

Advection approach for the gas volume fraction:

The transport equation for the gas volume fraction is recalled as:

$$\frac{\partial \alpha_1}{\partial t} + u_j \frac{\partial \alpha_1}{\partial x_j} = 0 \tag{81}$$

where, α_1 is the gas volume fraction and u_j is the mixture velocity. This equation can also be thought of as a supplementary transport equation enabling the closure of the mixture EOS. Also, consideration of this transport equation in lieu of individual advection of each EOS parameter makes the number of equations in the model independent of the EOS. This has been shown by Allaire [4].

The discretization of the non-conservative transport equation is based on the condition of Abgrall [1] and Karni [92]. This condition states that if the material interface evolves under uniform pressure and velocity conditions, both the pressure and velocity must remain uniform at all times.

The first-order accurate form in 1D is given by [4]:

$$(\alpha_1)_i^{n+1} = (\alpha_1)_i^n - \frac{\Delta t}{\Delta x}\left[(\bar{u}_{i+\frac{1}{2}})^-[\frac{\alpha_{1,i+1} - \alpha_{1,i}}{2}] + (\bar{u}_{i-\frac{1}{2}})^+[\frac{\alpha_{1,i} - \alpha_{1,i-1}}{2}]\right] \tag{82}$$

where, $\bar{u}_{i+\frac{1}{2}}$ is the Roe average of u between the cells i and $i+1$ and $u^{\pm} = (u \pm |u|)/2$. Here, Δt is the time-step and Δx is the mesh spacing.

Similarly, a second-order spatially accurate scheme can be designed based on the forementioned condition. Allaire [4] suggested to write the transport equation for α_1 as:

$$\frac{\partial \alpha_1}{\partial t} + \frac{\partial \alpha_1 u_j}{\partial x_j} - \alpha_1 \frac{\partial u_j}{\partial x_j} = 0 \tag{83}$$

and to apply a second-order scheme for the conservative part (second term) together with a non-conservative correction (third term). The discretization in 1D is given as:

$$(\alpha_1)_i^{n+1} = (\alpha_1)_i^n - \frac{\Delta t}{\Delta x}\left[f_{i+\frac{1}{2}} - f_{i-\frac{1}{2}}\right] + \frac{\Delta t}{\Delta x}(\alpha_1)_i^n\left[r_{i+\frac{1}{2}} - r_{i-\frac{1}{2}}\right] \tag{84}$$

where, $f_{i\pm\frac{1}{2}}$ is the conservative flux update and $r_{i\pm\frac{1}{2}}$ is the non-conservative correction. The flux and the correction term on the $(i+\frac{1}{2})$ cell face is given by:

$$f_{i+\frac{1}{2}} = f(\mathbf{W}^L_{i+\frac{1}{2}}, \mathbf{W}^R_{i+\frac{1}{2}}), \tag{85}$$

$$f(\mathbf{W}_L, \mathbf{W}_R) = \frac{1}{2}\left[u_R\alpha_{1,R} + u_L\alpha_{1,L}\right] - \frac{1}{2}\left|\frac{u_R + u_L}{2}\right|(\alpha_{1,R} - \alpha_{1,L}) \tag{86}$$

$$r_{i+\frac{1}{2}} = \frac{u^R_{i+\frac{1}{2}} + u^L_{i+\frac{1}{2}}}{2} \tag{87}$$

Its multi-dimensional extension is given as:

$$(\alpha_1)_i^{n+1} = (\alpha_1)_i^n - \frac{\Delta t}{V_i}\sum_{k=1}^{6}\left[\mathbf{f}_{ik} - (\alpha_1)_i^n\ \mathbf{r}_{ik}\right] d\mathbf{A}_{ik} \tag{88}$$

where, V_i is the $i-$th cell volume, $d\mathbf{A}_{ik}$ is the cell face area, and the summation index k runs from one to six cell faces. Also, $\mathbf{f}_{ik}$ is the conservative flux on the $k-$th cell face and the corresponding non-conservative correction is represented by $\mathbf{r}_{ik}$. The $predictor - corrector$ approach in Eqn. 46 for the time integration is then applied to the gas volume fraction advection.

Conservative flux treatment:

The five-equation interface model in Eqn. 10 is a quasi-conservative system of equations containing conservation relations for the mass of each phase k, mixture momentum, and mixture energy. The seventh equation of gas volume fraction transport forms the non-conservative aspect of Eqn. 10 as discussed above. Here, we summarize the flux components of the conservative part and discuss the treatment of surface tension tensor.

We define the subset of the six conserved variables as: $\mathbf{Q} = [\alpha_1\rho_1, \alpha_2\rho_2, \rho u, \rho v, \rho w, \rho E]^T$ such that $\mathbf{W} = [\mathbf{Q}, \alpha_1]^T$. The last item is the gas volume fraction. The system of equations in the strict conservation form for this subset can be recalled as:

$$\frac{\partial \mathbf{Q}}{\partial t} + \frac{\partial \mathbf{F}}{\partial x} + \frac{\partial \mathbf{G}}{\partial y} + \frac{\partial \mathbf{H}}{\partial z} = \mathbf{S} \tag{89}$$

where, the flux vectors $\mathbf{F}$, $\mathbf{G}$, and $\mathbf{H}$ represent components in x, y, and z directions, respectively. The source vector is of the form: $\mathbf{S} = [0, 0, \rho g_x, \rho g_y, \rho g_z, \rho g_i u_i]^T$. The flux component in the $x-$direction is then given as:

$$\mathbf{F} = \underbrace{\begin{pmatrix} \alpha_1\rho_1 u \\ \alpha_2\rho_2 u \\ \rho uu + P \\ \rho uv \\ \rho uw \\ \rho Hu \end{pmatrix}}_{\textbf{Inviscid}} - \underbrace{\begin{pmatrix} 0 \\ 0 \\ \tau_{xx} \\ \tau_{xy} \\ \tau_{xz} \\ u\tau_{xx} + v\tau_{xy} + w\tau_{xz} \end{pmatrix}}_{\textbf{Viscous}} - \sigma|\vec{\mathbf{m}}| \underbrace{\begin{pmatrix} 0 \\ 0 \\ \psi_{xx} \\ \psi_{xy} \\ \psi_{xz} \\ u\psi_{xx} + v\psi_{xy} + w\psi_{xz} \end{pmatrix}}_{\textbf{Capillary}}$$

where, the usual notation of ρ, u, v, w, H, P apply in form of mixture quantities. Phase-specific α_k and ρ_k represent volume fraction and density, respectively. The gravitational components $\vec{\mathbf{g}} = [g_x, g_y, g_z]$ in conjunction with mixture density form the source term. The viscous stress tensor is given by $\tau_{ij} = 2\mu[S_{ij} - \frac{1}{3}S_{kk}\delta_{ij}]$ where, S_{ij} is the strain rate and $\mu = \sum_k \alpha_k\mu_k$ is the mixture viscosity. The capillary term involves the gas volume fraction gradient vector defined as: $\vec{\mathbf{m}} = \overrightarrow{\nabla\alpha_1}$ and σ is the surface tension coefficient. The volume fraction gradient vector is specific to the cell face or boundary where the flux is evaluated. A corresponding normalized volume fraction gradient vector can be considered as: $\vec{\mathbf{n}} = \vec{\mathbf{m}}/|\vec{\mathbf{m}}|$. Based on this, the capillary tensor components are then given as: $\psi_{ij} = \delta_{ij} - n_i n_j$ where, n_k is the $k-$th component of the vector $\vec{\mathbf{n}}$.

Similarly, the flux components in the other two directions can be expressed as:

$$\mathbf{G} = \begin{pmatrix} \alpha_1\rho_1 v \\ \alpha_2\rho_2 v \\ \rho v u \\ \rho v v + P \\ \rho v w \\ \rho H v \end{pmatrix} - \begin{pmatrix} 0 \\ 0 \\ \tau_{yx} \\ \tau_{yy} \\ \tau_{yz} \\ u\tau_{yx} + v\tau_{yy} + w\tau_{yz} \end{pmatrix} - \sigma|\vec{\mathbf{m}}| \begin{pmatrix} 0 \\ 0 \\ \psi_{yx} \\ \psi_{yy} \\ \psi_{yz} \\ u\psi_{yx} + v\psi_{yy} + w\psi_{yz} \end{pmatrix}$$

$$\mathbf{H} = \begin{pmatrix} \alpha_1\rho_1 w \\ \alpha_2\rho_2 w \\ \rho w u \\ \rho w v \\ \rho w w + P \\ \rho H w \end{pmatrix} - \begin{pmatrix} 0 \\ 0 \\ \tau_{zx} \\ \tau_{zy} \\ \tau_{zz} \\ u\tau_{zx} + v\tau_{zy} + w\tau_{zz} \end{pmatrix} - \sigma|\vec{\mathbf{m}}| \begin{pmatrix} 0 \\ 0 \\ \psi_{zx} \\ \psi_{zy} \\ \psi_{zz} \\ u\psi_{zx} + v\psi_{zy} + w\psi_{zz} \end{pmatrix}$$

here, $\vec{\mathbf{m}}$ is the volume fraction gradient vector specific to the cell face or boundary where the flux is evaluated.

It is important to emphasis here that the five-equation interface model is solved directly without invoking LES. And therefore, no closure or filtering terms appear in the ongoing discussion. The conservative part of the five-equation interface model is then updated by:

$$\mathbf{Q}_i^{n+1} = \mathbf{Q}_i^n - \frac{\Delta t}{V_i}\left[\sum_l \mathbf{F}_{i+\frac{l}{2}} \cdot d\mathbf{A}_{i+\frac{l}{2}} + \sum_l \mathbf{G}_{j+\frac{l}{2}} \cdot d\mathbf{A}_{j+\frac{l}{2}} + \sum_l \mathbf{H}_{k+\frac{l}{2}} \cdot d\mathbf{A}_{k+\frac{l}{2}}\right] + \Delta t\ \mathbf{S}_i \tag{90}$$

where, V_i is the $i-$th cell volume, $d\mathbf{A}$ is the cell face area, $\mathbf{S}_i$ is the $i-$th cell source term, and Δt is the time-step. In the summation, the variable l takes on the value of $l = 1$ and $l = -1$ for cell faces on either sides of the cell center. The $predictor - corrector$ approach in Eqn. 46 for the time integration is then applied to the conservative update.

The corresponding Roe numerical flux at the cell boundary is given by the Eqn. 75 recalled here as:

$$\mathbf{F}_{i+\frac{1}{2}} = \frac{1}{2}[\mathbf{F}_L + \mathbf{F}_R] - \frac{1}{2}\sum_{i=1}^{n} |\lambda_i| \varsigma_i \mathbf{r}_i$$

where, n is the total number of eigenvalues of the Roe matrix. The summation term on the right-hand side is evaluated as the Roe dissipation vector $\mathbf{R}$ in Eqn. 77 whose components were also computed (see Eqn. 80). Similar process can be applied to compute the fluxes in the other two directions. It must be noted that the left and right states for the fluxes, excluding the viscous part, is obtained using aforementioned MUSCL approach based on the primitive variable extrapolation. The Roe solution is based on the Euler equations plus the capillary effects. Therefore, the viscous fluxes are added to the summation in Eqn. 90 after the Roe flux is computed.

4.7 Hybrid Switch

The basic premise behind a hybrid scheme is to apply an algorithm that is known ($a-priori$) to be best suited for a region in the flow field. Also, in flows involving moving discontinuities, a dynamic "switching" mechanism is part of the hybrid scheme. It is well-known that upwind schemes perform well in capturing discontinuities in the flow field. However, in addition to high computational cost associated with the resolution of large gradients, they are not suited [213, 58] to resolving unsteady shear regions, e.g., recirculation region behind a moving liquid drop. This is primarily due to relatively large dissipation present in upwind schemes. On the other hand, central schemes work well in smooth flows involving unsteady shear and turbulence activity. But they produce large dispersion errors in the event of a discontinuity. Therefore, a hybrid approach is designed to retain advantages of each scheme in different parts of the flow field and enabling the combined scheme to resolve diverse effects.

Studies have been reported in the past that deal with blending different schemes based on a dynamic evaluation of a blending parameter. In this technique, the flux

considered at the cell boundary takes a weighted average of fluxes from different schemes. Harten and Zwas [71] suggested the blending parameter based on the velocity difference of adjacent cells across a boundary. Other techniques have also been reported that relies on switching schemes from cell to cell based on the local flow conditions. Again, a dynamic switching function is developed to determine which scheme to apply. However, definition of the switching function has varied widely.

In this study, we follow a hybrid scheme developed by Fryxell and Menon [52] to selectively apply the upwind method in the vicinity of the liquid/gas interface. Fryxell and Menon [52] employed a measure of smoothness similar to the one proposed by Löhner in the context of adaptive mesh methods. The main concept is to compare the relative magnitude of the second derivative of a given variable Q to its first derivative in the computational space. The resulting switch is defined by a smoothness parameter S_l:

$$S_l \approx \frac{\partial^2 Q/\partial \xi^2}{\partial Q/\partial \xi} = \frac{|Q_{l+1} - 2Q_l + Q_{l-1}|}{|Q_{l+1} - Q_l| + |Q_l - Q_{l-1}|} \tag{91}$$

where, Q is any flow variable of interest, l is a computational index for any direction ($l = i, j, k$). To prevent switching due to numerical noise, the above parameter was set to zero if either the numerator or the denominator divided by Q_l is less than 0.01. In case the smoothness parameter exceeds some threshold, typically 0.5, the upwind scheme was used in order to compute the fluxes at the cell boundary. Fryxell and Menon [52] applied this technique to bridge the Piecewise Parabolic Method (PPM) and a MacCormack-based central scheme. They applied this technique to Richtmyer-Meshkov instabilities in multi-dimensions and showed that the approach was able to capture growth of small perturbations leading to a noticeable effect on the flow field.

Genin and Menon [58] extended the above concept to LES and later [57] evaluated the smoothness parameter at the cell interface. The resulting smoothness parameter was formulated as:

$$S_{l+1/2} = \frac{|Q_{l+2} - 3Q_{l+1} + 3Q_l - Q_{l-1}|}{|Q_{l+2} - 2Q_{l+1} + Q_l| + |Q_{l+1} - 2Q_l + Q_{l-1}|} \tag{92}$$

where, l is a computational index for any direction. The formulation at the cell boundary helps in reducing the extent of the switching region as the evaluation of the smoothness parameter is at the same location as the solution of the Riemann problem. Both the above formulations employed pressure and density as the variables for computing the smoothness parameter. The emphasis for using the pressure is to capture compression wave discontinuity, whereas, the density can be used to detect a contact discontinuity. The switch is then constructed taking into account the maximum of the two values. These aspects are retained in the current study.

In addition to the compressive and convective effects, the present flow configuration also involves a material interface. In light of Abgrall's condition [1] of pressure and velocity uniformity across the material interface, a smoothness parameter based on the pressure will not yield an upwind flux in the interface vicinity. However, there is a density change across the interface and a switch based on density is expected to provide a dynamic switching. In addition, for cases involving low density ratios and excessively diffused interface zones, the density-based smoothness parameter does not guarantee upwind flux implementation.

Alternatively, information regarding the material interface itself in form of phasic volume fraction can be used. Two scenarios are possible. In the first scenario, the volume fraction can be used directly to evaluate the smoothness parameter. In the other case, the interface curvature (or alternatively volume fraction gradient) is observed to be non-zero in the interface region and can be exclusively used to set the upwind flux. Both these scenarios have been observed to produce similar results. Therefore, volume fraction gradient in combination with the pressure and density, a switching logic is developed. The logic has the same framework as above with noise cancellation limited by 0.02 cutoff and threshold of 0.5 for the smoothness parameter based on density and pressure. In addition, the a non-zero curvature exclusively invokes the

upwind flux computation.

In multi-dimensions, the implementation of the switching logic takes the maximum value of the smoothness parameter for each coordinate direction. For example, if the an upwind flux on the i-th face is used, then the same upwind scheme is applied on the other two flux directions of the cell. The conserved quantities are updated by inserting the appropriate fluxes into the MacCormack time integration seen in equations (46) and (47). For cell faces which use the upwind scheme, the same flux is used for both the *predictor* and *corrector* steps.

4.8 Boundary Conditions

The purpose of boundary conditions is to provide information on flow variables at the domain boundaries and such a specification is essential in the solution of partial differential equations such as the Navier-Stokes equations. These boundary conditions for fluid dynamic applications can be categorized as no-slip or wall, adiabatic, isothermal, periodic, inflow, and outflow conditions.

In a subsonic field, due to the elliptic nature of the flow, both inward and outward propagating waves in relation to the computational domain are experienced. The outward propagating waves have their behavior defined by the solution interior to the boundary. Whereas, the inward propagating waves depend on flow conditions exterior to the computational domain and therefore, require boundary conditions to completely specify their behavior. Hence, for both inflow and outflow boundaries, a reduced set of governing equations, recast into characteristic form normal to the boundary are solved simultaneously with the interior domain solution procedure.

4.8.1 Characteristic Boundary Conditions

The derivation of the boundary conditions in this study follows the work of Poinsot and Lele [154]. In this section, a general set of equations is derived for a viscous, three-dimensional LES equations including the subgrid kinetic energy. The method

is then applied to inflow and outflow boundary condition in the next section.

In the case of five-equation model, the derived inflow and outflow boundary conditions can be used by disregarding the filtered aspect of variables appearing in the expressions. The primary limitation of the current boundary condition formulation when applied to the case of interface problems is that either pure liquid or gas can be considered moving through the boundary. No such limitation applies to point-volume approach used for the dispersed phase in conjunction with LES.

The technique used in the derivation of the boundary conditions is based on the characteristic analysis of the different waves crossing a domain boundary. This approach is valid in any hyperbolic system of equations. Using this analysis [154], to modify the hyperbolic terms, the governing LES equations can be recast into the system of following equations:

$$
\begin{aligned}
&\frac{\partial \bar{\rho}}{\partial t} + \tilde{d}_1 + \frac{\partial(\bar{\rho}\tilde{u}_2)}{\partial x_2} + \frac{\partial(\bar{\rho}\tilde{u}_3)}{\partial x_3} = 0 \\
&\frac{\partial(\bar{\rho}\tilde{u}_1)}{\partial t} + \tilde{u}_1\tilde{d}_1 + \bar{\rho}\tilde{d}_3 + \frac{\partial \bar{\rho}\tilde{u}_1\tilde{u}_2}{\partial x_2} + \frac{\partial \bar{\rho}\tilde{u}_1\tilde{u}_3}{\partial x_3} = \frac{\partial \overline{\tau_{1j}}}{\partial x_j} \\
&\frac{\partial(\bar{\rho}\tilde{u}_2)}{\partial t} + \tilde{u}_2\tilde{d}_1 + \bar{\rho}\tilde{d}_4 + \frac{\partial \bar{\rho}\tilde{u}_2\tilde{u}_2}{\partial x_2} + \frac{\partial \bar{\rho}\tilde{u}_3\tilde{u}_2}{\partial x_3} + \frac{\partial \bar{p}}{\partial x_2} = \frac{\partial \overline{\tau_{2j}}}{\partial x_j} \\
&\frac{\partial(\bar{\rho}\tilde{u}_3)}{\partial t} + \tilde{u}_3\tilde{d}_1 + \bar{\rho}\tilde{d}_5 + \frac{\partial \bar{\rho}\tilde{u}_2\tilde{u}_3}{\partial x_2} + \frac{\partial \bar{\rho}\tilde{u}_3\tilde{u}_3}{\partial x_3} + \frac{\partial \bar{p}}{\partial x_3} = \frac{\partial \overline{\tau_{3j}}}{\partial x_j} \\
&\frac{\partial(\bar{\rho}\tilde{E})}{\partial t} + \bar{\rho}\tilde{u}_1\tilde{d}_3 + \bar{\rho}\tilde{u}_2\tilde{d}_4 + \bar{\rho}\tilde{u}_3\tilde{d}_5 + \frac{1}{2}(\tilde{u}_{11}^2 + \tilde{u}_{22}^2 + \tilde{u}_{33}^2)\tilde{d}_1 + \frac{\tilde{d}_2}{\gamma - 1} \\
&\qquad + \frac{\partial}{\partial x_2}(\bar{\rho}\tilde{E} + \bar{p})\tilde{u}_2 + \frac{\partial}{\partial x_3}(\bar{\rho}\tilde{E} + \bar{p})\tilde{u}_3 + \left[(\tilde{e} - \frac{a^2}{\gamma(\gamma-1)})\tilde{d}_1\right] \\
&\qquad + \sum_{m=1}^{N_s} \bar{\rho}\tilde{d}_{6+m}\left[\tilde{e}_m - \frac{\tilde{R}_u\tilde{T}}{W_m(\gamma-1)}\right] = -\frac{\partial \overline{q}_j}{\partial x_j} + \frac{\partial \tilde{u}_j\overline{\tau_{ij}}}{\partial x_j} \\
&\frac{\partial \bar{\rho}k^{sgs}}{\partial t} + k^{sgs}\tilde{d}_1 + \bar{\rho}\tilde{d}_6 + \frac{\partial \bar{\rho}\tilde{u}_2k^{sgs}}{\partial x_2} + \frac{\partial \bar{\rho}\tilde{u}_3k^{sgs}}{\partial x_3} = \frac{\partial}{\partial x_j}\left(\rho\nu_t\frac{\partial k^{sgs}}{\partial x_j}\right) + P^{sgs} - D^{sgs} \\
&\frac{\partial \bar{\rho}\tilde{Y}_m}{\partial t} + \tilde{Y}_m\tilde{d}_1 + \bar{\rho}\tilde{d}_{6+m} + \frac{\partial \bar{\rho}\tilde{u}_2\tilde{Y}_m}{\partial x_2} + \frac{\partial \bar{\rho}\tilde{u}_3\tilde{Y}_m}{\partial x_3} = \frac{\partial}{\partial x_j}\left(\bar{\rho}\tilde{D}_m\frac{\partial \tilde{Y}_m}{\partial x_j}\right) + \tilde{\dot{w}}_m; \quad m = 1, N_s
\end{aligned}
\tag{93}
$$

The above formulation assumes that the boundary conditions are derived for boundaries located in the $x_2 - x_3$ plane such that the derivatives in the x_1 direction (denoted as $\tilde{d}_i$) are unknown and need to be modelled. The $\tilde{d}_i$'s in the above equations are

functions of the characteristic wave amplitudes, $\mathscr{L}_i$:

$$\tilde{\mathbf{d}} = \begin{pmatrix} \frac{1}{c^2}\left[\mathscr{L}_2 + \frac{1}{2}\left(\mathscr{L}_5 + \mathscr{L}_1\right)\right] \\ \frac{1}{2}\left(\mathscr{L}_5 + \mathscr{L}_1\right) \\ \frac{1}{2\overline{\rho}\overline{c}}\left(\mathscr{L}_5 - \mathscr{L}_1\right) \\ \mathscr{L}_3 \\ \mathscr{L}_4 \\ \mathscr{L}_6 \\ \mathscr{L}_{6+m} \end{pmatrix} ; \mathscr{L} = \begin{pmatrix} \lambda_1(\frac{\partial \overline{p}}{\partial x_1} - \overline{\rho}\overline{c}\frac{\partial \tilde{u_1}}{\partial x_1}) \\ \lambda_2(\overline{c}^2\,\frac{\partial \overline{\rho}}{\partial x_1} - \frac{\partial \overline{p}}{\partial x_1}) \\ \lambda_3(\frac{\partial \tilde{u_2}}{\partial x_1}) \\ \lambda_4(\frac{\partial \tilde{u_3}}{\partial x_1}) \\ \lambda_5(\frac{\partial \overline{p}}{\partial x_1} + \overline{\rho}\overline{c}\frac{\partial \tilde{u_1}}{\partial x_1}) \\ \lambda_6(\frac{\partial k^{sgs}}{\partial x_1}) \\ \lambda_{6+m}(\frac{\partial \widetilde{Y_m}}{\partial x_1}) \end{pmatrix} ; \lambda = \begin{pmatrix} \tilde{u_1} - \overline{c} \\ \tilde{u_1} \\ \tilde{u_1} \\ \tilde{u_1} \\ \tilde{u_1} + \overline{c} \\ \tilde{u_1} \\ \tilde{u_1} \end{pmatrix}$$

where, $\bar{c}$ is the speed of sound defined as: $\sqrt{\gamma \widetilde{R}\widetilde{T}}$. Also, λ_1 and λ_5 are the velocity of the sound waves in the positive and negative x_1-direction; λ_2 is the convection velocity (the speed of the entropy wave), λ_3, λ_4, λ_6 and λ_{6+m} are the velocity at which $\widetilde{u_2}$, $\widetilde{u_3}$, k^{sgs} and $\widetilde{Y_m}$ are advected in the x_1-direction, respectively.

The analysis of Poinsot and Lele [154] provides Local One-Dimensional Inviscid ($LODI$) relations. This approach is used to infer values of the wave amplitude variations in the viscous, three-dimensional LES equations. The $LODI$ relations are given by:

$$\begin{aligned} \frac{\partial \overline{p}}{\partial t} + \frac{1}{c^2}\Big[\mathscr{L}_2 + \frac{1}{2}\big(\mathscr{L}_5 + \mathscr{L}_1\big)\Big] &= 0 \\ \frac{\partial \overline{p}}{\partial t} + \frac{1}{2}\big(\mathscr{L}_5 + \mathscr{L}_1\big) &= 0 \\ \frac{\partial \widetilde{u_1}}{\partial t} + \frac{1}{2\overline{\rho}\overline{c}}\big(\mathscr{L}_5 - \mathscr{L}_1\big) &= 0 \\ \frac{\partial \widetilde{u_2}}{\partial t} + \mathscr{L}_3 &= 0 \\ \frac{\partial \widetilde{u_3}}{\partial t} + \mathscr{L}_4 &= 0 \end{aligned} \tag{94}$$

Based on the above set of characteristic wave equations and their amplitudes, different boundary conditions can be computed and this is discussed next.

4.8.2 Subsonic Inflow BC

In our LES study, u_1, u_2 and u_3 as well as the temperature T are imposed at the inflow boundary. This case is typical of LES of turbulent reacting flows, where we wish to control the inlet shear and introduce flow perturbations. For a subsonic,

three dimensional, N_s-species reacting flow, five+N_s characteristic waves enter the domain; namely $\mathscr{L}_2$, $\mathscr{L}_3$, $\mathscr{L}_4$, $\mathscr{L}_5$, $\mathscr{L}_6$ and $\mathscr{L}_{6+N_s}$. $\mathscr{L}_1$ exit the domain at λ_1=$u_1 - c$. The density ρ (and as a result pressure p) has to be determined from the local flow conditions.

The amplitude of $\mathscr{L}_1$ is found from the interior of the domain, whereas, the amplitude of the entering waves should be specified. By imposing the velocities (u_1, u_2, u_3, and temperature T), momentum and energy equations are eliminated, and only the continuity equation remains. In the continuity equation, $\tilde{d_1}$, is found based on $\mathscr{L}_5$ and $\mathscr{L}_2$. These are then are found in terms of $\mathscr{L}_1$ (or leaving wave amplitude) as:

$$\mathscr{L}_5 = \mathscr{L}_1 - \frac{1}{2}\overline{\rho c}\frac{\partial \widetilde{u_1}}{\partial t} \tag{95}$$

$$\mathscr{L}_2 = \frac{1}{2}\big(\gamma - 1\big)\big(\mathscr{L}_5 + \mathscr{L}_1\big) + \frac{\overline{\rho} c^2}{\widetilde{T}}\frac{\partial \widetilde{T}}{\partial t} \tag{96}$$

where,

$$\frac{\partial \widetilde{u_1}}{\partial t} = \frac{\widetilde{u_1}(t+\Delta t) - \widetilde{u_1}(t)}{\Delta t}; \qquad \frac{\partial \widetilde{T}}{\partial t} = \frac{\widetilde{T}(t+\Delta t) - \widetilde{T}(t)}{\Delta t} \tag{97}$$

Finally, $\tilde{d_1}$ is computed as:

$$d_1 = \frac{1}{c^2}\Big[\mathscr{L}_2 + \frac{1}{2}\big(\mathscr{L}_1 + \mathscr{L}_5\big)\Big] \tag{98}$$

and the density is updated as:

$$d\overline{\rho} = -d_1 * \Delta t \tag{99}$$

In this case, $\mathscr{L}_3$ and $\mathscr{L}_4$ are not needed.

4.8.3 Subsonic Outflow BC

In case of a subsonic outflow, using perfectly non-reflecting (no incoming waves into the domain) boundary condition might lead to an "ill-posedeness" of the problem as is shown by Rudy [174] and Poinsot and Lele [154]. For the problem to remain well-posed, the pressure at far-field, p_∞, must be added to the boundary condition. This is done by linking the incoming wave amplitude to the pressure difference $p - p_\infty$. This

correction to the non-reflecting boundary treatment makes it partially reflecting [154] and thus controls the mean pressure in the flow domain.

All the characteristic wave amplitudes, except for $\mathscr{L}_1$, are known since they are leaving the domain. The only unknown is $\mathscr{L}_1$ is found from the pressure at far-field as:

$$\mathscr{L}_1 = \psi[1 - \mathscr{M}^2]\ \bar{c}\ \frac{p - p_\infty}{L} \tag{100}$$

where, $\mathscr{M}$ is the maximum Mach number in the domain and L is the characteristic length of the domain, $\bar{c}$ is the speed of sound and ψ is the reflection coefficient which sets the amplitude of the reflected waves and is chosen [178] to be 0.15 for this study. This completes the outflow boundary condition treatment for subsonic flows.

CHAPTER V

TWO-PHASE MODEL VALIDATIONS

The two-phase flow model capabilities are illustrated in this chapter for various physical problems involving (i) surface-tension, (ii) viscous effects, and (iii) gravity. Numerical tests are carried out to validate the method for capillary, dissipative, buoyancy effects and their combination. Several test problems in multi-dimensions (2D/3D) are examined: (1) Laplace pressure differential or static drop in equilibrium, (2) Deformed drop oscillations, (3) Bubble rise in a liquid bulk, (4) Drop creation under gravity effects, and (5) Drag force over an isolated droplet. For these tests, computed results are compared to analytical/experimental data. Finally, we illustrate the ability of the method for complex problems involving coupled effects. In particular, two cases of colliding drops are presented.

The choice of cases as well as their conditions were primarily based on past studies. Specifically, cases of static drop in equilibrium and deformed drop oscillations represent standard validation test cases for interface formulations typically reported in the literature. Also, the choice of similar parameters enable us to directly compare current results. Moreover, test cases of bubble rise and gravity-induced drop creation involve complex interface dynamics and are compared directly with similar past efforts. The liquid drop drag as well as binary drop collision cases are studied at realistic dimensions and parameters to illustrate the algorithm capability to study physical processes driving the interface motion. Overall, in all test cases the relevant dimensionless parameters selected are within the range of interest and applicability.

5.1 Static Drop in Equilibrium

A standard test case for validating two-fluid interface formulations is to consider a static liquid drop in equilibrium and evaluate the pressure jump across the curved interface. It is a well-known fact [16] that surface-tension causes a static liquid drop to become and remain spherical. In absence of external forces and initial velocities, the exact pressure jump across the interface was quantified by the Laplace-Young law and is given by [56]:

$$\Delta P = \sigma(\kappa_1 + \kappa_2) \tag{101}$$

where, ΔP is the theoretical pressure jump, σ is the surface- tension coefficient, and κ_1 and κ_2 are the main local interface curvatures. In two-dimensions (2D), the pressure jump simplifies to $\sigma\kappa$. The exact curvature is given by $\kappa = 1/R$, where R is the initial drop radius.

In the 2D test case, we consider a liquid cylinder in a 1mx1m square domain with an initial radius of $R = 0.15$m and centered at (0.5, 0.5)m location. All sides of the domain are considered as periodic boundaries. The liquid cylinder is filled with fluid, whose thermodynamic parameters are $\gamma_l = 2.4$ and $P_{\infty,l} = 10^7$ Pa, and is surrounded by air, with $\gamma_g = 1.4$ and $P_{\infty,g} = 0$ Pa. The flow is initially quiescent at atmospheric pressure. The density (ρ_l/ρ_g) and viscosity (μ_l/μ_g) ratio considered are 100 and 1.0, respectively, and the surface-tension coefficient is 200 N/m with resulting Laplace number ($La = 2R\sigma\rho/\mu^2$) of 6000. Under these conditions, the exact pressure jump based on the Laplace-Young law is: $\Delta P = 1333.34$ Pa. From a numerical standpoint, the pressure inside and outside the drop are built on basis of an averaging procedure depending on a limit value for the liquid volume fraction (α_l). The average pressure inside the drop is defined as:

$$\overline{P_l} = \frac{1}{N_{cells}} \sum_{i,j=1}^{N_{cells}} p_{i,j}$$

where, $p_{i,j}$ is the time-averaged pressure obtained from the simulation and the sum

Grid	$2R/\Delta x$	ΔP_{NUM}, Pa	L_2	TPS (s)
64×64	19.2	1326.3	8.956×10^{-2}	0.023
128×128	38.4	1350.7	4.702×10^{-2}	0.099
256×256	76.8	1334.9	2.566×10^{-2}	0.471

Table 2: L_2 error norms, computed pressure jump, and computational time-per-step (TPS) as a function of three grid sizes for Laplace 2D test case. Here, ρ_l/ρ_g=100 and La=6000.

is over the N_{cells} lying within the drop that have $\alpha_l > 0.9$. Similarly, for the pressure outside the drop. The difference between the pressures inside and outside the drop gives us the computational pressure jump: $\Delta P_{NUM} = \overline{P_l} - \overline{P_g}$ across the drop interface. The resulting value is then compared with the theoretical pressure jump. Another measure of the relative error is given by the mean square root error (L_2 error norm),

$$L_2 = \sqrt{\frac{1}{P_{TH}^2 N_{cells}} \sum_{i,j=1}^{N_{cells}} (p_{i,j} - P_{TH})^2}$$

where, $P_{TH}(= \Delta P + P_{ATM})$ is the analytical pressure inside the drop and the sum is over the N_{cells} lying within the drop that have $\alpha_l > 0.9$. The variation of L_2 for different grid sizes give a measure for the numerical convergence and accuracy.

The computations have been performed for three grids sizes ranging from very coarse (64x64) to fine (256x256). The computational mesh is uniform with Δx=Δy=$1/N$, where N is total number of cells in one direction. The results are time-averaged for approximately 15 capillary time-scales ($\tau_{CAP} = 2R\mu_l/\sigma$) and are shown in Table 2 as a function of grid sizes for the 2D test case. Alternatively, the results can be considered as a function of mesh spacing ($2R/\Delta x$) indicating the number of cells resolving the drop. Average pressure jump across the interface is well captured and is within 2% of the analytical value. L_2 error norms are observed to decrease with increase in grid resolution indicating a mesh convergent algorithm. Also, to ascertain computational cost of each mesh size, average time-per-step (TPS) is tabuled indicating a four-fold increase in computational cost with four-fold increase in overall grid size.

In this case, same number of processors were used for all three cases. The solver is observed to scale linearly (≈ 0.85, 1.0 being perfect scaleup) with increase in overall mesh size.

In the 3D test case, we similarly consider a liquid sphere in a 1m cube domain with an initial radius of $R = 0.15$ m and centered at (0.5, 0.5, 0.5) m location. The liquid and gas thermodynamic parameters and boundary conditions are the same as in the 2D test case. The flow is initially quiescent at atmospheric pressure. Under these conditions, the exact pressure jump based on the Laplace-Young law is: $\Delta P = 2666.67$ Pa. Recall that in 3D the effective curvature is the sum of curvatures in two orthogonal directions along the interface. Therefore, the pressure jump is twice that of 2D case.

The computations have been performed for similar grids sizes as seen in 2D cases. The results are time-averaged for approximately $15\tau_{CAP}$ and are presented in Table 3 as a function of grid sizes. Average pressure jump across the interface is observed to be well-captured and is within 3% of the analytical value. Reduction of L_2 error norm with increase in grid resolution is also observed with similar mesh convergence characteristics. Comparison between the 2D and 3D cases, for identical mesh resolution, shows similar magnitude of L_2 error norms. However, in general, the 3D case has slightly higher value probably due to larger (two-times) pressure jump for the same overall resolution. An estimate of computational cost is also tabulated in form of average time-per-step for each mesh resolution. Cost increases linearly (≈ 0.8) with increase in 3D resolution. Also, 3D computations may seem costly at first glance, for example, TPS=1.44 for 64^3 versus TPS=0.023 for 64^2. However, such sixty-fold increase in cost is a result of 64 times increase in mesh resolution. Overall, the solver is able to scale well with mesh resolution.

Figure 9 illustrates the pressure field and its dependence on the mesh size for 2D test case. Pressure is constant both within and outside the drop with monotonic rise along the interface. Increase in mesh resolution makes this variation confined

Grid	$2R/\Delta x$	ΔP_{NUM}, Pa	L_2	TPS (s)
64×64×64	19.2	2582.4	1.021×10^{-1}	1.44
128×128×128	38.4	2620.8	6.528×10^{-2}	10.62
256×256×256	76.8	2641.3	3.697×10^{-2}	92.5

Table 3: L_2 Error Norms, computed pressure jump, and computational time-per-step (TPS) as a function of three grid sizes for Laplace 3D test case. Here, ρ_l/ρ_g=100 and La=6000.

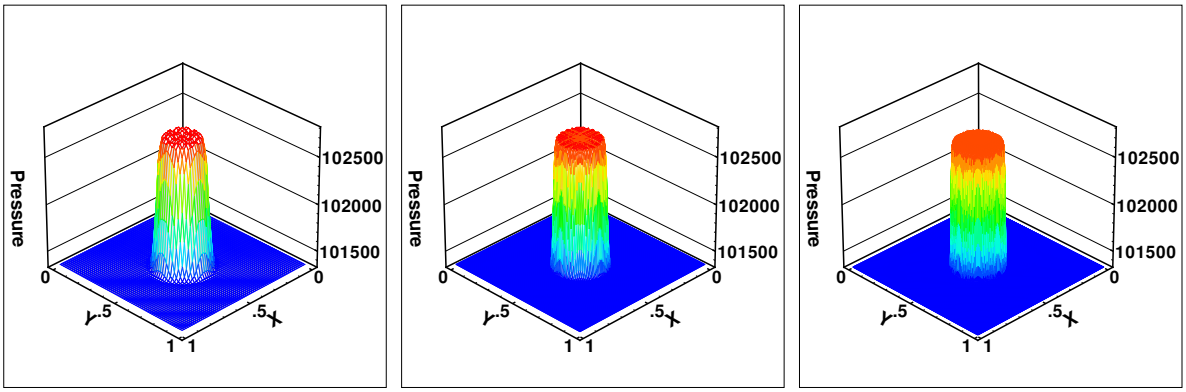

(a) 64x64 (b) 128x128 (c) 256x256

Figure 9: Pressure field corresponding to three different mesh sizes.

to a small spatial region, and therefore, it appears as a sharp discontinuity (see Fig. 9c). Rise in pressure inside the drop due to surface-tension and curvature effects is expected in accordance to the Laplace-Young law. Overall, both qualitative and quantitative aspects of the Laplace-Young law are reproduced by the approach.

5.1.0.1 Spurious velocity currents

A major difficulty [187] with current methods of interface calculation is the existence of the so-called spurious or parasite currents. These un-physical currents are vortices appearing in the vicinity of the interface when surface-tension forces are dominant. Such currents cause interface distortion and disruptive instabilities at the interface. This often results in computational failure. Several studies [104, 51, 211] are reported on this aspect, however a consensus for its origin is still debated. Lafaurie *et al.* [104]

and others [51] have suggested that a small amplitude but non-vanishing velocity field appears due to unbalance between surface-tension force and the associated pressure gradient in the interfacial region. However, Jacqmin [85] argues that these currents are due to non-conservation of energy (in the context of incompressible formulation) by the CSF method. Recent studies [51, 211] report on ways to reduce the spurious currents and improve the modeling of surface-tension effect. Two key areas in this context are identified: (i) accuracy of curvature estimation, and (ii) implementation of the surface-tension force. More details are reported elsewhere [211].

Aware of these drawbacks, we have performed a preliminary study of the possible appearance of such currents in our method. Tests are performed for a 2D circular drop in static equilibrium (seen before). In this problem, the net surface force should be zero as at each interface location the surface-tension force is counteracted by an equal and opposite force at a diametrically opposed point. The correct solution is a zero velocity field. A computational domain is a 1mx1m square box with a liquid drop of radius $R = 0.15$ centered at (0.5, 0.5)m location. All sides of the domain are considered as periodic boundaries. The flow is initially quiescent at uniform atmospheric pressure. The density (ρ_l/ρ_g) and viscosity (μ_l/μ_g) ratio considered are 100 and 1.0, respectively. The gravity is neglected; the surface-tension coefficient (σ) will be varied, thus yielding different values of the Laplace number (La). A 64×64 mesh is selected which gives approximately 20 cell resolution for the drop. The computations are performed for $100\tau_{CAP}$ and both the velocity field as well as quantitative variation is reported.

The surface-tension coefficient is varied from 0.2 to 2,000 N/m giving corresponding Laplace number in the range of 6 to 60,000. Surface-tension forces dominate at large La. Figure 10 shows close-up of velocity profiles for the case of $La = 60,000$ at four time-instants. A line contour indicating the position of the drop in form of liquid volume fraction is also shown. Presence of spurious currents in form of small vortices

La	6.0	6×10^{1}	6×10^{2}	6×10^{3}	6×10^{4}
Ca	4.8×10^{-4}	5.2×10^{-4}	5.0×10^{-4}	4.9×10^{-4}	5.1×10^{-4}

Table 4: Capillary number (Ca) variation as a function of the Laplace number (La) for ρ_l/ρ_g=100 and mesh size of 64×64.

is observed on the periphery of the line contours. The currents are observed for a generic (other than parallel or at 45^o) orientation of the interface with respect to the grid directions as seen in Fig. 10a. These isolated velocity vectors unphysically drive the flow in their vicinity generating the resulting field. Similar observations were reported by other studies [104, 51, 211]. The magnitude of the velocity is observed to decrease with time as the static equilibrium is approached. Also, despite the presence of spurious velocity in the interfacial region, the shape of the drop remains circular at all times.

In the work of Lafaurie *et al.* [104], it was conjectured that the magnitude (U_s) of the spurious currents must be proportional to σ/μ. This is equivalent to having an approximately constant value of the Capillary number $Ca = U_s\mu/\sigma$. Table 4 shows the variation of Ca as a function of La. The results are presented after 100 time-steps (corresponding time to Fig. 10a) and show a constant value for Ca over a broad range of Laplace numbers. After equilibrium is reached (corresponding to Fig. 10d), a decrease of approximately one-sixth in Ca is observed for all La cases. Also, to ascertain the accuracy of this method, we compare the magnitude of these currents with those reported in the literature: VOF method of Lafaurie *et al.* [104] reported $Ca \approx 10^{-2}$; the marker method of Tryggvason *et al.* [215] yields $Ca \approx 10^{-4}$; and the FELSOS (Finite-element/level-set/operator-splitting) approach of Smolianski [196] reported $Ca \approx 9.0 \times 10^{-3}$. All considered similar grid resolution of approximately 30-40 cells resolving the drop diameter. In this regard, our approach yields Capillary numbers of comparable magnitude to those reported by Tryggvason *et al.* [215].

To summarize the results presented for the static drop in equilibrium, the approach

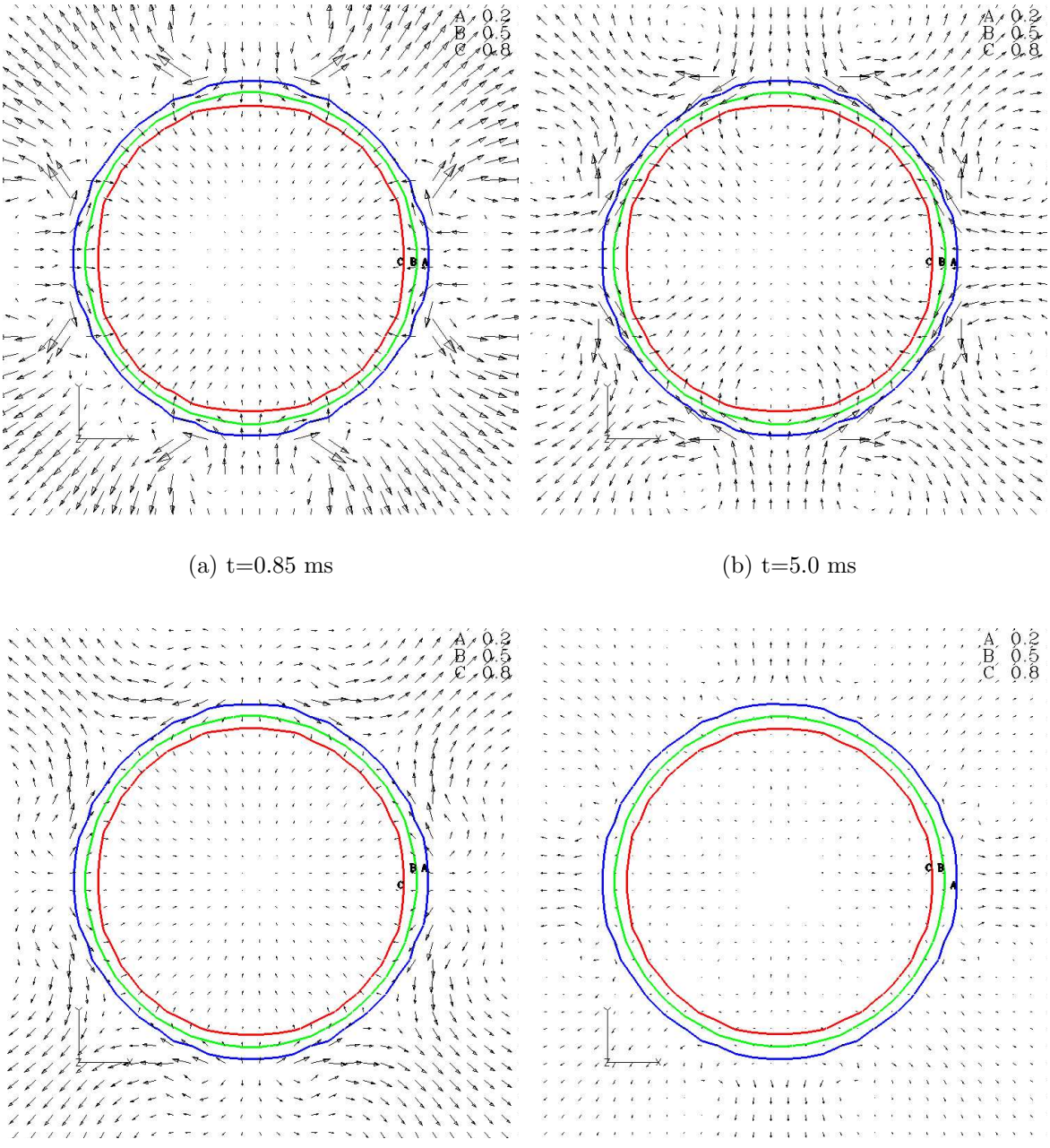

(a) t=0.85 ms

(b) t=5.0 ms

(c) t=19.0 ms

(d) t=51.0 ms

Figure 10: Spurious velocity field for a stationary drop at various times for La=60,000 and ρ_l/ρ_g=100. A close-up view is chosen to clarify visualization of the velocity field.

demonstrates that it is able to recover pressure rise within the drop as required by the Laplace-Young law for both 2D and 3D field. The grid variation study show a mesh convergent method. The magnitude of spurious currents is also quantified indicating similar order of accuracy as reported by other studies. A constancy in the Capillary number as a function of Laplace numbers is also verified. It is also demonstrated that the presence of spurious currents does not materially alter the flow field to invalidate the results. Computational cost (in terms of time) is also reported for a range of grid sizes in both 2D and 3D configurations. The solver is demonstrated to scale linearly (≈ 0.8, 1.0 being perfect scaling) with mesh resolution. The timing study for processor scaling will be presented later in this chapter.

5.2 Oscillations of Ellipsoidal Drop

An initially non-circular (in 2D, non-spherical in 3D) drop with subsequent oscillations represent another standard and demanding test for interface models. Such oscillations are result of the surface-tension forces on the deformed interface and its amplitude decays with time to achieve an equilibrium static shape. Rayleigh's linear theory for small amplitude oscillations gives the frequency, ω_n, for the oscillation as [105]:

$$\omega_n^2 = (n^3 - n)\frac{\sigma}{\rho_l R_o^3}$$

where, ρ_l is the liquid density, σ is the surface-tension coefficient, R_o is the unperturbed radius, and n prescribes the mode of oscillation. Fyfe *et al.* [56] extended Rayleigh's theory to include the presence of an external fluid. The resulting oscillation frequency is now given as:

$$\omega_{n,2D}^2 = (n^3 - n)\frac{\sigma}{(\rho_l + \rho_g)R_o^3}$$

where, ρ_g is the density of the external fluid. The time period (τ_{OSC}) of oscillations is then related to the frequency as: $\tau_{OSC,2D} = 2\pi/\omega_{n,2D}$. In case of three dimensions, a slightly different expression for the oscillation frequency is noted [105, 38]:

$$\omega_{n,3D}^2 = n(n-1)(n+2)\frac{\sigma}{(\rho_l+\rho_g)R_o^3}$$

The corresponding oscillation period is: $\tau_{OSC,3D} = 2\pi/\omega_{n,3D}$. This physical period corresponds to two periods of the oscillation (discussed next).

We consider an initially deformed drop whose shape is in form of an ellipse in 2D, and ellipsoid in 3D and is given by the following equation:

$$\frac{(x-0.5)^2}{0.2^2} + \frac{(y-0.5)^2}{0.12^2} = 1 \quad (2D)$$

$$\frac{(x-0.5)^2}{0.2^2} + \frac{(y-0.5)^2}{0.12^2} + \frac{(z-0.5)^2}{0.12^2} = 1 \quad (3D)$$

where, (x, y, z) are local coordinates and the drop is centered in a one-meter long square (in 2D) or cubic (in 3D) domain. An uniform mesh of 128x128 in 2D and 128x128x128 in 3D is used. All sides of the domain are considered as periodic boundaries for both 2D and 3D cases. This mesh size gives a resolution of approximately 20 cells for the drop. Gravitational forces are neglected. The fluid properties are: $\rho_l = 100$ kg/m^3, $\sigma = 342$ N/m, $\gamma_l = 2.4$, $P_{\infty,l} = 10^7$ Pa for the liquid phase and $\rho_g = 1.17$ kg/m^3, $\gamma_g = 1.4$, $P_{\infty,g} = 0$ Pa, and $\mu_g = 19.3 \times 10^{-6}$ Pa-s for the surrounding ideal gas.

Figure 11a shows the time evolution of the average kinetic energy evaluated within the drop for both 2D and 3D cases for different Ohnesorge numbers ($Oh = \mu_l/\sqrt{\rho_l R_o \sigma}$). The average kinetic energy is determined based on aforementioned averaging procedure by considering a limit value for the liquid volume fraction as $\alpha_l > 0.9$. Initially, the deformed interface is at rest having zero kinetic energy. This position is denoted on the plot as location "1". Due to unbalanced surface-tension forces, the interface moves resulting in increase in kinetic energy. The kinetic energy peaks when the drop assumes a circular (in 2D, spherical in 3D) shape as seen by location "2" on the plot. At this moment, all the initial potential energy due to capillarity is converted to kinetic energy. Due to motion the drop cannot remain circular and goes on deforming into an ellipse. There is a corresponding decrease in kinetic energy till it

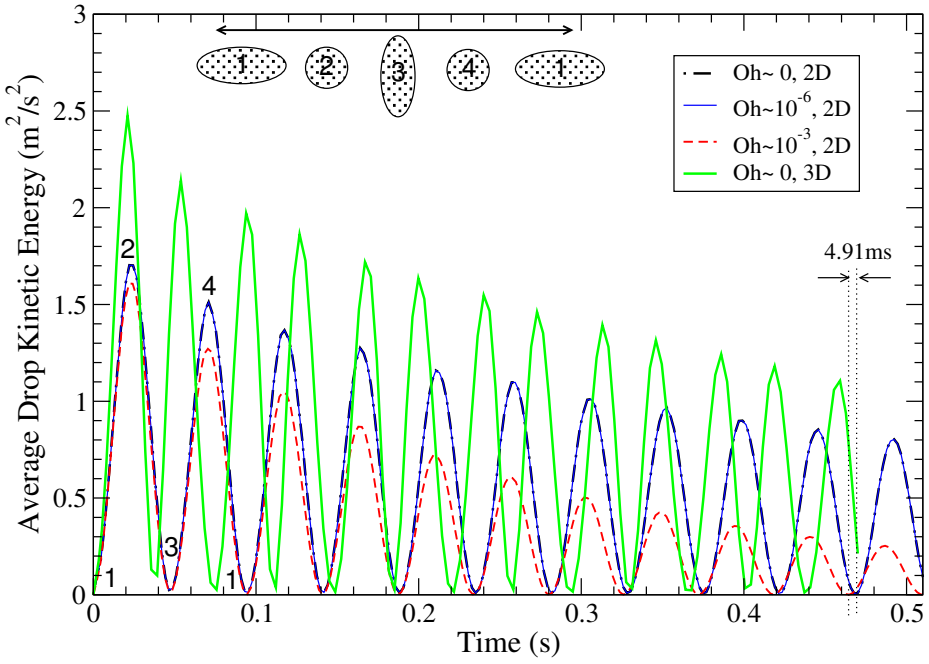

(a) KE vs. Time

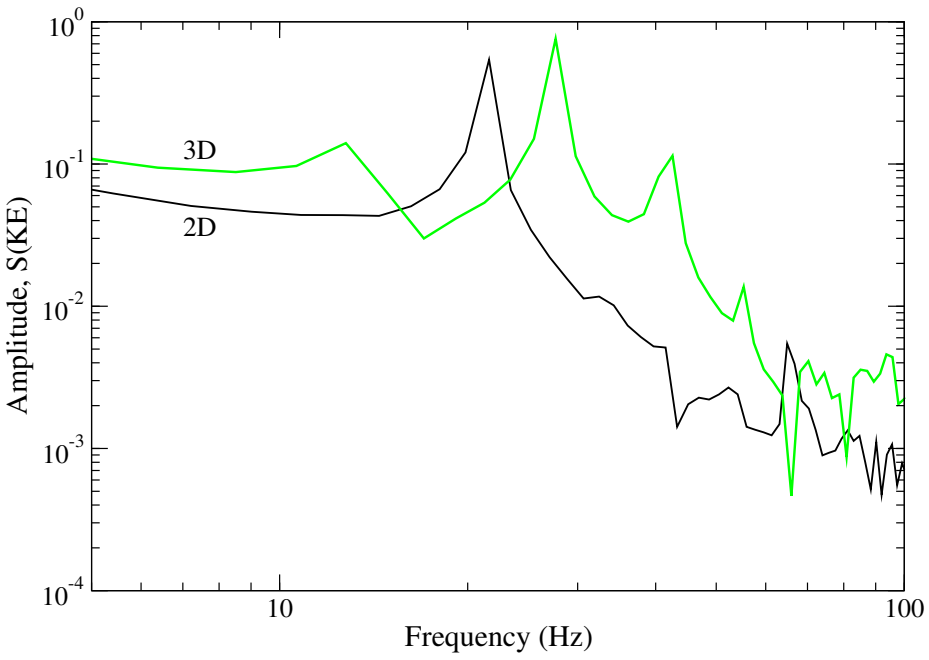

(b) FFT

Figure 11: Kinetic energy versus time for both 2D and 3D oscillating drops. Also, shown in (b) is the frequency content of the signal. In (a), cases for three different Oh are shown for 2D drop and $Oh \approx 10^{-6}$ for the 3D case. Mesh is 128x128 in a 1mx1m square box.

reaches zero denoted by location "3". The velocity is close to zero everywhere but the interface deformation is large. Also, the elliptical shape assume has the major axis is oriented perpendicular to that of initial shape. The resulting unbalance capillary force induces motion to restore the drop back to circular shape (location "4") and the cycle continues. The oscillations are thus due to interchange of energy between capillary induced potential and kinetic parts. Also, for each cycle of oscillation, the peak amplitude in the drop kinetic energy decreases with time due to transfer of mechanical energy to the carrier fluid.

A schematic of the shape evolution is also shown in Fig.11a. The evolution shows a switch in major axis after one oscillation (1-2-3) and then switches again in the next cycle (3-4-1) and thereby returning to a similar orientation. Thus, the overall cycle (1-2-3-4-1) is composed to two periods of kinetic energy evolution. Analytical estimate of the oscillation frequency (ω_n) of an initially deformed drop is available (seen before). In case of 2D ellipse, an equivalent circular shape (based on area) is considered and the resulting radius is used to compute the analytical period. With $R_o = 0.1594$ m and $n = 2$, the analytical period is evaluated to be: $\tau_{2D} = 0.08878$ s. The numerical period is obtained by taking a fourier transform of the signal. This is shown in Fig. 11b. For 2D case, $\tau_{NUM,2D} = 0.09238$ s or equivalently one-half of one-period frequency of kinetic energy evolution of 21.6 Hz. This represents an error of approximately 4% in the oscillation period. Similarly, for the 3D case, the theoretical period is: $\tau_{3D} = 0.06851$ s; and numerical value based on fourier transform: $\tau_{NUM,3D} = 0.07155$ s. An error is approximately 4.4%. An effect of grid resolution does exist on the overall error for both cases and from previous grid studies of static drop equilibrium, the error is expected to decrease considerably with increase in drop resolution. However, such grid-sensitivity study is not reported for this case as the overall error is within a few percent of the analytical estimate for a relatively coarse drop resolution. Overall, both 2D and 3D test cases reasonably predict the interface

dynamics.

Three cases with varying Ohnesorge number for the 2D configuration are presented to show the effect of viscosity on the time evolution of the drop. The time evolution of average drop kinetic energy for these cases were shown in Fig. 11a. The validation of the oscillation period discussed is based on inviscid configuration or equivalently $Oh = 0$. This is consistent with inviscid analytical estimate. A slight increase in viscosity to $Oh \approx 10^{-6}$ shows no material change in the time evolution from the inviscid case. A further increase in viscosity to $Oh \approx 10^{-3}$ shows significant change in the overall kinetic energy evolution. For each cycle, the case with higher liquid viscosity has smaller oscillation amplitude. Also, the rate at which the amplitude decays is higher for $Oh \approx 10^{-3}$ case. Due to build-up of viscous effects over time, $Oh \approx 10^{-3}$ case is observed to be trailing approximately 4.91 ms after five oscillation cycles.

Figure 12 shows the temporal evolution of a 2D deformed drop for one cycle of oscillation in the form of velocity field (shown every other vector) and line contours of liquid volume fraction. From outermost to innermost, line contours represent: 0.2, 0.5, and 0.8 volume fraction values. The initial state for the 2D case is shown in Fig. 12a. Due to previously discussed unbalance in surface-tension force and pressure gradient, isolated spurious currents are observed at the beginning of the simulation (Fig. 12b). They primarily appear on the jagged edges of the interface. Although their presence is unwanted, they do not materially impact the calculation and quickly disappear due to smoothing of jagged edges. This is attributed to both numerical diffusion and viscous dissipation. Also, the velocity field created by the capillary imbalance quickly overshadows the spurious currents.

Four stages of evolution are shown in Figs. 12(c-f) each representing a quarter of oscillation cycle. Starting from an initial state of an ellipse, the drop deforms to a circular shape as seen in Fig. 12c. Velocity field corresponding to peak kinetic energy

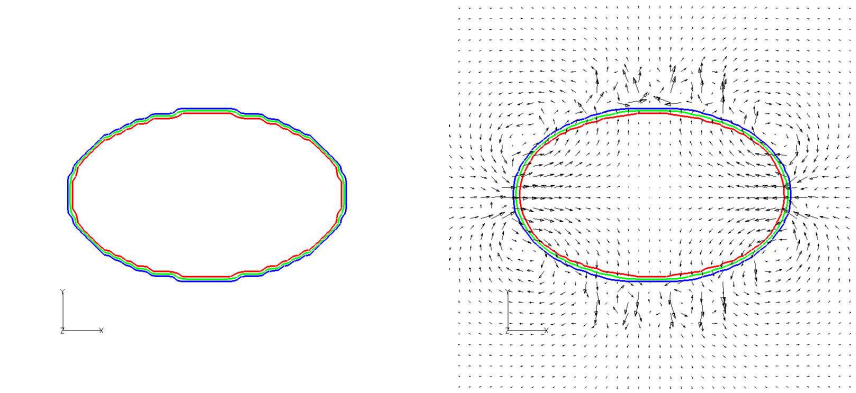

(a) t=0.0 ms

(b) t=4.4 ms

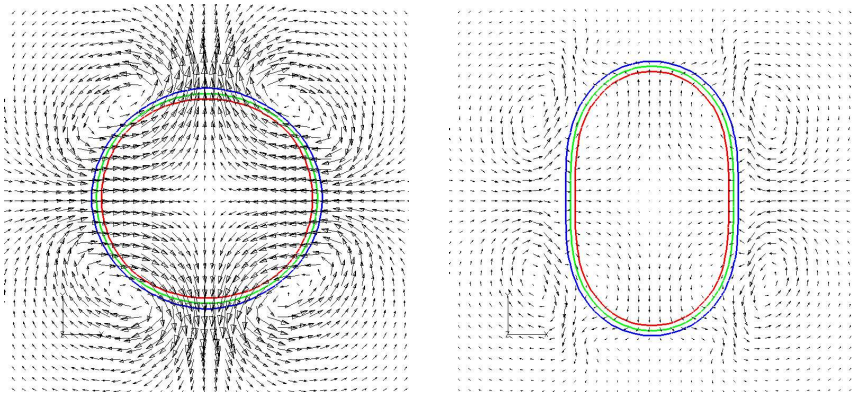

(c) t/τ_{OSC}=0.25

(d) t/τ_{OSC}=0.48

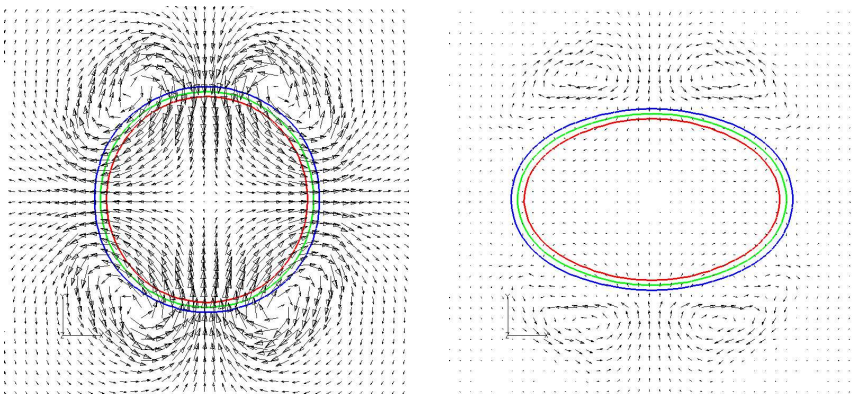

(e) t/τ_{OSC}=0.75

(f) t/τ_{OSC}=1.00

Figure 12: Velocity field (in vectors) and line contours for liquid volume fraction are shown for an oscillating 2D drop at various times. Here, $Oh = 0$, ρ_l/ρ_g=100, and period of oscillation is approximately 92 ms. Mesh size is 128x128 for a 1mx1m square box.

is also shown and is observed to be perfectly symmetric. The next stage is that of an ellipse, however this time with its major axis oriented along the y-direction. The corresponding velocity magnitude is reduced significantly since for this stage most of the energy resides in potential form. The third stage is that of circular drop with perfectly symmetric velocity field. However, for this stage the velocity vectors are observed to be oriented in an opposite direction in relation to the second stage. With further deformation in the drop, elliptical shape is recovered with corresponding negligible kinetic energy.

Pressure distribution within and outside the drop corresponding to the velocity field are shown in Fig. 13. The pressure is shown in form of solid contour and volume fraction in form of three lines contour. Initially, the pressure is the same everywhere. Due to surface-tension effects, capillary pressure inside the drop is established. However, due to dynamically moving interface, the pressure within the drop also adjusts. For circular shape, seen in Figs. 13(c, e), the pressure field is almost constant within the drop. This could be due to similar values of curvature around the drop. However, for elliptical shapes seen in Figs. 13(d, f), the pressure field has variation from high pressure on either lobes and low pressure around the center. In all cases, the pressure field is observed to be smooth and continuous except for the interface region where a monotonous rise is expected.

Flow visualization for the 3D oscillating and deforming ellipsoid is shown in Fig. 14 in the form volume fraction iso-surface (at $\alpha_l = 0.5$) colored by local pressure (in Pa). Velocity field in center horizontal plane ($X - Z$) is also shown. Four stages of energy interchange between potential and kinetic are observed in the form of two spherical and two ellipsoidal shapes. The velocity profiles are similar to those observed in the 2D case. Local pressure is observed to have complex pattern for each stage suggesting multi-mode behavior. A glimpse of this was noted in the Fourier transform of the kinetic energy signal in the form of sub- and super-harmonics about the dominant

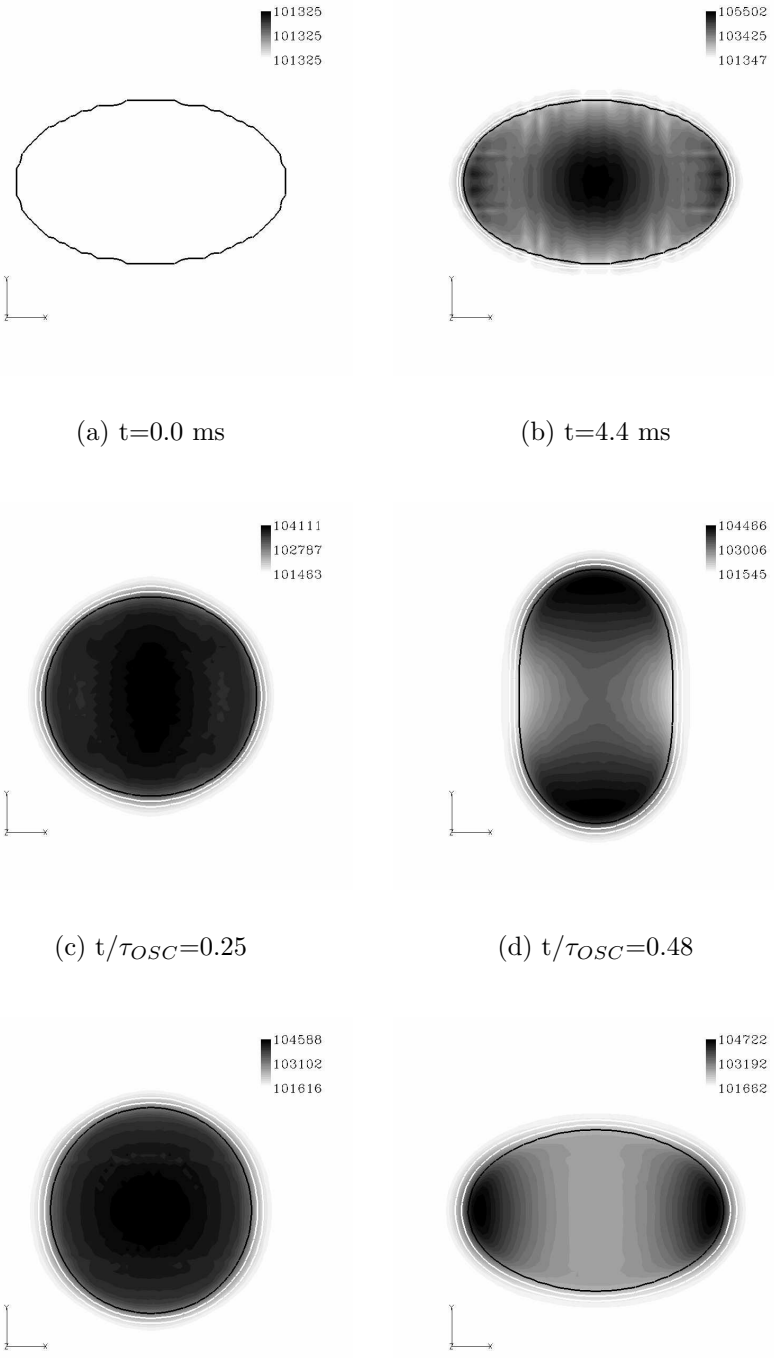

(a) t=0.0 ms

(b) t=4.4 ms

(c) t/τ_{OSC}=0.25

(d) t/τ_{OSC}=0.48

(e) t/τ_{OSC}=0.75

(f) t/τ_{OSC}=1.00

Figure 13: Pressure field (solid contours) and line contours for liquid volume fraction are shown for an oscillating 2D drop at various times. Here, $Oh = 0$, ρ_l/ρ_g=100, and period of oscillation is approximately 92 ms. Mesh size is 128x128 for a 1mx1m square box.

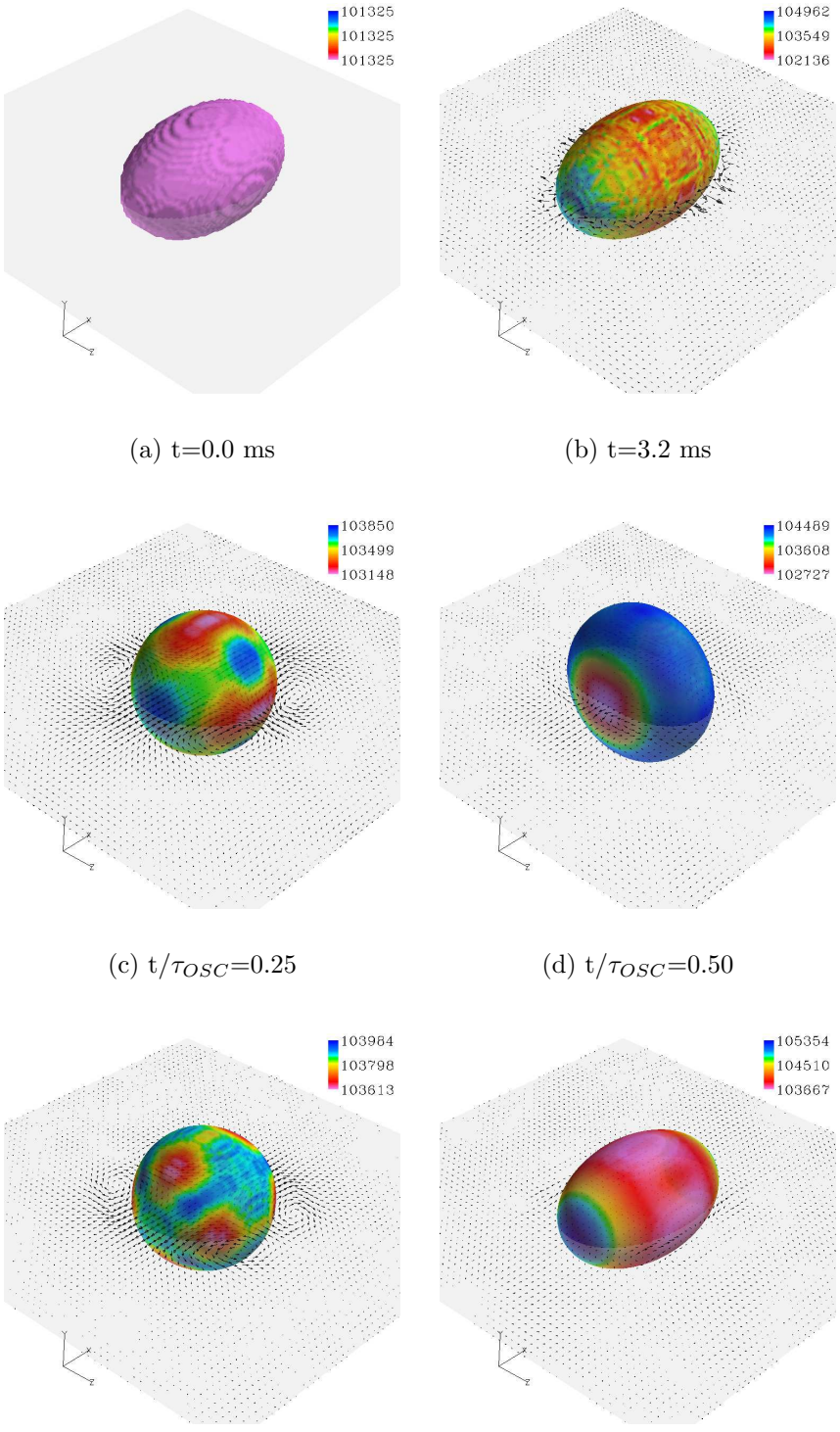

(a) t=0.0 ms (b) t=3.2 ms

(c) t/τ_{OSC}=0.25 (d) t/τ_{OSC}=0.50

(e) t/τ_{OSC}=0.75 (f) t/τ_{OSC}=1.0

Figure 14: An iso-surface for liquid volume fraction $\alpha_l = 0.5$ colored by pressure is shown for a 3D ellipsoid for one oscillation cycle. Also, velocity field is shown in the center horizontal $(X-Z)$ plane. Here, $Oh = 0$, ρ_l/ρ_g=100, and τ_{OSC} is approximately 71.5 ms. Mesh size is 128x128x128 for a one-meter cubic box.

frequency. Also, in contrast to the 2D case, an addition of the third spatial direction in the 3D case allows for interface relaxation in two transverse directions. This effect allows for retaintion of elliptical cross-section in the plane passing through the axis oriented in the direction of initial stretching at each half-cycle of oscillation. However, in the plane normal to direction of initial stretching, the cross-section shapes remain circular but do increase/decrease in radius due to oscillations.

To summarize the results presented for the oscillating drop, the approach is capable of reproducing dynamic as well as static behaviors related to the interface movement. Both 2D and 3D test cases for an initially deformed drop reasonably predict the oscillation period to within 4.5% of the theoretical value. Flow field visualization indicate a smoothly varying and symmetric velocity field. Four stages of energy interchange are visualized demonstrating physically reasonable behavior. Complex pressure patterns are observed for the 3D ellipsoidal case suggesting a multi-mode dynamics.

5.3 Bubble Rise in a Liquid Bulk

The next test is the simulation of a single bubble rising in an initially quiescent fluid due to the effects of buoyancy. The shape of a gas bubble rising in a liquid bulk is influenced by surface-tension, viscosity, and gravity. The problem is characterized by four dimensionless numbers: (i) the density ratio (ρ_l/ρ_g) ; (ii) the viscosity ratio (μ_l/μ_g); (iii) the Reynolds number based on initial bubble diameter ($Re_D = \rho_l D\sqrt{gD}/\mu_l$); and (iv) the E$\ddot{o}tv\ddot{o}$s number ($E_o = g(\rho_l - \rho_g)D^2/\sigma$). Here, $D(= 2R)$ is the initial diameter of the bubble, g is gravity, and subscripts "l" and "g" correspond to the liquid bulk and gas phase, respectively.

Bubble rising in bulk fluids has been widely studied and many experimental and computational results are available for comparison purposes. Also, a general diagram of bubble shapes as a function of the E$\ddot{o}$tv$\ddot{o}$s and Reynolds number has been reported

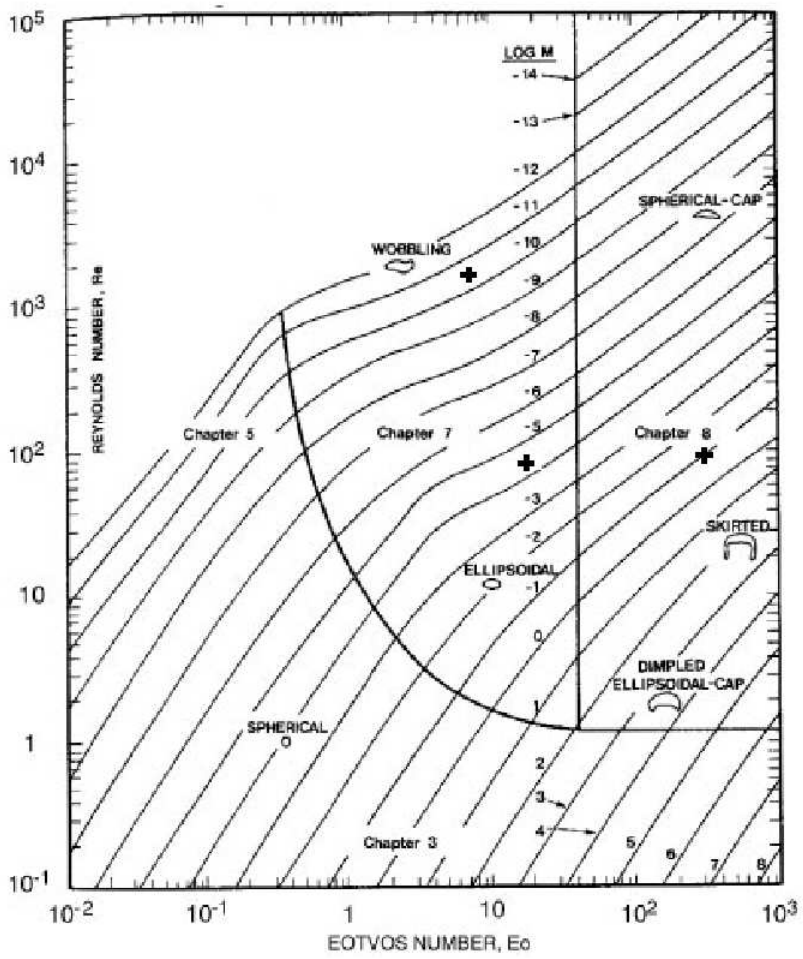

Figure 15: A general shape diagram for rising bubbles following Clift *et al.* [34].

by Clift *et al.* [34], as shown in Fig. 15. Although all experimental results are known for 3D bubbles, a qualitative comparison is possible. We first report on a widely studied case of rising bubble and compare its shape evolution with other computational results. We then report on effects of varying surface-tension on bubble shape in conjuction with the bubble regime diagram of Clift *et al.* [34].

A two-dimensional rising air bubble in water is considered here and is also reported by other studies [89, 150]. The computational domain employed is a 40 mm square discretized into 256×256 mesh cells. The bubble is initialized as a circle with $D = 6.8$ mm and centered at (0.02, 0.01) m location. The lower side of the domain is a wall

with periodic boundaries on either sides. A choice of wide domain limits the impact of "mirrored" bubble due to periodic boundaries on either sides. Alternately, absorbing boundaries can be employed to reduce the domain width, however such an application is not considered in the current study. The fluid properties are: $\rho_l = 1000$ kg/m^3, $\sigma = 0.0728$ N/m, $\mu_l = 1.14 \times 10^{-3}$ kg/(m-s), $\gamma_l = 2.1$, $P_{\infty,l} = 10^7$ Pa for the liquid bulk and $\rho_g = 1.17$ kg/m^3, $\mu_l = 1.78 \times 10^{-5}$ kg/(m-s), $\gamma_g = 1.4$, $P_{\infty,g} = 0$ Pa for the gas bubble. The gravity is taken to be: $g = 9.8$ m/s^2.

Under these conditions, characteristics of this case are: $\rho_l/\rho_g = 10^3$, $\mu_l/\mu_g = 65$, $Re_D = 1544$, and $E_o = 6.218$. A "wobbling" regime is effective for this case as marked in the shape diagram. In this shape regime, the bubble initially has a nearly spherical cap shape, however at a later stage, flattening of the bubble top is expected. Figure 16 compares the evolution of the bubble shape (right) to that of van der Pijl [150] (left) for three different time instants. Initial circular shape of the bubble is observed to undergo permanent deformation on the lower side due to evolution of the bubble wake (shown later). Also, flattening of the bubble top is noted. The evolution of the bubble shape compares well with that of van der Pijl *et al.* [150].

Figure 17 shows the temporal evolution of the velocity field in relation to the bubble shape in the form of liquid volume fraction contours. Pressure field is shown in the background. Hydrostatic pressure gradient due to downward acting gravitational acceleration is expected and observed in the pressure field. An initially quiescent velocity field is observed to build up within the gas bubble and propel it upwards due to buoyancy effects as seen in Fig. 17b. Two vortices, counter-rotating to each other, centered on either sides inside the bubble are observed to induce a wake region. Significant deformation on the lower side of the bubble is observed as the wake region is established. Further rise in the bubble pushes the vortex centers further apart laterally, widening the wake region. Relatively low pressure mark these vortex centers and their path as seen in Figs. 17(d-f). The rate of change in shape gradually decreases

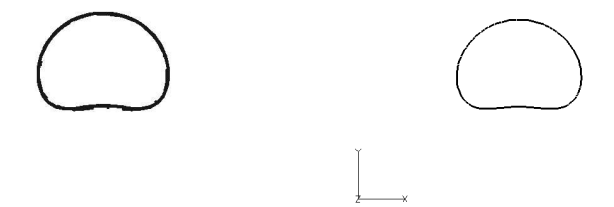

(a) t=0.025 s (b) t=0.025 s

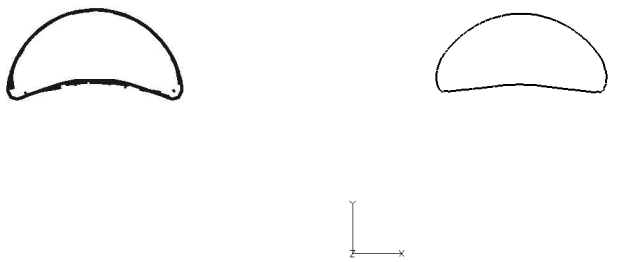

(c) t=0.05 s (d) t=0.05 s

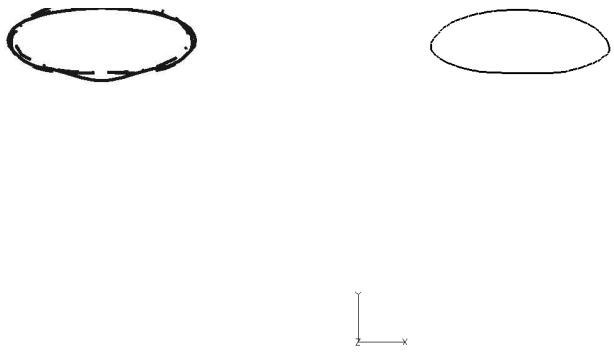

(e) t=0.1 s (f) t=0.1 s

Figure 16: Comparison of 2D bubble shapes (right) with van der Pijl *et al.* [150] (left) at three different equivalent times. Solid line for figures on the left column indicate a fine grid. Here, ρ_l/ρ_g=1000, E_o = 6.22, and Re_D = 1544. Mesh size is 256x256.

with time and reaches some steady state as observed in the evolution. Effect of interface smearing is noted in the wake region which diffuses the interface over several cells. Several interface sharpening techniques exist [102, 187] that can be applied to limit the numerical smearing, however this was not undertaken in the current study.

One of the major effect of surface-tension is to keep the bubble circular which is its minimum energy profile. It counteracts other forces to keep the bubble intact. To assess its impact on the bubble shape evolution, two cases are studied at constant $Re_D = 100$ and varying the surface-tension coefficient. Other fluid properties and the geometrical parameters of the bubble are same as before. The results of these two cases are shown in Fig. 18 where the E*ö*tv*ö*s numbers are respectively $E_o = 15$ (left) and $E_o = 300$ (right). According to the regime map, the case with lower surface-tension ($E_o = 300$) lies in the "skirted" regime. Significant deformation in bubble shape is expected and observed as seen in Figs. 18(b,d,f). For the higher surface -tension case ($E_o = 15$), relatively less shape deformation is noted and the bubble achieves dimpled ellipsoidal shape. Inspite of different shape evolution, both cases indicate upward rise approximately at the same rate. This is expected as all other parameters including gravity and viscosity of both fluids are identical.

The velocity field is also significantly different for the two cases. The "skirted" case shows the counter-rotating vortex pair trailing the bubble. It is the influence of such vortices in the bubble wake region to break the skirt, and the remaining part of the bubble develops a spherical-cap shape [196]. Such effects and breakup of the bubble are shown in Fig. 19 for the case of $E_o = 300$. The breakup evolution is similar to that reported by Smolianski [196]. The field is also noted to be perfectly symmetrical about the vertical center axis. After breakup, the secondary bubbles rotate in the same direction as the vortex that generated them and progressively trail the primary bubble rise.

In summary, a two-dimensional gas bubble rise in a liquid bulk parameterized by

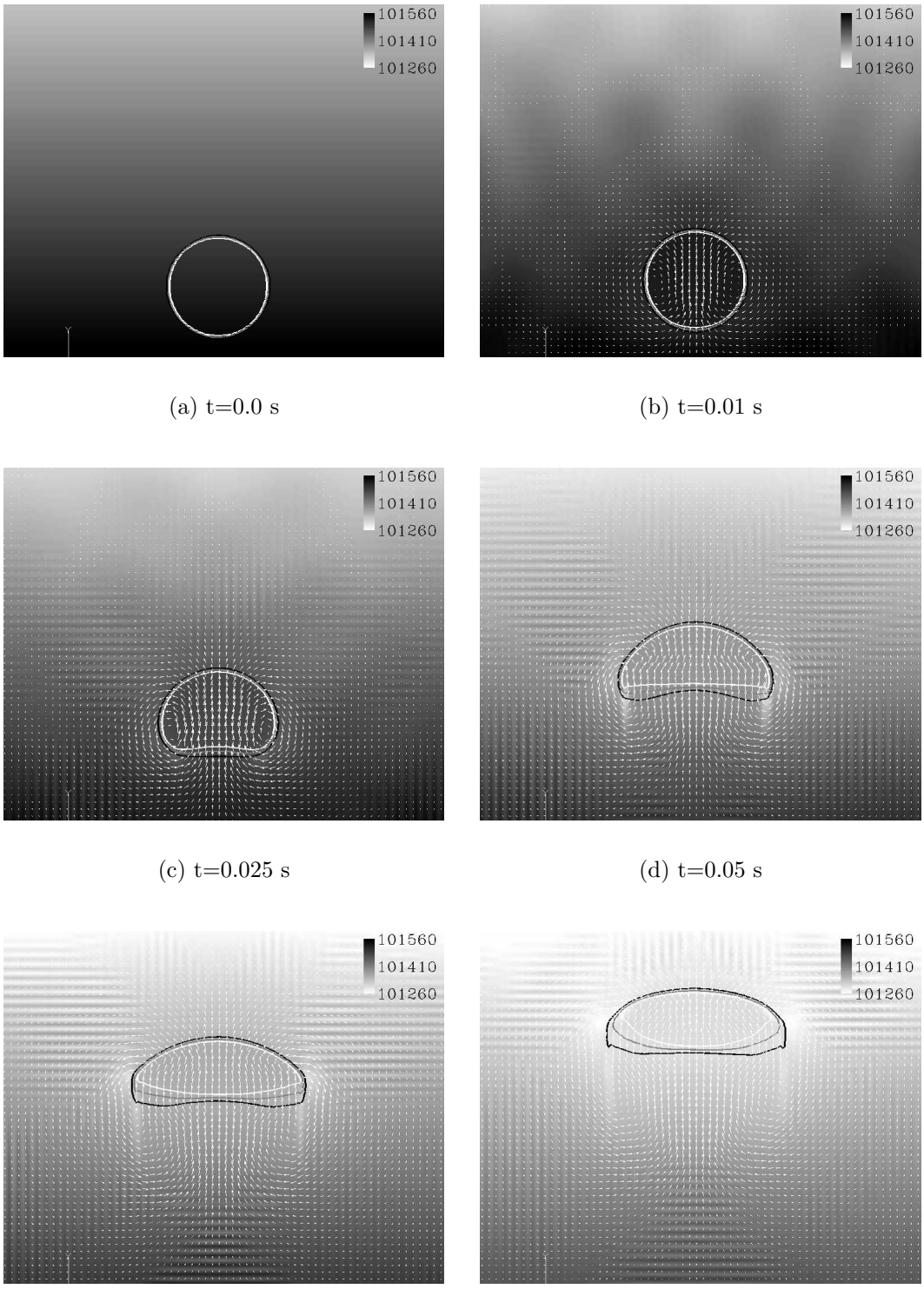

(a) t=0.0 s

(b) t=0.01 s

(c) t=0.025 s

(d) t=0.05 s

(e) t=0.075 s

(f) t=0.1 s

Figure 17: Interface positions in form of volume fraction contours for a rising 2D bubble. Background is colored by pressure (in Pa) and velocity field is also shown. Here, ρ_l/ρ_g=1000, $E_o = 6.22$, and $Re_D = 1544$. Mesh size is 256x256.

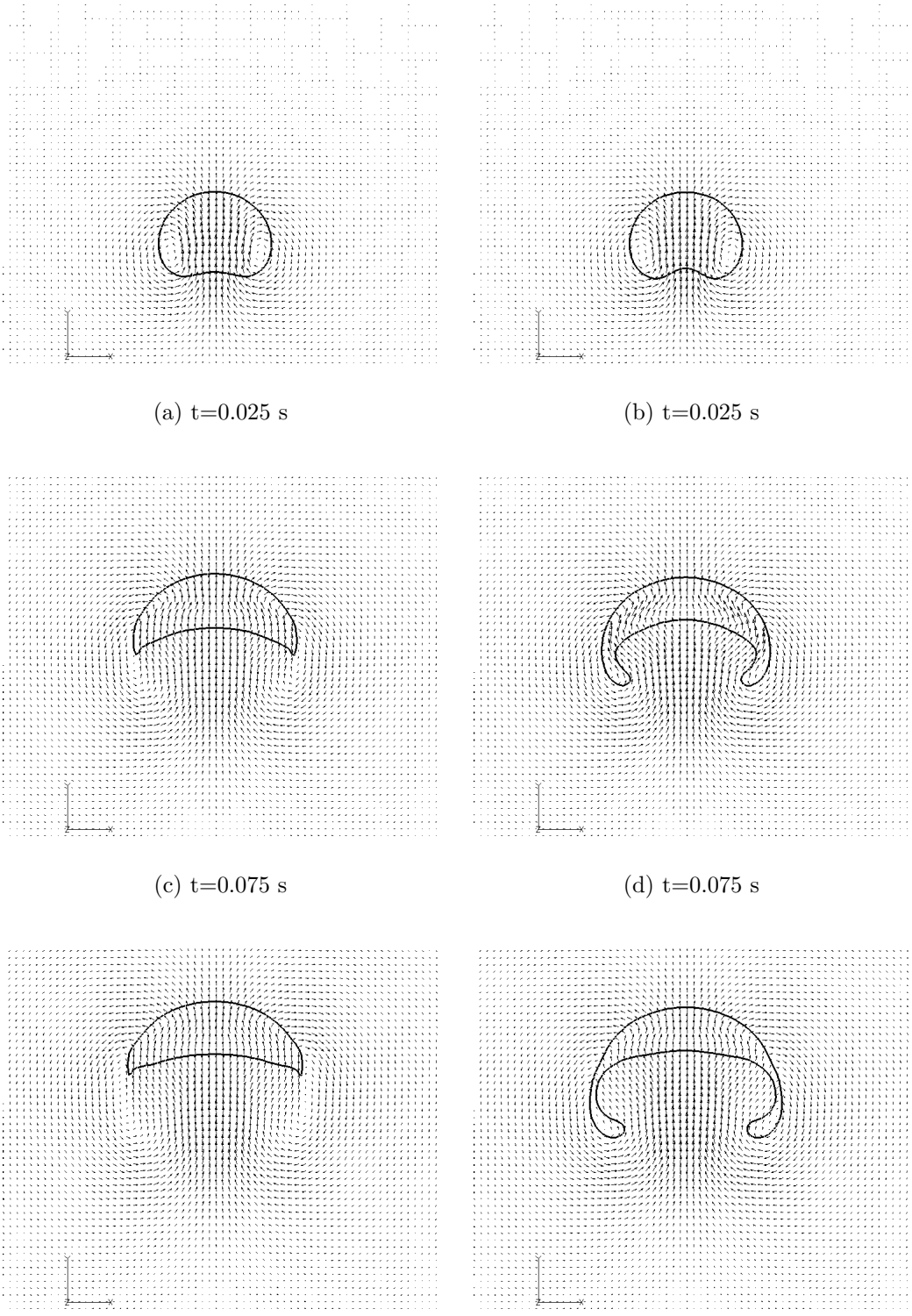

(a) t=0.025 s (b) t=0.025 s

(c) t=0.075 s (d) t=0.075 s

(e) t=0.1 s (f) t=0.1 s

Figure 18: Interface positions in form of volume fraction contour ($\alpha_l = 1/2$) for a rising 2D bubble: (left) $E_o = 15$, $Re_D = 100$; (right) $E_o = 300$, $Re_D = 100$. Here, $\rho_l/\rho_g = 10^3$ and mesh size is 256x256.

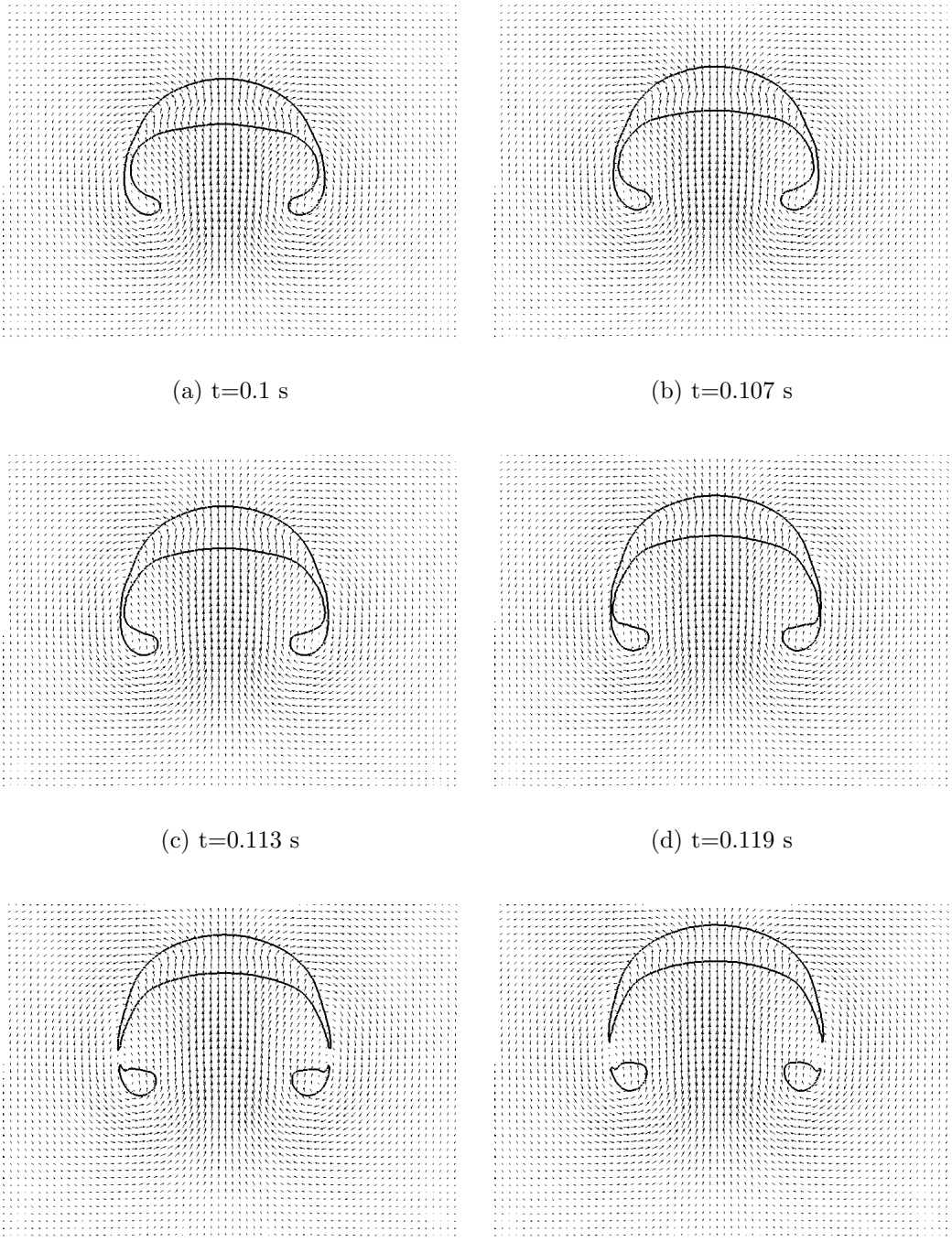

(a) t=0.1 s

(b) t=0.107 s

(c) t=0.113 s

(d) t=0.119 s

(e) t=0.125 s

(f) t=0.132 s

Figure 19: Interface positions in form of volume fraction contour ($\alpha_l = 1/2$) for a rising 2D bubble for: $E_o = 300$, $Re_D = 100$. Here, $\rho_l/\rho_g = 10^3$ and mesh size is 256x256.

$\rho_l/\rho_g = 10^3$ is presented for various Reynolds and Eötvös numbers. The method is demonstrated to account for buoyancy effects on the bubble dynamics. No special treatment or change in algorithm is needed to model bubble rise. The dependence of an initially circular bubble on surface-tension and Reynolds number is shown to reasonably predict the shape-regimes of Clift *et al.* [34]. All cases show presence of counter-rotating vortices and its effect on the bubble shape. Especially, in the case of low surface-tension, the vortices are demonstrated to break the bubble into one primary and two secondary pieces. The method is shown to naturally account for breaking and merging of interfaces. Despite the two-dimensionality aspect of current simulations, a qualitative picture of the bubble rise, shape deformation, and breakup is captured well. Simulation of a three-dimensional configuration can be pursued with equal ease, however due to high computational cost and time requirements it is deferred for future studies.

5.4 Liquid Breakup under Gravity Effects

In this test case, we assess the method's capability to manage interface dynamics in the context of drop creation. The physical problem considers elongation and breakup of liquid under gravitational acceleration leading to drop formation. Initially, a circular drop suspended on an upper wall undergoes large deformation due to competiting gravity (acting downwards) and surface-tension generated adhesion (acting upwards) forces. A thin filament is formed connecting the upper wall adhered liquid and downward moving liquid bulk. This filament eventually breaks up into satellite drops. The problem is characterized by two dimensionless numbers: (i) the density ratio (ρ_l/ρ_g), and (ii) the Bond number ($B_o = \rho_l g D^2/\sigma$, also called Eötvös number). Here, D is the initial diameter of the liquid drop suspended on the ceiling and g is the gravitational acceleration.

A two-dimensional drop of initial radius $R = 0.25$ m is centered on the upper

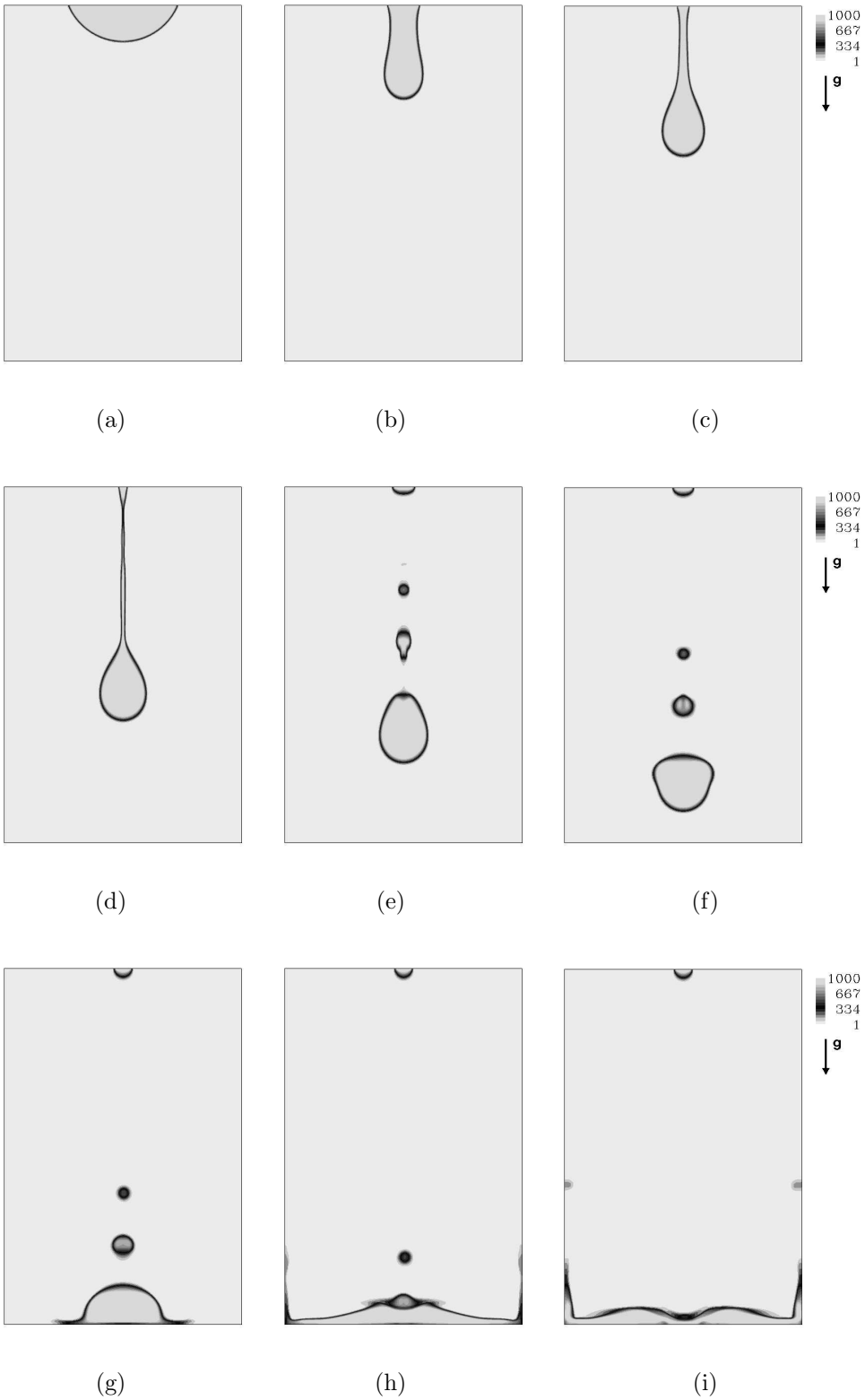

Figure 20: Transient evolution of interface positions in form of density contours are shown for a liquid breakup under gravity effects. The gravity is oriented downwards. Here, $\rho_l/\rho_g = 10^3$, $B_o = 32$, and mesh size is 200×300.

wall at (0.5, 1.6) m. The computational domain is one-meter wide and 1.5 m tall discretized into 200×300 cells. Both the upper and lower sides of the domain are considered as wall with periodic boundaries on either sides. The fluid properties are: $\rho_l = 10^3$ kg/m^3, $\sigma = 200$ N/m, $\gamma_l = 4.1$, $P_{\infty,l} = 5 \times 10^7$ Pa for the liquid phase, and $\rho_g = 1.17$ kg/m^3, $\gamma_g = 1.4$, $P_{\infty,g} = 0$ Pa for the surrounding ideal gas. Associated Bond number is $B_o = 32$. The gravity acting downwards is taken to be: $g = 25.0$ m/s^2. The contact angle at the wall boundary is taken equal to 25^o. The initial field is quiescent with uniform pressure throughout the domain.

Figure 20 shows the temporal evolution of the liquid drop breakup due to gravity effects. Density contours are shown in solid background with appropriate shade grading to elucidate the interface location. The initial state is shown in Fig. 20a with a circular liquid drop suspended on the upper wall. The presence of gravity quickly distorts the circular shape to an elongated sack-like structure; however it adheres to the upper wall due to surface-tension, as seen in Fig. 20b. Gradually the lower lobe increases in size via drainage of the suspended fluid. A filament (or also called drop "neck") connecting the upper cap with the downward moving bulk/lobe appears due to elongation and serves to further drain the fluid as seen in Fig. 20c. This filament gets thinner with time and eventually breaks up into several satellite drops as seen in Figs. 20(d-e). Such breakup happens at two places: one connecting to the upper cap and the other connecting the lobe. Figure 20e shows presence of three distinct entities: one primary drop and two satellite droplets. All these move downwards under the gravitational pull as seen in Fig. 20f.

Due to the presence of the lower wall, drop splashing is expected as the drops move further downwards. Figure 20g shows contact of the primary drop with the lower wall creating a liquid wall-jet moving parallel to the boundary. Such an effect for a falling drop hitting a wall was reported by van der Pijl *et al.* [150]. The fluid moves sideways as the rest of the primary drop moves downwards. This creates a

shallow pool of fluid as seen in Fig. 20h. Satellite drops following the primary splash onto the liquid pool creating waves on the surface as seen Fig. 20(h-i). Also, due to assumed periodicity on the side walls, the fluid from either sides creates a "tower" which leads to formation of yet another satellite drop as seen in Fig. 20i. Some mass of liquid is observed to remain suspended on the upper wall inspite of some brief oscillations as seen in Figs. 20(e-i). This indicates dominance of surface-tension forces as there is not enough mass to make it fall.

A qualitative comparison of the above liquid breakup phenomena is possible with a similar drop configuration studied earlier [148]. Two aspects differentiates their configuration: (i) they did not have a lower wall, and (ii) a spherical drop was considered in the measurements. Figure 21 shows the time evolution of liquid breakup for experimental (top row) and computational (bottom row) study. Essential features such as: (i) the drop distortion creating a sack-like structure, (ii) the appearance of a (thin) filament, (iii) the breakup of the filament leading to primary and secondary drops, and (iv) the suspension of some liquid mass on the upper wall are all recovered in the current simulation.

In summary, a two-dimensional liquid drop breakup under gravitational acceleration is presented for $\rho_l/\rho_g = 10^3$ and $B_o = 32$. Temporal evolution of the field indicates significant deformation of the interface that undergoes elongation and eventually breakup. Thin filament formation is confirmed and its ensuing breakup generated primary and secondary drops. Drops splashing on the lower wall creates wall-jet effect and culminate in a pool of fluid. Waves are generated when the secondary drops impinge on the liquid surface. Overall, this case demonstrates the capability of the approach to account of significant deformation dynamics even under high density ratios. Dynamic appearance and disappearance of the interface are well captured. Also, several complex and transient behaviors: filament formation, ensuing breakup, liquid-wall effects, and liquid-liquid effects are also captured. Simulations in 3D can

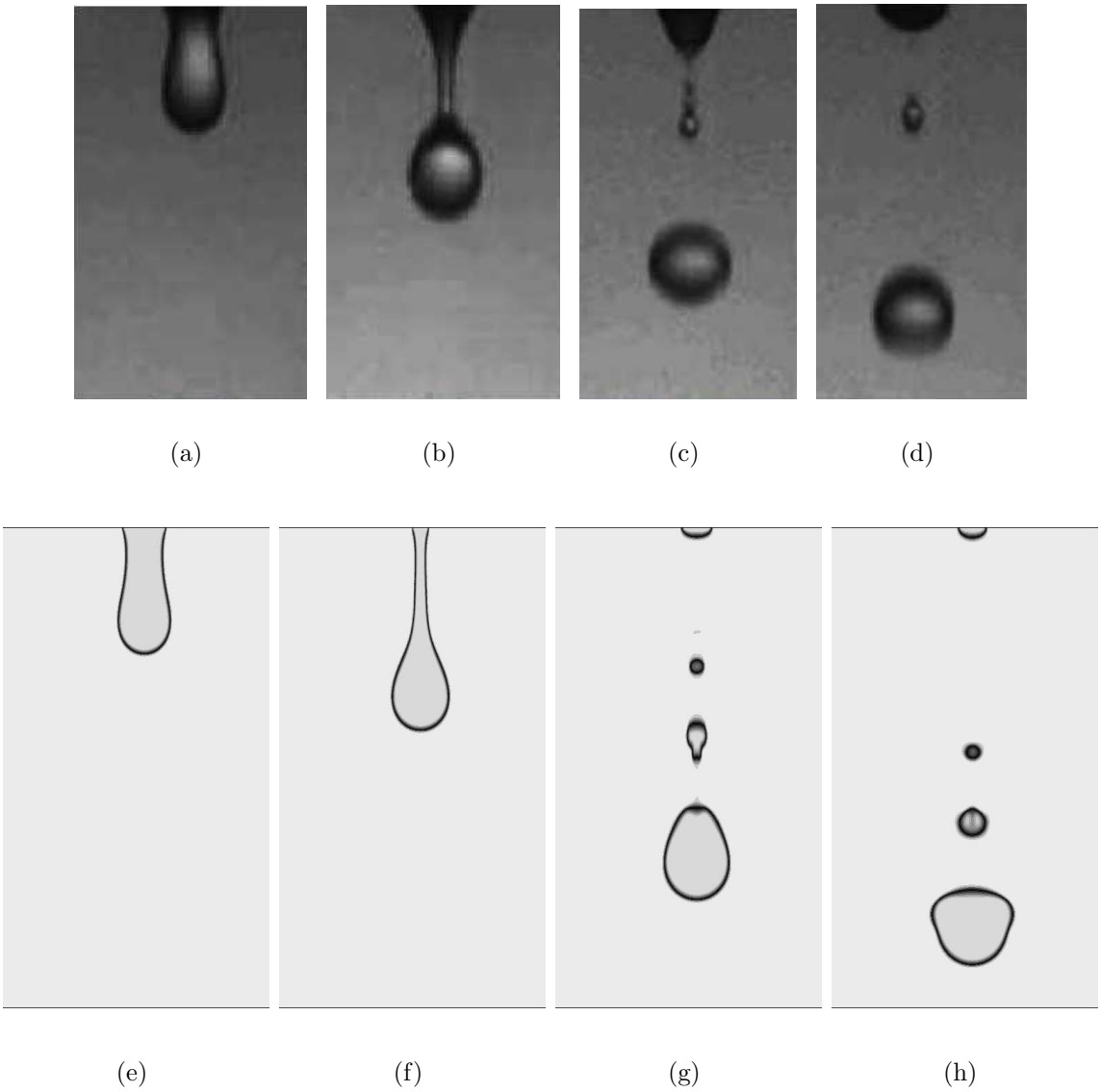

Figure 21: Qualitative comparison between experiment [148] (top row) and 2D computational (bottom row) evolution for liquid breakup under gravity effects.

be performed for a range of density ratios and Bond numbers; however they are deferred for future studies due to high computational cost/time requirements.

5.5 Drag on an Isolated Liquid Drop

In this test case, we address the fundamental coupling of the liquid drop with its surrounding gas. This coupling arises in the form of drag force exerted on each fluid due to viscosity. Also, such inter-phase coupling, in addition to other effects such as evaporation, collisions, and atomization significantly influence the spray (in the context of multiphase flows) characteristics and its evolution. Common practice is to develop reduced drag models based on correlations for use in the multiphase spray simulations. Under the assumption of a low Weber number (We), drag correlations for solid spheres in steady flows are used to estimate [47] interphase momentum transfer in spray simulations. However, several interactions like relative acceleration, deformation, and atomization are neglected [47] in such reduced models. Despite their fundamental nature and significant influence, these interactions are still not well understood as they happen on very small length- and time-scales [208, 162]. It is well documented that spherical drops undergo significant deformation and acceleration, and then become flattened due to the drag forces [49, 162]. The resulting drag is significantly higher relative to that of an undeformed sphere.

Several studies [34, 77, 72, 162] have looked into the effects of deformation, however such effects have proven difficult to quantify. The primary reason for this is due to the transient nature of the deformation effect. According to Quan and Schmidt [162], the transient nature acts as an additional parameter making the drag depend on Ohnesorge number (Oh) and history effects. This has been affirmed by the conclusions of several experimental studies [34, 208, 77]. Our purpose here is two-fold: (i) to assess the capability of our approach to address the drag dynamics at such small length- and time-scales; and (ii) to study drag variation for unsteady fields.

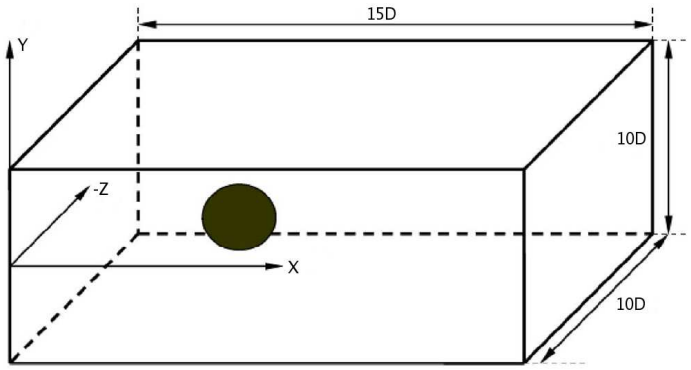

Figure 22: Schematic of the computational domain for a droplet in a moving gaseous field.

Figure 22 shows the problem setup and the computational domain for our study. We consider both 2D and 3D configurations. Initially, a circular (in 2D, spherical in 3D) drop of $D(= 2R) = 250$ μm is located in a box of length $15D$ and height of $10D$. In the case of a 3D sphere, it is centrally located along the domain width of $10D$. Flow is from left to right. Inflow (left side) and outflow (right side) boundaries are assumed in the streamwise (X) direction whereas periodicity is applied on rest of the boundaries. An inlet boundary condition considers an uniform velocity profile of U_o magnitude. The box domain is large enough so that boundary effects can be assumed small. The computational domain is discretized into 384×256 cells in the case of 2D configuration and $384 \times 256 \times 256$ for 3D cases. This resolution gives approximately 25 cells within the droplet.

The fluid properties are: $\rho_l = 10^3$ kg/m^3, $\sigma = 0.0728$ N/m, $\mu_l = 1.14 \times 10^{-3}$ kg/(m-s), $\gamma_l = 4.1$, $P_{\infty,l} = 5 \times 10^7$ Pa for the liquid drop; and $\rho_g = 1.17$ kg/m^3, $\mu_l = 1.8 \times 10^{-5}$ kg/(m-s), $\gamma_g = 1.4$, $P_{\infty,g} = 0$ Pa for the carrier gas. The gravity is neglected in this study. Three dimensionless numbers characterize this test case: (i) the Weber number ($We_g = \rho_g D U_o^2/\sigma$), (ii) the Reynolds number ($Re_D = \rho_g D U_o/\mu_g$), and (iii) the Ohnesorge number ($Oh = \mu_l/\sqrt{\rho_l D \sigma}$). For these fluid characteristics, $Oh = 7.4 \times 10^{-3}$. Several cases in 2D and 3D configurations are studied for various

	C1	C2	C3	C4	C5	D1	D2
U_o	0.24	1.0	2.0	3.9	5.0	10	50
Re_D	3.9	16.3	32.5	64.0	81.3	163	813
We_g	0.23×10^{-3}	4×10^{-3}	0.016	0.061	0.1	0.4	10.05
τ (μs)	521	125	63	32	25	12.5	2.5

Table 5: Tabulated Re_D and We_g for various droplet drag cases. Here, $\rho_l/\rho_g = 10^3$ and $Oh = 7.4 \times 10^{-3}$.

Re_D and We_g by systematically varying the oncoming gas velocity U_o. Table 5 shows different cases along with characteristic time scales ($\tau = R/U_o$) for each configuration.

Following Fyfe *et al.* [56], the initial conditions are specified in form of the steady-state potential flow about a cylinderical/spherical drop. This gives a smooth and divergence-free velocity field. In the 2D case, the flow over a circular cylinder is a combination of a uniform flow and a doublet. The stream function (ψ) for the combined flow is given by [6]:

$$\psi = (U_o r sin\theta)[1 - R_o^2/r^2] \quad (2D)$$

where, r is the radial distance from the drop center, θ is the angle between the freestream velocity direction and radial vector, and R_o is the drop radius. The velocity field is then obtained by differentiating the stream function. Similarly, in the 3D case, a super-position of a 3D doublet and a uniform flow gives us the potential flow profile over a sphere. Such a specification of the initial profile is aimed to give a smooth start to the simulation.

Similar to Quan and Schmidt [162], the equation for the droplet acceleration is given by:

$$m_l \frac{dU_c}{dt} = \frac{1}{2}\rho_g S(U_o - U_c)^2 C_D$$

where, m_l is the droplet mass, U_c is the droplet centroid velocity, S is the frontal surface area, and C_D is the total drag coefficient, which includes added viscous, history, and acceleration reaction effects [208]. The droplet centroid velocity is computed based on the aforementioned averaging procedure with limit volume fraction

of $\alpha_l > 0.9$. The frontal surface area is given by: $S = DL$ for 2D, where L is the unit cylinder width; $S = \pi R^2$ for 3D case. In all the above expressions, $D = 2R$ is the initial diameter of the droplet.

The total drag coefficient can then be calculated from the acceleration equation by:

$$C_D = \frac{\rho_l}{\rho_g} \frac{dU_c}{dt} \frac{\Pi}{(U_o - U_c)^2}$$

where, Π is a length constant depending on the configuration: $\Pi = \pi R$ for the 2D case; $\Pi = (8/3)R$ in 3D. Again, R is the initial radius of the droplet. The deformation factor (D_F) of the droplet is defined as the ratio between the length of the shortest (a) axis and that of the longest (b) axis: $D_F = a/b$. For a perfect circle/sphere (initial state) the D_F is equal to 1.0. The Reynolds number and the Weber number are redefined based on the relative velocity as:

$$Re_g = \frac{\rho_g (U_o - U_c) D}{\mu_g}; \quad We_g = \frac{\rho_g (U_o - U_c)^2 D}{\sigma}$$

With $U_c = 0$ initially, the newly redefined dimensionless numbers revert back to their previous definition based only on gas freestream velocity.

5.5.0.2 Drag over a cylinder

Five cases of non-deforming and two cases of a deforming 2D drop are studied. Several essential characteristics of each of the cases were tabulated in Tbl. 5. Figure 23 compares computational drag coefficient (symbols) for various cases with empirical correlations (dashed/solid lines). Two lines showing standard curve-fit (solid line) based on steady, non-deforming rigid cylinder [226] and liquid cylinder curve-fit (dashed line) based on Temkin and Kim's [208] steady drag corrections. Non-deforming cases are shown in solid-symbols and open-symbols represent deforming drop cases.

Temkin and Kim [208] reported on measurements of transient drag of impulsively accelerated liquid drop (sphere) by the carrier gas. Data was collected for small Weber numbers (resulting in negligible deformation) and $3.2 < Re_g < 90$. They

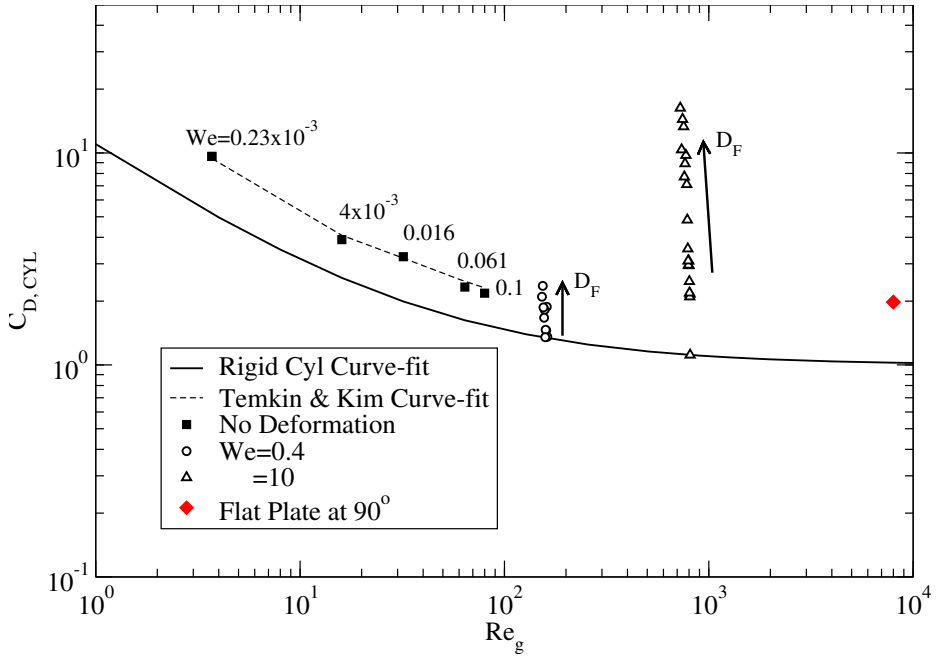

Figure 23: Comparison of computed drag coefficient (symbols) with experimental correlations (solid/dashed lines) for a 2D drop. Increasing drag with drop deformation is indicated in form of an arrow.

showed that the unsteady drag was always larger than the steady values at the same Reynolds number. The difference was attributed to time changes of the relative fluid velocity (U_r). The drag data was then quantified in terms of the relative acceleration parameter and the Reynolds number. The relative acceleration parameter (A) is defined as: $(\eta - 1)(D/U_r^2)\frac{dU_r}{dt}$, where $U_r = |U_o - U_c|$ is the velocity in the moving reference frame of the drop, $\eta = \rho_l/\rho_g$ is the density ratio, and D is the initial drop diameter. The resulting correlation expressed the data as: $C_D = C_{DS}(Re_g) - \kappa A$, where $C_{DS}(Re_g)$ is the steady drag at the instantaneous Reynolds number, and κ is a constant of $O(1)$.

For the current 2D case, a similar correlation is used to fit the larger transient drag with $\kappa = 0.68$. This value of κ was obtained by plotting the drag difference $C_D - C_{DS}$ against the relative acceleration parameter A as shown in Fig. 24. Transient drag data for three Re_g is shown along with a best-fit curve. The best-fit curve is given by:

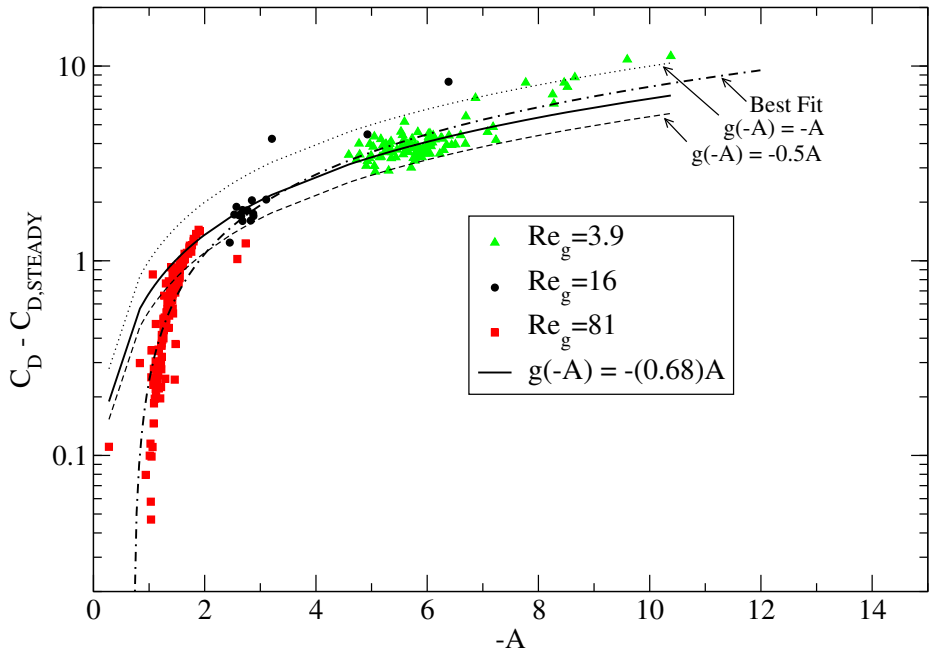

Figure 24: Difference between transient and steady drag as a function of relative acceleration parameter (A) for a cylinder. Multiple points are for different times.

$C_D - C_{DS} = -0.603 + 0.843(-A)$ and is a result of data regression with confidence level of 0.95. However, in the event that $A \to 0$, the transient drag does not revert back to its steady value. Data points having small values of $C_D - C_{DS}$ also happens to be at small values of A, and significantly impact the regression analysis leading to a non-zero intercept in the equation. Similar behavior was also noted by Temkin and Kim [208] and they attributed such effects to errors in C_D and A evaluations that magnify in relation to small $C_D - C_{DS}$ at high Re_g. Other three linear functions without an intercept are also plotted of which $g(-A) = -0.68A$ shows a closer fit to the data. This gives value of $\kappa = 0.68$.

Several effects of impulsively accelerated 2D drops can be noticed in Fig. 23. For all cases of non-deforming cylinders, transient drag consistently shows higher values in relation to steady drag represented by the standard curve-fit. Also, the difference between the transient and steady drag increases with decrease in Re_g. The main reason, as proposed by Temkin and Kim [208], for these variations is due to unsteady

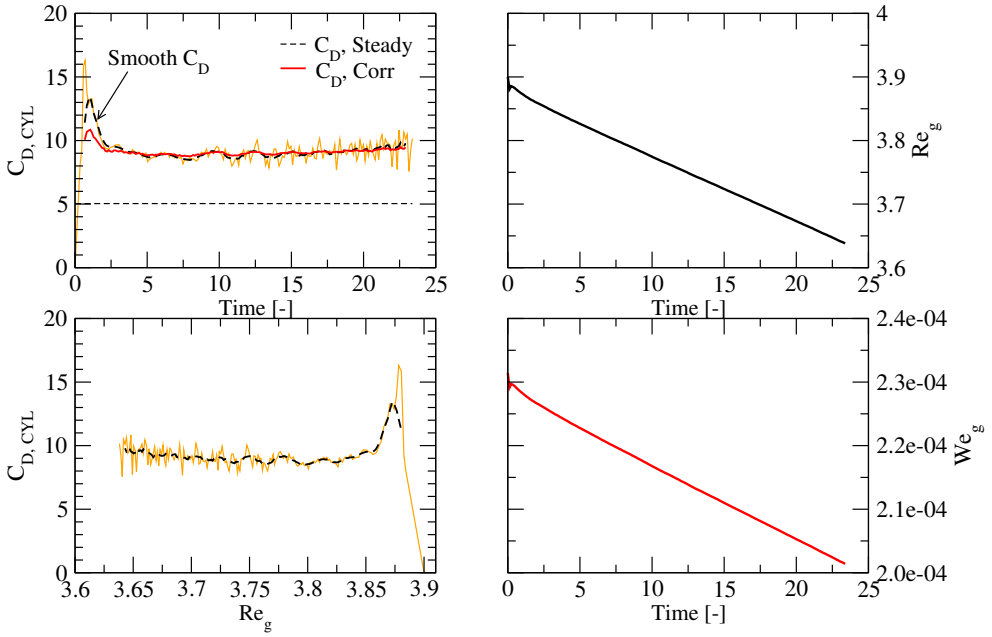

(a) $Re_g = 3.9$

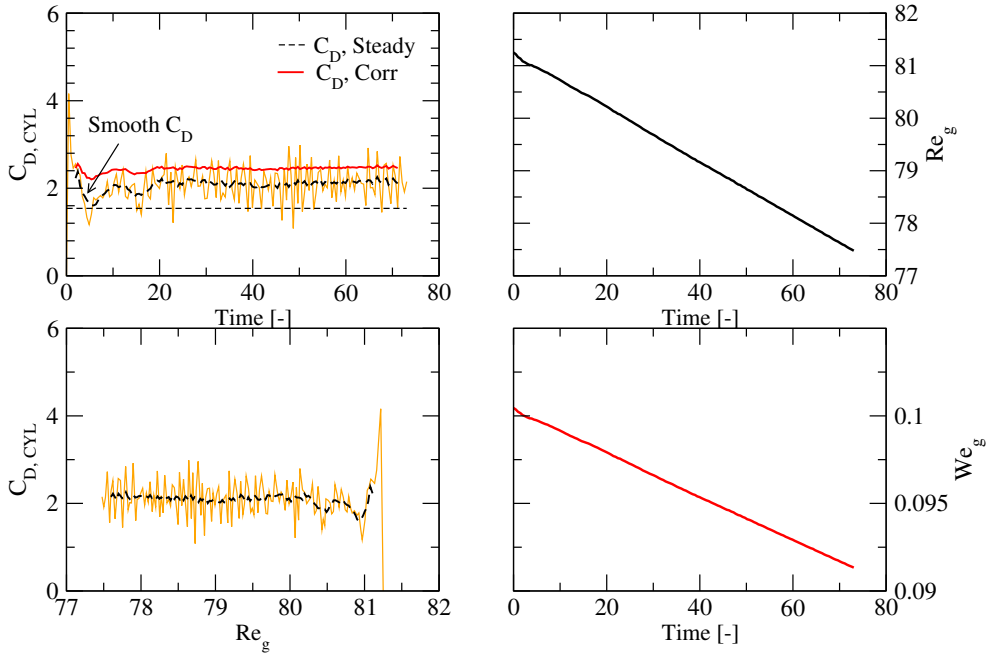

(b) $Re_g = 81.0$

Figure 25: Temporal variation of C_D for a 2D drop at an initial $Re_g = 3.9$ (a) and $Re_g = 81.0$ (b) is shown with transient variations of Re_g and We_g. Plot of C_D as function of varying Re_g is also shown.

effects amounting to relative movement of the particle. This is clearly shown in Fig. 24 where the drag difference ($C_D - C_{DS}$) increases with increase in the magnitude of the relative acceleration parameter (A). The primary consequence of this relative motion is to affect the recirculation region behind the particle and thereby, the drag. Thus, the drag coefficient of the liquid drop is a function of both the Reynolds number, as well as the relative acceleration parameter: $C_D = C_D(Re_g, A)$.

A temporal variation of the droplet drag is shown in Fig. 25 for cases: $Re_g = 3.9$ (top) and $Re_g = 81.0$ (bottom). The time axis is non-dimensionalized by the time scale of the flow (τ). Initially, there is a steep rise in the drag due to slowly accelerating drop from zero velocity ($U_c = 0$). Within a few cycles, the drop achieves a steady acceleration and the drag levels off. Both of these effects are also explained by the corrected C_D curve based on the Temkin and Kim's correlation [208]. Aforementioned effects of small drag difference are seen in the $Re_g = 81.0$ case. A closer examination indicates that the computed drag is within 10% of the correlated drag curve. This is reasonable in light of the fact that the functional fit for the correlated drag curve neglected these data points (having simultaneous small values of $C_D - C_{DS}$ and A). A monotonic decrease in the Reynolds and Weber number with time is also observed. This is explained by decrease in relative velocity magnitude due to accelerating drop.

Similar transient variation of C_D for a deforming drop initially at $Re_g = 813$ and $We_g = 10$ is shown in Fig. 26a. The drag coefficient is noticed to quickly increase to several times that of the steady value due to drop deformation. Associated decrease in both the Reynolds and Weber numbers is also observed. An increase in drag coefficient with decreasing Re_g is noticed to be more pronounced in the case of deforming drop. Deformation of the drop is quantified in terms of aforementioned deformation factor (D_F). This is plotted for two We_g and Re_g cases (corresponding to $D1$ and $D2$) in Fig. 26b. Deformation increases with increase in Weber number. This is expected due to the reduced effect of surface-tension forces to keep the drop in circular

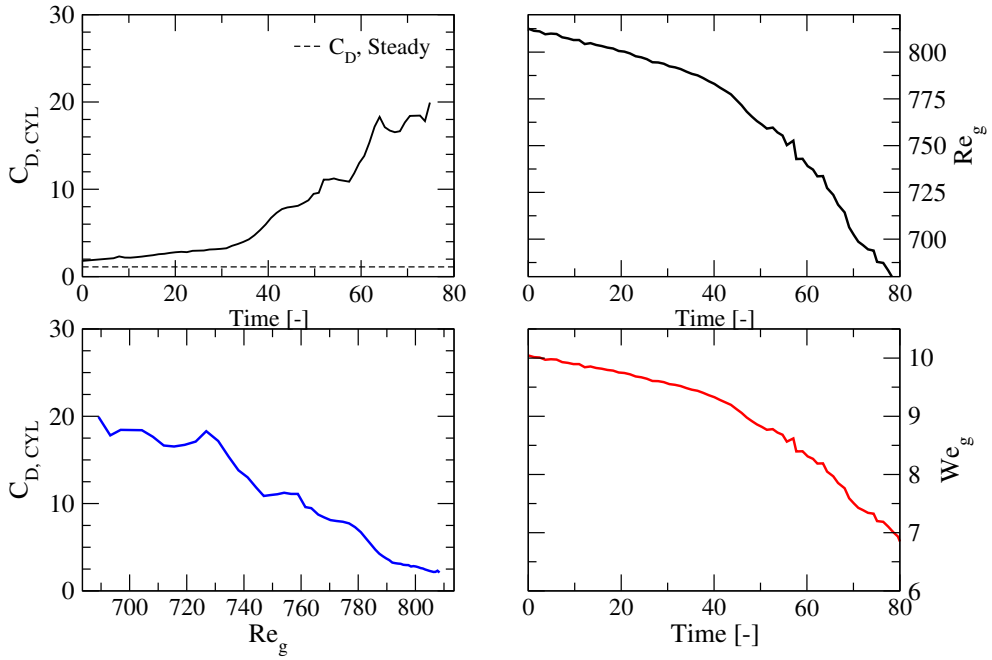

(a) $Re_g = 813$ and $We_g = 10$

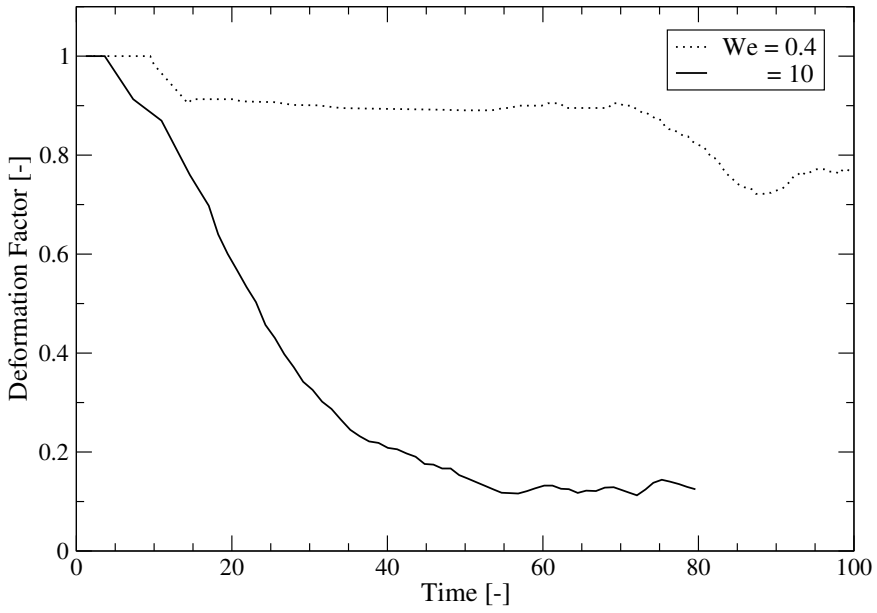

(b) Deformation Factor

Figure 26: Temporal variation of C_D for a 2D drop at an initial $Re_g = 813$ and $We_g = 10$ (a) is shown with transient variations of Re_g and We_g. Plot of deformation factor (D_F) as a function of time for two different We_g is also shown. $D_F = 1.0$ indicates no deformation

shape. Correlation of increase in drag coefficient with an increase in deformation factor conclusively indicates the dependency of drag coefficient on deformation. Similar observations were made by Hsiang and Faeth [77] in context of an experimental study.

Flow visualization for a non-deforming drop in form of spanwise (Z) vorticity in solid background and a line contour for $U = 0$ indicating the boundary of a recirculation region is shown in Fig. 27. The non-deforming drop case corresponds to $Re_g = 81$ and $We_g = 0.1$. The liquid drop is shown in the form a liquid volume fraction contour at $\alpha_l = 0.5$. Vorticity generation is observed at the forward stagnation point. This vorticity is then convected downstream as seen in the time progression. No deformation of the liquid drop is observed. This is expected as the onset of deformation occur at $We_g \approx 0.3$ [78]. The drop remains intact and moves downstream as its gains momentum via the drag forces. The recirculation zone is observed to be attached to the drop at the beginning, as seen in Fig. 27a. However, as time passes, the recirculation region detaches from the drop as seen in Figs. 27(b-c). Also, the stand-off distance (between the end of the drop and the start of the recirculation zone) increases with time until the formation of an unsteady wake. Above $Re_g \approx 40$ [226], an unsteady Karman vortex street is expected to form for a circular cylinder. The vortices which were initially in a fixed position now alternately shed and convect downstream. This is clearly seen in Figs. 27(g-i) in form alternately spaced (in streamwise direction) dark/light patches on the lee-side of the drop.

With increase in the Weber number, a 2D drop undergoes deformation as seen in Fig. 28. This case corresponds to $Re_g = 813$ and $We_g = 10$. Due to increase in gaseous flow velocity, a corresponding rise in vorticity magnitude is noted. The time progression indicates that the drop quickly deforms from a circular to a flattened profile. The recirculation region is noted to be quite different from that observed in the non-deforming case. Also, it is observed to remain attached to the drop till significant deformation leading to a flattened profile is reached. The wake region is

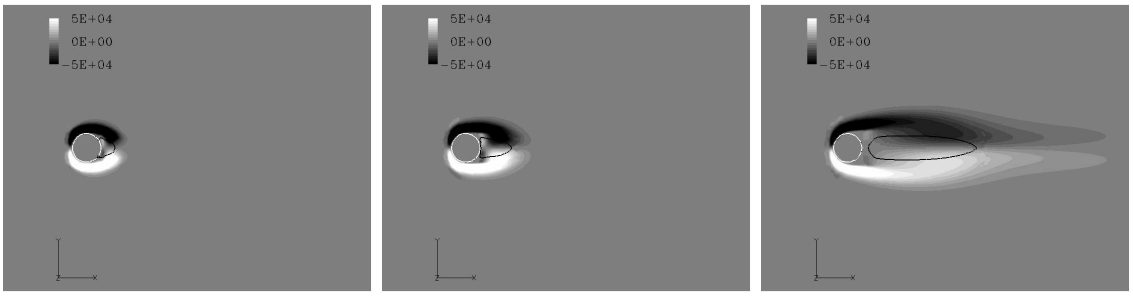

(a) t/τ=1.95 (b) t/τ=4.4 (c) t/τ=23.84

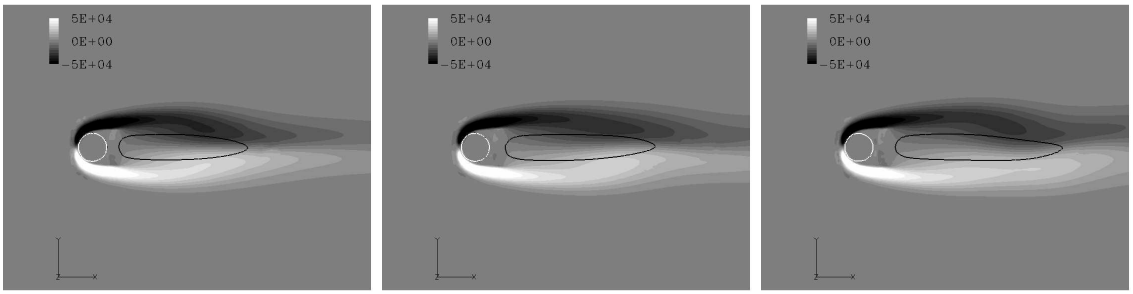

(d) t/τ=33.6 (e) t/τ=43.2 (f) t/τ=53.0

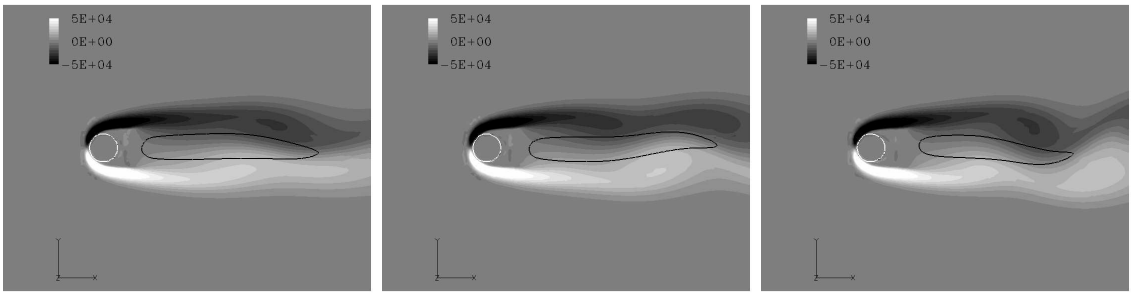

(g) t/τ=58.0 (h) t/τ=65.2 (i) t/τ=73.0

Figure 27: Flow visualization of a non-deforming 2D drop at $Re_g = 81.0$ and $We_g = 0.1$ is shown in form spanwise (Z) vorticity as background. The liquid drop is shown in form of a white contour line whereas, the black line represents $U = 0$.

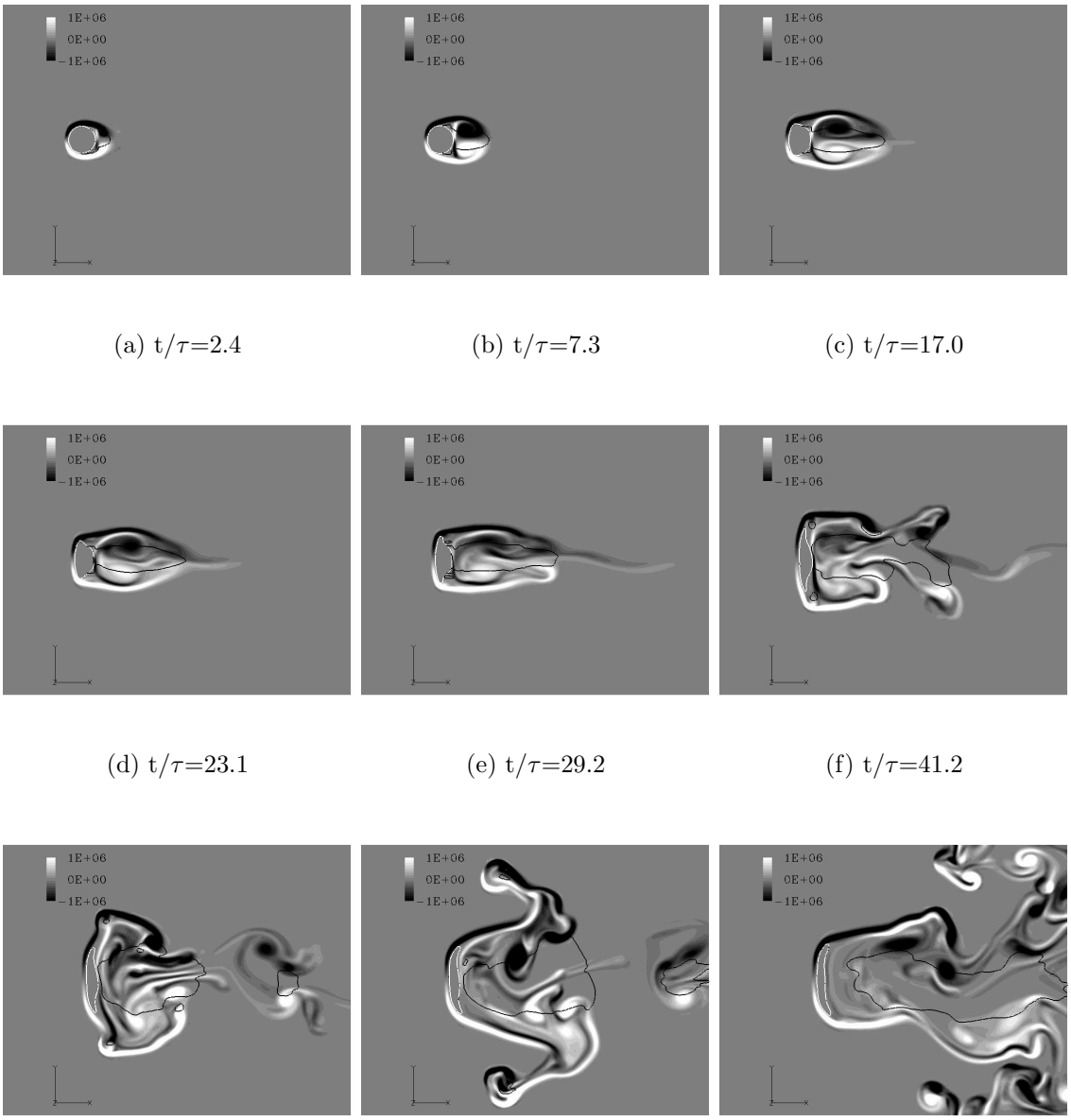

(a) t/τ=2.4 (b) t/τ=7.3 (c) t/τ=17.0

(d) t/τ=23.1 (e) t/τ=29.2 (f) t/τ=41.2

(g) t/τ=47.0 (h) t/τ=52.6 (i) t/τ=61.2

Figure 28: Flow visualization of a deforming 2D drop at $Re_g = 813$ and $We_g = 10$ is shown in form spanwise (Z) vorticity as background. The liquid drop is shown in form of a white contour line whereas, the black line represents $U = 0$.

quite unsteady with intermittent vortex shedding. Formation of a counter-rotating vortex pair on the lee-side of the deformed drop, as seen in Fig. 28e in the form of two detached (from the central) recirculation zones, convects side-ways eventually shedding from the drop as seen in Figs. 28(f-h). Overall, a strong two-way interaction between the liquid drop and gasesous flow is observed leading to a very complex flow field. It is also important to note that such processes are happening at very small time-scales: a flattened state is reached in 153 μs.

Figure 29 shows a close-up view of the relative velocity field (every other vector) along with $U = 0$ boundary (in form of a black line) and the spanwise vorticity in the background. Both non-deforming $We_g = 0.1$ (top row) and deforming $We_g = 10$ (bottom row) cases are shown for two time-instants corresponding to Fig. 27 and Fig. 28, respectively. Two different vector scaling, one within the drop and the other for the outer field, is employed to discern the flow patterns. The non-deforming case shows presence of internal drop circulation as seen in Figs. 29(a-b). This is called a "Hill Vortex" [37, 226]. The smooth velocity across the drop interface is observed with a zero radial component. The outer flow profile shows the recirculation zone positioned at some distance downstream of the drop. Within this stand-off distance, a non-zero and streamwise moving ($+X$) flow is noted. It is proposed [37, 162] that the observed internal recirculation is responsible for significantly altering the wake region and thereby the drag. Drop deformation changes the character of the flow field as seen in Figs. 29(c-d). Presence of internal vortical circulation vanishes within the drop and compression from either (front and back) sides results in an internal flow approaching towards each other. The wake region is observed to remain attached to the drop, however it is quite unsteady with significant vortex shedding.

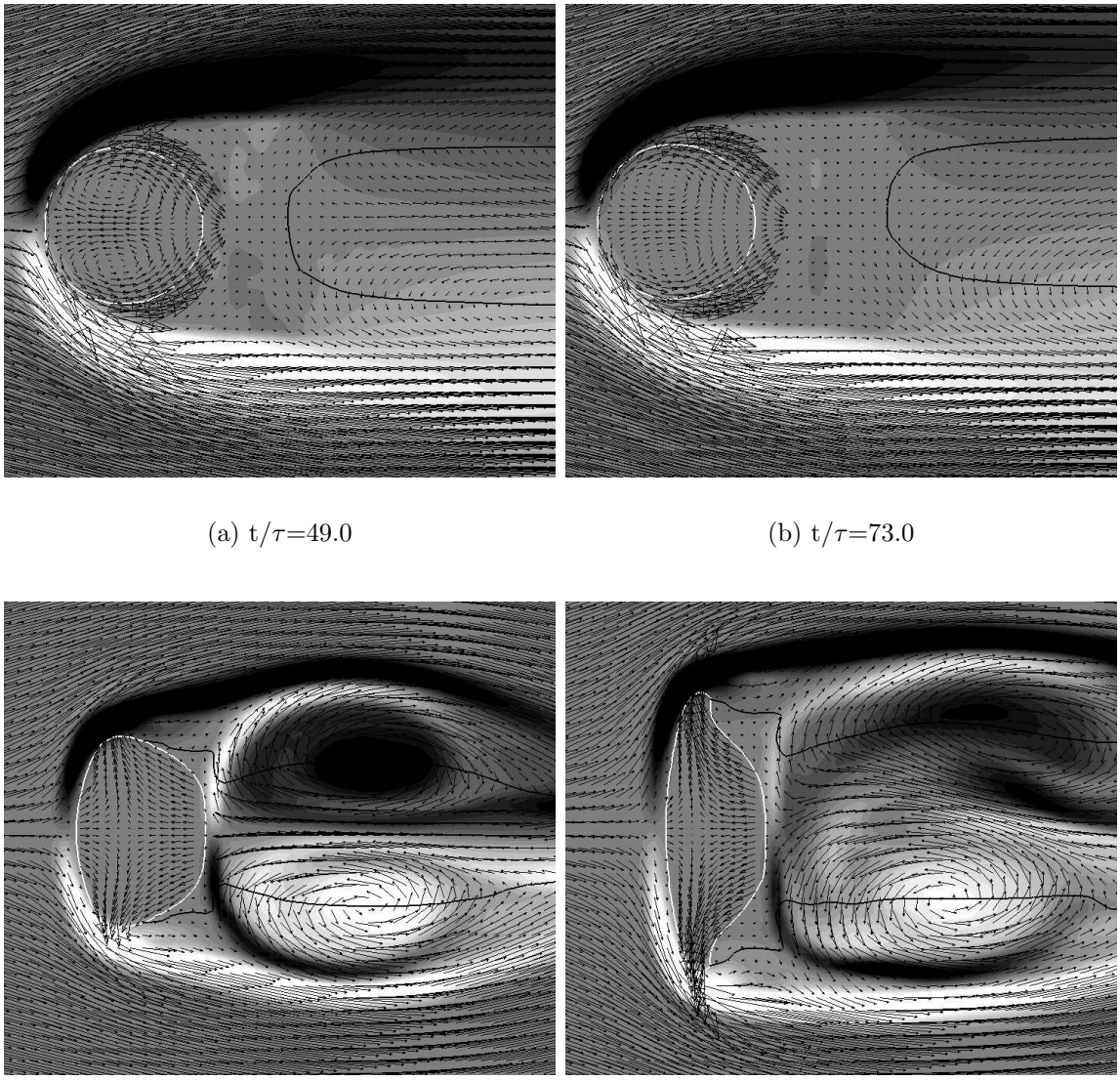

(a) t/τ=49.0

(b) t/τ=73.0

(c) t/τ=17.0

(d) t/τ=29.2

Figure 29: Relative velocity field visualization for a non-deforming (top row) and deforming (bottom row) 2D drop is shown along with spanwise (Z) vorticity in the background. The liquid drop is shown in form of a white contour line whereas, the black line represents $U = 0$.

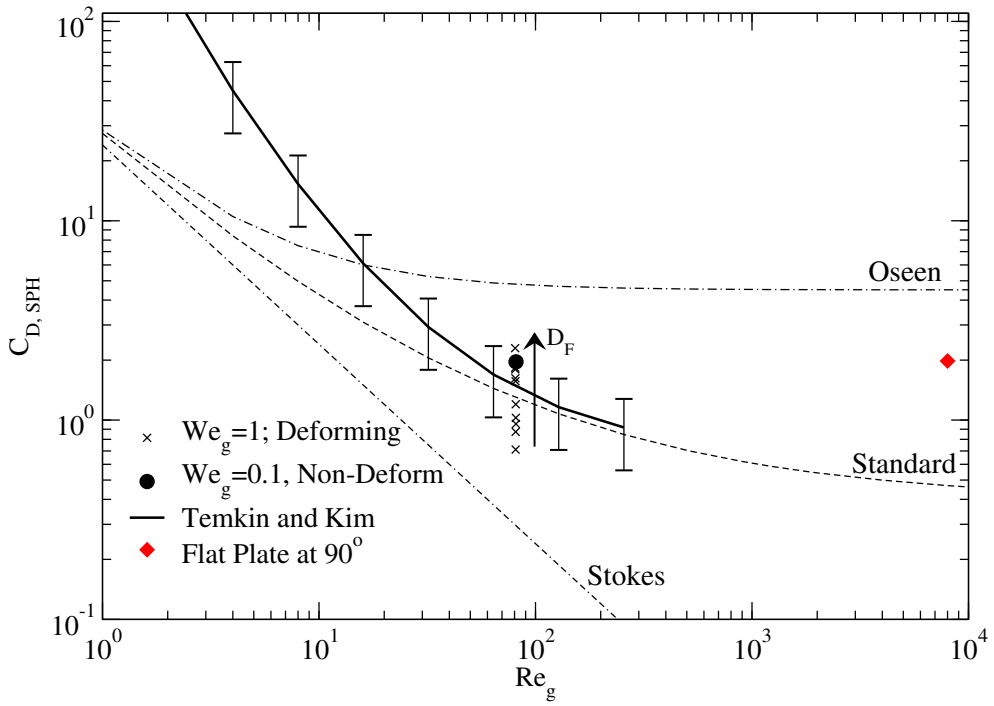

Figure 30: Comparison of computational drag coefficient (symbols) and experimental correlations (solid/dashed lines) for a spherical drop. Increasing drag with drop deformation is shown in form of an arrow.

5.5.0.3 Drag over a sphere

A computational study of a viscous flow over a spherical drop was also carried out to demonstrate the application of the method for complex 3D flows. Two cases were studied: (i) non-deforming sphere at $Re_g = 81.25$ and $We_g = 0.1$; (ii) deforming sphere at the same Reynolds number but at $We_g = 1.0$. The fluid and geometrical properties remain the same as before for the non-deforming case. However an increase in We_g for the deforming case (at same Re_g) was obtained by artifically reducing the surface-tension by one-tenth. Drag results obtained for both cases are directly compared with the measurement data of Temkin and Kim [208].

Figure 30 shows the variation of the drag coefficient (C_D) as a function of Re_g. Three dashed lines are shown each indicating the variation of C_D for a stationary rigid sphere. The standard curve-fit was based on the following curve-fit formula [226]:

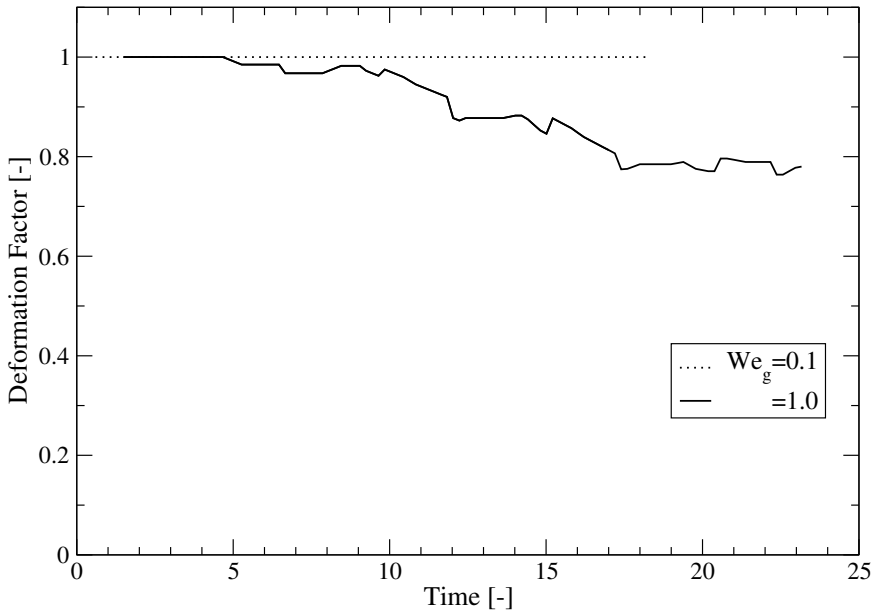

Figure 31: Time variation of the deformation factor (D_F) for two We_g cases for a spherical drop. $D_F = 1.0$ indicates no deformation.

$C_D = \frac{24}{Re_g} + \frac{6}{1+\sqrt{Re_g}} + 0.4$, where $0 < Re_g < 2 \times 10^5$. Both Stokes and Oseen drag profiles are also shown. For $Re_g > 1$, neither curve is accurate. Computational data in the form of symbols are compared with the best-fit curve of Temkin and Kim [208]. The best-fit curve is a second-order polynomial of the form: $C_D = b_0 + \frac{b_1}{Re_g} + \frac{b_2}{Re_g^2}$, where, b_n $(n = 0, 1, 2)$ are the coefficients such that $b_0 = 0.69$, $b_1 = 56.58$, and $b_2 = 482.49$. The standard deviation of the best-fit was reported to be 0.39. Both the predicted and experimental drag for a moving liquid drop are larger than the standard C_D. Predicted drag for a non-deforming drop is noted to fall within the experimental data range at $Re_g = 81$. As for the deforming drop, a range of C_D values is observed corresponding to its transient rise.

The deformation history of the spherical drop is shown in Fig. 31 for both We_g cases. No deformation is observed for the lower Weber number drop. The only effect for this case is convection of the drop while maintaning its spherical shape. At higher Weber numbers, deformation is expected and this is seen for $We_g = 1.0$ drop. The

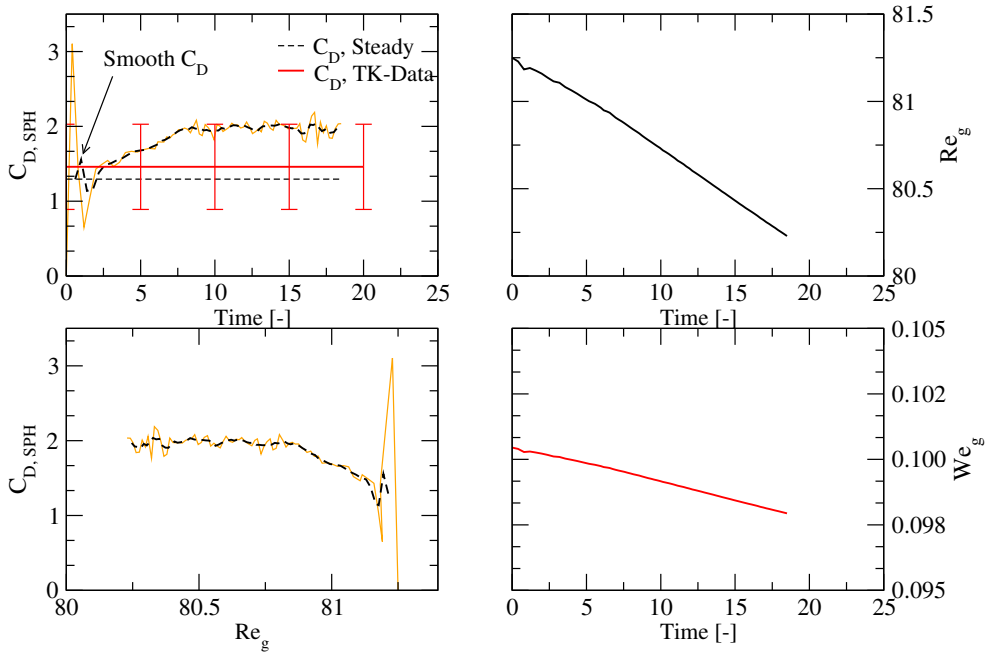

(a) $We_g = 0.1$

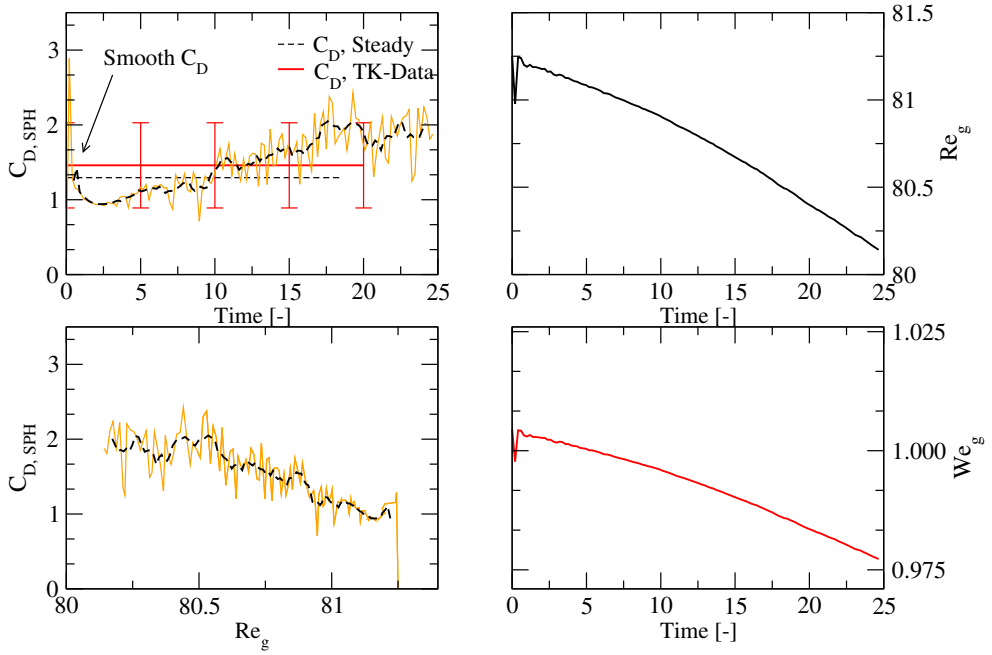

(b) $We_g = 1.0$

Figure 32: Temporal variation of C_D for a 3D drop at an initial $We_g = 0.1$ (a) and $We_g = 1.0$ (b) is shown with transient variations of Re_g and We_g. Plot of C_D as function of varying Re_g is also shown.

deformation rate is higher in early stages but this levels off at a later time as was seen in the 2D case. This is due to effect of surface-tension magnifying as drop deforms and the radius of curvature of the interface increases.

Temporal variation of the drag coefficient is shown in Fig. 32 for non-deforming (top) and deforming (bottom) spherical drop. Figure 32a shows initial rise in C_D and then leveling off to approximately 1.96. Temkin and Kim's (TK) data fit [208] is also shown along with its expected range. Predicted drag for non-deforming drop is observed to fall within this range. Increase in drop velocity due to acceleration reduces the relative velocity leading to a decrease in both Re_g and We_g with time. A deforming drop is observed to have a significantly different time history of drag variation. Except for very early stages ($t/\tau < 2$), the higher Weber number drop is observed to continuously deform and achieve a steady rise in C_D. Also, C_D for the deforming drop is within or slightly higher than the TK data range and is observed to level-off past $t = 18\tau$. The corresponding deformation is about $D_F = 0.8$. Both the drag history as well as the variability in C_D differentiates the deforming case from the non-deforming drop.

Figure 33 shows the flow visualization for the deforming drop along with the relative velocity field (shown every fourth vector) in the $Z = 0$ center-plane. The drop is shown in form of a liquid volume fraction iso-surface colored by local pressure. All time instants show higher pressure (dark patches) around the stagnation region due to slow down in the gas motion by the presence of the drop. Also, lighter regions indicating relatively low pressure are noted on the sides due to flow acceleration. The size of the recirculation region is observed to increase with time as the drop moves downstream and undergoes progressive deformation.

Flow fields for a non-deforming (left column) and deforming (right column) drop are compared in Fig. 34 at $t = 18.5\tau$. A perspective view in the top row shows the change in shape for the deforming drop in relation to the spherical drop. Both

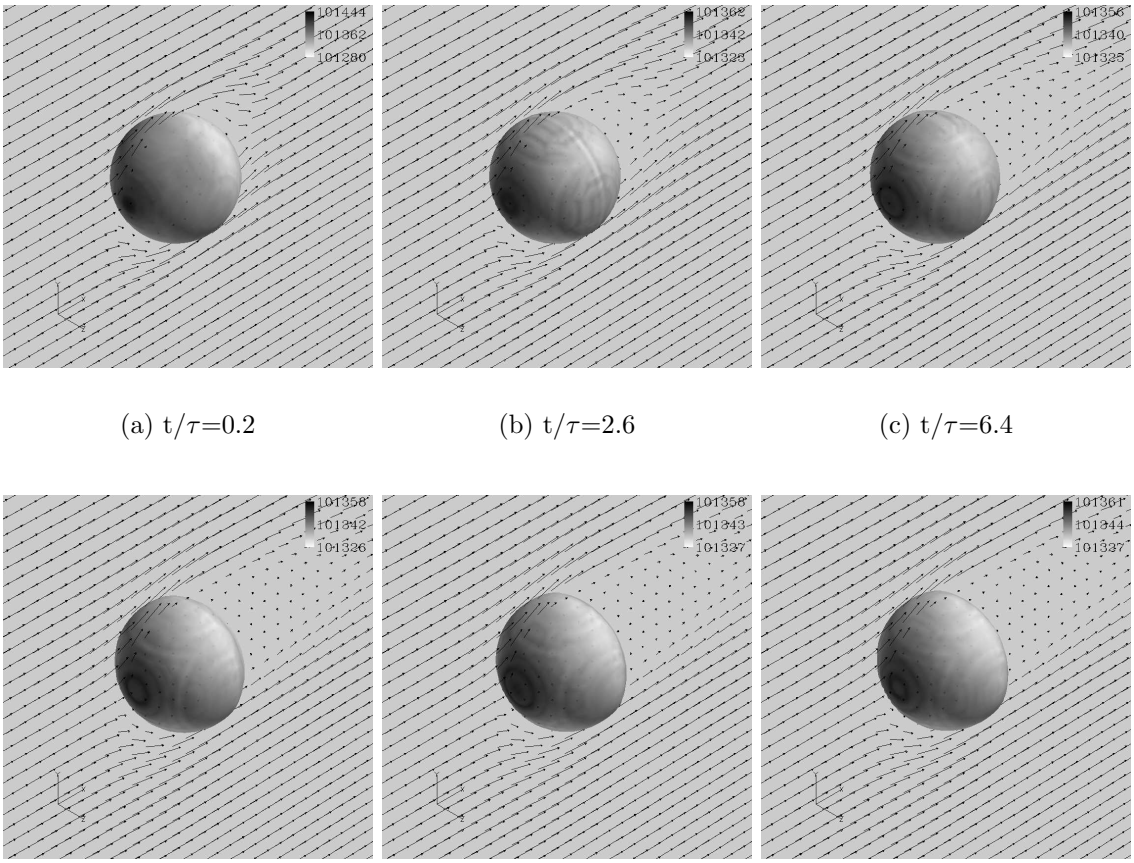

(a) t/τ=0.2 (b) t/τ=2.6 (c) t/τ=6.4

(d) t/τ=12.3 (e) t/τ=15.9 (f) t/τ=18.5

Figure 33: Deformation progression for a 3D drop at an initial $We_g = 1.0$ is shown in the form a liquid volume fraction iso-surface colored by local pressure. Also shown is the relative velocity field.

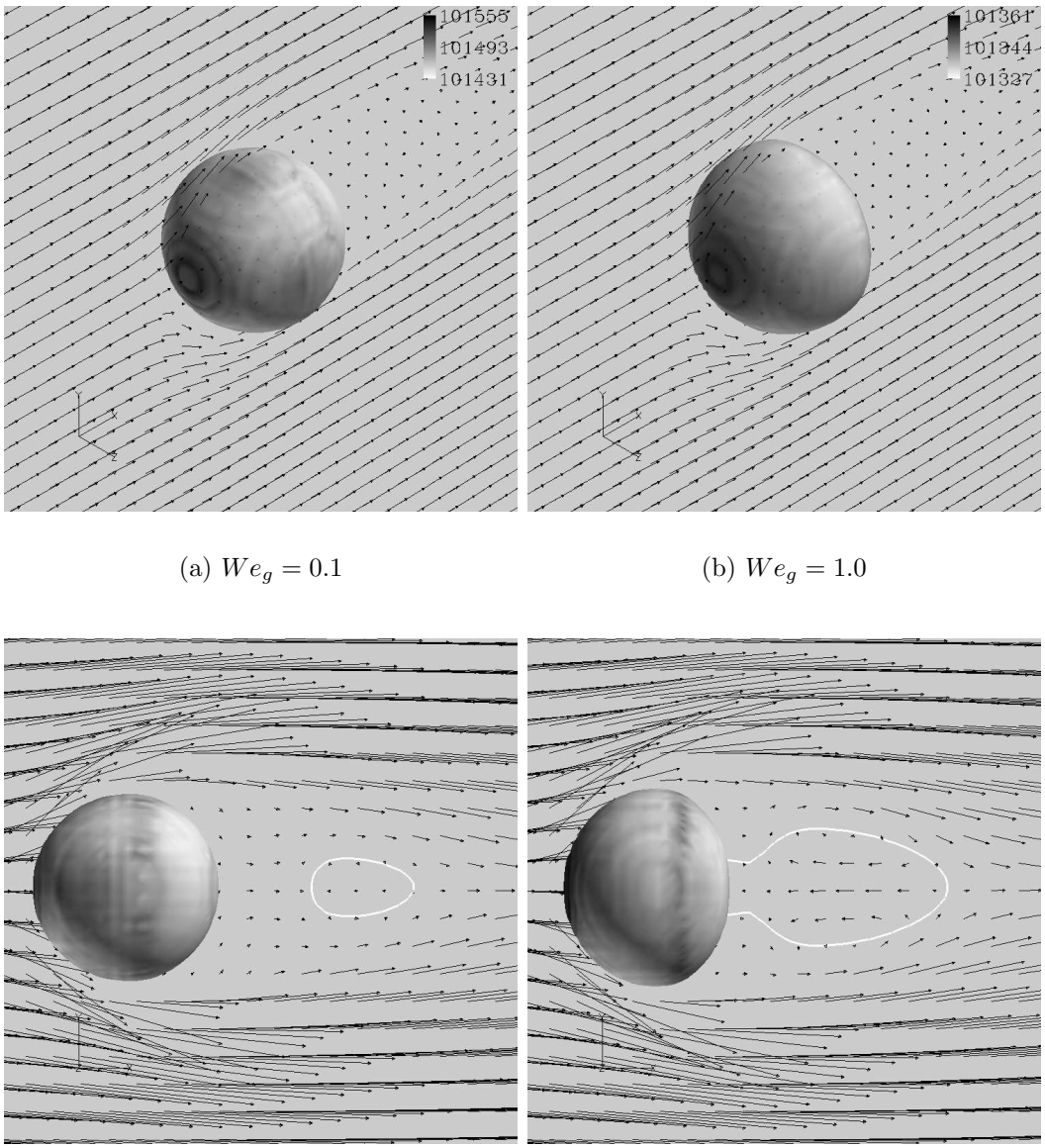

(a) $We_g = 0.1$ (b) $We_g = 1.0$

(c) $We_g = 0.1$ (d) $We_g = 1.0$

Figure 34: Flow field comparison between spherical drop at an initial $We_g = 0.1$ (left column) and $We_g = 1.0$ (right column) at $t/\tau = 18.5$. Drop is shown in form of a liquid volume fraction iso-surface colored by local pressure. Also shown is the relative velocity field with $U = 0$ line contour.

cases show expected pressure rise in the stagnation region. Figure 34(c-d) shows the side view of the field along with $U = 0$ line contour. This line contour indicates the extent of the reverse flow region. As was seen in the 2D case, the recirculation region is detached from the non-deforming drop. Also, an axially moving (in $+X$) flow is noted in the region between the drop and the start of the reverse flow region. Whereas, in the case of the deforming drop, the recirculation zone is attached to the drop and a much wider wake region is observed.

In summary, a series of simulations in both 2D and 3D are performed for a liquid drop to study the transient drag behavior and the drop deformation. The effects of the Reynolds number and the Weber number on the drag dynamics are investigated. For both 2D and 3D cases, the drag coefficient for the liquid drop is always larger than the steady C_D of a rigid sphere at the same Reynolds number. Also, the predicted coefficients is compared and found to be in good agreement with the measurement data of Temkin and Kim [208]. The drag coefficient include effects of acceleration, internal circulation, and deformation; however the aspect of individual quantification of the above effects is left as a future study. Initial Weber number is observed to have significant impact on drag dynamics. It is found that decrease in surface-tension (thereby increase in the Weber number) leads to deformation as well as a larger drag. Flow motion within the drop is also investigated. Presence of so-called "Hill Vortex" for a non-deforming drop is verified. Also, deforming drops forms significantly different wake region with attached recirculation zone. The results thus demonstrate the capability of the method to simulate and predict drop dynamics at both small time- and length-scales.

5.6 Head-on Collision of Binary Drops

In this test case, simulation of head-on collision of two equally sized liquid drops is performed. The outcome of such a collision is influenced by the initial momentum

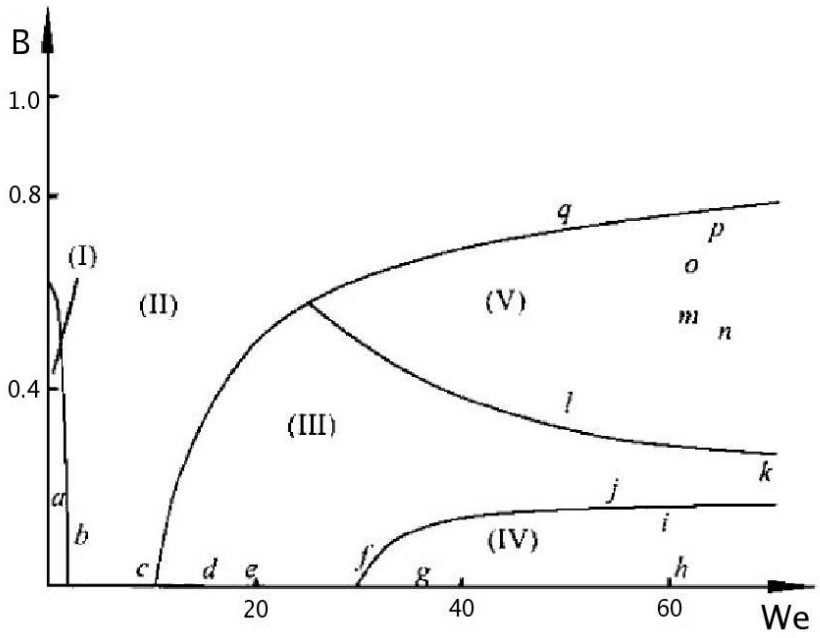

Figure 35: Binary drop collision regimes following Qian and Law [161].

(or inertia) of approaching drops, surface-tension, and viscosity of the fluids. The problem is then characterized by four dimensionless numbers: (i) the density ratio (ρ_l/ρ_g); (ii) the Reynolds number based on initial drop diameter ($Re_D = \rho_l U_r D_o/\mu_l$); (iii) the Weber number ($We_l = D_o U_r^2 \rho_l/\sigma$); and (iv) the Ohnesorge number ($Oh = 16\mu_l/\sqrt{\rho_l R_o \sigma}$). Here, $D_o = 2R_o$ is the initial diameter of the drop, U_r is the relative (to each other) drop velocity, σ is the surface-tension coefficient, and subscripts "l" and "g" represent liquid and gas properties, respectively. The impact parameter (B), defined as the perpendicular distance between the center of one particle and the undeflected trajectory of the other, is zero for head-on collisions.

Several studies exist in the literature that touch upon the aspect of binary collision. Detailed investigations and reviews on this topic were provided by Ashgriz and Pool [10], Qian and Law [161], Neitzel and Dell'Aversana [132], Morozumi *et al.* [130] and very recently by Villermaux [222] in the general context of fragmentation. Figure 35 maps the outcomes of binary droplet collisions into five regimes [161], based on

	U_r (m/s)	U_o (m/s)	We_l	Re_D	$\tau = D_o/U_r$ (ms)
C1	1.955	0.9775	15.75	514.5	0.153
C2	5.6	2.8	129.0	1472.8	0.053

Table 6: Tabulated U_r and We_l for two binary collision cases. Here, $\rho_l/\rho_g = 10^3$ and $Oh = 17.5 \times 10^{-2}$.

the Weber number (We) and the impact parameter (B): (I) permanent coalescence to form a single droplet; (II) bouncing without merging; (III) coalescence followed by separation; (IV) separation with satellite drop formation; and (V) off-center separation. Qian and Law [161] also proposed the critical Weber number criterion to predict the boundary between permanent coalescence and separation for head-on collisions.

A two-dimensional drop-drop collision is considered here for two cases of the Weber number. The computational domain employed is a 4 mm square box discretized into 512×512 cells. Two equally sized droplets of $D_o = 300$ μm are initialized with velocity (U_o) within each particle directed towards each other and quiescent surrounding gas field. The two drops are positioned such that their center-to-center distance is two diameters apart. Periodicity is assumed on all four sides of the domain and uniform grid is employed. The current grid resolves the drop with approximately 38 mesh cells.

The fluid properties are: $\rho_l = 10^3$ kg/m^3, $\sigma = 0.0728$ N/m, $\mu_l = 1.14 \times 10^{-3}$ kg/(m-s), $\gamma_l = 4.1$, $P_{\infty,l} = 5 \times 10^7$ Pa for the liquid drop; and $\rho_g = 1.17$ kg/m^3, $\mu_l = 1.8 \times 10^{-5}$ kg/(m-s), $\gamma_g = 1.4$, $P_{\infty,g} = 0$ Pa for the carrier gas. The gravity is neglected in this study. For these fluid characteristics, $Oh = 17.5 \times 10^{-2}$. Two cases are studied by varying the approaching velocity of the droplets: (1) $U_o = 0.9775$ m/s giving the relative velocity of $U_r = 1.955$ m/s; and (2) $U_o = 2.8$ m/s such that $U_r = 5.6$ m/s. Table 6 show these two cases along with other characteristic parameters.

Figure 36 shows binary collision sequence for the case $C1$ with $We_l = 16$ in the

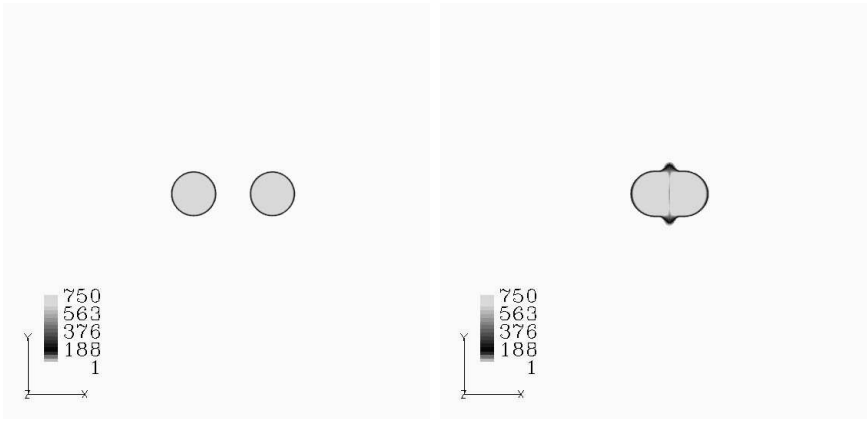

(a) $t/\tau = 0.0$ (b) $t/\tau = 0.64$

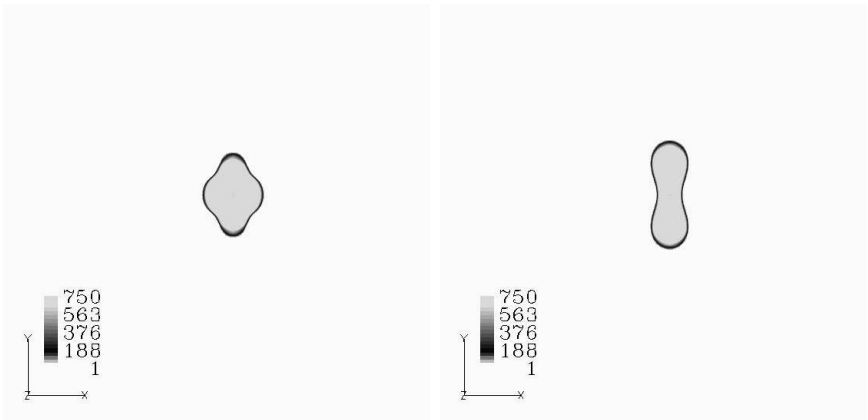

(c) $t/\tau = 0.89$ (d) $t/\tau = 1.78$

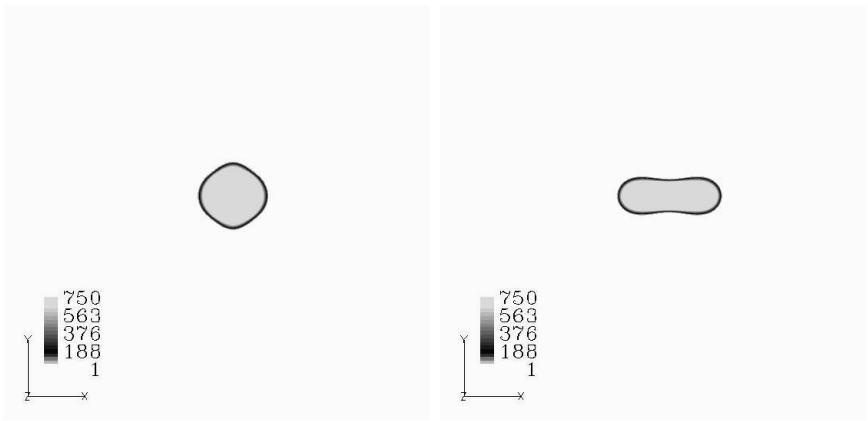

(e) $t/\tau = 2.79$ (f) $t/\tau = 3.87$

Figure 36: Transient flow visualization of a 2D binary drop collision at an initial $We_l = 16$ is shown in the form of a density contour. Here, $\rho_l/\rho_g = 10^3$ and $Oh = 17.5 \times 10^{-2}$.

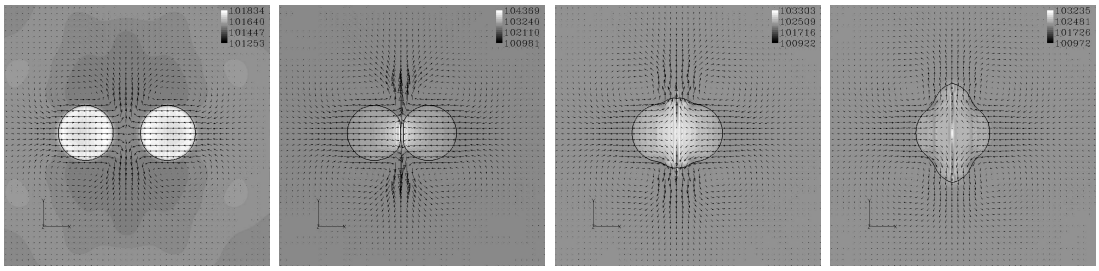

(a) $t/\tau = 0.25$ (b) $t/\tau = 0.51$ (c) $t/\tau = 0.69$ (d) $t/\tau = 0.89$

Figure 37: Transient flow visualization of a 2D binary drop collision at an initial $We_l = 16$ is shown in the form of pressure (solid background) and velocity (every fourth vector) field.

form of density contours. Initial position of the drops is seen in Fig. 36a spaced two-diameter distance apart from their centers. Two approaching drops undergo collision at $t \approx 0.5\tau$ and their free surfaces merge as shown in Fig. 36b. Upon impact, the liquid matter is expulsed in lateral direction away from the impact zone creating a bulb or expansion (Fig. 36c). The liquid keeps draining into this protruding region leading to further expansion. Depending on the ratio of (restoring) capillary forces and (breaking) inertial force, the expansion may lead to a liquid filament formation and eventually breaking up into discrete drops. However, for the current $We_l = 16$, the capillary forces dominate over the inertial forces resulting in a permanent coalescence. Few cycles of oscillations between the elliptical and the circular shape are observed before the merged drop settle to a circular shape.

Flow visualization in form of pressure and velocity field for the drop collision is shown in the Fig. 37. Due to the effect of surface-tension, a pressure rise within the drop is noticed by a light-colored region, as shown in Fig. 37a. Also, an approximate jet arises expulsing the gas away from the impact region (Figs. 37(a-b)) as the distance between the particles decreases. The presence of impact pressure at the merging of the drops at $t = 0.5\tau$ is indicated by a light-colored high pressure region in the center, as shown in Figs. 37(b-c). The impact pressure acts to slow down the incoming liquid

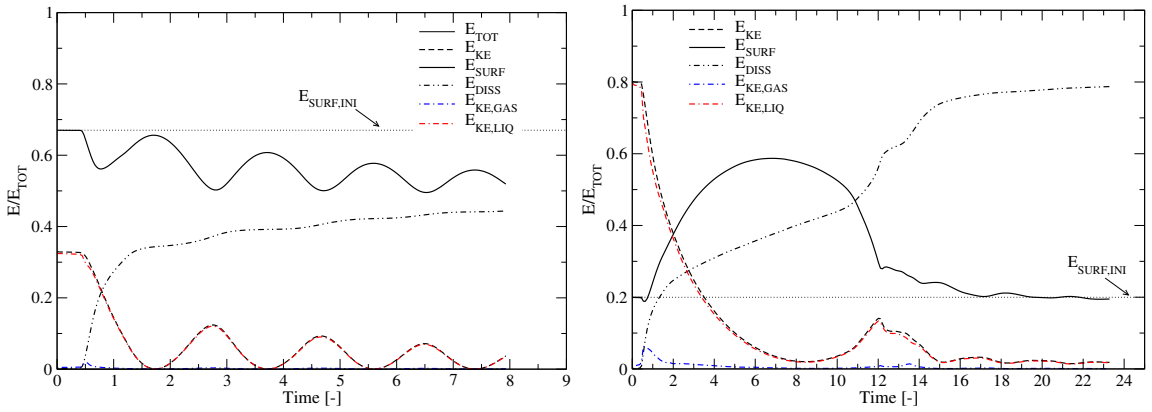

(a) $We_l = 16$ (b) $We_l = 129$

Figure 38: Variation of surface energy, total kinetic energy, and viscous dissipation for coalescing (a) and separating (b) 2D binary collisions.

mass and propel it sideways. Very active gaseous field is also observed with multiple counter-rotating vortex pairs. These vortex pairs arise due to the formentioned gaseous jet.

From energy conservation, the total energy of the collided drop is the sum of surface energy (E_{SURF}), kinetic energy ($E_{KE,TOT}$), and internal energy (E_{INT}). Here, we are interested to assess how either the kinetic or the potential energy and their mutual exchange impact the interface motion and lead to breakup. Therefore, we only consider the balance among the non-internal energy modes and their conversion to internal mode. The total non-internal energy is obtained from the initial surface energy and kinetic energy of the droplets:

$$E_{TOT} = N_D[\sigma S + \frac{1}{2} m_d U_o^2]$$

where, S is the initial surface area of the drop, m_d is the drop mass, U_o is the initial drop velocity, σ is the surface-tension coefficient, and N_D is the number of drops. In 2D, the initial surface area is given by: $S = 2\pi R_o L$, where L is of unit length. The surface energy can also be given as: $E_{SURF} = \int \sigma |\vec{\bigtriangledown} \alpha_l| dV$ where, dV is the cell volume and the integration is carried out over the entire computational domain.

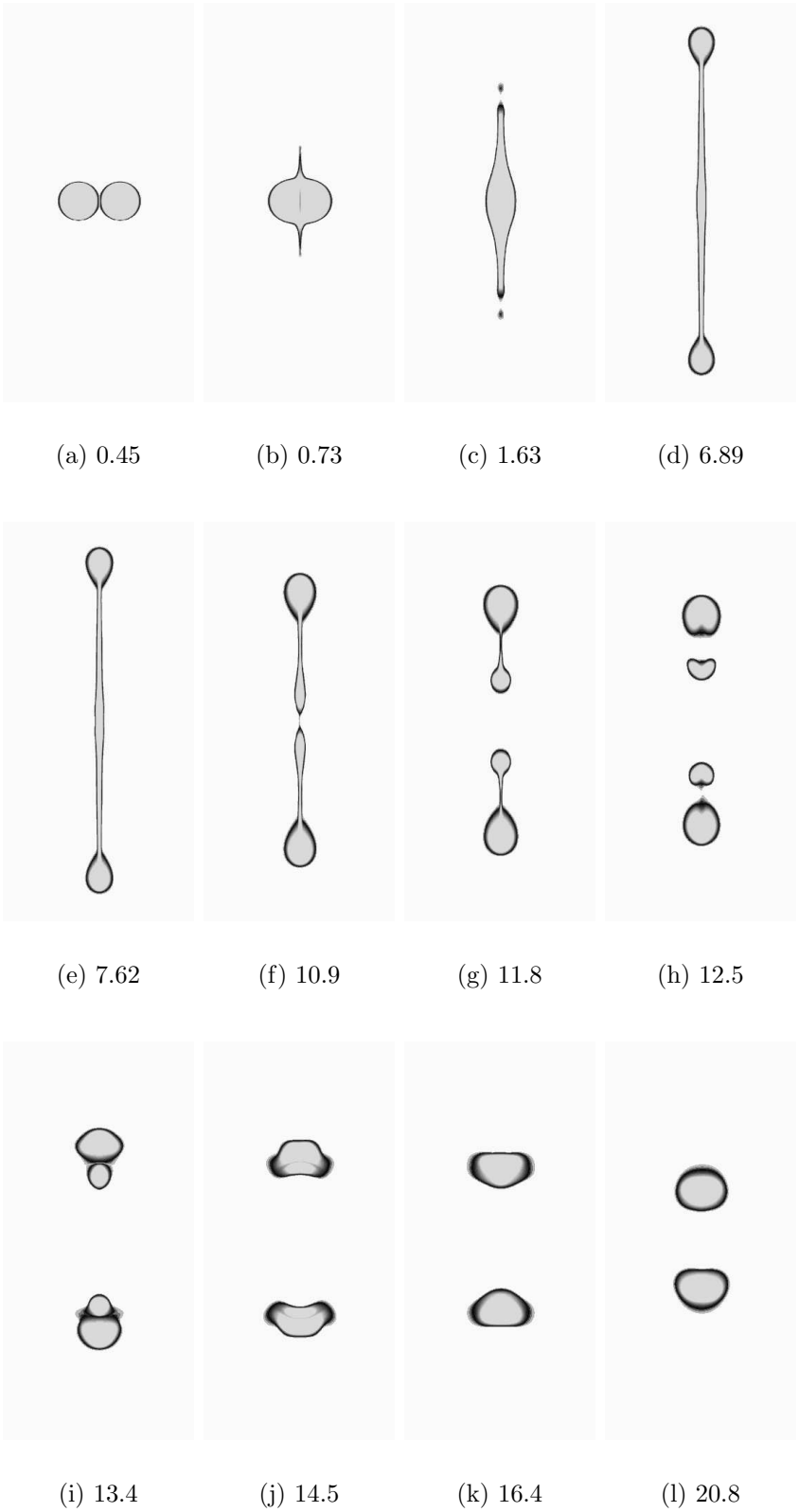

(a) 0.45 (b) 0.73 (c) 1.63 (d) 6.89

(e) 7.62 (f) 10.9 (g) 11.8 (h) 12.5

(i) 13.4 (j) 14.5 (k) 16.4 (l) 20.8

Figure 39: Binary collision sequence at an initial $We_l = 129$ is shown for various t/τ instants. The density contour scaling is the same as in Fig. 36. Here, $\rho_l/\rho_g = 10^3$ and $Oh = 17.5 \times 10^{-2}$.

Similarly, the total kinetic energy is given by: $E_{KE,TOT} = \int \rho \frac{1}{2}(U^2 + V^2 + W^2)dV$ where, ρ is the local density. Further division of the total kinetic energy within each fluid can be obtained by some limit value of the liquid volume fraction over which the volume integration is performed.

Figure 38 shows the energy balance for both the coalescing (left) and separating (right) binary collisions. All variations are normalized by the total non-internal energy of the system. Both the kinetic and surface energy undergo several oscillation cycles, especially for the coalescence case. Also, the cycles are mutually linked such that kinetic energy attains a local maximum when the surface energy reaches local minimum, and vice-versa. Their sum is then subtracted from the initial total non-internal energy resulting in the energy transfered to the internal mode, E_{DISS}. Physically, the transfered energy no longer plays a role in deformation dynamics. The surface energy has a local maximum when the droplet shows the maximum spread/elongation as seen in Figs. 36(d,f). In contrast, kinetic energy attains a local maximum for the least deformed interface as seen in the Fig. 36e.

In the coalescence case, the surface energy peak reaches almost to the initial surface energy at the maximum elongation. However, never exceeding the initial surface energy and the peak magnitude decreasing for the subsequent cycles. In contrast, for the separation case, the surface energy easily surpasses the initial surface energy at the maximum elongation. Such a rise is powered by the initial momentum of the drops which, is observed to be a major portion of the initial total non-internal energy. The aforementioned presence of a gaseous jet is observed in the form of the peak in gaseous kinetic energy around $t = 0.5\tau$ for $We_l = 16$ and $t = 0.75\tau$ for $We_l = 129$. Also, due to large ρ_l/ρ_g ratio, bulk of the kinetic energy resides in the liquid phase.

Qian and Law [161] showed that the outcome of a head-on, equally-sized drop collision resulted in a separation when the initial kinetic energy was large enough

to overcome the dissipation during the deformation. This is verified in Fig. 38b in form of precipitous rise in energy being lost to internal mode but equally steep increase in surface energy resulting in highly elongated filament which eventually breaks up into discrete particles. Also, resulting Weber number criterion [161]: $We_c = 30Oh + 15$ where, We_c is the critical Weber number for separating collision in gaseous environment. For our case of $Oh = 17.5 \times 10^{-2}$, $We_c \approx 20.2$ further verifying the permanent coalescence of the case $C1$.

Figure 39 shows the collision sequence for the separating case. The merged drop configuration is markedly different from the low Weber number case with sharp cusps on the edges due to high velocity impact as seen in Fig. 39b. Further, the sharp cusps shatter into two tiny drops as seen in Fig. 39c which, convect away from the impact zone. Due to high impact pressure in the center, the liquid matter is quickly drained sideways forming bulbs which elongate to form a thin filament. Drop configuration corresponding to maximum surface energy is seen in Fig. 39e and that for first major breakup in Fig. 39f. Further breakup is noticed in Fig. 39(g-h) leading to formation of two secondary drops. Due to their proximity to the primary particles, the newly formed secondary drops collide and merge with the primary particles as seen in Fig. 39(i-j). Finally, rapid decrease in the surface energy as well as the kinetic energy results in a steady configuration of two drops as seen in Fig. 39(k-l). The surface energy is now below the initial surface energy and thus no further breakup is expected [161, 130].

In summary, two cases of head-on binary collision are performed for equally-sized liquid drops. Several physical characteristics of the problem: surface merging upon impact, impact pressure generated liquid matter expulsion, formation of a thin filament, and filament breakup into secondary particles are captured well. Energy balance indicated the impact of high initial momentum in increasing the surface energy to surpass the initial surface energy to result in a non-coalescence outcome of

the collision. This is in agreement with studies of Morozumi *et al.* [130] and Qian and Law [161]. Overall, the method is able to simulate drop breakup and complex interface oscillations taking into account capillarity and viscosity as well as the surrounding medium all within an unified compressible formulation.

5.7 Parallel Computing Performance of the Solver

All previous test cases involve simultaneous presence of small length- and time-scales. In order to achieve resolution of such small scale processes as well as to make the computational algorithm an affordable research/design tool, large-scale computing systems must be employed. Most computing systems used for large-scale computations are designed under a distributed memory model [199]. For a distributed memory platform, a data decomposition method is suitable and is employed for the current algorithm. In this method, the computational domain is partitioned and distributed evenly among the available processors. This allows for easy scalability with increase in the domain size. The standarized Message-Passing Interface (MPI) protocol is used for parallel communication among the processors.

In order to gauge the overall parallel computing performance of the current algorithm, a 2D static drop in equilibrium is simulated for various grid sizes and a number of processors. This test case is used due to its geometric simplicity which allows for a wide variety of processor distributions as well as domain sizes. For this test case, a liquid cylinder of diameter 0.30 m is centered in a one-meter square domain. The liquid cylinder is filled with fluid, whose thermodynamic parameters are: $\gamma_l = 2.4$ and $P_{\infty,l} = 10^7$ Pa, and is surrounded by air, with $\gamma_g = 1.4$ and $P_{\infty,g} = 0$ Pa. The flow is initially quiescent at atmospheric pressure. The density (ρ_l/ρ_g) and viscosity (μ_l/μ_g) ratio considered are 100 and 1.0, respectively, and the surface-tension coefficient is 200 N/m with resulting Laplace number ($La = 2R\sigma\rho/\mu^2$) of 6000. This case was validated against the Laplace-Young law at the beginning of this chapter.

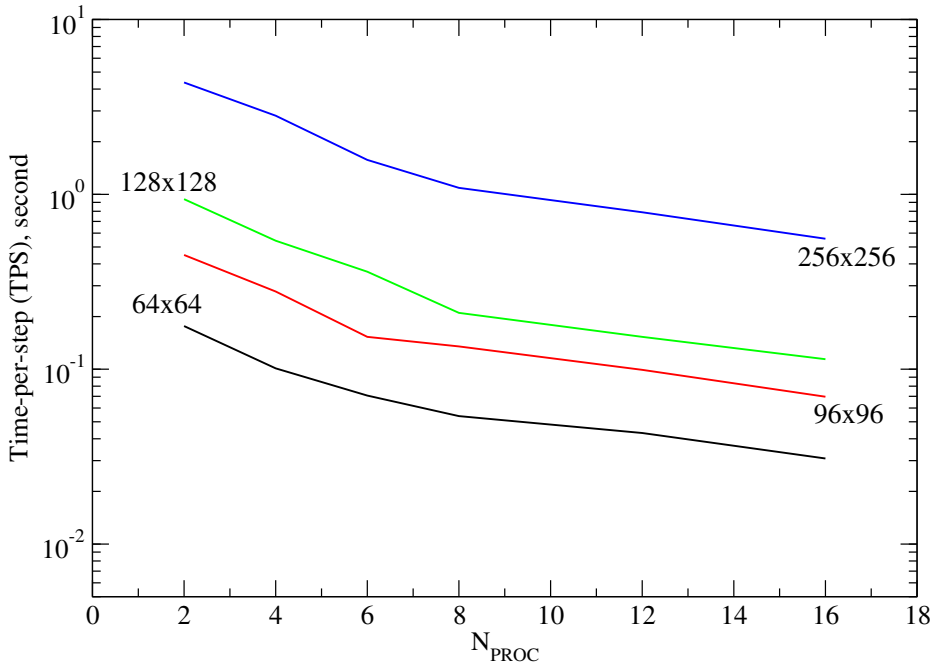

(a) Timing

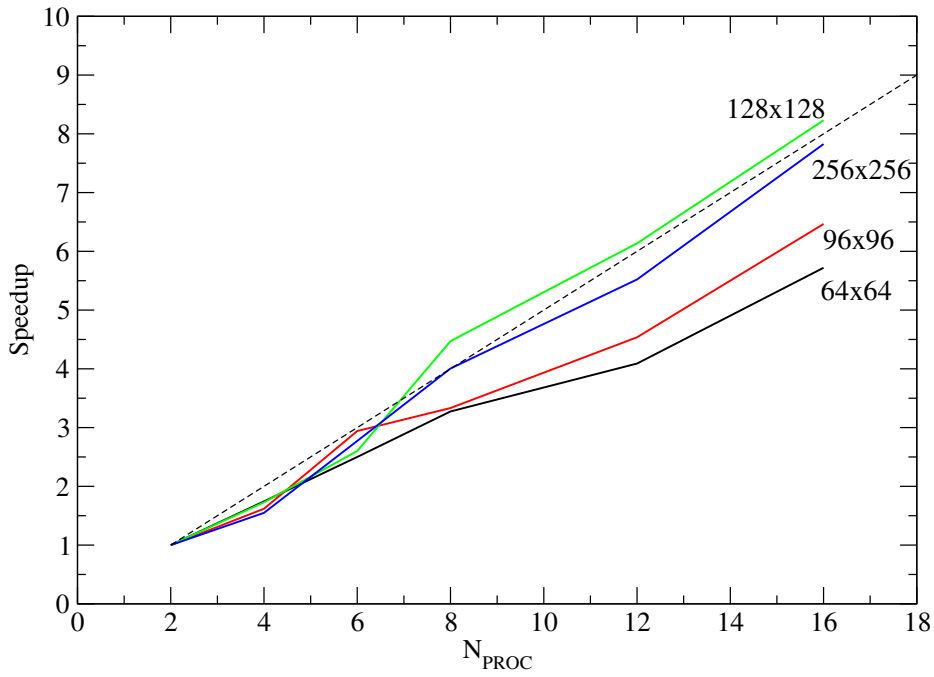

(b) Speedup

Figure 40: The code-timing plots for domains of various mesh sizes and varying number of processors is shown in (a). Also, shown in (b) is the overall speedup of the solver.

	2		4		8	
64×64	0.176		0.101		0.054	
		5.32		5.37		3.88
128×128	0.939		0.543		0.210	
		4.64		5.19		5.18
256×256	4.362		2.817		1.089	

Table 7: Problem scaling efficiency of the solver is demonstrated for various number of processors in form of time-per-step (TPS) of three grid sizes for a Laplace 2D test case. Here, ρ_l/ρ_g=100 and La=6000.

The tests were performed on a Dell Intel PC Cluster with 128 Pentium 4 Xeon 2.4-2.8 GHz (2-CPU Dual 2650s and 1750s) and 132 GB of memory. For MPI parallel operation, the cluster processors are connected via a high-speed Topspin Infiniband Switch. Four grid sizes are simulated for 1000 iteration steps without invoking any read/write from the solver. Average time for one iteration step, called time-per-step (TPS), is then evaluated by taking the ratio of the resulting wall-time for the simulation and the total number of iteration steps. Figure 40a shows the TPS as a function of number of processors for a range of domain size. For a given number of processors, an increase in domain size results in an increase in the time needed to complete one iteration. This is expected due to the increase in number of mesh cells per processor undergoing floating-point operations. Also, for a given grid size, there is a decrease in TPS with increase in number of processors. This is attributed to a reduction in the computational load per processor. However, the rate at which TPS decreases tapers off with increase in number of processors due to parallel communication overhead. This is seen by large or exponentail decrease in TPS for small number of processors followed by gradual reduction at larger number of processors.

One of the characteristic of the computing performance is the problem-scaling efficiency. This relates to the change in time for one-iteration step with respect to a change in the domain size. For an ideal problem and an optimized code, a linear scaling is expected. This means that if the domain is doubled in size, the time

	64×64	256×256	64×64×64	256×256×256
8	0.069	5.57	4.36	-
16	0.029	2.41	2.24	576

Table 8: Computation expense in terms of hours of run-time for one characteristic flow time in the case of a static drop in equilibrium. Two processor setup is shown. Here, ρ_l/ρ_g=100 and La=6000.

taken to complete one-iteration also doubles. Table 7 shows the increase in TPS for each four-fold increase in the domain size. Overall, the average increase in TPS is approximately 4.93 resulting in 81.1% scaling efficiency. Similar scaling efficiency was noted for the 3D simulations in the Sec. 5.1.

The other important characteristic of code performance in the context of parallel computing is the speedup efficiency. The speedup is defined as the time per iteration for one processor divided by the time per iteration on multiple processors. In the current study, the minimum number of processors used for evaluating the speedup is two. Figure 40b shows the speedup efficiency of the solver for four domain sizes. The ideal speedup is also shown in form of a dashed line. Good speedup characteristics are observed for all mesh configurations especially for larger domain sizes. Ratio of computing to communication time plays a major role [199] in the speedup characteristics. In cases of low computational load, the parallel performance is degraded as most time spent is in communication mode. This is seen in form of saturating speedup profiles for 64×64 and 96×96 domains.

Final important characteristic of the algorithm is the time-to-solution which determines the total number of computing hours needed to achieve a solution. This is particularly relevant if the computational algorithm is to be used as a design tool in an industrial setup. Table 8 shows typical computational cost in terms of hours of run-time for one characteristic flow time. Two processor configuration is shown indicating a range of few seconds to several days. Significant time is needed for the 3D setup, however this cost can be reduced by increasing the number of processors.

The other limiting factor is the memory for the data stack which can prevent from using small number of processors for large domain sizes. For example, approximately 569 MB of memory per processor is needed for a 256×256 configuration compared to just 136 MB for a 96×96 mesh.

In summary, the code performance characteristic in terms of problem scaling efficiency, speedup efficiency, and time-to-solution is documented for the algorithm. A geometrically simple configuration of a static drop in equilibrium is used as a test case. Detailed validation of this case was presented in the Sec. 5.1. Here, the computing performance of the solver is mapped and demonstrate that the solver scales well (approximately 81%) with increase in mesh size. Equally good speedup characteristics are obtained for varying number of processors. Overall, the algorithm demonstrates good parallel computing performance.

5.8 Summary

A detailed validation of the five-equation interface model with capillary and viscous effects is presented along with parallel computing performance of the algorithm. Two standard test cases–static drop in equilibrium and deformed drop oscillations–in multi-dimensions (2D and 3D) quantified the accuracy of the model. The model recovers pressure rise across the liquid/gas interface consistent with Laplace-Young law. A series of simulations with varying grid sizes indicates a mesh convergent algorithm. The magnitude of spurious currents is also quantified showing similar order of accuracy as reported in the literature. The oscillating drop case demonstrates that the model consistently captures the four stages of energy exchange between the potential and kinetic modes resulting in a dynamic behavior of the interface.

The buoyancy effects on the bubble dynamics for various Reynolds and E*ötvös* numbers are also shown. Bubble shape-regimes are observed to be reasonably predicted by the model. In the fourth test case, interface dynamics in relation to drop

creation is examined. The method is shown to manage significant interface deformation including filament formation and breakup. A series of simulations in both 2D and 3D for a liquid drop are also undertaken to study the transient drag behavior and the drop deformation. The effects of the Reynolds and Weber number on the drag dynamics are investigated. The drag coefficient for the liquid drop is observed to be always larger than the steady drag of a rigid sphere at the same Reynolds number. Flow motion within the drop confirmed the presence of "Hill Vortex" for non-deforming cases.

Finally, two cases of head-on binary collision for equally-sized liquid drops are studied. The outcome of collision is shown to depend on the initial momentum of the drops. The energy balance for surface and kinetic energy indicates a coalescence outcome in cases where the surface energy variation does not exceed the initial surface energy. Several relevant characteristics like surface merging upon impact, and thin filament formation and its breakup leading to secondary particles are well-captured.

CHAPTER VI

LES OF A LDI COMBUSTOR

Detailed interface resolution cases seen in the previous chapter provides an opportunity to study processes and their driving mechanisms. But seldom is such a detailed methodology is applied to practical configurations. Time-to-solution and overall computational cost are the primary driving factors for any design study. Accordingly, a fuel spray is considered here in the form of a point-volume [114] particle and processes acting on it are averaged over the cell volume.

The detailed simulation approach developed here compliments the engineering models used for practical applications by providing basic closures from first principles like drag effects, time-dependent deformation and atomization, evaporation rates, etc. Also, the detailed two-phase approach provides avenues to develop curve-fits for wide range of conditions, typically not available via measurements, which can be used within a LES simulation.

In this chapter, we report on the LES of spray combustion in an axial-swirler type LDI combustor [20] with a particular emphasis on the impact of an engineering breakup model on the predictions. The focus here is on an application of the liquid atomization process and evaluation of an existing engineering breakup model within the context of LES of a complex combustor flow field.

This chapter is organized as follows. We discuss the experimental and numerical setup for the combustor in the next section. This is followed by validation of the subgrid breakup model and the combustor simulations. Finally, the chapter ends with a brief summary.

6.1 Experimental and Numerical Setup

The LDI combustor [20] consists of a 60-degree, six helical swirl-vaned inlet that leads to a venturi, followed by a short divergent diffuser section that ends at the dump plane of a square combustion chamber. The converging-diverging venturi is designed [20] to reduce the possibility of the return of the spray droplet from downstream and to prevent the flashback of the flame and auto ignition inside the swirler. The swirler has outer diameter of 22.5 mm with the inner diameter of 8.8 mm. The calculated swirl number is 1.0 [20]. Both converging and diverging angles are set at 45 degrees. Figures 41a and 41b show respectively, the computational dimensions, and the grid in the swirl vane region. Air at stagnation temperature $T_o = 294$K and 1 atmosphere enters with a bulk velocity of $U_o = 20.14$ m/s [20]. The combustor square cross-sectional area is $4R_o \times 4R_o$ ($R_o = 12.6$ mm). For the nominal conditions noted above, the Reynolds number (based on inlet diameter $D_o = 2R_o$ and U_o), Re_{D_o} is 30,759. The fuel is injected at 0.415 g/s, which in combination with air mass flow rate of 8.16 g/s gives an equivalence ratio of 0.75 for the reacting case.

Experimental data [20] have been acquired for velocity (mean and fluctuating) at six streamwise locations for non-reacting (gas velocity) and reacting (gas and drop velocity) cases. No temperature or species data have been reported so far.

Characteristic inflow and outflow conditions [155] are used along with no-slip, adiabatic and non-catalytic walls. The inflow conditions for the spray is particularly critical for accurate predictions. Without breakup, a log-normal profile with the Sauter-Mean-Radius ($R32$) of 18 μm and a droplet cut-off radius of 1 μm is used with the spray inner cone angle of 90 degrees based on experimental data [20]. With breakup included no initial distribution is specified. Rather, a mono-modal size distribution of 100 μm (radius) "blob" is injected at every 7.68 μs (to satisfy fuel mass flow rate). Particles are injected along the centerline just behind the center-body approximately 1 mm downstream of the injector tip. Typically, around 30,000

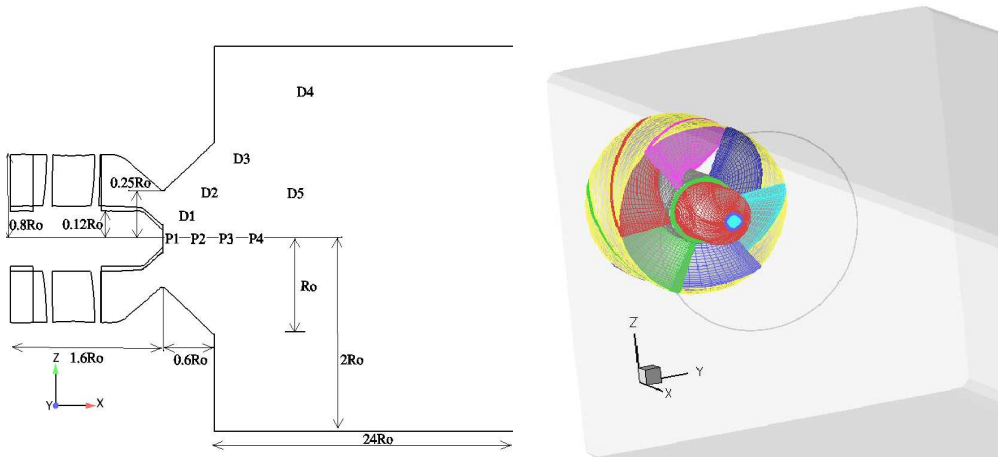

(a) Schematic Diagram

(b) Grid through Swirler Vanes

Figure 41: LDI combustor schematic in the center-plane (a) and computational grid through the swirler vanes (b). The dump plane marks the position $x = 0$ for streamwise locations. Probe locations ($P1-P4$,$D1-D5$) used for collecting unsteady signal and statistics are also shown.

and 10,000 droplet parcels are present in the combustor in an average sense in the no-breakup and breakup cases, respectively. Larger number of parcels are observed in the no-breakup simulation due to relatively smaller drop sizes and less number of particles per group.

The numerical scheme is an explicit finite volume scheme that is second-order accurate in space and time [127]. A butterfly two-domain grid of $253 \times 84 \times 97$ for the cylindrical and $253 \times 25 \times 25$ for the inner cartesian grid is used in the streamwise, radial and azimuthal directions, respectively. Clustering is employed near the walls and regions of high shear. Within the swirler assembly the minimum spacing is $y^+ \approx 6$ along the walls and approximately 8-12 cells are in the shear layer near the dump plane. Here, $y^+ = yu_\tau/\nu$ where, u_τ is the friction velocity and ν is the kinematic viscosity. Grid stretching is limited everywhere to be below 2% in the near field of the injector.

The maximum sub-grid Reynolds number, $Re_{\bar{\Delta}}$ (based on k_{sgs} and LES filter

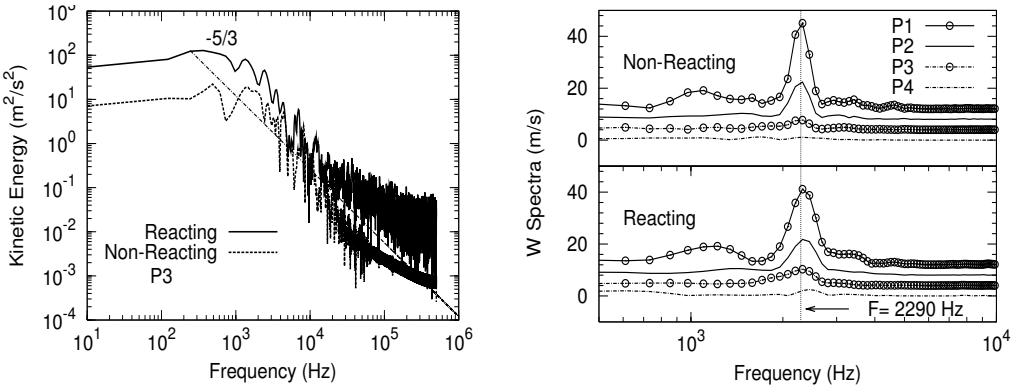

(a) Energy Spectra

(b) W Spectra

Figure 42: Turbulent kinetic energy (TKE) and the azimuthal velocity (W) spectra for non-reacting and reacting cases at specified probe locations. Probe signals are shifted upwards nominally by 5 m/s in (b) for clarity.

width, $\bar{\Delta}$) is about 56 in regions of high turbulence, which suggests that the Kolmogorov scale (η) is around 18 μm. Twelve LEM cells are used in each LES volume, which implies that the minimum sub-grid resolution is 2-3η in the high shear region. In other regions, $Re_{\bar{\Delta}}$ is lower and the LEM resolution becomes closer to η. Even though grid independence study has not been performed for this particular rig, past experience with LEMLES for gas turbine combustors [121, 43, 126, 127] suggests that this resolution is reasonable.

For a single characteristic time τ, around 170 and 1800 single-processor hours are needed on a Linux (2.66 GHz Xeon) cluster for the non-reacting and reacting cases, respectively. Here, τ is defined as the time for one revolution of the precessing vortex core (see discussion later). After the initial transient, approximately 25τ and 21τ of data is statistically averaged for the non-reacting and reacting cases, respectively. Although LEMLES is expensive, due to the high parallel scalability of the solver the turn-around time is reduced by using a larger number of processors.

Figure 42 shows the typical spectra of the resolved turbulent kinetic energy for

both reacting and non-reacting simulations in the region of high shear. For both cases, a reasonable inertial range spectrum (-5/3 law) is recovered suggesting that the current resolution is acceptable to resolve momentum transport in the shear layer regions.

6.2 Results and Discussion

Results for the non-reacting and reacting (with and without breakup) cases are presented in the following subsections. Validation for sub-grid breakup models have been conducted to verify the implementation and are presented next.

6.2.1 Validation of Breakup Model

A standard test case of non-evaporating, solid-cone, high-speed liquid atomization in a cylindrical chamber by Hiroyasu and Kadota [74] is first used to validate the breakup models. Measurements [74] of solid-cone diesel spray were conducted in an enclosed cylindrical apparatus with inside gas as nitrogen at iso-thermal (293 K) and quiescent conditions for varying (0.1 to 5.0 MPa) chamber pressures. The injector is a single-hole nozzle with orifice diameter of 300 μm and 9.9 MPa nozzle-opening pressure. Table 9 presents the test conditions for the three cases used here for validations. Since liquid injection velocity was not measured, it was estimated [42, 169, 138] based on pressure drop (ΔP) across the nozzle as $C_Q\sqrt{2\Delta P/\rho_p}$, where C_Q is nozzle discharge coefficient (0.705). The droplet size distribution were measured using a collection system located about 65 mm (or 217 nozzle diameters) downstream of the injector.

The computational domain is a closed cylinder of 150 mm in length and 200 mm in diameter discretized by a two-domain butter-fly grid approach. Wall boundary conditions are applied on the top (injector end) and the side walls whereas, the characteristic outflow is employed at the bottom boundary. The domain is composed of (axial, radial, azimuthal) $\equiv (50 \times 50 \times 80)$ for the outer cylindrical portion and

Orifice diameter $d_o = 300\mu m$; Liquid density of 840 kg/m^3;
Liquid surface tension of 29.5×10^{-3}N/m;
Liquid kinematic viscosity $\mu_l = 2.1 \times 10^{-3}$Pa-s.

	Case-1	Case-2	Case-3
P_{gas} (MPa)	1.1	3.0	5.0
ρ_{gas} (kg/m^3)	12.6	34.4	57.7
V_{inj} (m/s)	102.0	90.3	86.4

Table 9: Test conditions for the measurements of solid-cone spray by Hiroyasu and Kadota [74].

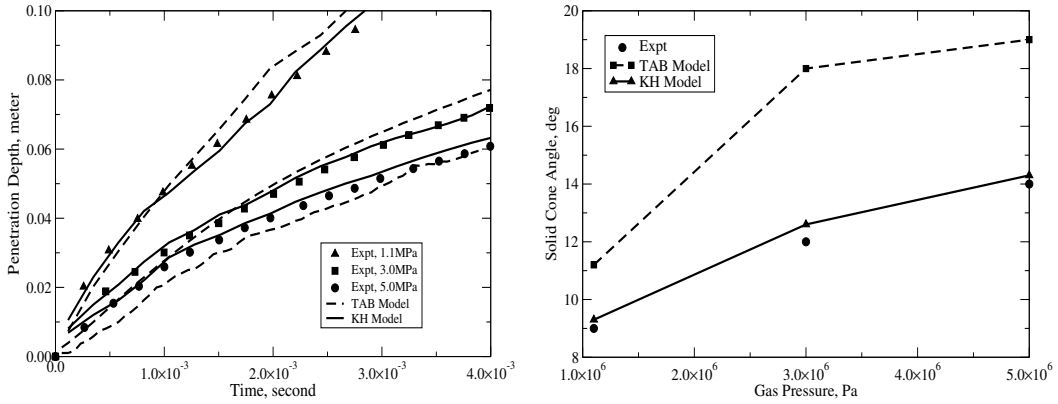

(a) Penetration (b) Spray Angle

Figure 43: Transient spray tip penetration (a) for different back pressures and time-averaged spray angle (b) comparisons with measurements [74].

$(50 \times 21 \times 21)$ for the inner cartesian domain. Non-uniform grid spacing is employed in the axial and radial directions such that the minimum resolution of (axial, radial)$\equiv$ $(1, 0.6)\times10^{-3}$ m near the injector (located at the center-axis) and gradually stretching outwards. Uniform grid was used in the azimuthal direction.

Figures 43a and 43b show respectively, transient spray tip penetration (left) and time-averaged spray angle (right) for three back-pressures compared with experimental data [74]. Overall, a reasonable agreement for transient spray penetration depth has been obtained for both models. Due to no precise definition of spray tip position either in measurements or computations, the tip penetration is the location of the

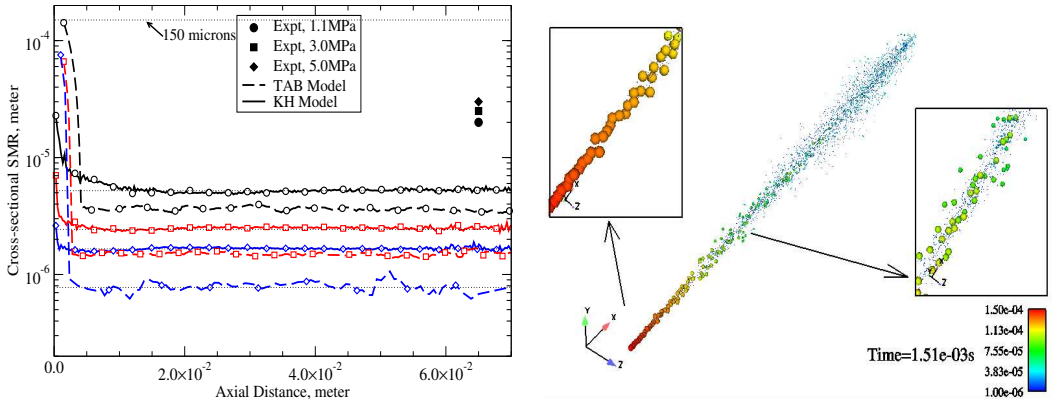

(a) Sauter-Mean Radius (b) KH Model Visualization

Figure 44: Cross-sectional averaged Sauter-mean radius (SMR) variation with axial distance for different back pressures. Closed symbols represent measurement data. Transient spray visualization of the KH model [165] for 1.1 MPa case is shown in (b). Particle spheres shown in (b) are proportional to drop diameter.

leading spray drop parcel or alternatively is the location where 99% of the liquid mass is included. The spray angle is determined by drawing a tangent to the radial spread of the spray starting from the end of the jet breakup and assuring 99% of injected liquid mass. Increase in back pressure is observed to decrease the penetration depth and increase the spray angle. This is due to efficient momentum exchange between the denser gas-phase (at higher pressures) and liquid droplets. Overall, the TAB model [138] is observed to over-estimate the spray cone angle in part due to rapid breakup of injected blobs causing smaller particles to be entrained in the gas vorticity.

The cross-section averaged Sauter-mean radius (SMR) variation with axial distance is shown in Fig. 44a. Closer to the injector, for both the models, the SMR is around 150 μm corresponding to the size of the injected droplets. It decreases rapidly over a small distance from the injector exit indicating breakup/atomization of parent (or injected) drops. Further downstream, it remains more or less constant. In this study, we have neglected agglomeration/coalescence of droplets and therefore, under-prediction of SMR at the measurement location is expected. Both models give

similar size distribution in the far-field. However, there are differences in the near-field with the TAB model predicting an instantaneous breakup of parent droplet from 150 μm to the final size. In contrast, in the KH model, the parent drop size decreases gradually according to the rate equation (which is based on measured mass loss). As is observed by other researchers [8, 207], both the models, especially the TAB model, predict excessive breakup leading to very small drop sizes and thus, small SMR (not accounting for coalescence). The presence of liquid core (in form of large particles) is seen in the wave model and its length has been observed (not shown here) to decrease with increase in gas pressure. No such features are evident in the TAB model due to its step-like breakup of parent drops.

Figure 44b shows an instantaneous snapshot of transient spray field for the 1.1 MPa case using the KH model. The size of the spheres scales with the diameter of the droplets as represented by the computational parcels. Two inset boxes indicates presence of broad spectrum of drop sizes with simultaneous existence of large and small droplets. The stripping breakup of liquid core is also seen in the top-left inset picture. As the spray evolves downstream, the drop size decreases and radial spreading forms a *cone* shaped structure with its apex at the injector exit.

In summary, both break-up models perform adequately even though there are still some well known deficiencies in both models. Since overall the KH model is superior in terms of tip penetration, spray angle, and presence of liquid core, it is used for the combustor simulations discussed in this chapter.

6.2.2 Stationary State Analysis

In this section, we will focus on stationary state statistics of both non-reacting and reacting (with and without breakup) simulations. Comparisons with measurements [20] for gas and droplet velocity field are reported. Earlier gas phase velocity predictions without break-up [146] are included here only to compare with the new results with

break-up. However, all comparison of the prediction (with and without break-up) droplet velocity, size distribution and SMD with data are new results. The analysis therefore, will focus substantially on the droplet statistics and the impact of the break-up model (if any).

6.2.2.1 Gas Phase Velocity Field

Centerline mean streamwise velocity along the length of the combustor is shown in Fig. 45. A prominent central re-circulation zone (CRZ) along the axis is observed for the non-reacting [146] (not shown) and reacting cases. This CRZ is created by the swirling inflow [115, 202] due to a radial pressure gradient caused by the centrifugal effect, which in turn gives rise to axial (and adverse) pressure gradient. For high swirl numbers (amount of rotation imparted to axial flow, >0.6), a strong coupling between axial and tangential velocity occurs and the adverse pressure gradient is strong enough to overcome the axial motion of fluid. This establishes a recirculation zone, a form of vortex breakdown [115], in the central region and this region is the primary aerodynamic flame holding and stabilizing mechanism in gas turbine combustors.

The streamwise extent of the CRZ for the non-reacting case is approximately twice that for the reacting case. However, the CRZ has significantly stronger reverse flow region in the reacting simulations due to heat-release effects. Flow acceleration from 0.9 m/s (non-reacting) to 15.0 m/s for reacting cases is observed further downstream. The starting location along the axial centerline for the CRZ (where axial velocity is zero) is slightly upstream of the dump plane ($x/D_o = 0$). This location ($x/D_o \approx -0.2$) is coincident for both non-reacting and reacting cases as observed in close-up view in Fig. 45b. High streamwise velocity is seen for all cases around $x/D_o = -0.35$ and it is related to the precessing vortex core (PVC), as discussed later. The phenomenon of displacement of vortex core and (as a consequence) reverse flow region from the central axis of symmetry to a new precessional center is known as the PVC [203].

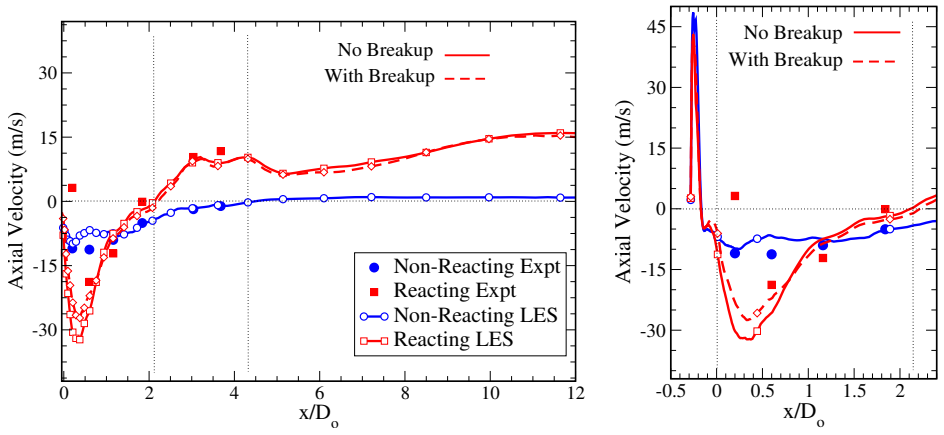

(a) Centerline Variation

(b) Close-up

Figure 45: Centerline mean streamwise velocity comparisons with measurements are shown for both non-reacting and reacting simulations. Axial distance is non-dimensionalized by the diffuser diameter. Close-up near the injector and the dump plane region is shown in (b).

The effect of breakup is seen primarily closer to the dump plane around $x/D_o = 0.4$, as expected. With breakup the reverse flow region is slightly weaker (by ≈ 5 m/s). Such a variation can be attributed to the flame position moving due to change in fuel evaporation rate with the relatively larger initial particles in the breakup case. In the far field, there is not much noticeable difference, suggesting that once the droplets have vaporized and burned the far field evolution is no longer dependent on the features near the fuel injectors.

Flow visualization and comparison of the gas phase velocity profiles were reported to some extent earlier [146] and therefore, are not repeated here for brevity. Nevertheless, some comments are necessary here so that these earlier results can be contrasted with the cases discussed in much detail here. As noted earlier, the vortex breakdown bubble (VBB) or CRZ for the non-reacting case is shallower (in width) but longer in (streamwise) extent when compared to the reacting cases. It is observed to be a single contiguous region with mean flow swirling into and around the VBB. The sense of

rotation is counter-clockwise (CCW) when viewed from the outflow boundary. The presence of corner recirculation zone just past the dump plane near the outer combustor walls is also observed [146]. A high level of turbulence is concentrated between the VBB and the incoming flow, especially in the shear layer region that is around the VBB. As discussed later, for the reacting case, it is in these regions where fuel-air mixing occurs.

Radial profiles of the time-averaged streamwise and tangential mean and fluctuating (or RMS) velocity at various locations were compared with data [146] and very good quantitative agreement was obtained at all locations except the first location at $x = 5$ mm. At $x = 5$ mm location, both measurements and LES indicate presence of peak mean axial velocity away from the center line and a reverse flow region in the central zone. However, the LES data exhibits symmetry in the profiles in contrast to the experiments. The discrepancy at this location may be due to a variety of reasons. In addition to the obvious computational reasons such as grid resolution, there was also some experimental difficulty in obtaining data at this location (for both non-reacting and reacting cases), as discussed earlier in [101, 146]. Nevertheless, the overall agreement with measurements for the non-reacting case offered confidence in the LDKM based LES approach and in the strategy of simulating the entire swirler assembly to eliminate any ambiguity in the inflow conditions.

The presence of heat-release alters the flow-field significantly, especially making the flow motion stronger and more compact in the VBB (Fig. 45). In the earlier paper [146], we focused on comparing the gas phase velocity field for the non-reacting and reaction (without breakup) cases. Here, we focus on comparing some of these features (as well as the droplet properties) with and without breakup.

3D flow visualization of mean streamlines and the reaction rate contours for the two reacting cases are presented in Figs. 46a and 46b. For both cases, the VBB is observed to be a contiguous region with mean flow swirling into and around it.

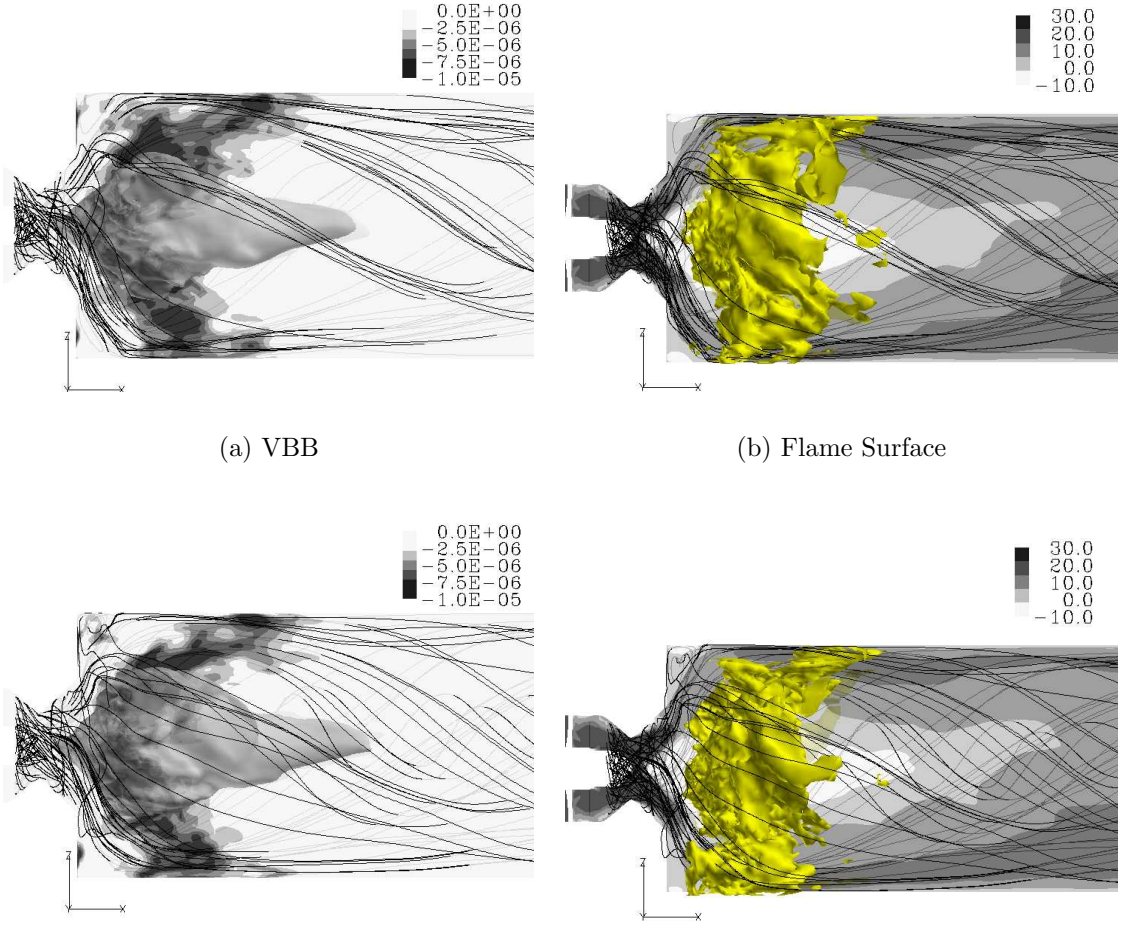

(a) VBB

(b) Flame Surface

(c) VBB

(d) Flame Surface

Figure 46: Streamlines along with zero mean streamwise velocity iso-surface and solid-contours for fuel reaction rate are shown in left column visualizing 3D flow field and the associated VBB. Also, fuel reaction rate iso-surface at 8×10^{-6} along with mean axial velocity contours are shown in the right column. The top row is for simulation without breakup and the bottom row is with breakup.

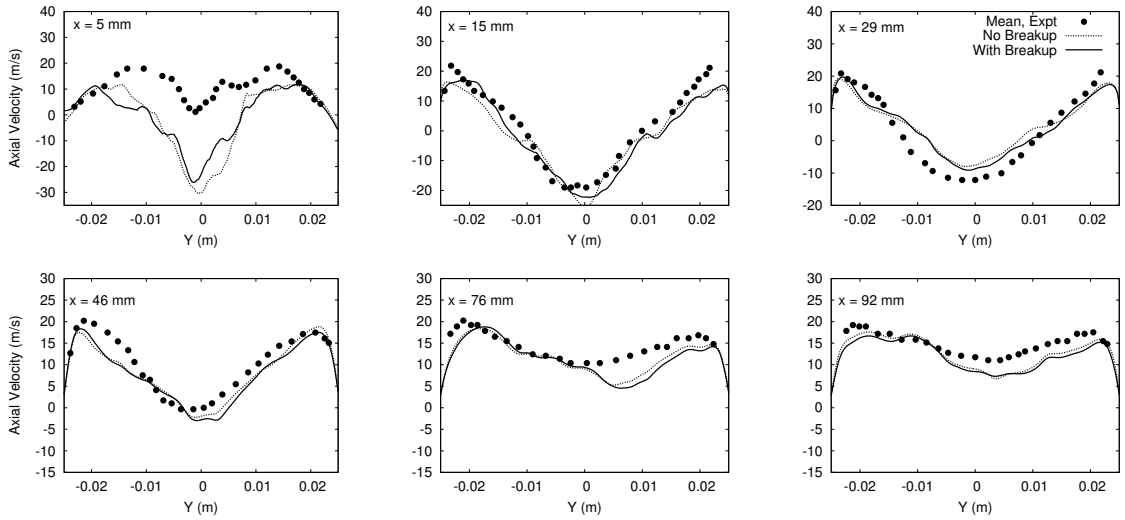

Figure 47: Radial profiles of the time-averaged streamwise velocity at various axial locations for the reacting simulations. Solid lines represent simulation with breakup whereas, the dashed lines are for simulation without breakup.

Streamlines undergoing CCW rotation are observed to move downstream relatively quickly at a smaller radial angle in part due to a smaller VBB (when compared to the non-reacting case). The mean flame represented as fuel oxidation rate (in background) is observed to be lifted-off and positioned in high-shear region between the VBB and incoming reactants. The time-averaged flame region appears here spread over wide area primarily due to unsteady movements of thin flame surface (discussed later). The time-averaged flow field with and without breakup show very similar global features. However, a closer examination shows that the effect of larger particles upstream of the dump plane in the breakup case is to position flame slightly downstream to compensate for overall slower evaporation rate. This shift is more noticeable in the centerline mean axial velocity profile, as discussed above.

The time-averaged radial profiles for mean streamwise axial velocity are compared to measurements [20] for various axial locations in Fig. 47. At first measurement station, LES data predicts strong recirculation in the central portion with almost symmetric peaks on either sides. However, the measurement data is devoid of any

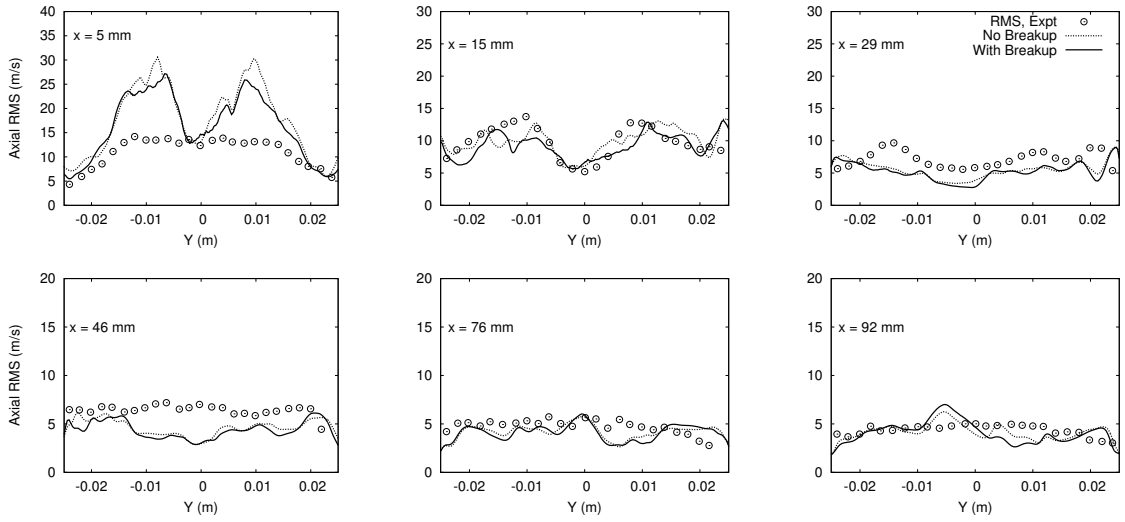

Figure 48: Radial profiles of the time-averaged streamwise fluctuating velocity at various axial locations for the reacting simulations. Solid lines represent simulation with breakup whereas, the dashed lines are for simulation without breakup.

reverse flow and the velocity magnitude is relatively higher. In the experimental study [20], the authors have acknowledged difficulty in sorting seeder particles from high-momentum spray particles at this location and this may be the reason for the positive axial velocity measured inspite of a recirculation zone.

Further downstream, the comparison between the LES and the measurements are reasonable, although there are some discrepancies. The profiles become uniform further downstream indicating rapid 3D mixing. The velocity magnitudes are significantly higher relatively to the non-reacting case especially for wall-jet (closer to the outer combustor walls). Effect of breakup is more dominant again, only in the near field of the injector (e.g., $x = 5$mm); unfortunately, this is also the same location where measurements are uncertain. The breakup case predicts slightly different radial variation with a weaker reverse flow peak velocity.

Streamwise RMS profiles for both reacting cases are compared in Fig. 48. Profiles are observed to become progressively uniform going downstream with reasonable comparisons for intensity. The highest intensity is observed at the first location with

clear peaks on either sides of the VBB. The measurement data is erroneous at this position, as noted before. Although the magnitude and overall trend of the radial velocity is similar to data at all axial locations, the computational results show more fluctuations when compared to data. This may be attributed to a combination of the limited time signal used for statistics (typically, the RMS takes much longer to converge than the mean) and the relatively coarser grid used in the downstream locations. Within the constraint of the computational effort for this simulation, the overall agreement is considered quite reasonable. Similar comments are relevant for the azimuthal components (both mean and RMS). For brevity, these comparisons are not shown here, although some of these for both the non-reacting and without breakup cases were discussed earlier [146].

6.2.2.2 Droplet Velocity Fields and Statistics

The droplet statistics offer more insight into the flow just downstream of the injector and around the VBB. It is also these regions where the breakup model should have any noticeable impact on the flow features.

Radial profiles of the time-averaged Sauter-mean-diameter (SMD or D32) and arithmetic mean diameter (D10) at various axial locations are shown in Fig. 49. Closer to the dump plane at $x = 5$mm, the measurements indicate an increase (from 22 μm to 90 μm) in SMD as the centerline is approached. LES data for both cases also indicate similar increase (from 22 μm to 45 μm); however this increase is not as strong as seen for measurements. Again, this discrepancy may be due to the reasons discussed earlier for the velocity field. In addition, the under-prediction in D32 but a reasonable prediction of D10 may be also a consequence of meager presence of smaller diameter particles. This effect is more pronounced in LES due to the parcel approach, which assigns more particles per parcel for smaller diameters. This creates a situation where evaporation of one parcel with smaller diameter takes away several particles

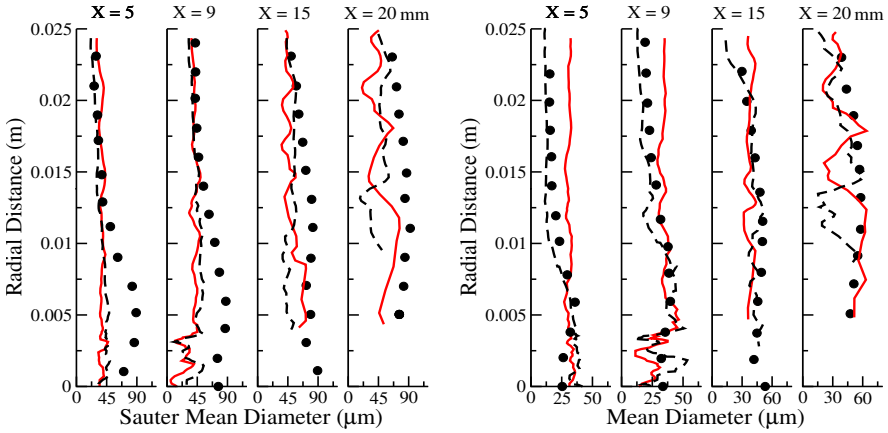

(a) Sauter-Mean (D32) (b) Arithmetic Mean (D10)

Figure 49: Radial profiles of time-averaged sauter-mean (SMD) and arithmetic mean (D10) diameter at various axial locations. Closed symbols represent measurement data whereas solid and dashed lines indicate simulation with and without breakup, respectively.

(associated with that parcel), thereby artificially reducing the total count. This error can be easily removed by tracking more particles but at an added expense.

Further downstream, both D32 and D10 profiles becomes more uniform and approach approximately 80 μm and 55 μm, respectively. Simulations without breakup under predict D32, although the D10 predictions are more reasonable. Some oscillations are noted in the LES data especially at downstream locations. This is again due to low particle count in this region. In the simulation with breakup more particles are seen closer to the centerline. This is likely due to the penetration of initially larger particles into the VBB and their subsequent evaporation.

Measurements [20] for drop velocity components were obtained for five groups/bins based on their radius. Figure 50 shows the radial variation of the time-averaged streamwise velocity for the 16-30 μm, 31-45 μm, 46-60 μm bin sizes. Closer to the dump plane, smaller particles move more swiftly than the larger particles. Also, smaller particles are more likely to be entrained and achieve momentum equilibrium

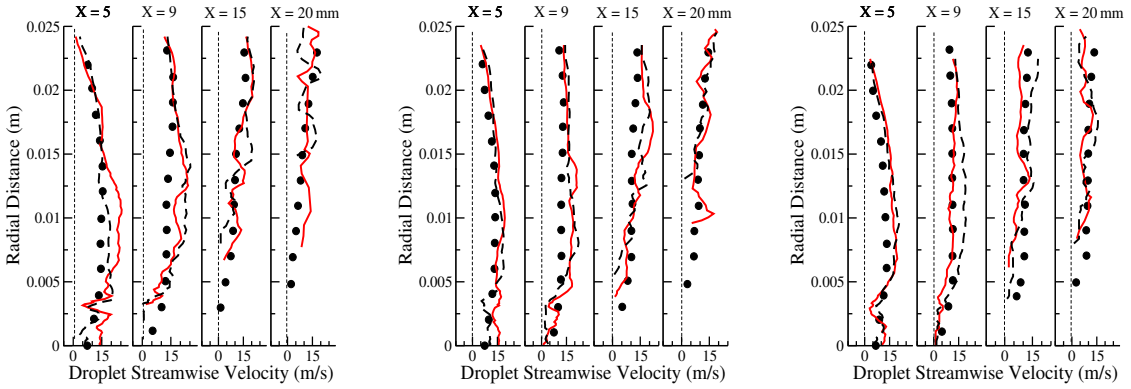

(a) 16-30μm (b) 31-45μm (c) 46-60μm

Figure 50: Radial profiles of the time-averaged droplet streamwise velocity at various axial locations for the 16-30μm (left), 31-45μm (middle), and 46-60μm (right) bin sizes. Symbol represent measurement data whereas the solid and dashed lines indicate simulation with and without breakup, respectively.

with carrier gas due to their lower inertia. Further downstream, sudden expansion at the dump plane and adverse pressure gradient due to the swirling motion slows down the gas-phase, however particles do not respond to these changes as swiftly due to their higher inertia.

As the spray evolves past the dump plane, effects of drag decelerates its motion, which appears in form of lower velocity for all bin sizes. Radial variation observed closer to the dump plane in the form of distinct (broad) peaks disappears further downstream and oblique line profile emerge with high velocity regions away from the centerline.

Particle radial velocity profiles for the same three bin sizes are compared with measurement data in Fig. 51. Closer to the dump plane the radial motion of the spray is reflected in these profiles with the velocity increasing with radial distance. However, the magnitude of the peak decreases with axial distance possibly due to 3D effect. Velocity lag between the large and small particles is again observed with peaks for 16-30 μm bin size approaching 32 m/s, whereas for 46-60 μm bin size closer

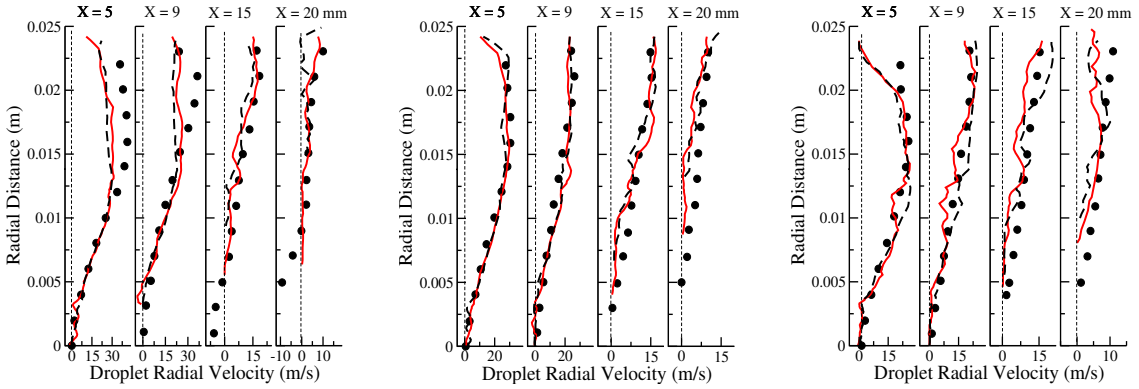

(a) 16-30μm (b) 31-45μm (c) 46-60μm

Figure 51: Radial profiles of the time-averaged droplet radial velocity at various axial locations for the 16-30μm (left), 31-45μm (middle), and 46-60μm (right) bin sizes. Symbol represent measurement data whereas the solid and dashed lines indicate simulation with and without breakup, respectively.

to 22 m/s. This effect is more prominent for smaller particles due to reduced inertia effect. Both simulations show similar behavior for all three bin sizes with slightly more radial extent towards the centerline for the breakup case.

The peak magnitude for the azimuthal component (not shown here, for brevity) significantly dwarfs that for axial and radial velocity. Also, the peak magnitude for large particles is almost half that for smaller bin sizes. The latter being of comparable magnitude to the gas-phase tangential component. The strength of rotation is maintained for all bin sizes further downstream indicating effects of momentum equilibrium with gas-phase and undergoing solid-body rotation. Profiles become more uniform while moving downstream and this is observed for all bin sizes.

In summary, the time-averaged particle velocity profiles for the droplets show reasonable agreement with data except at the first location at $x = 5$ mm. The reason for this initial disagreement has been discussed earlier. Both cases, with and without breakup show very similar results, especially in the far field indicating that once the spray is formed, rapid evaporation, fuel-air mixing and combustion process,

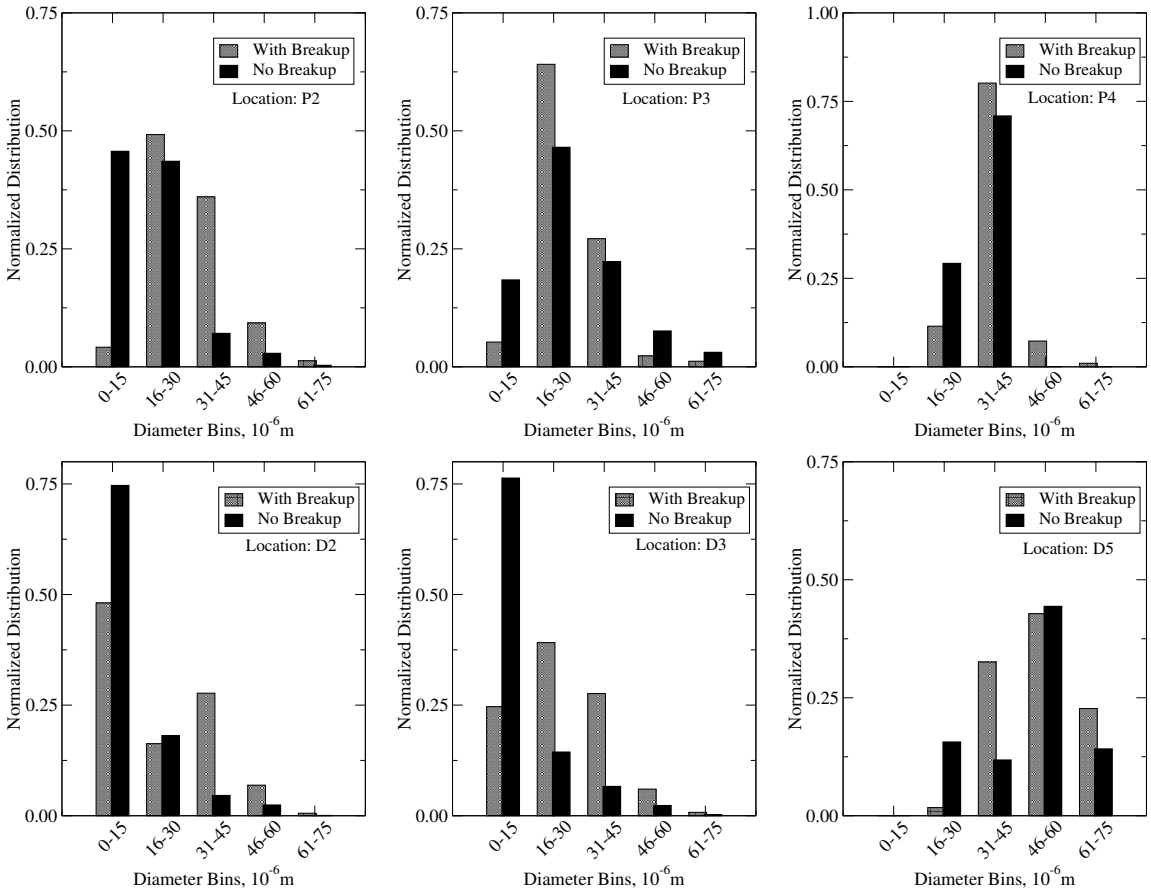

Figure 52: Particle size histograms at six locations as indicated in the schematic are shown for both with and without breakup simulations. Spatial variation of discrete locations includes pre-flame as well as post-flame regions.

all of which are gas phase processes dominate. Closer observation show one feature consistently in the breakup simulations: the particle field shows droplets closer to the centerline in the far field (especially for the smaller particles). This is consistent with the measurements and suggest that one contribution of the breakup model is to provide a broad spectrum of drop sizes (especially large), and therefore, increase the dispersion into the region closer to the centerline where there is substantial recirculation. However, overall, this effect does not seem to dominate the flame holding characteristics in this combustor.

As noted earlier, the case without breakup employed an inflow droplet distribution extracted from measurements and therefore, reasonable agreement is expected

if the LES is conducted properly (as is the case here). However, the reasonable prediction of droplet statistics (both magnitude and radial extent for various bin sizes) for the breakup case demonstrates that the breakup model in conjunction with the Lagrangian tracking approach is able to achieve correct momentum for a spectrum of drop sizes.

Another way to demonstrate the effect of breakup is to examine the predicted particle distribution at various locations. Particle size histograms at six locations (as indicated in the schematic) are shown in Fig. 52. For each set, the time-averaged data in terms of number of particles per bin size for a particular control volume is used. Number density for each bin is obtained as the ratio of the number of particles in that bin to the sum of particles across all bins for that control volume. The number of particles and its sum across all bins varies in space, and it is also different for with- and without-breakup cases. Therefore, similar to SMD or D10 at a particular location, size histogram is dependent on characteristics of particles present in the control volume of interest.

Locations for histogram are positioned such that the spray quality can be assessed (i) just after injection ($P2$, 3 mm after injection), (ii) just downstream of the dump plane ($P3$, 7 mm after injection), and (iii) in the VBB ($P4$). All these location are along the centerline. Additional two locations diagonally (at 45^o; $D2$, $D3$) and an off-center location ($D5$) within the VBB are also analyzed. These histograms clearly show the effect of breakup. At $P2$, without breakup the size distribution is similar to a spray with D10 of 18 μm. However, with breakup, since a mono-modal distribution of 200 μm diameter drops is injected, the subsequent breakup results in a broader distribution (with D10 of 31 μm) of particle sizes.

Further downstream at $P3$, both cases show similar distribution among bin sizes, however proportion for mid-size bins (16-45) bin in case of with-breakup is relatively higher. Within the VBB region (location $P4$), predominantly large particles are

noted for both cases. Similar observation can be made at $D5$. Conspicuous absence of small particles (0-15) is also noted. Both these locations within the VBB have high temperature making existence of small particles rare. Diagonal locations ($D2$, $D3$) show not only the radial dispersion of droplets due to PVC but also the effect of evaporation. This is especially true in the breakup case.

Time-averaged gaseous fuel mass-fraction in the vicinity of the VBB for the two cases is compared in Fig. 53a-b in the $X-Z$ center plane. Difference in injection size distribution is observed just downstream of the nozzle exit in form of significant region gaseous fuel for no-breakup simulation. This is because its initial distribution already contains small droplets, which due to higher surface area per volume, evaporates faster right after injection. Further downstream, both cases achieve similar gaseous fuel profile with maximum gaseous fuel located in or around the VBB. Complete oxidation of fuel is observed by $x/D_o \approx 1.0$ with most of the fuel located upstream of $x/D_o \approx 0.5$. Visualization of D10 variation (solid-contours) along the $X-Z$ center plane superimposed with fuel reaction rate line contours is shown in Fig. 53c-d. Within the reaction front, for both the cases, larger particle size is observed. However, no particles exist past the downstream end of the flame brush.

6.2.3 Transient Analysis

Spray interaction with the turbulent shear layer and the subsequent mixing of the vaporized fuel with air and combustion are all unsteady events. In addition to the steady data discussed above, analysis of the time-evolving features in the combustor is expected to shed further insight into these interactions as well as any effect of breakup in the near field. Therefore, a closer examination of the flow in and near the vicinity of the VBB and the swirling shear layer is carried out to determine the performance of the breakup model and its relevance for this type of combustor simulations.

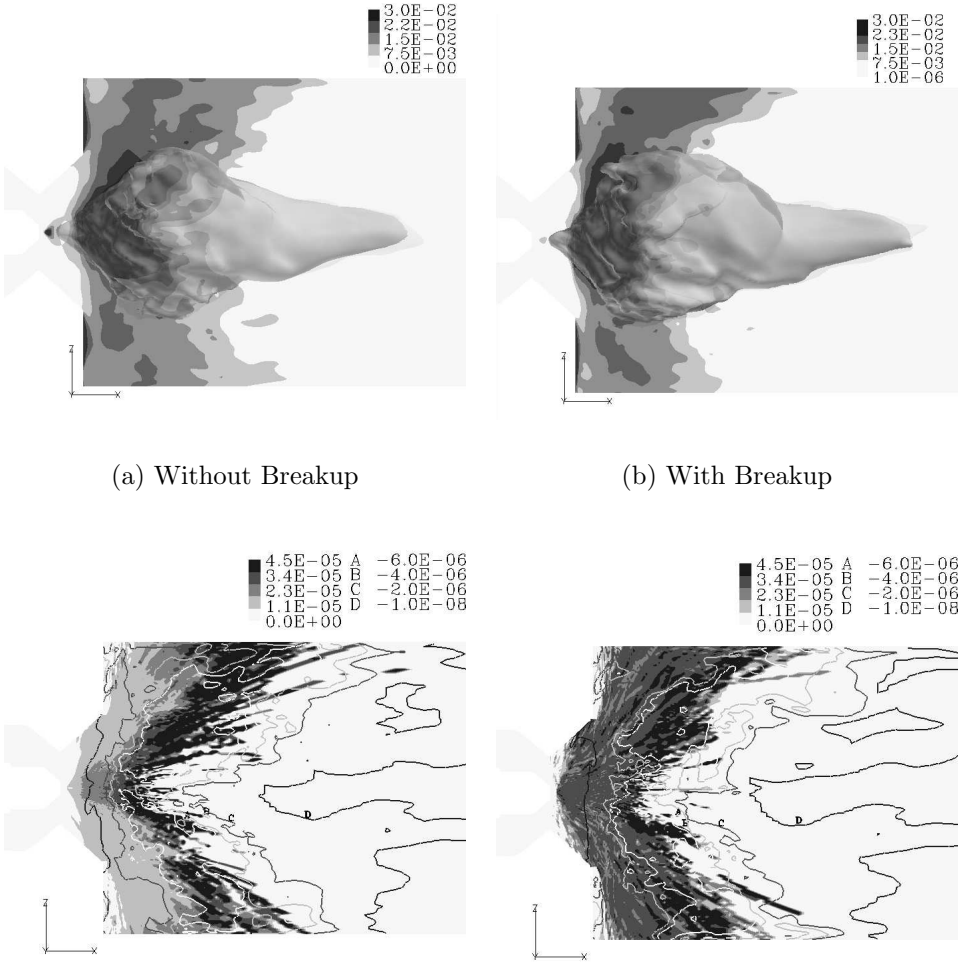

(a) Without Breakup

(b) With Breakup

(c) Without Breakup

(d) With Breakup

Figure 53: Spatial distribution of fuel mass fraction (top row) is shown along with an iso-surface for zero mean axial velocity. Bottom row indicates spatial variation of D10 (solid contours) in relation to mean fuel reaction rate (line contours).

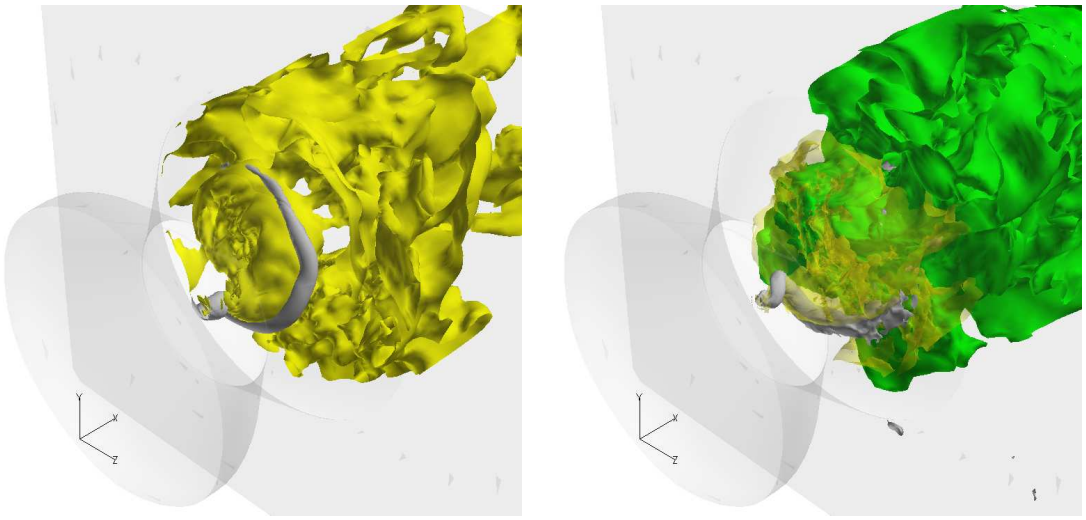

(a) Non-reacting (b) Reacting

Figure 54: Instantaneous visualization of PVC (grey) precessing VBB (yellow) and flame surface (green) at some arbitrary time-instant for both non-reacting (left) and reacting (right) simulations. VBB and flame portions past $r > R_o$ are not shown to increase clarity of visualization.

6.2.3.1 Vortex-Spray-Flame Interactions

Unlike the steady state picture of VBB (discussed earlier) that showed a single contiguous (and symmetric) region, the instantaneous picture is quite different with significant local asymmetry that is highly unsteady. Figures 54a and 54b show, for non-reacting and reacting cases, respectively, precession of reverse flow region and flame surface (reacting case) by the PVC rotation. Presence of swirling motion creates hydrodynamic instability in form of a spiral around the reverse flow region just past the stagnation point where axial vortex breaks down occurs. PVC is visualized using pressure iso-surface (at 93.5 kPa) and is observed to be a helical (or spiral) filament with anti-clockwise (looking from inflow boundary) winding in space and clockwise rotation in time. The turnover (or one rotation) time is estimated at τ=0.4 ms, corresponding to a frequency of about 2.3 kHz (this frequency shows up in the spanwise spectra, Fig. 42b).

Velocity vectors (not shown) around the PVC showed clockwise rotation all along the filament. Also, the leading (or outer) edge was observed to have positive axial velocity whereas the inner regions a reverse flow. Both reacting and non-reacting cases show reverse flow region positioned along the inner confines of the PVC and forming a similar spatially-winding helical shape. However, since it is located on the trailing side of the temporal rotation, it lags behind the PVC. When averaged over time gives a simple, geometrically centered VBB as noted in previous discussion.

Precessing motion of the carrier gas entrains the particles (except for large Stokes number drops) and thus, the PVC plays an effective role in their dispersion (shown later). The flame is also confined by the PVC and the reverse flow region created by the VBB, as shown in Fig. 54b. Transient analysis (not shown) of the flow field indicated that the most upstream (in streamwise direction) point of the flame surface never protrudes into the diffuser section. However, it is positioned closest to the dump plane based on the PVC rotation (described below).

Figure 55 shows two snapshots of transient motion of particles, flame surface, and the PVC for with- and without-breakup cases. The rotation of the PVC disperses the liquid fuel particles around and into the VBB region (its boundary is identified by a zero axial velocity line contour). The particles are dispersed radially right to the venturi walls just half-way to the dump plane. Preferential accumulation of small droplets around the PVC, while the heavier droplets move downstream relatively unaffected by the local flow structures is clearly observed. The instantaneous flame structure (visualized in form of fuel oxidation rate) is relatively thin in the central portion, while it is somewhat thicker near the outer combustor. These features are just representative as the flame motion is highly transient. Analysis shows that the flame thickness is approximately $0.5 - 0.7$ mm in the center (resolved with 2-4 LES cells and hence 24-48 LEM cells). Thicker flame regions could be explained by both the (coarse) grid resolution and the multiple flame-regime behavior (discussed next).

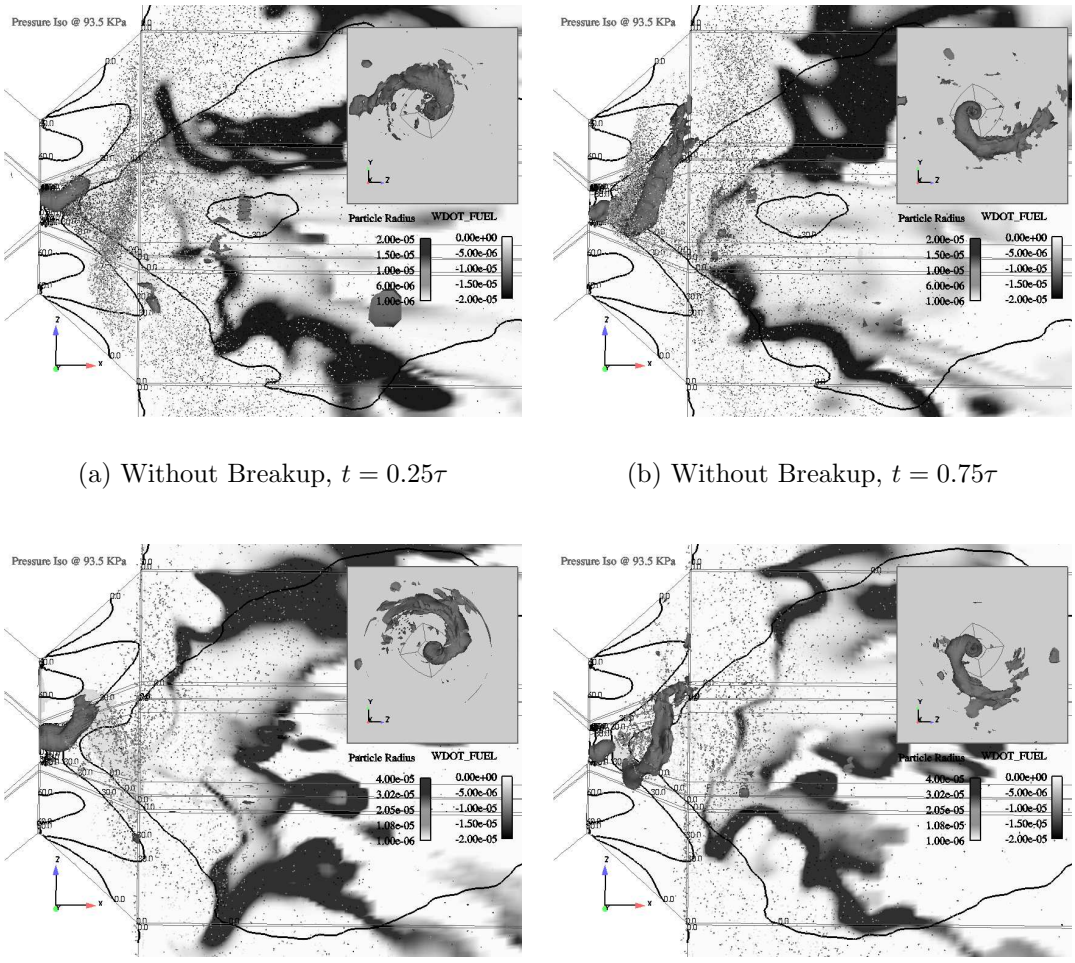

(a) Without Breakup, $t = 0.25\tau$

(b) Without Breakup, $t = 0.75\tau$

(c) With Breakup, $t = 0.25\tau$

(d) With Breakup, $t = 0.75\tau$

Figure 55: Instantaneous droplets, the fuel reaction rate (dark-colored), and the PVC (light-colored iso-surface and inset) at two instants for simulation with and without breakup. Also shown are the time-averaged streamwise velocity contours.

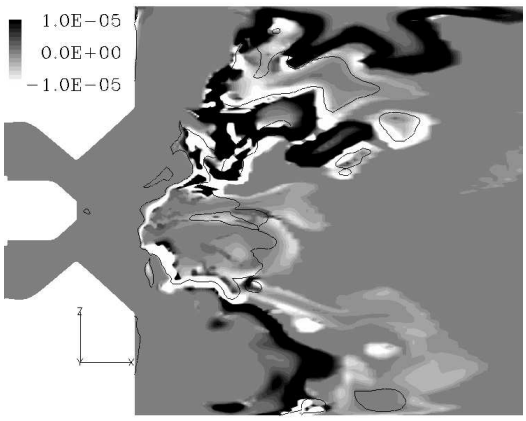

Figure 56: Flame index at some time instant is shown for the reacting simulation. Instantaneous fuel oxidation rate is represented solid gray scale contours. Also, the stoichiometric equivalence ratio is indicated as a thin line.

Instantaneous flame structure is analyzed using the Takeno flame index, FI=$\nabla Y_{FUEL}.\nabla Y_{O_2}$ [230]. To determine the flame regime, an indexed reaction rate is defined based on the flame index as: $\dot{\omega}_F^* = |\dot{\omega}_F|\frac{FI}{|FI|}$, and is shown in Fig. 56. The stoichiometric equivalence ratio is shown as a thin line in the same figure. The flame is premixed when the FI (and consequently $\dot{\omega}_F^*$) is positive and diffusion when the FI is negative. In the central region, presence of fuel vapor in proximity of recirculating hot gases devoid of oxidizer generates diffusion flame, as seen by light colored "V" shaped flame surface. This is confirmed by the coincidence between the flame and the stoichiometric line. Further outwards in the radial direction, significant dark colored contours are seen, indicating a premixed flame. Along the outer edges there is sufficient time for fuel-air mixing to complete before ignition. It is also noted that non-premixed and premixed flames occur adjacently near the top-half of the combustor making the overall flame surface to appear thick, as seen in Fig. 55b. Several light-colored regions are seen in the post-flame region. There regions indicate diffusion burning fuel vapor evaporated from the particles that have gone through the primary flame without completely losing their identity.

These results confirm earlier observations [127] that in complex swirling spray combustion systems the flame structure can be very complex and locally range from non-premixed to premixed burning. The current LEMLES approach does not make any a priori assumptions regarding the nature of the flame and therefore, is able to capture the multi-faceted flame structure in these combustors.

6.2.3.2 Effect of Breakup on Near-field Spray Evolution

Instantaneous spray visualization at some arbitrary time is shown in Figs. 57a and 57b, for without and with breakup cases, respectively. All droplets are colored and sized by their respective particle radius. Progressive sequence of breakup events is seen in Fig. 57(b) with 200 μm diameter particle/blob injected into the swirling airstream. Effect of PVC is seen by the change in trajectory of streamwise particle evolution. Within the first 1 mm of injection location, initial breakup appears to be completed with the formation of several (approximately 70-150 groups) product particles. Furthermore, shear stripping of the parent blob continues forming more product parcels downstream and depending on local conditions and Weber number, both product and parent particles undergo further breakup. It appears that in the present test case, all breakup events are completed within the first 4 mm of injection and a finer particle distribution emerges downstream.

Quantitative metrics in form of particle size histograms are presented in Fig. 57(c-d). A 15 μm diameter bin is chosen for both histograms. Quality of spray is accessed by considering histogram of particles in certain regions. Figure 57(c) is taken over a space encompassing all particles from injection location to 4 mm downstream. Large sized particles are seen for the breakup simulation, as expected. For intermediate size range, both simulations produce similar distribution. Further downstream, around the dump plane region in the high-shear mixing region, Fig. 57(d) indicates that the breakup simulation achieve distribution similar to that of without-breakup case.

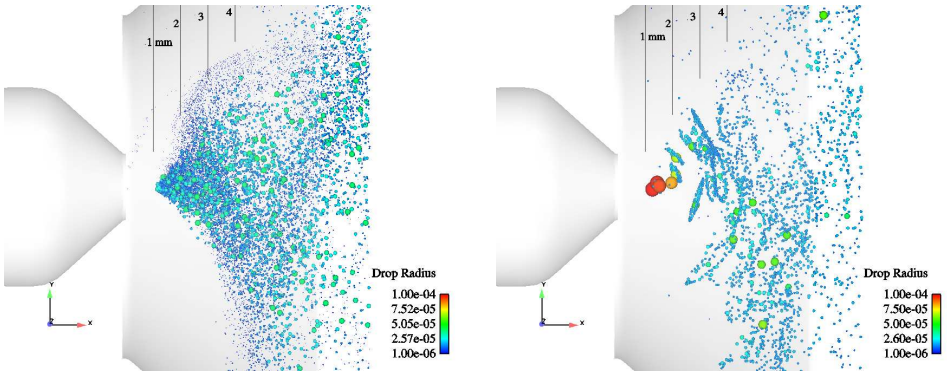

(a) Without Breakup

(b) With Breakup

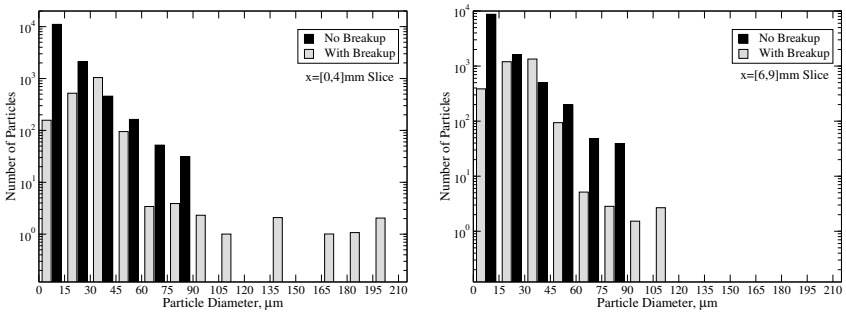

(c) X=0 – 4 mm Slice

(d) X=6 – 9 mm Slice

Figure 57: Instantaneous visualization of droplets for both with and without breakup simulations. All droplets are colored and sized by their particle radius. Also, droplet diameter histogram over specified volume for respective simulations is presented and compared.

Analysis shows that the droplet distribution created in the breakup simulation is equivalent to the pre-specified distribution in the no-breakup case.

Since the breakup process occurs within a narrow 4 mm region just downstream of the injector, the major impact of breakup is on the fuel evaporation in this region. This was shown before in the form of steady state gaseous fuel mass fraction in the center-plane. The other processes in the injector vicinity such as the PVC is not affected by the breakup since it is driven by the incoming swirling gas flow from the swirler vane assembly. Since the spray distribution downstream of the initial breakup region is similar to the no-breakup case (where the spray was adjusted to match experimental data), the gaseous fuel concentration and its eventual mixing with incoming swirling air produces similar flame response, as seen in Fig. 55.

6.2.3.3 Thermo-chemical Behaviour

The thermo-chemical states of fuel-air mixing and oxidation provides information on flame structure in the mixture-fraction space. Spray flame response in the mixture-fraction (f) space was studied by Reveillon and Vervisch [170]. They showed that spray flame behavior differs significantly from the classical gaseous diffusion flames [149]. The two-phase ($2PH$) oxidation limits were noted to be lower and depart from the single-phase (SPH) limits. Both no-breakup and breakup cases show similar results (as seen next) and therefore, only characteristic results for the no-breakup case are discussed.

Instantaneous scatter plots for temperature versus mixture fraction at various streamwise locations (from the fuel injector exit) are shown in Fig. 58 for both with and without breakup cases. Lines are shown for both the mixing and the reacting equilibrium limits. The stoichiometric mixture fraction (f_{STOIC}) based on assumed $C_{12}H_{23}$ chemistry is approximately 0.064 and the corresponding adiabatic flame temperature (T_{ADIA}) is about 2320 K. The global mixture fraction (f_{glob}) based on global

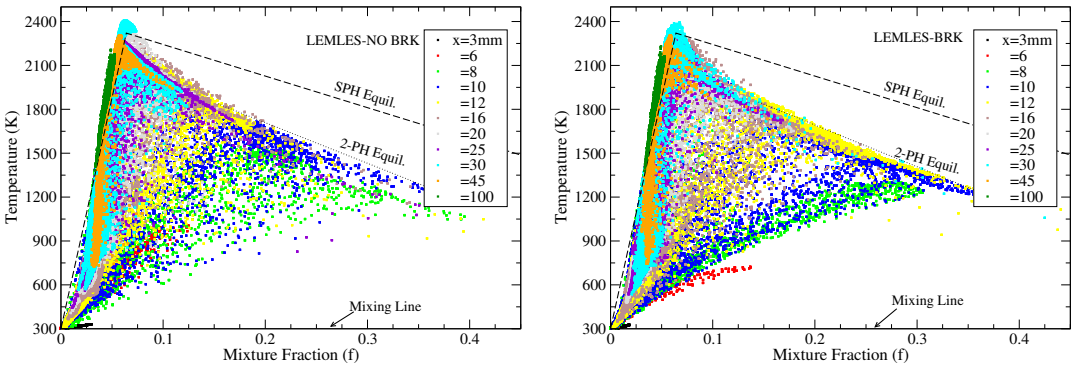

(a) Without Breakup

(b) With Breakup

Figure 58: Instantaneous scatter plot for temperature versus mixture fraction at various streamwise locations for simulations with and without breakup. The analytical stoichiometric mixture fraction is noted to be around 0.064.

equivalence ratio (of 0.75) is 0.049.

The scatter in the mixture-fraction space varies from $f = 0$ (pure air) to $f \approx 0.4$ (equivalence ratio $\phi = 9.7$), with majority of the samples within $f < 0.1$. This is indicative of fast mixing process among the fuel, air, and post-flame gases. Samples closer to the mixing line ($T \approx 300$) are noted only for the 3 mm location suggesting some ($f < 0.03$) mixing. Further downstream at 6 mm, samples are in the intermediate temperature $(400 - 1000)$ range indicating both pre-heating of the vaporized fuel as well as the presence of post-flame species. Presence of flame (in the form of high temperature samples) is observed only downstream of the dump plane. For example, at the 12 mm location, two distinct branches are observed. One along the SPH equilibrium line on the left ($f < f_{STOIC}$) and the other along the $2PH$ equilibrium ($f > f_{STOIC}$) on the right. The equilibrium limit on the left is followed well, however aforementioned departure from the SPH equilibrium is observed on the right. Peak temperature is observed around the f_{STOIC}.

Further downstream (past 16 mm), thermo-chemical state reach an equilibrium

state with most samples lying around the designated limits. Peak temperatures predicted by the LES are close to analytically computed T_{ADIA}. Scatter in both the mixture fraction as well as temperature reduces beyond 60 mm with almost all samples falling along the left equilibrium line. This is indicative of completely reacted mixture undergoing bulk advection with no further reaction.

Radial distribution of thermo-chemical states at 12 mm downstream of the injector exit is shown in Fig. 59. This location lies about 5 mm downstream of the dump plane. Instantaneous temperature, fuel, water vapor and oxygen mass fractions, and fuel oxidation rates are plotted in the mixture-fraction space. Analyzing the scatter data as a function of the radial location bins helps identifying local states in the regions of interest. Five radial bins are selected to separate regions of VBB, high-shear, and corner re-circulation zone. Temperature scatter shows distinct regions of highest temperatures around the VBB (all red, some green and blue) region. These samples lie very close to the adiabatic equilibrium line, indicating completely reacted mixture. Intermediate samples ($400 - 1000$K) are also noted (mostly blue and magenta, some green) in the scatter indicating mixed states of fluid: presence of pre-heated vaporized fuel and partially reacted gas. This state stems from high-shear region between the venturi walls and the VBB. Additionally, high turbulence activity within this region forms wide range of gas composition (reactant-product mixture) and temperatures. Such mixtures undergoing reaction are subject [119] to ignition delay giving rise to the observed partially reacted mixtures. Samples beyond $r > 15$ mm (cyan) show lower values for f and temperature with scatter around $f \approx 0.01 - 0.06$, $T \approx 500 - 1900$K, indicating both completely reacted samples (those along the equilibrium line) and partially reacted (intermediate temperature) mixtures. This region is part of corner re-circulation zone, which provides longer residence time for complete reactions but also entrains fresh reactants at the same time forming samples with intermediate temperatures.

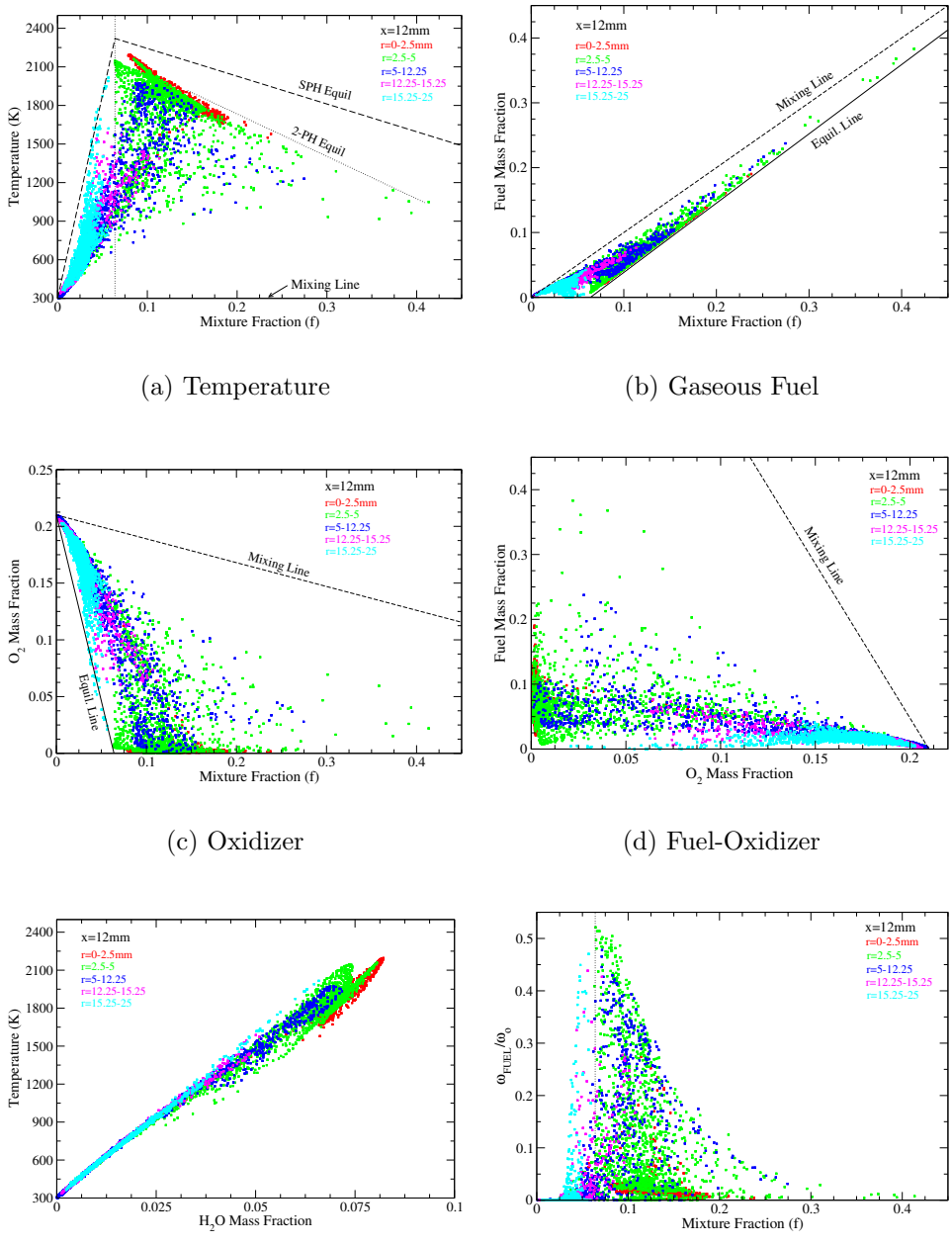

(a) Temperature

(b) Gaseous Fuel

(c) Oxidizer

(d) Fuel-Oxidizer

(e) Temp-H_2O

(f) Fuel Oxidation Rate

Figure 59: Instantaneous scatter plot for various quantities like temperature, gaseous fuel, oxidizer, water-vapour, and fuel reaction rate at 12 mm downstream of the injector. The data is dissected into five radial bins from the combustor centerline. The fuel reaction rate is normalized by $\omega_o = 10^{-4}$.

Scatter plot for species mass fractions at 12 mm location are also shown in Fig. 59, which to a large extent are in agreement with above explanation for temperature field. Samples from the VBB ($r < 8$ mm) are noted to lie along the equilibrium line seen in Fig. 59b and contains negligible oxidizer, as seen in Fig. 59c. Very few samples in either plots are noted along the mixing line indicating diffusion burning mode at this location. Fuel mass content seen in Fig. 59b and Fig. 59d for the VBB region is due to penetration of large fuel particles undergoing evaporation. Highest product species is observed for the VBB region, as seen in Fig. 59e consistent with the presence of high temperature region in the VBB. Reaction rates (normalized) shown in Fig. 59f in this region are found to be relatively low both due to equilibrium limits reached for certain samples, as well as negligible content of oxidizer available for the gaseous fuel to burn. Samples for the corner recirculation zone are observed to contain significant amount of oxidizer compared to the fuel content as seen in Fig. 59d, indicating recirculation zone allowing for complete fuel burning. All range of product species is observed in this region as seen in Fig. 59e. Scatter for the reaction rate is observed to have peak around the stoichiometric mixture fraction. This is in agreement with observations of Reveillon and Vervisch [170].

6.2.3.4 Particle-particle and Particle-gas Correlations

Scatter plots at two axial locations of parcel temperature, streamwise, and azimuthal velocity versus parcel diameter are shown in Fig. 60. Both with- and without-breakup results are shown side-by-side to understand the effect of breakup modeling. In order to further visualize the spatial dependence of these correlations, the data is separated into radial bins. Some overall comments valid for both with and without breakup cases can be made based on the analysis of these results. In the current case, the liquid parcel is at 380 K when injected while the gas temperature is initially 300 K. Thus, when the droplets evaporate their temperature drops. Also, the thermal

response time [37] is proportional to square of drop diameter and is relatively smaller for smaller size droplets. As shown in Fig. 60a the smaller droplets respond more quickly to the local changes. Presence of heat source (VBB) further downstream (beyond the dump plane) is observed in the form of higher drop temperatures in the $400 - 650$ range (Fig. 60b). Again, smaller parcels overwhelmingly show both the higher and lower temperature peaks.

The effect of breakup is clearly noticeable in these figures. Closer to the injector location (radial location $r < 5$ mm) particles are observed to have larger diameters and temperatures close to the injection temperature. Only after breakup, for radial locations $r > 5$ mm, smaller particles are observed with significant thermal response. Further downstream past the dump plane, both cases show similar diameter ranges and thermal response with most scatter in diameter range of [20-40]μm for the breakup case. The presence of smaller particles at this location in the no-breakup case is from the specified inflow distribution. This is evident from their thermal response and their radial position in the shear layer ($r \approx [5 - 12]$ mm) region.

Parcel velocity correlations with its size are shown in Figs. 60(c-d) and Figs. 60(e-f) for axial and tangential components, respectively. Dashed line shown in these figures indicate initial velocity imparted to parcels during injection. The velocity response time for particles is also proportional to the square of drop diameter. Thus, particles with lower inertia are able to follow gas-phase more closely and this is seen in form of peaks (min, max) for smaller sizes. At 3 mm downstream, however parcels in the outer regions (green, blue) have significantly differing velocity. This is in part due to the presence of the PVC, which entrains the droplets into its vortical flow. Further downstream (at 12 mm), parcels in the $5 < r < 15$ mm range move quickly, whereas those in the outer regions ($r > 15$ mm) have slowed down to around 10 m/s. Tangential correlation shows mostly counter-rotating motion of particles closer to the injection location, however further downstream negative tangential component

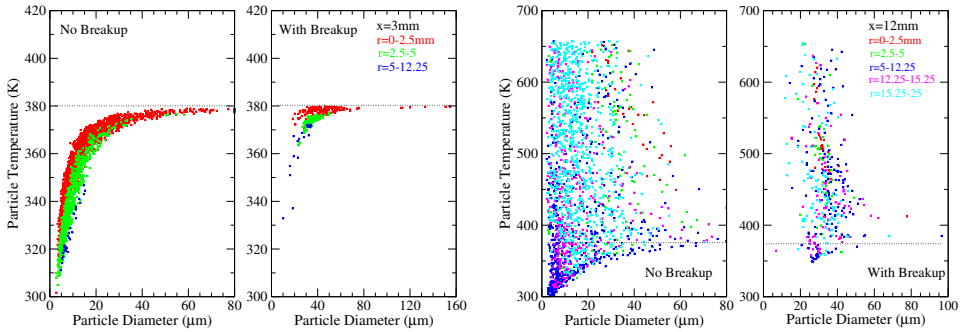

(a) x =3 mm

(b) x =12 mm

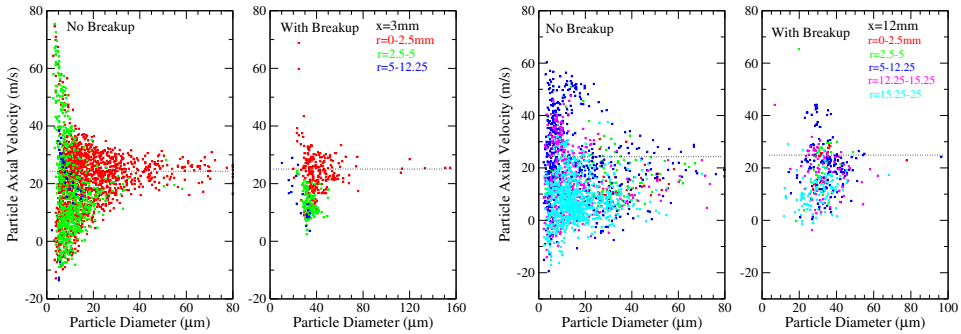

(c) x =3 mm

(d) x =12 mm

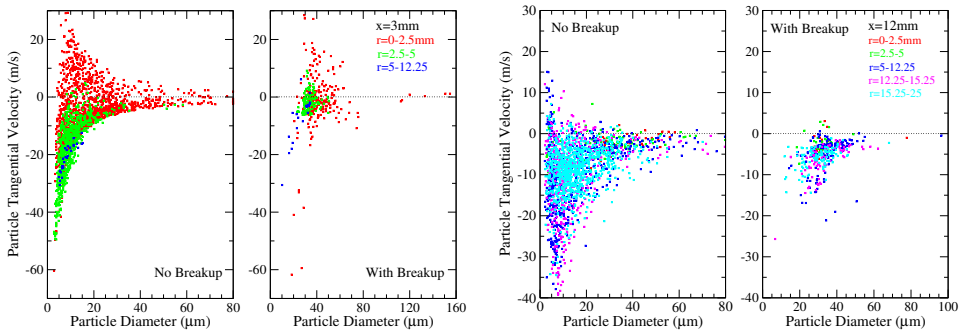

(e) x =3 mm

(f) x =12 mm

Figure 60: Drop-drop correlations at two axial locations for droplet temperature (top row), axial (middle row) and azimuthal (bottom row) velocity versus drop diameter. The scatter data is dissected into three to five radial bins.

is dominant (same as the gas-phase). Parcels within $r < 2.5$ mm are show low positive component in part due to flow field provided by the off-centered PVC switches directions in the central region close to the injector based on its movements. Flow past the dump plane is rotating in counter-clockwise direction and analogous attributes are observed for the liquid phase as seen in Fig. 60f.

Overall, the breakup case yields larger particles closer to the injector, and thereby exhibits delayed response. Also, the PVC rotation is observed to affect the breakup somewhat by entraining the parent droplet, as seen in Fig. 57b. This entrainment imparts velocity components different from those of injection condition to the parent droplets. After breakup, the new droplets inherit these velocities. Also, since the velocity of a particle is based on its temporal evolution, the history of its trajectory and diameter changes plays a major role on its velocity as well. This is clearly seen in the breakup case for both velocity correlations.

Correlation of gas-particle characteristics are shown in Fig. 61 for 1 mm downstream of the dump plane in form of temperature and all three velocity components. Each set of scatter data is separated into four particle radii bins (in microns) to show the effect of particle inertia. Figure 61a shows scatter for gas and drop parcel temperature for with- and without-breakup simulations. Carrier flow field has a significant temperature range $300 - 1500$K, whereas the liquid phase varies about $300 - 650$K. The upper limit for the liquid phase is set by the critical temperature limit beyond which distinct phases cease to exist. Most of the scatter lies within 500K, which is the boiling point limit. Thin line at 45^o indicates perfect correlation among the phases. Smaller size particles are observed to follow this line well. Thermal response for large particles (black, red) are noted to follow almost horizontal line implying negligible correlation with gas-phase. Momentum coupling among the phases is observed in the form of scatter for three components of velocity shown in Fig. 61(b-d). Two dashed lines indicating positive and negative correlations are shown for reference.

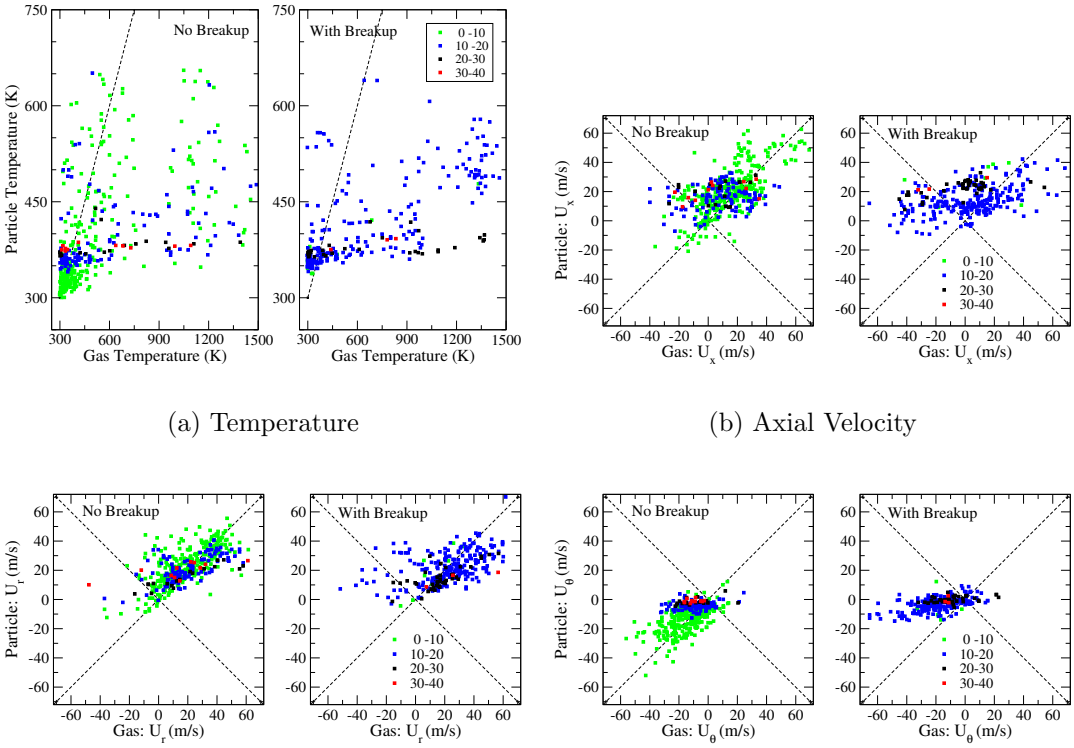

(a) Temperature

(b) Axial Velocity

(c) Radial Velocity

(d) Azimuthal Velocity

Figure 61: Drop-gas correlations at 8 mm downstream of injector for temperature and all three components of velocity are shown. The scatter data is dissected into four bins of droplet radius (in microns).

All three components exhibit a positive correlation especially for smaller particles (green). With increase in particle size, the correlation deviates from 45^o line and gets flatter (or horizontal). This is to be expected based on higher velocity response time for such particles and is more prominent in the breakup case.

6.2.3.5 PVC and Spray Correlation

Spatial structure of the PVC as well as its entrainment effect of particles can be seen in form of spatial correlation among the drop parcel and PVC position. No substantial differences are observed between the two simulations. Two characteristic time-instants for the no breakup simulation are shown in Fig. 62. The PVC position is characterized in the form of lowest pressure position (shown as big solid circle) at a particular streamwise $Y - Z$ plane. The parcel positions coincident in this plane are shown in form of small (open) squares. Combination of colors (black, red) and (blue, green) show distinct time sequence half-wavelength ($\tau/2$) apart. At 1.5 mm downstream of the injection location, the parcels are noted to be clustered close to the PVC. Progressing further downstream, the particles move radially outwards as well as rotate with the PVC. The PVC has an anti-clockwise twist in space and the diameter of the path traced out by the temporal rotation of the PVC increases further downstream. The particle movement is observed to follow the PVC motion with some particles lagged behind. Radial dispersion of particles enabled by the PVC is observed to be effective. For example, the particles are dispersed approximately 12 mm radially outwards by 7.5 mm downstream of the injector. This is close to 120^o inner cone angle for the dispersion. The cross-sectional spray structure is neither solid- nor hollow-cone.

Preferential entrainment of particles into the PVC structure can be observed by sparsing the spatial correlation among the droplet parcels and the PVC into bins of

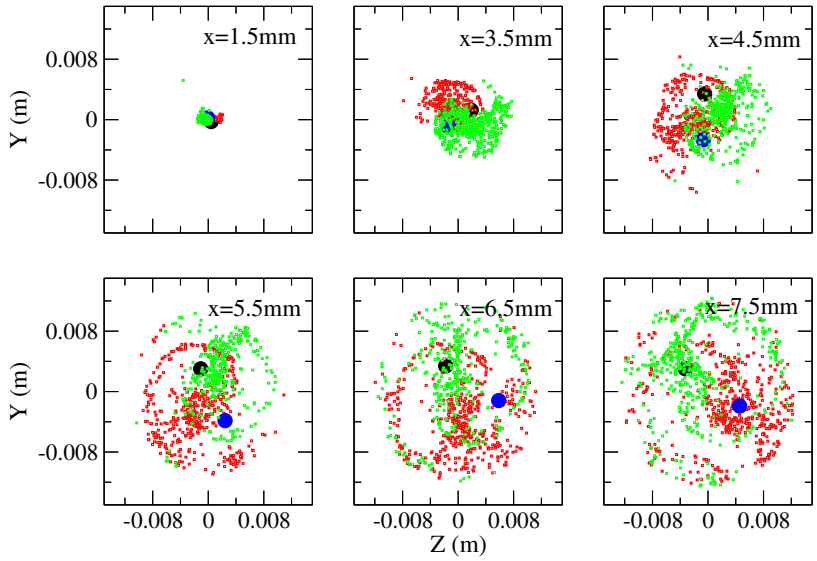

Figure 62: Spatial correlation among droplet parcel and PVC position at two time-instants for without-breakup simulations. Big solid circle indicates PVC position whereas small open squares represent droplets. Black and red colors indicate positions at $t = 0.25\tau$ whereas blue and green at $t = 0.75\tau$ time-instant.

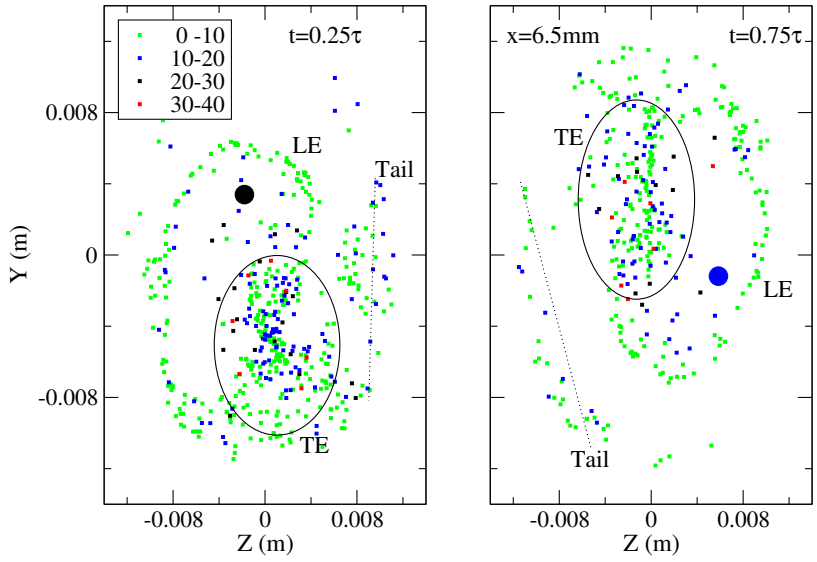

Figure 63: Spatial correlation among droplet parcel and PVC position at two time-instants for 6.5 mm downstream of the injector. Big solid circle indicates PVC position whereas small squares represent droplets. The data is dissected into four bins of droplet radius (in microns).

parcel radius. This is performed at 6.5 mm downstream of the injector at two time-instants shown in Fig. 63. As seen previously, the big solid circle indicates the PVC position whereas small open squares locate the parcels. Transient spatial structure in terms of particle positions relative to the PVC is observed. The scatter is made up of three regions: the leading edge (LE), the trailing edge (TE) and the tail region. The leading edge region contains small particles (green color), whereas the large particles (black, red) are mainly concentrated in the trailing edges. Primary reason for this is the faster response of the smaller particles to movement of PVC via outwardly oriented (from the PVC position) velocity field. There is also a tail region, which is considered to be lag effect from the previous PVC rotation. Overall effect of the PVC is to increase spatial dispersion of the spray particles by entrainment.

6.3 Summary

LES of an experimental liquid-fueled LDI combustor is performed using a subgrid mixing and combustion model. In this approach, no adjustable parameters are required and the entire flow path through the inlet swirl vanes is resolved. Incorporation of a subgrid liquid breakup model eliminated the need to specify liquid-phase size-velocity inflow condition and still able to recover global spray characteristics. Stand-alone validation on a solid-cone spray jet are performed for two breakup models and overall reasonable agreement for transient spray tip progression and spreading angle is obtained. Kelvin-Helmholtz (or aerodynamic) breakup model by Reitz is adopted for the combustor simulation. Two simulations (with- and without-breakup) are performed and compared with measurements. Time-averaged velocity prediction comparison for both gas- and liquid-phase with available data show reasonable agreement. The major impact of breakup is on the fuel evaporation in the vicinity of the injector. Further downstream, a wide range of drop sizes are recovered by the breakup simulation and produces similar spray quality as in the no-breakup case.

CHAPTER VII

CONCLUSIONS

The primary objective of the study is to develop a first principles simulation methodology to resolve the entire two-phase flow field including the material interface. The emphasis is to develop an algorithm suitable to study multi-dimensional (two- and three-dimensions) configurations. In this regard, a compressible five-equation interface model for the simulation of material boundaries between immiscible fluids with arbitrary equation of state is developed and validated. This model extends the work of Allaire [4] to include capillary effects within a Roe-type scheme in addition to accounting for acoustic, viscous, and body-force effects in the flow field. The need for multi-dimensional simulation capability is addressed by employing an approximate Riemann solver following Roe, which represents a cost-effective alternative to an exact Riemann solution. The simulation methodology combines a high-resolution discontinuity capturing method with a low-dissipation central scheme based on MacCormack resulting in a hybrid approach for the solution of time- and space-accurate interface problems. Such an approach is designed to retain advantages of each scheme in different parts of the flow field and enabling the combined scheme to resolve diverse effects.

Mathematical analysis of the five-equation interface model showed that the system of equations are hyperbolic in character. Also, the eigenvalues of the interface model with capillary effects are noted to be the same as for the Euler system of equations. Wave amplitudes corresponding to the eigenstructure are also noted to revert back to those of the Euler system in absence of capillarity. Effect of surface tension on the Riemann wave structure is also discussed. It is observed that capillary effects appear

in form of a contact discontinuity corresponding to a linearly degenerate eigenvalue. The corresponding pressure jump across the contact discontinuity is noted to be proportional to the surface tension coefficient and the interface curvature.

A Roe matrix and associated numerical flux accounting for the capillary effects are defined based on the eigenstructure of the interface model. Both the matrix and the numerical flux showed the effect of capillarity in form of an additional term in conjuction with pressure. A variable extrapolation method following the MUSCL approach is implemented to compute the numerical flux at the cell boundaries.

Detailed validation of the interface model is presented along with parallel computing performance of the algorithm. Several test cases are chosen in line with the focus of developing algorithm for multi-dimensional configuration. The accuracy of the interface model is quantified by comparing the pressure jump across the material interface with the Laplace-Young law in case of a static drop in equilibrium. Both two- and three-dimensional liquid drops are considered. The effect of varying grid size on the solution is also studied and the algorithm is observed to be mesh convergent. The magnitude of spurious currents is also quantified showing Capillary number (or non-dimensional velocity) of $O(10^{-4})$ which is of similar order of accuracy as reported by other studies.

Dynamics of interface movement is also studied in the context of a deformed elliptical liquid drop. The surface tension induced interface oscillations and change of drop shape are correllated to interchange of potential and kinetic energy of the drop. The frequency of the energy interchange is then compared to the analytical result following Fyfe *et al.* [56]. Both 2D and 3D test cases predicted the oscillation period to within 4.5% of the theoretical value. Four stages of energy interchange between the potential and kinetic modes are also visualized indicating a complex set of vortical patterns in and around the interface.

To further demonstrate the applicability of the model to diverse set of applications,

we presented a test case involving a gas bubble rise in a liquid bulk. Gravity generated buoyancy forces accounted for the bubble rise and its effect for various Reynolds and Eötvös numbers is presented. The deformation of an initially circular bubble is shown to reasonably predict the shape-regimes of Clift *et al.* [34]. All cases showed presence of counter-rotating vortices and their effects on the bubble shape. Vortices are also shown to break the bubble into one primary and two secondary entities in case of a low surface tension fluid.

Capability of the model to account for large deformation and eventual breakup in cases of large density ratios between the fluids is assessed in form of liquid drop breakup under gravitational acceleration. Visualization of the flow field indicated significant drop distortion creating a sack-like structure. This is followed by a filament formation and its ensuing breakup into primary and several secondary drops. Suspension of some liquid mass on the upper wall due to surface tension generated wall adhesion is also noted. These characteristics are shown to be in good agreement with measurement observations.

A series of simulations in both 2D and 3D are performed for a liquid drop in a convecting gas medium to study the transient drag behavior and drop deformation. Effects of the Reynolds number and the Weber number on drag dynamics are also investigated. All cases showed that the liquid drop drag coefficient is always larger than the steady counterpart of a rigid cylinder (for 2D) or sphere (for 3D) at the same Reynolds number. These observations are consistent with the measurement data of Temkin and Kim [208]. Initial Weber number is observed to have significant impact on the drag dynamics in form of increased deformation for a low surface tension fluid and resulting larger drag. Presence of "Hill Vortex" is also confirmed in case of a non-deforming drop.

The fifth and final test case for the interface model considered two scenarios of head-on binary collision for equally-sized liquid drops. The outcome of the collision

is shown to depend on the initial momentum of the drops. Energy balance indicated the impact of high initial momentum in increasing the surface energy to surpass the initial surface energy to result in a non-coalescence outcome of the collision. Several physical characteristics of the problem: surface merging upon impact, impact pressure generated liquid matter expulsion, formation of a thin filament, and filament breakup into secondary particles are also well-captured.

The main advantage of this approach is its simplicity of algorithm both as a single solver for different phases as well as demonstrated multi-dimensional capability. The approach also provides a comprehensive consideration in a cost-effective manner of several processes inherent to interface dynamics. The detailed simulation approach of the five-equation interface model is shown to accurately capture interface dynamics as well as is able to deal with dynamic appearance and disappearance of material boundaries. Several test cases involving both high density and viscosity ratios are simulated showing the capability of the method to manage wide range of physical problems.

The study is also aimed to identify the modeling requirements to perform Large-Eddy Simulation (LES) of spray combustion in engineering devices. Three requirements are identified and implemented in a gas turbine combustor simulation to study effects of subgrid liquid atomization model on the reacting flow field. The modeling requirements fall into three categories: (i) simulation methodology free of model parameters, (ii) realistic inflow boundary information, and (iii) inclusion of atomization processes. Accordingly, LES of an experimental, liquid-fueled LDI combustor is performed using a subgrid mixing and combustion model. This approach has no adjustable parameters and the entire flow-path through the inlet swirl vanes is resolved. These aspects fulfills the first two modeling requirements. The third requirement is satisfied by incorporating a subgrid liquid breakup model. The inclusion of the

atomization aspects within LES eliminated the need to specify dispersed-phase size-velocity correlations at the inflow boundary.

Stand-alone validation on a solid-cone non-evaporating spray jet following measurements of Hiroyasu and Kadota [74] are performed for two breakup models and overall reasonable agreement for transient spray tip progression and spreading angle is obtained. Kelvin-Helmholtz (or aerodynamic) breakup model by Reitz is adopted for the combustor simulation. Two simulations (with- and without-breakup) are performed and compared with measurements of Cai *et al.* [20]. Time-averaged velocity prediction comparison for both gas- and liquid-phase with available data show reasonable agreement. The major impact of breakup is on the fuel evaporation in the vicinity of the injector. Further downstream, a wide range of drop sizes are recovered by the breakup simulation and produces similar spray quality as in the no-breakup case.

Unsteady features such as the efficient dispersion of the spray by the rotating Precessing Vortex Core (PVC) structure and the flame stabilization by the recirculation zone are also captured in the simulations thereby, providing an opportunity to investigate the coupling between these features in the combustor. Flame structure in form of Takeno flame index showed presence of diffusion flame in the central portion whereas premixed burning mode farther away. Instantaneous thermo-chemical states of fuel-air mixing and oxidation are also presented indicating significant departure from the gaseous diffusion limits and consistent with two-phase studies of Reveillon and Vervisch [170]. Particle-particle correlations showed effects of particle response time for both thermal and velocity inertia in form of faster response of smaller droplets. Particle-gas scatter indicated overall positive correlations among their temperature and all three velocity components. This is especially true for smaller particles. Spatial structure of the PVC and resulting entrainment of particles indicated highly temporal- and spatial-dependent particle behavior.

The compressible two-phase approach developed here compliments the engineering models used for practical applications by providing basic closures from first principles like drag effects, time-dependent deformation and atomization, evaporation rates, etc. Also, the detailed two-phase approach provides avenues to develop curve-fits for wide range of conditions, typically not available via measurements, which can be used within a LES simulation. In summary, this research provides both detailed as well as engineering solutions to study atomization processes and the aspect of linking the two solutions is left for future studies.

CHAPTER VIII

RECOMMENDATIONS FOR FUTURE WORK

There several unresolved aspects both in the five-equation interface model as well as the LEMLES engineering model that could be pursued in the future.

Heat and Mass Transfer The five-equation interface model extension to account for heat and mass transfer effects will lead to a valuable contribution. Detailed simulation of fuel evaporation in presence of thermal gradients or an engulfing flame surface would lead to better understanding of interface processes and related coupling of capillary, viscous, and mass diffusivity effects. In order to capture such phenomenon, some of the assumptions (such as immiscibility of fluids) employed in this study would have to be relaxed.

Interface Sharpening and Curvature Estimation In the current study, the interface is observed to occupy approximately 4-8 cells especially in cases with large density ratios. Interface sharpening techniques could be applied at each time-step to obtain a sharp material boundary. Also, a higher-order gradient evaluation could be applied to compute the interface curvature. This will lead to overall higher-order spatial accuracy.

Coupling Eulerian Interface Model with Lagrangian Tracking The five-equation interface model considers both phases in an Eulerian framework. Consider a case of a liquid jet breakup where the interface model is applied in the injector region and thereby resolving dense atomization aspects. Further downstream, breakup of liquid jet has formed discrete entities which can then be tracked within the Lagrangian

framework. The combined approach can then be used to study complete spray field evolution including far downstream.

Dense-regime Corrections Current LEMLES formulation is based on a dilute-spray assumption. This means that the gas-phase does not consider the volume occupied by the liquid drops. Dense-regime corrections can be included to account for the space occupied by the liquid-phase. Also, the drop-drop collision can be included as a subgrid model for the dispersed phase.

Fragmentation Research Several exciting areas exist well beyond the coverage of this work. Especially, areas in super-critical and effervescent atomization. The former is related to processes in the proximity of liquid-vapour transition typically observed in LOX/H2 rocket motors. Effervescent fragmentation is related to explosion of cavities in a liquid volume. Other areas such as solid fragmentation and ligament dynamics also hold great promise.

REFERENCES

[1] Abgrall, R., "How to prevent pressure oscillations in multicomponent flow calculations: A quasi-conservative approach," *Journal of Computational Physics*, vol. 125, pp. 150–160, 1996.

[2] Abgrall, R. and Karni, S., "Computations of compressible multifluids," *Journal of Computational Physics*, vol. 169, pp. 594–623, 2001.

[3] Abgrall, R. and Saurel, R., "Discrete equations for physical and numerical compressible multiphase mixtures," *Journal of Computational Physics*, vol. 186, pp. 361–396, 2003.

[4] Allaire, G., Clerc, S., and Kokh, S., "A Five-equation model for the simulation of interfaces between compressible fluids," *Journal of Computational Physics*, vol. 181, pp. 577–616, 2002.

[5] Amsden, A. A., Ramshaw, J. D., O'Rourke, P. J., and Dukowicz, J. K., "KIVA: A computer program for two- and three-dimensional fluid flows with chemical reactions and fuel sprays," Los Alamos Report No. LA-10245-MS, 1985.

[6] Anderson, J., *Fundamentals of Aerodynamics*. New York, USA: McGraw-Hill, Inc., 2nd ed., 1991.

[7] Andrianov, N. and Warnecke, G., "The Riemann problem for the Baer-Nunziato two-phase flow model," *Journal of Computational Physics*, vol. 195, pp. 434–464, 2004.

[8] Apte, S. V., Goroskhovski, M., and Moin, P., "LES of atomizing spray with stochastic modeling of secondary breakup," *International Journal of Multiphase Flow*, vol. 29, pp. 1503–1522, 2003.

[9] Arai, M., Tabata, M., Hiroyasu, H., and Shimizu, M., "Disintegrating process and spray characterization of fuel jet injected by a diesel nozzle," *Society of Automotive Engineers, SAE 84-0275*, 1984.

[10] Ashgriz, N. and Poo, J., "Coalescence and separation in binary collisions of liquid drops," *Journal of Fluid Mechanics*, vol. 221, pp. 183–204, 1990.

[11] Baer, M. and Nunziato, J., "A two-phase mixture theory for deflagration to detonation transition in granular materials," *International Journal of Multiphase Flows*, vol. 12, no. 6, pp. 861–889, 1986.

[12] Bayvel, L. and Orzechowski, Z., *Liquid Atomization*. Washington, DC 20005-3521: Taylor and Francis, 1993.

[13] Beale, J. C. and Reitz, R. D., "Modeling spray atomization with the kelvin-helmholtz/rayleigh-taylor hybrid model," *Atomization and Sprays*, vol. 9, pp. 623–650, 1999.

[14] Benson, D., "Computational methods in lagrangian and eulerian hydrocodes," *Computer Methods in Applied Mechanics and Engineering*, vol. 99, pp. 235–394, 1992.

[15] Boris, J. and Book, D., "Flux corrected transport: I. SHASTA, a fluid transport algorithm that works," *Journal of Computational Physics*, vol. 11, pp. 38–69, 1973.

[16] Brackbill, J., Kothe, D., and Zemach, C., "A Continuum Method for Modeling Surface Tension," *Journal of Computational Physics*, vol. 100, pp. 335–354, 1992.

[17] Butler, P., Lambeck, M., and Krier, H., "Modeling of shock development and transition to detonation initiated by burning in porous propellant beds," *Combustion and Flame*, vol. 46, pp. 75–93, 1982.

[18] Caboussat, A., Picasso, M., and Rappaz, J., "Numerical simulation of free surface incompressible liquid flows surrounded by compressible gas," *Journal of Computational Physics*, vol. 203, pp. 626–649, 2005.

[19] Cahn, J. and Hilliard, J., "Free energy of a nonuniform system. Part I: Interfacial free energy," *Journal of Chemical Physics*, vol. 28, no. 2, p. 258, 1958.

[20] Cai, J., Jeng, S.-M., and Tacina, R., "The Structure of A Swirl–Stabilized Reacting Spray Issued From an Axial Swirler," AIAA Paper 2005-1424, 2005.

[21] Caiden, R., Fedkiw, R., and Anderson, C., "A numerical method for two-phase flow consisting of separate compressible and incompressible regions," *Journal of Computational Physics*, vol. 166, pp. 1–27, 2001.

[22] Chakravarthy, S. R. and Osher, S., "High resolution applications of the osher upwind scheme for the euler equations," 1983.

[23] Chakravarthy, V. and Menon, S., "Subgrid modeling of premixed flames in the flamelet regime." Flow, Turbulence and Combustion, 2000.

[24] Chakravarthy, V. and Menon, S., "Large-eddy simulations of turbulent premixed flames in the flamelet regime," *Combustion Science and Technology*, vol. 162, pp. 175–222, 2001.

[25] Chakravathy, V. K. and Menon, S., "Subgrid modeling of turbulent premixed flames in the flamelet regime," *Flow, Turbulence and Combustion*, vol. 5, pp. 23–45, 2000.

[26] Chargy, D., Abgrall, R., Fezoui, L., and Larrouturou, B., "Conservative numerical schemes for multicomponent inviscid flows," *La Recherche Aérospatiale*, vol. 2, pp. 61–80, 1992. (English Version).

[27] Chaudary, K. and Redekopp, L., "The non-linear capillary instability of a liquid jet: Part I. Theory," *Journal of Fluid Mechanics*, vol. 96, no. 2, pp. 257–274, 1980.

[28] Chaudary, K. and Redekopp, L., "The non-linear capillary instability of a liquid jet: Part II. Experiments on jet behavior before drop deformation," *Journal of Fluid Mechanics*, vol. 96, no. 2, pp. 275–286, 1980.

[29] Chehroudi, B., Chen, S. H., Bracco, F. V., and Onuma, Y., "On the intact core of full-cone sprays," *Society of Automotive Engineering, SAE 85-0126*, 1985.

[30] Chein, R. and Chung, J., "Effects of vortex pairing on particle dispersion in turbulent shear flows," *International Journal of Multiphase Flows*, vol. 13, no. 6, pp. 785–802, 1987.

[31] Chen, K. H. and Shuen, J. S., "A coupled multi-block solution procedure for spray combustion in complex geometries," *AIAA Paper 1993-0108*, 1993.

[32] Chigier, N., "The physics of atomization," Proceedings of the Fifth International Conference on Liquid Atomization and Spray Systems (ICLASS), Gaithersburg, MD, Paper A, 1991.

[33] Chigier, N. and Reitz, R. D., "Regimes of jet breakup and breakup mechanisms," pp. 109–135, AIAA Progress in Astronautics and Aeronautics, Recent Advances in Spray Combustion, K. Kuo, Ed. Volume 166, 1995.

[34] Clift, R., Grace, J., and Weber, M., *Bubbles, Drops and Particles*. New York: Academic Press, 1978.

[35] Colella, P. and Woodward, P., "The piecewise-parabolic method for hydrodynamics," *Journal of Computational Physics*, vol. 54, pp. 174–201, 1984.

[36] Courant, R., Isaacson, E., and Reeves, M., "On the solution of nonlinear hyperbolic differential equations by finite differences," *Comm. Pure and Applied Mathematics*, vol. 5, pp. 243–255, 1952.

[37] Crowe, C. T., Sommerfeld, M., and Tsuji, Y., "Multiphase flows with droplets and particles," CRC Press LLC, Boca Raton, FL, 1998.

[38] Dai, M., Wang, H., Perot, J., and Schmidt, D., "Direct Interface Tracking of Droplet Deformation," *Atomization and Sprays*, vol. 12, pp. 721–735, 2002.

[39] Deledicque, A. and Papalexandris, M., "An exact Riemann solver for compressible two-phase flow models containing non-conservative products," *Journal of Computational Physics*, p. (In Press), 2006.

[40] Drew, D., "Mathematical modeling of two-phase flow," *Annual Review of Fluid Mechanics*, vol. 15, pp. 261–291, 1983.

[41] Drew, D. and Passman, S., "Theory of Multicomponent Fluids," Applied Mathematical Sciences, Volume 135, Springer, New York, 1998.

[42] Dukowicz, J. K., "A particle-fluid numerical method for liquid sprays," *Journal of Computational Physics*, vol. 35, pp. 229–253, 1980.

[43] Eggenspieler, G. and Menon, S., "Combustion and emission modeling near lean blow-out in gas turbine engines," *Progress in Computational Fluid Dynamics*, vol. 5, pp. 281–297, 2005.

[44] Eggers, J., "Nonlinear dynamics and breakup of free-surface flows," *Reviews of Modern Physics*, vol. 69, no. 3, pp. 865–929, 1997.

[45] Erlebacher, G., Hussaini, M. Y., Speziale, C. G., and Zang, T. A., "Toward the large-eddy simulation of compressible turbulent flows," *Journal of Fluid Mechanics*, vol. 238, pp. 155–185, 1992.

[46] Faeth, G. M., "Evaporation and combustion of sprays," *Progress in Energy and Combustion Science*, vol. 9, pp. 1–76, 1983.

[47] Faeth, G. M., "Mixing, transport and combustion in sprays," *Progress in Energy and Combustion Science*, vol. 13, pp. 293–345, 1987.

[48] Faeth, G. M., "Spray combustion phenomena," *Proc. Combust. Inst.*, vol. 26, pp. 1593–1612, 1996.

[49] Faeth, G. M., Hsiang, L.-P., and Wu, P.-K., "Structure and Breakup Properties of Sprays," *Int. J. Multiphase Flow*, vol. 21, pp. 99–127, 1995.

[50] Fedkiw, R., Merriman, B., and Osher, S., "Numerical methods for a 1D interface separating compressible and incompressible flows," in: Barriers and Challenges in Computational Fluid Dynamics, Kluwer Academic Publishers, Dordrecht, 1998.

[51] Francois, M., Cummins, S., Dendy, E., Kothe, D., Sicilian, J., and Williams, M., "A balanced-force algorithm for continuous and sharp interfacial surface tension models within a volume tracking framework," *Journal of Computational Physics*, vol. 213, pp. 141–173, 2006.

[52] Fryxell, B. and Menon, S., "Hybrid Simulations of Richtmyer-Meshkov Instability," 43rd AIAA Aerospace Sciences Meeting, AIAA Paper 05-0314, Reno, NV., 2005.

[53] Fureby, C., Alin, N., Wikstrom, N., Menon, S., Svanstedt, N., and Persson, L., "Large-eddy simulation of high-reynolds number wall-bounded flows," *AIAA J.*, vol. 42, pp. 457–468, 2004.

[54] Fureby, C. and Lofstrom, C., "Large-eddy simulations of bluff-body stabilized flames," *Twenty-fifth Symposium (International) on Combustion, The Combustion Institute*, vol. 25, pp. 1257–1264, 1994.

[55] Fureby, C. and Möller, S.-I., "Large-eddy simulation of reacting flows applied to bluff body stabilized flames," *AIAA Journal*, vol. 33, no. 12, pp. 2339–2347, 1995.

[56] Fyfe, D., Oran, E., and Fritts, M., "Surface Tension and Viscosity with Lagrangian Hydrodynamics on a Triangular Mesh," *Journal of Computational Physics*, vol. 76, pp. 349–384, 1988.

[57] Génin, F., *Study of Compressible Turbulent Flows in Supersonic Environment by Large-Eddy Simulation.* PhD dissertation, Georgia Institute of Technology, Aerospace Engineering, 2007.

[58] Génin, F., Fryxell, B., and Menon, S., "Simulation of Detonation Propagation in Turbulent Gas-Solid Reactive Mixtures," 41st Joint Propulsion Conference and Exhibit, AIAA Paper 05-3967, Tucson, AZ., 2005.

[59] Glimm, J., McBryan, O., Menikoff, R., and Sharp, D., "Front tracking applied to rayleigh-taylor instability," *SIAM Journal on Scientific and Statistical Computing*, vol. 7, no. 1, pp. 230–251, 1986.

[60] Godunov, S. K., "A finite difference method for the computation of discontinuous solutions of the equations of fluid dynamics," *Mat. Sbornik*, vol. 47, pp. 357–393, 1959.

[61] Gonthier, K. and Powers, J., "A high-resolution numerical method for a two-phase model of deflagration-to-detonation transition," *Journal of Computational Physics*, vol. 163, pp. 376–433, 2000.

[62] Gorokhovski, M., "The stochastic lagrangian model of drop breakup in the computation of liquid sprays," *Atomization and Sprays*, vol. 11, pp. 505–519, 2001.

[63] Gueyffier, D., Li, J., Nadim, A., Scardovelli, R., and Zaleski, S., "Volume-of-fluid interface tracking with smoothed surface stress methods for three-dimensional flows," *Journal of Computational Physics*, vol. 152, pp. 423–456, 1999.

[64] Han, Z., Parrish, S., Farrell, P. V., and Reitz, R. D., "Modeling atomization processes of pressure swirl hollow-cone fuel sprays," *Atomization and Sprays*, vol. 7, pp. 663–684, 1997.

[65] Hankin, R., "The Euler Equations for Multiphase Compressible Flow in Conservative Form," *Journal of Computational Physics*, vol. 172, pp. 808–826, 2001.

[66] Harlow, F. and Amsden, A., "Fluid Dynamics," Monograph LA-4700 Los Alamos National Laboratory, Los Alamos, NM., 1971.

[67] Harlow, F. and Amsden, A., "Numerical calculation of multiphase fluid flow," *Journal of Computational Physics*, vol. 17, pp. 19–52, 1975.

[68] Harten, A., "On a class of high resolution total variation stable finite difference schemes," *SIAM Journal of Numerical Analysis*, vol. 21, pp. 1–23, 1984.

[69] Harten, A., Hyman, J., and Lax, P., "On finite difference approximation and entropy conditions for shocks," *Comm. Pure and Applied Mathematics*, vol. 29, pp. 297–322, 1976.

[70] Harten, A., Lax, P. D., and van Leer, B., "On upstream differencing and godunov-type schemes for hyperbolic conservation laws," *SIAM Review*, vol. 25, pp. 35–61, 1983.

[71] Harten, A. and Zwas, G., "Self-adjusting hybrid schemes for shock computations," *Journal of Computational Physics*, vol. 9, pp. 568–583, 1972.

[72] Helenbrook, B. and Edwards, C., "Quasi-steady deformation and drag of uncontaminated liquid drops," *International Journal of Multiphase Flows*, vol. 28, no. 10, pp. 1631–1657, 2002.

[73] Hiroyasu, H., Arai, M., and Shimizu, M., "Breakup length of a liquid jet and internal flow in a nozzle," *ICLASS-91, Gaithersburg, MD; July*, 1991.

[74] Hiroyasu, H. and Kadota, T., "Fuel droplet size distribution in diesel combustion chamber," *Society of Automotive Engineering, SAE 740715*, 1974.

[75] Hirsch, C., *Numerical Computation of Internal and External Flows*, vol. 2. New York: John Wiley and Sons, Inc., 1997.

[76] Hirt, C. and Nichols, B., "Volume-of-fluid method for the dynamics of free boundaries," *Journal of Computational Physics*, vol. 39, pp. 201–225, 1981.

[77] Hsiang, L. and Faeth, G., "Secondary breakup in the deformation regime," 30th AIAA Aerospace Sciences Meeting, AIAA Paper 92-0110, Reno, NV., 1992.

[78] Hsiang, L. and Faeth, G., "Drop deformation and breakup due to shock wave and steady disturbances," *International Journal of Multiphase Flow*, vol. 21, no. 4, pp. 545–560, 1995.

[79] Huh, K. Y. and Gosman, A. D., "A phenomenological model of diesel spray atomization," *Proceeding of International Conference on Multiphase Flow, Tsukuba, Japan; September 24-27*, 1991.

[80] Huh, K. Y., Lee, E., and Koo, J. Y., "Diesel spray atomization model considering nozzle exit turbulence conditions," *Atomization and Sprays*, vol. 8, pp. 453–469, 1998.

[81] Iannetti, A., Tacina, R., Cai, J., and Jeng, S, M., "Multi-Swirler Aerodynamics: CFD Predictions," AIAA Paper 2001-3575, 2001.

[82] Iannetti, A. C., Tacina, R., Jeng, S, M., and Cai, J., "Towards Accurate Prediction of Turbulent, Three-Dimensional, Recirculating Flows with the NCC," AIAA Paper 2001-0809, 2001.

[83] Ibrahim, E. A., Yang, H. Q., and Przekwas, A. J., "Modeling of spray droplets deformation and breakup," *Journal of Propulsion*, vol. 9, no. 4, pp. 651–654, 1993.

[84] Ishii, M., *Thermally induced flow instabilities in two-phase mixtures in thermal equilibrium*. PhD dissertation, Georgia Institute of Technology, 1971.

[85] Jacqmin, D., "An energy approach to the continuum surface tension method," 34th AIAA Aerospace Sciences Meeting, AIAA Paper 96-0858, Reno, NV., 1996.

[86] James, S., Zhu, J., and Anand, M., "Large-eddy simulations as a design tool for gas turbine combustion systems," *AIAA Journal*, vol. 44, no. 4, pp. 674–686, 2006.

[87] Jamet, D., Lebaigue, O., Coutris, N., and Delhaye, J., "The second gradient method for the direct numerical simulation of liquid-vapor flows with phase change," *Journal of Computational Physics*, vol. 169, no. 2, pp. 624–651, 2001.

[88] Jamet, D., Torres, D., and Brackbill, J., "On the theory and computation of surface tension: the elimination of parasitic currents through energy conservation in the second gradient method," *Journal of Computational Physics*, vol. 182, no. 1, pp. 262–276, 2002.

[89] Kang, M., Fedkiw, R., and Liu, X., "A boundary condition capturing method for multiphase incompressible flow," *Journal of Scientific Computing*, vol. 15, no. 3, pp. 323–360, 2000.

[90] Kapila, A., Menikoff, R., Bdzil, J., Son, S., and Stewart, D., "Two-phase modeling of DDT in granular materials: reduced equations," *Physics of Fluids*, vol. 13, no. 10, pp. 3002–3024, 2001.

[91] Karni, S., "Viscous shock profiles and primitive formulations," *SIAM Journal on Numerical Analysis*, vol. 29, no. 6, pp. 1592–1609, 1992.

[92] Karni, S., "Multicomponent flow calculations by a consistent primitive algorithm," *Journal of Computational Physics*, vol. 112, no. 1, pp. 31–43, 1994.

[93] Kerstein, A. R., "Linear-eddy model of turbulent scalar transport and mixing," *Combustion Science and Technology*, vol. 60, pp. 391–421, 1988.

[94] Kerstein, A. R., "Linear-eddy model of turbulent transport: Part 2," *Combustion and Flame*, vol. 75, pp. 397–413, 1989.

[95] Kerstein, A. R., "Linear-eddy modeling of turbulent transport, part 4: Structure of diffusion-flames," *Combustion Science and Technology*, vol. 81, pp. 75–86, 1992.

[96] Kim, W.-W. and Menon, S., "A new incompressible solver for large-eddy simulations," *International Journal of Numerical Fluid Mechanics*, vol. 31, pp. 983–1017, 1999.

[97] Kim, W.-W., Menon, S., and Mongia, H. C., "Large-eddy simulation of a gas turbine combustor flow," *Combustion Science and Technology*, vol. 143, pp. 25–62, 1999.

[98] Kim, W. W., Menon, S., and Mongia, H. C., "Large-eddy simulation of a gas turbine combustor flow," *Combustion Science and Technology*, vol. 143, pp. 25–62, 1999.

[99] Kim, Y. M., Shang, H. M., Chen, C. P., and Wang, T. S., "Numerical studies on droplet breakup models," *Journal of Propulsion*, vol. 11, no. 2, pp. 389–392, 1994.

[100] Kirpekar, S. and Bogy, D., "A benchmark for the flow across a square cylinder using commercial cfd codes," *2005 APS Division of Fluid Dynamics 58th Annual Meeting, November 20-22, 2005, Chicago, IL*, 2005.

[101] Kirtas, M., Patel, N., Sankaran, V., and Menon, S., "Large-Eddy Simulation of a Swirl-Stabilized, Lean-Direct Injection Spray Combustor," *Proceedings of ASME GT2006 (Barcelona, Spain)*, vol. GT 2006-91310, 2006.

[102] Kokh, S. and Allaire, G., "Numerical simulation of 2D two-phase flows with interface," in *Godunov Methods: Theory and Applications*, pp. 513–518, Kluwer Academic/Plenum, 2001.

[103] Kreyszig, E., *Advanced Engineering Mathematics*. New York: John Wiley and Sons, Inc., 7th ed., 1993.

[104] Lafaurie, B., Nardone, C., Scardovelli, R., Zaleski, S., and Zanetti, G., "Modeling, Merging and Fragmentation in Multiphase Flows with SURFER," *Journal of Computational Physics*, vol. 113, pp. 134–147, 1994.

[105] Lamb, H., *Hydrodynamics*. New York: Dover, 6th ed., 1945.

[106] Larrouturou, A., "How to preserve the mass fractions positivity when computing compressible multi-component flows," *Journal of Computational Physics*, vol. 95, no. 1, pp. 59–84, 1991.

[107] Lax, P. D., "Hyperbolic systems of conservation laws and the mathematical theory of shock waves," *SIAM Regional Conference Series in Applied Mathematics*, no. 11, 1972.

[108] Lefebvre, A. H. in *Gas Turbine Combustion, 2nd Edition*, Taylor and Francis, 1998.

[109] Leonard, A., "Vortex methods for flow simulation," *Journal of Computational Physics*, vol. 37, pp. 289–335, 1980.

[110] Lilly, D. K., "A proposed modification of the germano subgrid-scale closure method," *Physics of Fluids A*, vol. 4, no. 3, pp. 633–635, 1992.

[111] Liu, A. B., Mather, D., and Reitz, R. D., "Modeling the effects of drop drag and breakup on fuel sprays," *Society of Automotive Engineers, SAE 93-0072*, 1993.

[112] Liu, A. B. and Reitz, R. D., "Mechanisms of air-assisted liquid atomization," *Atomization and Sprays*, vol. 3, pp. 55–75, 1993.

[113] Liu, S., Meneveau, C., and Katz, J., "On the properties of similarity subgrid-scale models as deduced from measurements in a turbulent jet," *Journal of Fluid Mechanics*, vol. 275, pp. 83–119, 1994.

[114] Loth, E., "Numerical Approaches to Dilute Two-Phase Flow," *Progress in Energy and Combustion Science*, vol. 26, no. 3, pp. 161–223, 2000.

[115] Lucca-Negro, O. and O'Doherty, T., "Vortex Breakdown: A Review," *Progress in Energy and Combustion Science*, vol. 27, no. 4, pp. 431–481, 2001.

[116] MacCormack, R. W., "The effects of viscosity in hyper–velocity impact cratering," *AIAA Paper 1969-354*, 1969.

[117] MacCormack, R. W., "An efficient numerical method for solving the time-dependent compressible navier-stokes equations at high reynolds number," Tech. Rep. NASA Technical Memorandum x-73, National Aeronautics and Space Administration, 1976.

[118] Massoni, J., Saurel, R., Nkonga, B., and Abgrall, R., "Some models and eulerian methods for interface problems between compressible fluids with heat transfer," *International Journal of Heat and Mass Transfer*, vol. 45, pp. 1287–1307, 2002.

[119] Meier, W., Duan, X., and Weigand, P., "Investigations of Swirl Flames in a Gas Turbine model Combustor, Part II: Turbulence-Chemistry Interactions," *Combustion and Flame*, vol. 144, pp. 225–236, 2006.

[120] Menon, S., "Subgrid combustion modeling for large-eddy simulations of single and two-phase flow," in *LES of Complex Transitional and Turbulent Flows*, pp. 329–352, Kluwer Press, 2000.

[121] Menon, S., "Co emission and combustion dynamics near lean blow-out in gas turbine engines," *ASME-GT2004-53290*, 2004.

[122] Menon, S. and Calhoon, W., "Subgrid mixing and molecular transport modeling for large-eddy simulations of turbulent reacting flows," *Proceedings of the Combustion Institute*, vol. 26, pp. 59–66, 1996.

[123] Menon, S. and Kim, W.-W., "High reynolds number flow simulations using the localized dynamic subgrid-scale model," *AIAA Paper 96–0425*, 1996.

[124] Menon, S., McMurtry, P., and Kerstein, A. R., "A linear eddy mixing model for large eddy simulation of turbulent combustion," in *LES of Complex Engineering and Geophysical Flows* (Galperin, B. and Orszag, S., eds.), pp. 287–314, Cambridge University Press, 1993.

[125] Menon, S. and Pannala, S., "Subgrid Modeling of Unsteady Two-Phase Turbulent Flows," *AIAA Paper 97-3113*, 1997.

[126] Menon, S. and Patel, N., "Perspective on subgrid spray injection modeling in gas turbine engines," in *XVII International Symposium on Air Breathing Engines*, no. 2005-1105, AIAA, 2005.

[127] Menon, S. and Patel, N., "Subgrid modeling for les of spray combustion in large-scale combustors," *AIAA Journal*, vol. 44, no. 4, pp. 709–723, 2006.

[128] Menon, S., Yeung, P. K., and Kim, W. W., "Effect of subgrid models on the computed interscale energy transfer in isotropic turbulence," *Computers and fluids*, vol. 25, no. 2, pp. 165–180, 1996.

[129] Miller, R. S. and Bellan, J., "Direct numerical simulation of a confined three-dimensional gas mixing layer with one evaporating hydrocarbon-droplet-laden stream," *Journal of Fluid Mechanics*, vol. 384, pp. 293–338, 1999.

[130] Morozumi, Y., Ishizuka, H., and Fukai, J., "Criterion between permanent coalescence and separation for head-on binary droplet collision," *Atomization and Sprays*, vol. 15, pp. 61–80, 2005.

[131] Murrone, A. and Guillard, H., "A five-equation reduced model for compressible two-phase flow problems," *Journal of Computational Physics*, vol. 202, pp. 664–698, 2005.

[132] Neitzel, G. and Dell'Aversana, P., "Noncoalescence and Nonwetting Behavior of Liquids," *Annual Review of Fluid Mechanics*, vol. 34, pp. 267–289, 2002.

[133] Nelson, C. C., *Simulations of spatially evolving compressible turbulence using a local dynamic subgrid model*. PhD thesis, Georgia Institute of Technology, Aerospace Engineering, 1997.

[134] Nicholls, J., "Stream and droplet breakup by shock waves," *NASA SP-194, Liquid Propellant Rocket Combustion Instability, Eds. D. T. Harrje and F. H. Reardon*, pp. 126–128, 1972.

[135] Nicol, D., Malte, P., Hamer, A., Roby, R., and Steele, R., "Development of a five-step global methane oxidation-no formation mechanism for lean-premixed gas turbine combustion," *Trans. of the ASME: J. of Eng. for Gas Turbine and Power*, vol. 121, no. April, pp. 272–280, 1999.

[136] Noh, W. and Woodward, P., "SLIC: Simple Line Interface Calculation," *In Proceedings of Fifth International Conference of Fluid Dynamics*, vol. 59, pp. 330–340, 1976.

[137] Oefelein, J. C. and Yang, V., "Simulation of high-pressure spray field dynamics," *Recent Advances in Spray Combustion:Spray Combustion and Droplet Burning Phenomena, Progress in Astronautics and Aeronautics*, vol. 166, pp. 263–304, 1995.

[138] O'Rourke, P. J. and Amsden, A. A., "The TAB method for numerical calculation of spray droplet breakup," *Society of Automotive Engineers, SAE 87-2089*, 1987.

[139] O'Rourke, P. J. and Bracco, F. V., "Modeling of drop interactions in thick sprays and comparison with experiments," *Institution of Mechanical Engineers, Pub. ISBN 0 85298 4693*, pp. 101–116, 1980.

[140] Osher, S., "Numerical solution of singular perturbation problems and hyperbolic systems of conservation laws," *In O. Axelsson* et al. *(eds), Mathematical Studies*, vol. 47, 1981.

[141] Osher, S. and Sethian, J., "Fronts propagating with curvature-dependent speed: Algorithms based on hamilton-jacobi formulations," *Journal of Computational Physics*, vol. 79, pp. 12–49, 1988.

[142] Papalexandris, M., "A two-phase model for compressible granular flows based on the theory of irreversible processes," *Journal of Fluid Mechanics*, vol. 517, pp. 103–112, 2004.

[143] Park, J. H., Yoon, T., and Hwang, S. S., "Improved tab model for prediction of spray droplet deformation and breakup," *Atomization and Sprays*, vol. 12, pp. 387–401, 2002.

[144] Park, S. W. and Lee, C. S., "Investigation of atomization and evaporation characteristics of high-pressure injection diesel spray using kh-ddb competition

model," *Proceeding of Institution of Mechanical Engineers, Part D: J. Automobile Engineering*, vol. 218, pp. 767–777, 2004.

[145] Patel, N. and Menon, S., "Simulation of Flow Separation and Reattachment over an Axisymmetric Hill," *Journal of Turbulence*, p. (Submitted), 2007.

[146] Patel, N. and Menon, S., "Simulation of Spray Combustion in a Lean-Direct Injection Combustor," *Thirty-First Symposium (International) on Combustion*, vol. 31, no. 2, pp. 2327–2334, 2007.

[147] Patterson, M. A. and Reitz, R. D., "Modeling the effects of fuel spray characteristics on diesel engine combustion and emission," *Society of Automotive Engineers, SAE 98-0131*, 1998.

[148] Perigaud, G. and Saurel, R., "A compressible flow model with capillary effects," *Journal of Computational Physics*, vol. 209, pp. 139–178, 2005.

[149] Peters, N., *Turbulent Combustion*. Cambridge Monographs on Mechanics, 2000.

[150] Pijl, S., Segal, A., Vuik, C., and Wesseling, P., "A mass-conserving Level-Set method for modeling of multi-phase flows," *International Journal for Numerical Methods in Fluids*, vol. 47, pp. 339–361, 2005.

[151] Pilch, M., Erdman, C., and Reynolds, A., "Acceleration induced fragmentation of liquid drops," U.S. Nuclear Regulatory Commission Report NUREG/CR-2247, 1981.

[152] Pilliod, J. and Puckett, E., "Second-order accurate volume-of-fluid algorithms for tracking material interfaces," *Journal of Computational Physics*, vol. 199, pp. 465–502, 1996.

[153] Poinsot, T. and Veynante, D. in *Theoretical and Numerical Combustion, 2nd Ed.*, R. T. Edwards Inc., 2005.

[154] Poinsot, T. and Lele, S., "Boundary conditions for direct simulations of compressible viscous flow," *Journal of Computational Physics*, vol. 101, pp. 104–129, 1992.

[155] Poinsot, T. and Lele, S., "Boundary conditions for direct simulations of compressible viscous flow," *Journal of Computational Physics*, vol. 101, pp. 104–129, 1992.

[156] Pope, S. B., "Pdf methods for turbulent reactive flows," *Progress in Energy and Combustion Science*, pp. 119–192, 1985.

[157] Pope, S. B. in *Turbulent Flows*, Cambridge University Press, 2000.

[158] Pope, S., "Computationally efficient implementation of combustion chemistry using in-situ adaptive tabulation," *Combustion Theory and Modeling*, vol. 1, pp. 41–63, 1997.

[159] Popinet, S. and Zaleski, S., "A front tracking algorithm for the accurate representation of surface tension," *International Journal of Numerical Methods Fluids*, pp. 775–793, 1999.

[160] Powers, J., Stewart, D., and Krier, H., "Theory of two-phase detonation. Part I. Modeling," *Combustion and Flame*, vol. 80, pp. 264–279, 1990.

[161] Qian, J. and Law, C., "Regimes of coalescence and separation in droplet collision," *Journal of Fluid Mechanics*, vol. 331, pp. 59–80, 1997.

[162] Quan, S. and Schmidt, D., "Direct numerical study of a liquid droplet impulsively accelerated by gaseous flow," *Physics of Fluids*, vol. 18, p. DOI: 102103, 2006.

[163] Reid, R. C., Prausniz, J. M., and Poling, B. E., *The Properties of Gases and Liquids*. Mcgraw Hill Publishing Company, 1988.

[164] Reinecke, W. G. and Waldman, G. D., "A study of drop breakup behind strong shocks with applications to flight," AVCO Report AVSD-0110-70-RR, 1970.

[165] Reitz, R. D., "Modeling atomization processes in high-pressure vaporizing sprays," *Atomization and Spray Technology*, vol. 3, pp. 309–337, 1987.

[166] Reitz, R. D. and Bracco, F. V., "Ultra high-speed filming of atomizing jets," *Physics of Fluids*, vol. 22, pp. 1054–1064, 1979.

[167] Reitz, R. D. and Bracco, F. V., "Mechanisms of atomization of a liquid jet," *Physics of Fluids*, vol. 25, no. 10, pp. 1730–1742, 1982.

[168] Reitz, R. D. and Diwakar, R., "Effect of drop breakup on fuel sprays," *Society of Automotive Engineering, SAE 86-0469*, 1986.

[169] Reitz, R. D. and Diwakar, R., "Structure of high-pressure fuel sprays," *Society of Automotive Engineering, SAE 87-0598*, 1987.

[170] Reveillon, J. and Vervisch, L., "Analysis of Weakly Turbulent Dilute-Spray Flames and Spray Combustion Regimes," *Journal of Fluid Mechanics*, vol. 537, pp. 317–347, 2005.

[171] Ricart, L. M., Xin, J., Bower, G. R., and Reitz, R. D., "In-cylinder measurements and modeling of liquid fuel spray penetration in a heavy-duty diesel engine," *Society of Automotive Engineers, SAE 97-1591*, 1997.

[172] Roe, P., "Approximate riemann solvers, parameter vectors and difference schemes," *Journal of Computational Physics*, vol. 43, pp. 357–372, 1981.

[173] Roe, P. and Pike, J., "Efficient construction and utilization of approximate riemann solutions," in: r. glowinski and j. lions (eds), computing methods in applied sciences and engineering, amsterdam, north holland, 1984.

[174] Rudy, D. H. and Strikwerda, J. C., "Boundary conditions for subsonic compressble navier-stokes calculations," *Computers and Fluids*, vol. 36, 1981.

[175] Rusanov, V., "Calculation of interaction on non-steady shock waves with obstacles," *Journal of Computational Mathematics and Mathematical Physics, USSR*, vol. 1, pp. 267–279, 1961.

[176] Sallam, K. A., Dai, Z., and Faeth, G. M., "Liquid breakup at the surface of turbulent round liquid jets in still gases," *International Journal of Multiphase Flows*, vol. 28, pp. 427–449, 2002.

[177] Sallam, K. A. and Faeth, G. M., "Surface properties during primary breakup of turbulent round liquid jets in still air," *AIAA Journal*, vol. 41, pp. 1514–1524, 2003.

[178] Sankaran, V., *Sub-grid combustion modeling for compressible two-phase flows*. PhD dissertation, Georgia Institute of Technology, Aerospace Engineering, 2003.

[179] Sankaran, V. and Menon, S., "The structure of premixed flame in the thin-reaction-zones regime," *Proc. Combust. Inst.*, vol. 28, pp. 203–210, 2000.

[180] Sankaran, V. and Menon, S., "Alignment statistics and small-scale structures in swirling spray combustion," *Proc. Combust. Inst.*, vol. 29, pp. 577–584, 2002.

[181] Sankaran, V. and Menon, S., "Les of scalar mixing in supersonic shear layers," *Proc. Combust. Inst.*, vol. 30, pp. 2835–2842, 2005.

[182] Sankaran, V. and Menon, S., "Subgrid combustion modeling of 3-d premixed flames in the thin-reaction-zone regime," *Proc. Combust. Inst.*, vol. 30, pp. 575–582, 2005.

[183] Saurel, R. and Abgrall, R., "A multiphase godunov method for compressible multifluid and multiphase flows," *Journal of Computational Physics*, vol. 150, pp. 425–467, 1999.

[184] Saurel, R. and Abgrall, R., "A simple method for compressible multifluid flows," *SIAM J. Sci. Comput.*, vol. 21, no. 3, pp. 1115–1145, 1999.

[185] Saurel, R., Gavrilyuk, S., and Renaud, F., "A multiphase model with internal degrees of freedom: Application to shock-bubble interaction," *Journal of Fluid Mechanics*, vol. 496, pp. 283–321, 2003.

[186] Saurel, R. and LeMetayer, O., "A multiphase model for compressible flows with interfaces, shocks, detonation waves and cavitation," *Journal of Fluid Mechanics*, vol. 431, pp. 239–271, 2001.

[187] Scardovelli, R. and Zaleski, S., "Direct numerical simulation of free-surface and interfacial flow," *Annual Review of Fluid Mechanics*, vol. 031, pp. 567–603, 1999.

[188] Scardovelli, R. and Zaleski, S., "Analytical relations connecting linear interfaces and volume fractions in rectangular grids," *Journal of Computational Physics*, vol. 164, pp. 228–237, 2000.

[189] Schumann, U., "Subgrid scale model for finite difference simulations of turbulent flows in plane channels and annuli," *Journal of Computational Physics*, vol. 18, pp. 376–404, 1975.

[190] Schumann, U., "Realizability of reynolds-stress turbulence models," *Physics of Fluids*, vol. 20, no. 5, pp. 721–725, 1977.

[191] Schwendeman, D., Wahle, C., and Kapila, A., "The Riemann Problem and a high-resolution Godunov method for a model of compressible two-phase flow," *Journal of Computational Physics*, vol. 212, pp. 490–526, 2006.

[192] Shaffer, S. W. and Samuelsen, G. S., "A liquid fueled, lean burn, gas turbine combustor injector," *Combustion Science and Technology*, vol. 139, pp. 41–47, 1998.

[193] Shearer, A. J. and Groff, E. G., "Injection system effects on oscillating-poppet injector sprays," pp. 33–42, Proceedings of the ASME Diesel and Gas Engine Power Division Conference, Ed. A. A. Zagotta, New York, 1984.

[194] Shyue, K., "An efficient shock-capturing algorithm for compressible multicomponent problems," *Journal of Computational Physics*, vol. 142, no. 1, pp. 208–242, 1998.

[195] Smith, T. and Menon, S., "One-dimensional simulations of freely propagating turbulent premixed flames," *Combustion Science and Technology*, vol. 128, pp. 99–130, 1996.

[196] Smolianski, A., "Finite-element/Level-Set/Operator-Splitting (FELSOS) approach for computing two-fluid unsteady flows with free moving interfaces," *International Journal for Numerical Methods in Fluids*, vol. 48, pp. 231–269, 2005.

[197] Steger, J. L. and Warming, R. F., "Flux vector splitting of the inviscid gas dynamics equations with application to finite difference methods," *Journal of Computational Physics*, vol. 40, pp. 263–293, 1981.

[198] Stiesch, G., "Modeling Engine Spray and Combustion Processes," Springer-Verlag, Heidelberg, Germany, 2003.

[199] Stone, C. and Menon, S., "Parallel Simulations of Swirling Turbulent Flames," *Journal of SuperComputing*, vol. 22, no. 1, pp. 7–28, 2002.

[200] Sussman, M., Smereka, P., and Osher, S., "A level set approach for computing solutions to incompressible two-phase flow," *Journal of Computational Physics*, vol. 114, pp. 146–159, 1994.

[201] Sweby, P., "High resolution schemes using flux limiters for hyperbolic conservation laws," *SIAM Journal of Numerical Analysis*, vol. 21, pp. 995–1011, 1984.

[202] Syred, N., "A Review of Oscilllation Mechanisms and the role of the Precessing Vortex Core (PVC) in Swirl Combustion Systems," *Progress in Energy and Combustion Science*, vol. 32, no. 2, pp. 93–161, 2006.

[203] Syred, N., Fick, W., O'Doherty, T., and Griffiths, A., "The Effect of the Precessing Vortex Core on Combustion in a Swirl Burner," *Combustion Science and Technology*, vol. 125, pp. 139–157, 1997.

[204] Tacina, R. R., "Low nox potential of gas turbine engines," AIAA Paper 90-0550, 1990.

[205] Tacina, R. R., Wey, C., Laing, P., and Mansour, A., "A low nox lean-direct injection, multipoint integrated module combustor concept for advanced aircraft gas turbines," NASA Technical Memorandum NASA TM-2002-211347, 2002.

[206] Tannehill, J. C., Anderson, D. A., and Pletcher, R. H. in *Computational Fluid Mechanics and Heat Transfer*, Taylor and Francis, 1997.

[207] Tanner, F. X., "Liquid jet atomization and droplet breakup modeling of non-evaporating diesel fuel sprays," *Society of Automotive Engineers, SAE 97-0050*, 1997.

[208] Temkin, S. and Kim, S., "Droplet motion induced by weak shock waves," *Journal of Fluid Mechanics*, vol. 96, no. 1, pp. 133–157, 1980.

[209] Teo, C. Y., Siow, Y. K., and Yang, S. L., "Flowfield study of ldi combustor with discrete-jet swirler using re–stress model," AIAA Paper 2001-0424, 2001.

[210] Terasaki, T. and Hayashi, S., "Lean non-premixed combustion for low-nox gas turbine combustor," 1995.

[211] Tong, A. and Wang, Z., "A numerical method for capillary-dominant free surface flows," *Journal of Computational Physics*, vol. 221, pp. 506–523, 2007.

[212] Toro, E. and Chou, C., "A linearized Riemann solver for the steady supersonic Euler equations," *International Journal for Numerical Methods in Fluids*, vol. 16, no. 3, pp. 173–186, 1993.

[213] Toro, E. F., *Riemann Solvers and Numerical Methods for Fluid Dynamics*. Heidelberg, Germany: Springer, 2nd ed., 1999.

[214] Trinh, H. P. and Chen, C. P., "Modeling of turbulence effects on liquid jet atomization and breakup," *AIAA 2005–0154*, 2005.

[215] Tryggvason, G., Bunner, B., Esmaeeli, A., Al-Rawahi, N., Tauber, W., Han, J., Jan, Y.-J., Juric, D., and Nas, S., "A front-tracking method for the computation of multiphase flow," *Journal of Computational Physics*, vol. 169, pp. 708–759, 2001.

[216] Tryggvason, G. and Unverdi, S., "Computations of three-dimensional rayleigh-taylor instability," *Physics of Fluids A*, vol. 2, no. 5, pp. 656–659, 1990.

[217] Turns, S. R., *An Introduction To Combustion*. McGraw-Hill, Inc., 2nd ed., 2000.

[218] Unverdi, S. and Tryggvason, G., "A front-tracking method for viscous, incompressible, multi-fluid flows," *Journal of Computational Physics*, vol. 100, pp. 25–37, 1992.

[219] Van Leer, B., "Towards the ultimate conservative difference scheme i. the quest for monotonicity," *Lecture Notes in Physics*, vol. 18, pp. 163–168, 1973.

[220] Van Leer, B., "Towards the ultimate conservative difference scheme iv. a new approach to numerical convection," *Journal of Computational Physics*, vol. 23, pp. 276–299, 1977.

[221] Van Leer, B., "Towards the ultimate conservative difference scheme v. a second order sequel to godunov's method," *Journal of Computational Physics*, vol. 32, pp. 101–136, 1979.

[222] Villermaux, E., "Fragmentation," *Annual Review of Fluid Mechanics*, vol. 39, pp. 419–446, 2007.

[223] Vincent, S. and Caltagirone, J., "Efficient solving method for unsteady incompressible interfacial flow problems," *International Journal for Numerical Methods in Fluids*, vol. 30, no. 6, pp. 795–811, 1999.

[224] Vreman, B., Geurts, B., and Kuerten, H., "Realizability conditions for the turbulent stress tensor in large-eddy simulation," *Journal of Fluid Mechanics*, vol. 278, pp. 351–362, 1994.

[225] Westbrook, C. K. and Dryer, F. L., "Simplified reaction mechanisms for the oxidation of hydrocarbon fuels in flames," *Combustion Science and Technology*, vol. 27, pp. 31–43, 1981.

[226] White, F., *Viscous Fluid Flow*. Boston, Massachusetts: McGraw-Hill, Inc., 2nd ed., 1991.

[227] Wu, P. K. and Faeth, G. M., "Onset and end of drop formation along the surface of turbulent liquid jets in still gases," *Physics of Fluids A*, vol. 7, pp. 2915–2917, 1995.

[228] Wu, P. K., Miranda, R. F., and Faeth, G. M., "Effects of initial flow conditions on primary breakup of non-turbulent and turbulent round jets," *Atomization and Sprays*, vol. 5, pp. 175–196, 1995.

[229] Xin, J., Ricart, L. M., and Reitz, R. D., "Computer modeling of diesel spray atomization and combustion," *Combustion Science and Technology*, vol. 137, pp. 171–, 1998.

[230] Yamashita, H., Shimada, M., and Takeno, T., "A Numerical Study on Flame Stability at Transition Point of Jet Diffusion Flames," *Proc. Combust. Inst.*, vol. 26, pp. 27–34, 1996.

[231] Yang, S. L., Siow, K., Teo, C. Y., and Hanjalic, K., "A kiva code with reynolds–stress model for engine flow simulation," *Energy*, vol. 30, pp. 427–445, 2005.

[232] Yang, S. L., Siow, Y. K., Peschke, B. D., and Tacina, R. R., "Numerical study of nonreacting gas turbine combustor swirl flow using reynolds stress model," *Journal of Engineering for Gas Turbines and Power*, vol. 125, pp. 804–811, 2003.

VITA

Nayan Patel grew up in the small university town of Vallabh Vidyanagar on the outskirts of Anand in the state of Gujarat, India. He is the only loving son of Vinodbhai and Sarojben Patel. Upon graduation from high-school in 1995, he began undergraduate studies in the Birla Vishwakarma Mahavidyalaya (BVM) Engineering College under the Sardar Patel University. He transferred to Georgia Institute of Technology in Atlanta, GA in 1997 to pursue Aerospace Engineering. He joined the graduate program at Georgia-Tech in Summer of 2001 under the guidance of Professor Menon where he received his Master of Science in Aerospace Engineering in July 2004 and a Doctorate in Aerospace Engineering in August 2007. Since then, he has been happily working in the field of combustion and liquid atomization.

He and Ishita Patel have been married since December 2003.